

A COUPLED DISCRETE SPECTRAL WAVE HINDCAST MODEL

By

LI-HWA LIN

A DISSERTATION PRESENTED TO THE GRADUATE SCHOOL  
OF THE UNIVERSITY OF FLORIDA IN  
PARTIAL FULFILLMENT OF THE REQUIREMENTS  
FOR THE DEGREE OF DOCTOR OF PHILOSOPHY

UNIVERSITY OF FLORIDA

1988

UNIVERSITY OF FLORIDA



3 1262 08552 3438

## ACKNOWLEDGEMENTS

The author would like to express his sincere gratitude to his adviser, Dr. Hsiang Wang, Department Chairman of Coastal and Oceanographic Engineering, for his ideas, advice and support throughout this study, and also to coadviser Dr. Bent A. Christensen, Professor of Civil Engineering, for his guidance and encouragement. The author is also grateful to Dr. Ashish J. Mehta, Dr. Daniel P. Spangler, and Dr. Louis H. Motz for their participation as members of his graduate committee.

The technical assistance and programing suggestion provided by Sidney Schofield and Subarna Malakar are also appreciated.

The author wishes to thank the U.S. Army Corps of Engineers, Coastal Engineering Research Center, for furnishing the WIS model and for supporting the Coastal Data Network program. The Kings Bay data were collected under the sponsorship of U.S. Navy, Ship Research and Development Center.

Finally, the author would like to thank his wife Li-chu for her support, encouragement and patience.

## TABLE OF CONTENTS

ACKNOWLEDGEMENTS . . . . .	ii
LIST OF FIGURES . . . . .	v
LIST OF TABLES . . . . .	viii
ABSTRACT . . . . .	ix
CHAPTERS	
1 INTRODUCTION . . . . .	1
1.1 Background . . . . .	1
1.2 Scope of Work . . . . .	4
2 REVIEW OF EXISTING MODELS AND THEIR PERFORMANCE . .	8
2.1 Introduction . . . . .	8
2.2 Spectral Definitions . . . . .	9
2.3 Spectral Shape Function Models . . . . .	11
2.4 Deepwater Parametric Model . . . . .	16
2.5 Deepwater Discrete Model . . . . .	21
2.6 Shallow Water Model . . . . .	26
2.7 Wave Data and Comparisons . . . . .	34
3 A UNIFIED COASTAL WAVE PREDICTION MODEL . . . . .	44
3.1 Introduction . . . . .	44
3.2 UCWP Deepwater Submodel . . . . .	45
3.2.1 Generation terms . . . . .	45
3.2.2 Dissipation Terms . . . . .	62
3.3 UCWP Shallow Water Submodel . . . . .	64

3.3.1	Wave Energy Growth in Shallow Water . . . . .	64
3.3.2	Wave Energy Dissipation in Shallow Water . . . . .	66
3.4	Wind Model . . . . .	66
4	MODEL PERFORMANCE . . . . .	69
4.1	Introduction . . . . .	69
4.2	Model Performance in Hypothetical Cases . . . . .	70
4.3	Model Performance in Real Cases . . . . .	76
4.4	Wind-Wave Relationship in a Fully Developed Sea . . . . .	96
4.5	Comparison of Various Wave Energy Flux Elements . . . . .	102
4.6	Influence of $c_f$ in Shallow Water Wave Transformation Process . . .	105
5	CONCLUSIONS . . . . .	115
5.1	Summary . . . . .	115
5.2	Conclusions . . . . .	119
5.3	Future Studies . . . . .	122
APPENDICES		
A	SUMMARY OF PARAMETERIZED PROGNOSTIC EQUATIONS . . .	123
A.1	Prognostic Equations . . . . .	123
A.2	Elements of $D_{ij}$ and $G_i$ . . . . .	123
B	PROCEDURE IN SOLVING PARAMETERIZED $G_{in,1}(f)$ . . . . .	125
C	SUMMARY OF COMPUTED AND MEASURED NON-DIRECTIONAL FREQUENCY SPECTRA AT THE BUOY #41006 LOCATION . . .	128
C.1	Introduction . . . . .	128
C.2	Summary of Figures . . . . .	128
D	PLOTS OF WAVE ENERGY FLUX ELEMENTS . . . . .	150
D.1	Summary of Figures . . . . .	150
BIBLIOGRAPHY . . . . .		157
BIOGRAPHICAL SKETCH . . . . .		161

## LIST OF FIGURES

2.1	Comparison of nondimensionalized shapes of the P-M spectrum, the Kitaigorodskii spectrum, the JONSWAP spectrum and the modified JONSWAP spectrum. . . . .	13
2.2	Plots of $H_S(f, \theta)$ versus $\theta - \theta_0$ . . . . .	15
2.3	Nonlinear transfer of energy (Hasselmann et al., 1973). . . . .	20
2.4	Schematic illustration of growth of a spectral component, $E(f)$ , at (a) fetch-limited case and at (b) duration-limited case. . . . .	30
2.5	Wave gage stations. . . . .	35
2.6	(a) Weather map showing northeast winds generated by a high pressure system (1/12/84). . . . .	36
2.6	(b) Weather map showing northeast winds generated by a high pressure system (1/21/84). . . . .	37
2.7	Deepwater grid coordinate system. . . . .	38
2.8	Comparison of NOAA and WIS wave spectra for January 1984 at the Buoy #41006 location. . . . .	40
2.9	Comparisons of NOAA and WIS modal periods and significant wave heights at the Buoy #41006 location. . . . .	41
2.10	Comparison of NOAA and WIS wave energy scale parameters at the Buoy #41006 location. . . . .	42
3.1	Combined sources of nonlinear term and generation term in WIS model. . . . .	47
3.2	Plots of $E(f_m)$ versus $f_m$ . . . . .	50
3.3	Plots of $a_{nl}$ versus $f_0/f_m^2 \Delta t$ . . . . .	52
3.4	Plot of $\alpha$ versus $f_m/f_0$ . . . . .	53
3.5	Plot of $\gamma$ computed from Eq.(3.8) versus $\gamma$ from the least square method. . . . .	55

3.6	Plots of $\sigma_{ab}$ versus $f_m/f_0$ . . . . .	56
3.7	Simulations of spectral growth at duration-limited case; $U_{10} =$ 30 knots. . . . .	61
3.8	Comparison of spectral decays between measured and computed values. . . . .	63
4.1	Comparison of Deepwater hindcast models in fetch-limited cases.	71
4.2	Comparison of Deepwater hindcast models in duration-limited cases. . . . .	74
4.3	Shallow water grid system. . . . .	76
4.4	Comparison of hindcasted and measured winds at the Buoy #41006 location. . . . .	78
4.5	Comparison of NOAA and UCWP wave spectra for January 1984 at the Buoy #41006 location. . . . .	80
4.6	Comparisons of NOAA and UCWP modal periods and signifi- cant wave heights at the Buoy #41006 location. . . . .	81
4.7	Comparison of NOAA and UCWP energy scale parameters at the Buoy #41006 location. . . . .	82
4.8	Comparison of CDN and UCWP wave spectra for January 1984 at the Kings Bay gage location. . . . .	83
4.9	Comparison of CDN and UCWP marginal directional spectra at the Kings Bay gage location. . . . .	85
4.10	Comparisons of CDN and UCWP average wave direction, modal periods and significant wave heights at the Kings Bay station. . .	86
4.11	Tracks of Hurricanes Diana, Isidore, and Josephine (1984). . . .	87
4.12	(a) Weather map showing northeast winds generated by the Hur- ricane Diana (9/8/84). . . . .	88
4.12	(b) Weather map showing northeast winds generated by the Hur- ricane Isidore (9/27/84). . . . .	89
4.12	(c) Weather map showing northeast winds generated by the Hur- ricane Josephine (10/11/84). . . . .	90
4.13	Comparisons of NOAA and UCWP modal periods and signifi- cant wave heights at the Buoy #41006 location. . . . .	92

4.14	(a) Comparisons of CDN and UCWP average wave direction, modal periods and significant wave heights at the Kings Bay gage location. . . . .	93
4.14	(b) Comparisons of CDN and UCWP average wave direction, modal periods and significant wave heights at the Marineland gage location. . . . .	94
4.14	(c) Comparisons of CDN and UCWP average wave direction, modal periods and significant wave heights at the Cape Canaveral Station. . . . .	95
4.15	Plots of (a) $H_s$ versus $U_{10}$ , and (b) $T_m$ versus $U_{10}$ at various fetch and duration. . . . .	98
4.16	Plots of $2\pi U_{10}/gT_m$ versus $10^3 H_s/gT_m^2$ in (a) fetch-limited case and in (b) duration-limited case. . . . .	101
4.17	Plots of $2\pi U_{10}/gT_m$ versus $10^3 H_s/gT_m^2$ based on the NOAA buoy #41006 1984-1985 data. . . . .	103
4.18	Comparisons of wave heights and modal periods computed in September 1984 for $c_f=0.0, 0.005, 0.01, 0.02, \text{ and } 0.04$ . . . . .	107
4.19	(a) Plot of individual shallow water effect sources for $c_f=0.0$ . . .	109
4.20	(b) Plot of individual shallow water effect sources for $c_f=0.005$ . . .	110
4.21	(c) Plot of individual shallow water effect sources for $c_f=0.01$ . . .	111
4.22	(d) Plot of individual shallow water effect sources for $c_f=0.02$ . . .	112
4.23	(e) Plot of individual shallow water effect sources for $c_f=0.04$ . . .	113
C.1	Summary of computed and measured frequency spectra. . . . .	129
D.1	Plot of deepwater energy fluxes in growing period; Case 1. . . . .	151
D.2	Plot of deepwater energy fluxes in decaying period; Case 2. . . . .	152
D.3	Plot of deepwater energy fluxes during small winds; Case 3. . . . .	153
D.4	Plot of individual shallow water effect sources during growing period; Case 4. . . . .	154
D.5	Plot of individual shallow water effect sources during decaying period; Case 5. . . . .	155
D.6	Plot of individual shallow water effect sources during decaying period; Case 6. . . . .	156

## LIST OF TABLES

4.1	Summary of Correlations between computed and measured values of $H_s$ and $T_m$ at the buoy #41006 location. . . . .	92
4.2	Summary of Correlations between computed and measured values of $H_s$ and $T_m$ at three shallow water stations. . . . .	96
4.3	Summary of energy flux budget at the buoy #41006 location. . .	104
4.4	Summary of energy flux budget at the Marineland station. . . .	105
4.5	Comparison of $\delta_{H_s, c_{H_s, m}}$ , $\delta_{T_m, c_{T_m, m}}$ , $\epsilon_{H_s, c_{H_s, m}}$ , and $\epsilon_{T_m, c_{T_m, m}}$ for $c_f=0.0, 0.005, 0.01, 0.02,$ and $0.04$ . . . . .	108
4.6	Summary of energy flux budget for cases with $c_f=0.0, 0.005, 0.01,$ $0.02,$ and $0.04,$ respectively. . . . .	114

Abstract of Dissertation Presented to the Graduate School  
of the University of Florida in Partial Fulfillment of the  
Requirements for the Degree of Doctor of Philosophy

A COUPLED DISCRETE SPECTRAL WAVE HINDCAST MODEL

By

LI-HWA LIN

April 1988

Chairman: Dr. Bent A. Christensen  
Cochairman: Dr. Hsiang Wang  
Major Department: Civil Engineering

In late 1976 a numerical wave hindcast model was developed by the Wave Information Study (WIS) at the U.S. Army Engineer Waterways Experiment Station (WES) and it was employed to generate 20 years of wave conditions in 10-meter water depth along the eastern seaboard of the United States. The model comprises of deepwater and shallow water submodels. The significant nonlinear wave-wave interaction process is included in the deepwater submodel based on the study of parametric model. Recently, more detailed field wave information became available in both offshore and nearshore regions, particularly shallow water directional wave information reduced from data collected along the Florida Coast. Based upon those data, the WIS model is reexamined.

A new wave model, named here as the Unified Coastal Wave Prediction (UCWP) model, is developed. This model is of a discrete type and it links a wind field model to a combined deepwater and shallow water wave prediction model. The deepwater wave submodel follows the WIS model but with revised source terms and dissipation terms. The shallow water wave submodel utilizes the refraction law and the equation of conservation of energy to solve for the shallow water waves.

The UCWP model represents a significant improvement over existing models, at least for applications to the southeastern region of the United States. The improvement is particularly evident in wave period and wave direction. In addition to the development of the new numerical model, a number of fundamental aspects of air-sea interactions are also examined in light of the field data. New semi-empirical formulas are proposed for a number of important parameters, including the JON-SWAP spectral parameters, required to define wind wave spectra.

# CHAPTER 1 INTRODUCTION

## 1.1 Background

Wave information is required for a variety of purposes, including design of coastal and offshore structures, planning of marine operations, ship design, coastal process studies, and coastal erosion prevention, etc. Because of a general lack of measured wave data, particularly long-term data, wave hindcast, which is a technique in calculating the events of wind-generated water surface waves in the past, is often the best means to estimate representative wave statistics and is almost always the only means to estimate characteristics of the infrequently occurring extreme waves.

In early days, methods utilized for hindcasting wind waves involved empirically based nomographs and tables to evaluate wave height and wave period for prominent waves. A well-known example is the Sverdrup-Munk-Bretschneider (SMB) model which was established by matching some prescribed math functions to measured wave heights and wave periods. The model was established in a period during and after World War II and was used exclusively for either hindcast or forecast of ocean waves before more modern wave models were developed later in the 1970s. With more physical processes governing the nature of waves being known and concepts of wave energy spectra becoming widely accepted, spectral models were then developed for wave hindcast, or forecast.

The spectral models are commonly categorized into two major branches: the discrete model and the parametric model. With wind information as input, both the discrete model and the parametric model generate wave energy as a function

of frequency and direction, propagate energy across oceanic region, and consider energy spreading and dissipation. The difference between the two models is that the discrete model evaluates wave spectra by summing all individual spectral components corresponding to different physical processes, while the parametric model constructs wave spectra by solving numerically spectral parameters from the prognostic equations which represent the projections of wind-wave relationships in the spectral parameter space.

The advantage of using parametric model to hindcast the wind wave spectra is that its numerical solution procedure is simple. Computations in solving spectral parameters in the parametric model are solely performed in the frequency domain. The directional spreading of wave energy is considered in the model by multiplying the resulting frequency spectrum with an angular distribution function. The assumed angular distribution function is a normalized bell-shaped, symmetrical function with respect to local wind direction. The disadvantage of using the parametric model is that it does not include swell and, hence, cannot rigorously consider all the physical processes involved in wave transformation. Furthermore, the parametric model can not properly generate wave spectra in shallow water where bottom effects become important. The discrete model is more flexible and can include swells just as easily as that of the regular wind waves. It can also handle easily the shallow water effects, such as refraction, shoaling, bottom friction, etc. However, in the discrete model computations involved are usually tedious and time-consuming since they have to be carried out in the combined frequency and direction domain.

Currently, there are a number of spectral models, both discrete and parametric types, available for wave hindcasting. Most of them are for deepwater wave application. These wave models are based upon similar theoretical considerations but their numerical methods and computational requirements are vastly different. They all contain empirical functions or coefficients derived from actual wave measurements

and are calibrated on limited data base. Due to the scarcity of the measured wave data, none of the present models were tested against a wide range of wind and wave conditions. Comparisons for extreme waves during severe storms and hurricanes were few and comparisons with measured wave energy directional spectra were extremely rare. Accordingly, there is considerable uncertainty about the accuracy of the existing wave models.

A few comparisons of different wave models were made with each other in the past. Among them, the work by Resio and Vincent (1979) offered an interesting comparison among the SMB model, Hasselmann's (1976) parametric model, a version of the Pierson et al.(1966) model, Barnett's (1968) model, and a discrete model by Resio and Vincent (1977, 1978). Comparisons of wave height versus fetch and duration for selected constant wind speeds indicate significant differences among these models and, thus, raise concern for their accuracy.

There are several problems which need to be addressed if wave models are to improve their accuracy and to be applicable for a wide range of conditions in both deep and shallow waters. First, source and sink terms should be continuously refined with availability of more and better wave data. Second, wave models should be calibrated with directional wave information and with a wide range of wind conditions, i.e., large systems, small systems, extreme events, etc. Finally, there is a need to acquire the accurate wind information since wave model relies on wind field as input. The wind information can be either measured from the field or generated by a wind model, based on the sea surface pressure distribution. Accurate specification of wind fields through a numerical model is sometimes difficult. Therefore, it is necessary to improve the wind model or to properly incorporate measured wind data as input to the wave model.

## 1.2 Scope of Work

Recently, more detailed field wave information became available in both deepwater and shallow water regions. For instance, long term wave data have been collected in deep water by several NOAA (National Oceanic and Atmospheric Administration) maintained buoys in the Northwest Atlantic Ocean and in shallow water by twelve CDN (Coastal Data Network) underwater stations along the Florida coast. Based upon these data, a new coupled wave hindcast model is developed. This model, referred to here as the Unified Coastal Wave Prediction (UCWP) model, is of a discrete type. It links a wind field model to a combined deepwater and shallow water wave prediction model. The deepwater submodel follows the same technique used in WIS with revised source and dissipation terms. The shallow water submodel utilizes the algorithm developed by Chen and Wang (1983) with modified source term proposed by Vincent (1984). The model is unified in the sense that the deepwater model and the shallow water model are based on the same set of fundamental equations; both employ discrete finite difference scheme with compatible source and dissipation terms; the models are on the same level in detail and are expected to yield same degree of accuracy.

A reexamination of two previously developed deepwater wave models, the WIS model and the parametric model by Hasselmann et al.(1973), has revealed some differences about the source functions utilized by the two models. First, the non-conservative term of wave energy dissipation is completely neglected from the parametric model while it is included in the discrete model to account for energy loss of low frequency components. Second, the conservative wave energy transfer, as a result of nonlinear wave-wave interactions, is included in the parametric model based on JONSWAP spectrum while it is included in the discrete model based on Kitaigorodskii spectrum. Third, the wave growth due to wind input is considered independent to the nonlinear wave-wave interactions in the parametric model, while

it is assumed to depend on the nonlinear wave-wave interactions in the discrete model. A well-known problem about the parametric model is its inability of treating swell components. The parametric is preferred by some due to its simplicity in computations, while the discrete model is preferred by others because of its straightforward physical interpretation.

Inspection of field wave data collected by NOAA buoys reveals that nonconservative turbulent dissipation of wave energy induced by wave motion should not be neglected in a wave model. This dissipation is incorporated in the UCWP model to consume wave energy corresponding to an exponential decay rate. The nonlinear wave-wave interactions are included in the UCWP model based on a modified JONSWAP spectrum proposed by Donelan et al.(1985). The migration of peak energy frequency caused by this wave-wave interaction mechanism is determined in the model based on the idealized prognostic equations derived by Hasselmann et al.(1976). The threshold spectrum which indicates a minimal condition for the occurrence of nonlinear wave-wave interactions is empirically determined based upon the field data.

The UCWP shallow water submodel is developed with the inclusion of most of the known significant shallow water effects, such as refraction, shoaling, percolation, bottom friction, and wave breaking due to depth limitation, etc. All these shallow water effects have been documented in the past (Chen and Wang, 1983; Shemdin et al., 1978). The turbulent dissipation of wave energy is also included in the model. The nonlinear wave-wave interaction is, however, not included in the model. The growth of waves due to wind input is evaluated in the model based on a TMA spectrum, as suggested by Bouws et al.(1983). The five parameter TMA spectrum has been correlated to wind and wave conditions by Vincent (1984).

During the autumn and winter seasons extratropical storms and hurricanes frequently occur in the Northwest Atlantic Ocean. Waves generated by the storms and

hurricanes in general are the major cause of severe coastal erosion along the south-east coast of the United States. The model's performance is, thus, tested against such severe weather conditions. The results obtained from the UCWP deepwater submodel are compared with measured wave data from NOAA buoys deployed in the Northwest Atlantic Ocean. The results obtained from the UCWP shallow water submodel are compared with measured wave data from CDN wave gages.

In summary, the detailed research included in this study can be briefly described as follows:

(1) A number of standard spectral functions and angular spreading distribution functions are reviewed. These are important in defining an appropriate general directional wave spectrum.

(2) Two existing deepwater wave energy spectral models, the discrete model by the Wave Study Information (WIS) group of Waterways Experiment Station (Resio and Tracy, 1983) and the parametric model by Hasselmann et al.(1973), are rederived to highlight the basic assumptions and fundamental principles.

(3) Deepwater wave generation mechanisms are reevaluated based upon the currently acquired wave data.

(4) Equations that are either theoretically derived or empirically proposed as shallow water source functions with respect to wave generation, propagation, and dissipation, are examined and summarized. These are later utilized to build a rigorous shallow water model.

(5) A new discrete model, named here as the Unified Coastal Wave Prediction (UCWP) model, is developed for generating wave spectra in the deep and shallow water. The model links a wind field model to a combined deepwater and shallow water wave prediction model.

(6) Computer algorithm for the UCWP model is developed to facilitate numerical computations.

(7) Results from the deepwater UCWP model are compared with the SMB model, the WIS model, and Hasselmann's (1976) parametric model for fetch-limited and duration-limited cases.

(8) Model outputs are compared with those measured by deepwater buoys and shallow water wave gages.

(9) Relative importance of individual elements affecting the deep and shallow water spectral transformations is analyzed.

(10) Different values of bottom friction coefficient are tested in the UCWP shallow water model to investigate the sensitivity of model responses.

## CHAPTER 2 REVIEW OF EXISTING MODELS AND THEIR PERFORMANCE

### 2.1 Introduction

The approach taken in the present study for ocean wave hindcasting along the Florida coast is to develop a numerical model based on state-of-the-art deepwater and shallow water wave prediction techniques. Currently, deepwater wave models are either of discrete type which calculate wave energy spectra based on discretized wave energy equation or parametric type which calculate a set of parameters that in turn specifies the energy spectra. The existing shallow water wave models are invariably of discrete type since the mechanisms involved in the wave transport in the shallow water, such as wave refraction, shoaling, percolation, wave energy dissipation, and shallow water wave-wave interactions, are too complicated to permit parameterization.

The material presented in this chapter includes the definitions of directional spectra as well as the unidirectional frequency spectra which play essential roles in wave hindcast models, and a presentation of the typical theories and methods applied to the current deepwater and shallow water wave models. Two widely known deepwater wave models, the parametric spectral model by Hasselmann et al.(1973) and the discrete spectral model by the Wave Information Study (WIS) group of the Waterways Experiment Station (WES), are reviewed as a demonstration of spectral methods. It is shown that the deepwater parametric spectral model in general is meant for wind waves only and cannot account for the swells while the deepwater discrete spectral model by WIS has no difficulty in tracing both. It is further shown that the WIS spectral model has the same ability as the parametric

model to include the nonlinear wave-wave interactions in computing wave energy transformation in the deep water; this is accomplished using the formula which estimates the nonlinear wave energy transformation rate in the frequency domain derived from the prognostic equations of parametric method.

The shallow water wave model is reviewed following the works done by Chen and Wang (1983), Collins (1972), and Shemdin et al.(1978). Among the major contributors of shallow water effects, wave refraction and shoaling are included in the advection terms, and others are acting as a part of the forcing functions governing the generation, dissipation, and nonlinear transfer of wave energy in shallow water region.

The model performance is only shown here for the deepwater model of WIS. The shallow water model which requires the output of deepwater model to specify the boundary condition is not tested until the latter is modified. Its performance will be discussed in Chapter 4.

## 2.2 Spectral Definitions

A directional wave spectrum is essentially a representation of the wave number spectrum of water surface waves that follow the linear wave theory dispersion relationship between wave number and wave frequency. By linear superposition of wave components, an irregular water surface can be approximated by taking the stochastic integral over the wave number plane,  $s$ , which is taken here as identical to the still water surface plane (Thomson, 1972).

$$\eta(\vec{s}_1, t) = \text{Re} \left[ \iint_s da(\vec{k}) e^{i(\vec{k} \cdot \vec{s}_1 - \sigma t)} \right] = \iint_s \frac{1}{2} [da(\vec{k}) e^{i(\vec{k} \cdot \vec{s}_1 - \sigma t)} + da^*(\vec{k}) e^{-i(\vec{k} \cdot \vec{s}_1 - \sigma t)}] \quad (2.1)$$

where  $\eta$  is water surface elevation,  $t$  is time,  $\vec{s}_1 = (x_1, y_1)$  is the horizontal location of interest in rectangular coordinates,  $\sigma$  is radian frequency,  $\vec{k} = (k \cdot \cos \theta, k \cdot \sin \theta)$  is a vector wave number with magnitude  $k = |\vec{k}|$  and direction  $\theta$ ,  $da(\vec{k})$  indicates an infinitesimal wave amplitude (complex number) which is the contribution of waves in a wave number interval  $d\vec{k}$ , an asterisk appearing in superscript indicates the

complex conjugate, the operator  $\text{Re}[\ ]$  indicates the real part of a complex number. The wave amplitude component  $da(\vec{k})$  can be transformed into  $da(\sigma, \theta)$  since  $\vec{k}$  can be expressed by a direction  $\theta$  and a frequency  $\sigma$ . To a first approximation, the wave frequency satisfies the well-known linear wave theory dispersion equation

$$\sigma^2 = gk \cdot \tanh(kh), \quad k = |\vec{k}| \quad (2.2)$$

where  $g$  is the gravitational constant and  $h$  is the water depth. A small contribution of the water surface waves representing a specific vector wave number is

$$d\eta(\vec{s}_1, t) = \frac{1}{2} [da(\vec{k})e^{i(\vec{k} \cdot \vec{s}_1 - \sigma t)} + da^*(\vec{k})e^{-i(\vec{k} \cdot \vec{s}_1 - \sigma t)}] \quad (2.3)$$

Thus, the mean square value of  $d\eta$  can be evaluated, which has a form

$$\begin{aligned} \overline{[d\eta(\vec{s}_1, t)]^2} &= \frac{1}{4} \lim_{T \rightarrow \infty} \frac{1}{T} \int_{-T/2}^{T/2} \{ [da(\vec{k})]^2 e^{i2(\vec{k} \cdot \vec{s}_1 - \sigma t)} + 2da(\vec{k})da^*(\vec{k}) \\ &\quad + [da^*(\vec{k})]^2 e^{-i2(\vec{k} \cdot \vec{s}_1 - \sigma t)} \} dt = \frac{1}{2} da(\vec{k})da^*(\vec{k}) \\ &= \frac{1}{2} |da(\vec{k})|^2 = \frac{1}{2} |da(\sigma, \theta)|^2 = E(\sigma, \theta) d\sigma d\theta = dE(\sigma, \theta) \end{aligned} \quad (2.4)$$

where  $T$  is the time duration of interest, an overhead bar indicates the operation of arithmetic mean;  $E(\sigma, \theta)$  is the directional frequency spectrum which is defined as

$$E(\sigma, \theta) = \overline{[d\eta(\vec{s}_1, t)]^2} / d\sigma d\theta = \frac{1}{2} |da(\sigma, \theta)|^2 / d\sigma d\theta \quad (2.5)$$

According to linear wave theory, the wave energy per unit water surface area per unit water weight is equal to half the squared value of wave amplitude (Ippen, 1966). Therefore, Eq.(2.4) specifies a quantity proportional to wave energy associated with a particular frequency range,  $d\sigma$ , and directional interval,  $d\theta$ . However, Eq.(2.4) may be regarded as a contribution from an infinitesimal amplitude wave with amplitude  $da(\sigma, \theta)$  at the mid  $d\sigma$  and  $d\theta$ . Thus,  $E(\sigma, \theta)$  is interpreted as the distribution of wave energy per unit water surface area per unit water weight per unit frequency per unit direction. The corresponding one-dimensional frequency spectrum  $E(\sigma)$  is

defined by integrating  $E(\sigma, \theta)$  over all  $\theta$ .

$$E(\sigma) = \int_{-\pi}^{\pi} E(\sigma, \theta) d\theta \quad (2.6)$$

The marginal directional spectrum is defined as

$$E(\theta) = \int_0^{\infty} E(\sigma, \theta) d\sigma \quad (2.7)$$

The total wave energy per unit water surface area per unit water weight is defined by integrating  $E(\sigma)$  over all  $\sigma$ , or integrating  $E(\theta)$  over all  $\theta$ , or integrating  $E(\sigma, \theta)$  over all  $\sigma$  and  $\theta$ . That is,

$$E_{total} = \int_0^{\infty} E(\sigma) d\sigma = \int_{-\pi}^{\pi} E(\theta) d\theta = \int_{-\pi}^{\pi} \int_0^{\infty} E(\sigma, \theta) d\sigma d\theta \quad (2.8)$$

Since the spectral density defined in Eq.(2.5) or Eq.(2.6) has dimensions of rate of change of wave energy density, the name ‘power spectral density’ is often used. However, an alternate name ‘energy spectral density’ is more commonly used in coastal engineering.

### 2.3 Spectral Shape Function Models

In the study of wave hindcast through spectral models, the standard spectral shape functions are served as fundamental structure unit in building the wave energy spectral states in the sea. Three frequency spectral shape functions are well-accepted in the past: (i) Pierson-Moskowitz (P-M) spectrum, (ii) Kitaigorodskii spectrum, and (iii) JONSWAP spectrum. The Pierson-Moskowitz spectrum (1964),  $E_{PM}(f)$ , is given by

$$E_{PM}(f) = \frac{\alpha_p g^2}{(2\pi)^4 f^5} \exp[-0.74(f_0/f)^4] = \frac{\alpha_p g^2}{(2\pi)^4 f^5} \exp[-\frac{5}{4}(f_m/f)^4] \quad (2.9)$$

where  $f = \sigma/2\pi$  is the wave frequency with units 1/time,  $\alpha_p$  is known as Phillips’ constant,  $f_0 = g/2\pi U_{19.5}$  is the frequency of the deepwater waves whose phase speed is identical to the wind speed  $U_{19.5}$  at a height 19.5 m above sea surface, and  $f_m = 0.88f_0$  is the wave frequency of the spectral peak. More often, the name

'spectral peak frequency' is referred to the frequency of spectral peak,  $f_m$ , and the wave period corresponding to this frequency is known as 'modal period'.

The Kitaigorodskii spectrum(1962),  $E_K(f)$ , is given by

$$E_K(f) = \begin{cases} \alpha g^2 f_m^{-5} (2\pi)^{-4} \exp[1 - (f_m/f)^4], & \text{if } f < f_m \\ \alpha g^2 f^{-5} (2\pi)^{-4}, & \text{if } f \geq f_m \end{cases} \quad (2.10)$$

which contains two free parameters, the energy scale factor  $\alpha$  and the spectral peak frequency  $f_m$ . The JONSWAP spectrum is derived from the Joint North Sea Wave Project (Hasselmann et al. 1973) and constitutes a modification to the P-M spectrum to provide for a much more sharply peaked spectrum. The JONSWAP spectrum,  $E_J(f)$ , is given by

$$E_J(f) = \frac{\alpha g^2}{(2\pi)^4 f^5} \exp[-\frac{5}{4}(f_m/f)^4] \gamma \exp[-\frac{1}{2}(\frac{f - f_m}{\sigma_{ab} f_m})^2] \quad (2.11)$$

with

$$\sigma_{ab} = \begin{cases} \sigma_a, & \text{if } f < f_m \\ \sigma_b, & \text{if } f \geq f_m \end{cases}$$

The function contains five free parameters, two scale parameters  $\alpha$  and  $f_m$ , and three shape parameters  $\gamma$ ,  $\sigma_a$  and  $\sigma_b$ . The parameter  $\gamma$  is the peak-enhancement factor which is the ratio of the peak value of the spectrum to the peak value of the corresponding P-M spectrum with the same values of  $\alpha$  and  $f_m$ . The parameters  $\sigma_a$  and  $\sigma_b$  yield the scales of left and right peak widths, respectively.

Figure 2.1 shows a comparison of spectral shapes, normalized by the spectral peak energy of the P-M spectrum, of the P-M spectrum, the Kitaigorodskii spectrum, and the mean JONSWAP spectrum, which has its spectral parameters  $\gamma$ ,  $\sigma_a$ , and  $\sigma_b$  equal to 3.3, 0.07, and 0.09, respectively. It is seen that the mean JONSWAP spectrum and the Kitaigorodskii spectrum have similar shape and they are much more sharply peaked than the P-M spectrum.

All three spectra shown above indicate an 'equilibrium range' on the rear face of the spectral shape with the associated spectral energy densities being inversely

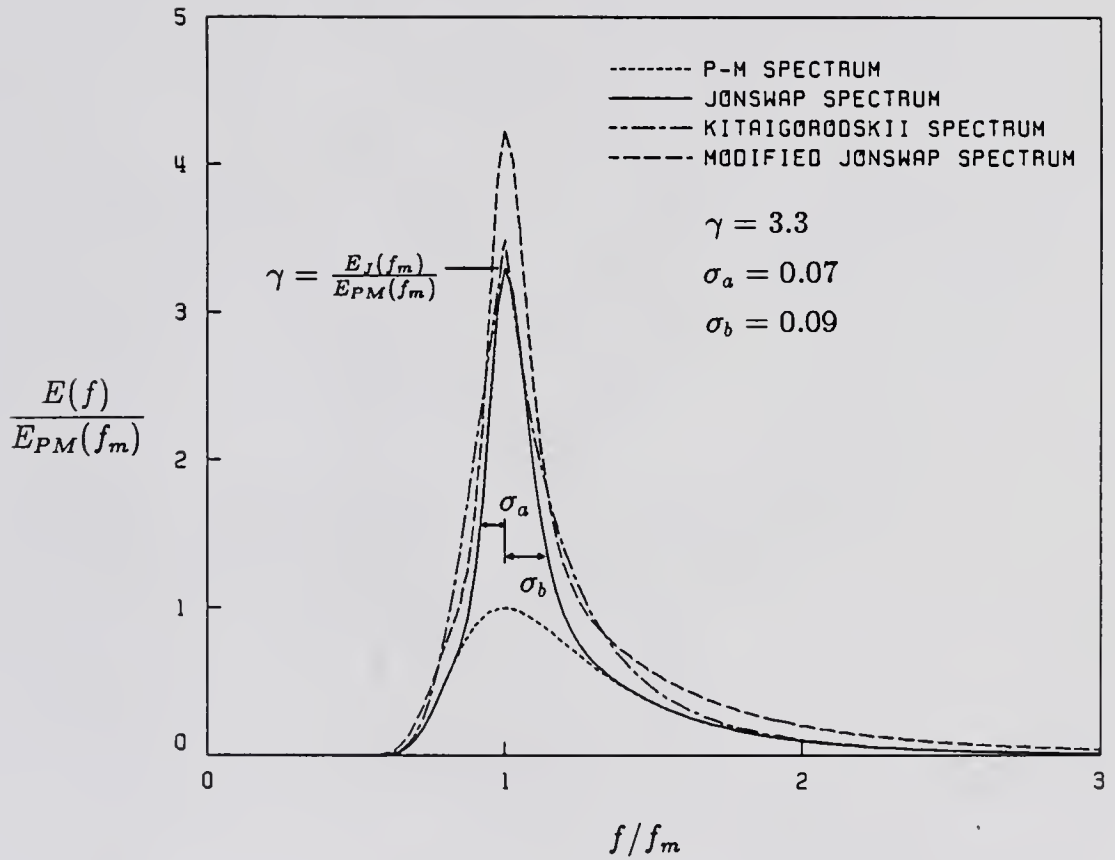


Figure 2.1: Comparison of nondimensionalized shapes of the P-M spectrum, the Kitaigorodskii spectrum, the JONSWAP spectrum and the modified JONSWAP spectrum.

proportional to frequency to the fifth power. However, more recent studies made by Donelan et al.(1985) and Battjes et al.(1987) using both field and laboratory data showed that an  $f^{-4}$  frequency dependence at the tail part of the wave spectrum may be more adequate for the wind-generated waves than the  $f^{-5}$  spectral shape. Based upon the assumption of the  $f^{-4}$  dependence on the rear face of frequency spectrum, Donelan et al.(1985) suggested a modified JONSWAP spectrum

$$E_{JM}(f) = \frac{\alpha g^2}{(2\pi)^4 f^4 f_m} \exp[-(f_m/f)^4] \gamma \exp[-\frac{1}{2}(\frac{f-f_m}{\sigma_{ab} f_m})^2] \quad (2.12)$$

with all its free parameters  $\alpha$ ,  $f_m$ ,  $\gamma$ , and  $\sigma_{ab}$  defined the same as in JONSWAP spectrum. This modified JONSWAP spectrum is immediately applicable to any discrete spectral method provided  $f_m$  is known or defined in advance. This is because all the empirical relationships between each of the free parameters  $\alpha$ ,  $\gamma$ , and  $\sigma_{ab}$  were established, based on field data, by Donelan et al.(1985) as functions of  $f_0/f_m$ . A modified JONSWAP spectrum with its parameters  $\gamma$  and  $\sigma_{ab}$  being equal to the mean JONSWAP ones is also shown in Fig. 2.1. This spectrum has wider width and higher peak than the mean JONSWAP spectrum, and it contains more energy in the high frequency components than the mean JONSWAP spectrum, the P-M spectrum and the Kitaigorodskii spectrum.

The directional dependence of the wave spectrum is usually modelled by a symmetrical directional distribution function which is also known as the 'angular distribution function' or 'spreading function'. It is often convenient to define a normalized spreading function as the ratio of (Cartwright, 1963)

$$H_S(f, \theta) = \frac{E(f, \theta)}{E(f)} \quad (2.13)$$

where  $E(f, \theta) = H_S(f, \theta)E(f)$  indicates the directional spectrum, which has its wave energy densities distributed in the  $(f, \theta)$  domains according to  $H_S(f, \theta)$ .

A number of functional forms of  $H_S(f, \theta)$  have been suggested but all with similar shape, i.e., they are bell-shaped and symmetric about a central direction. It

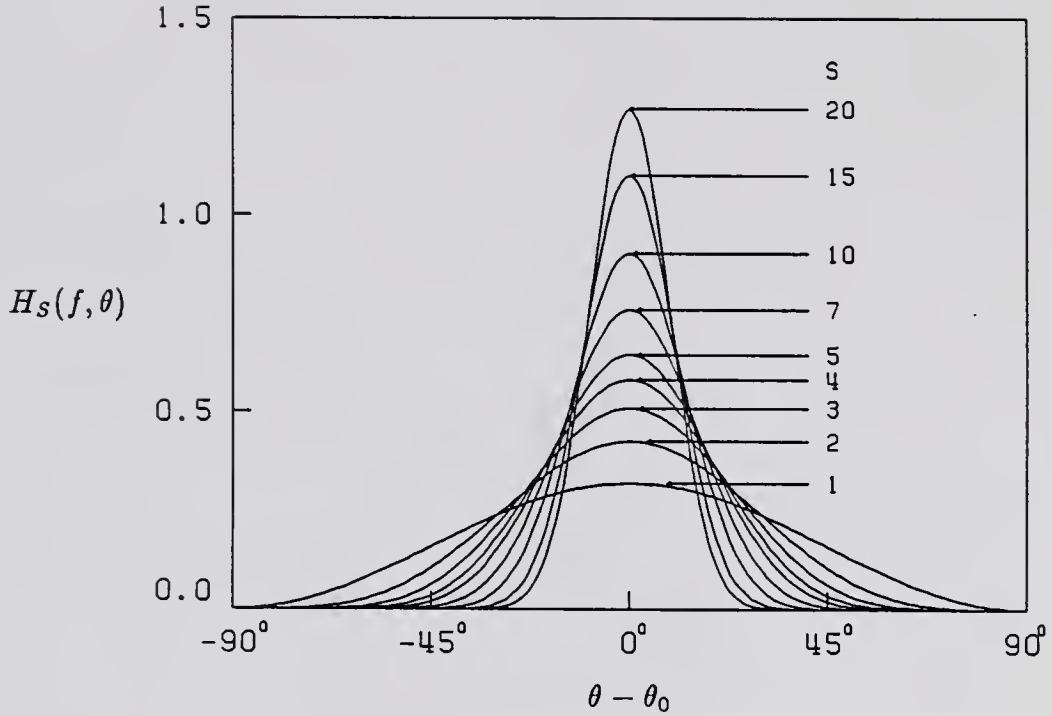


Figure 2.2: Plots of  $H_S(f, \theta)$  versus  $\theta - \theta_0$ .

is usually difficult to choose one in preference to another in practical applications. A commonly used function, which is proportional to a power cosine function, is given here (Sand, 1979).

$$H_S(f, \theta) = \begin{cases} \frac{2^{2S} \Gamma^2(S+1)}{\pi \Gamma(2S+1)} \cos^{2S}(\theta - \theta_0), & \text{if } |\theta - \theta_0| \leq \pi/2 \\ 0, & \text{elsewhere} \end{cases} \quad (2.14)$$

where  $S = S(f)$  is called the spreading parameter, which is always positive and a function of frequency,  $\theta_0 = \theta_0(f)$  is the central angle of the symmetric spreading directions. Figure 2.2 shows several distributions of  $H_S(f, \theta)$  with the spreading parameter ranging from 1 to 20. It is shown that  $H_S(f, \theta)$  associated with higher spreading parameter can have very sharply peaked, narrow-band directional distribution. When this  $H_S(f, \theta)$  is applied in a wave prediction model, the spreading parameter  $S$  is commonly defined equal to 1 and 2, respectively, for all frequency components of locally generated and nonlinearly transferred energies. It can be

seen in Fig. 2.2 that both spreading functions,  $H_S(f, \theta)$ , corresponding to  $S = 1$  and  $S = 2$ , respectively, have relatively wide distributions over a  $180^\circ$  directional domain.

#### 2.4 Deepwater Parametric Model

In the absence of current in the ocean, the general equation governing the transport of wave energy is given by (Hasselmann et al., 1973)

$$\frac{dE(f, \theta, \vec{s}, t)}{dt} = \frac{\partial E(f, \theta, \vec{s}, t)}{\partial t} + C_g(f, \vec{s}) \frac{\partial E(f, \theta, \vec{s}, t)}{\partial \ell} = G(f, \theta, \vec{s}, t) \quad (2.15)$$

where  $E(f, \theta, \vec{s}, t)$  is the energy density of the spectral element with reference to still water surface plane at horizontal location  $\vec{s}$  and time  $t$ , with frequency  $f$  and direction of propagation  $\theta$ ,  $\ell$  is the path of this spectral element in which  $d\ell = |d\ell|e^{i\theta}$ ,  $C_g(f, \vec{s}) = \partial\sigma/\partial k|_{\vec{s}} = \partial(2\pi f)/\partial k|_{\vec{s}}$  is the group velocity associated with this spectral element,  $k$  is the magnitude of the associated wave number, and  $G(f, \theta, \vec{s}, t)$  is the net source function representing the rate of energy transfer into or out of this element. This equation is commonly referred to as ‘wave energy balance equation’, or ‘wave energy transport equation’, or simply ‘transport equation’. In the text to follow, the notations of  $E(f, \theta)$  and  $G(f, \theta)$  are often used for simplicity.

The magnitude of wave group velocity  $C_g(f, \vec{s})$  can be derived from the dispersion relation given in Eq.(2.2) and expressed as

$$C_g(f, \vec{s}) = n \cdot C = \left( \frac{1}{2} + \frac{kh}{\sinh(2kh)} \right) C \quad (2.16)$$

where  $C = \sigma/k = 2\pi f/k$  is phase speed of waves with frequency equal to  $f$ ,  $h$  is water depth at the location  $\vec{s}$ , and  $n$  is the ratio of wave group velocity to wave phase velocity. It is noted that both phase velocity  $C$  and wave number  $k$  are implicit functions of  $f$ . The presence of the source function  $G(f, \theta, \vec{s}, t)$  is thought to include all the possible physical terms which are responsible for the local growth and decay of water surface waves.

The deepwater wave is usually defined in coastal engineering by

$$\tanh(kh) > 0.9962, \quad \text{or} \quad (kh) > \pi \quad (2.17)$$

Under the above condition, the wave properties are hardly influenced by the bottom. Therefore, the shallow water effects, such as shoaling, refraction, wave dissipation due to bottom friction, etc., are no longer important in the deepwater wave hindcast. It is noted that in deep water, the dispersion relation is reduced to

$$\sigma^2 = (2\pi f)^2 = gk$$

and the deepwater wave group velocity,  $C_{go}(f)$ , can be expressed as

$$C_{go}(f) = \frac{1}{2}C = \frac{g}{2\sigma} = \frac{g}{4\pi f}$$

which is not dependent on water depth and, hence, is not dependent on location.

The parametric spectral model was originally developed by Hasselmann et al. at 1973. The model was later applied by many investigators without further modifications (Weare and Worthington, 1978; Günther et al., 1979). The presentation of the parametric model in this section is mainly based on the work of Hasselmann et al.(1973).

To derive the equations solving the spectral parameters, the directional wave spectrum used in the transport equation, Eq.(2.14), is assumed to have the following expression:

$$E_J(f, \theta) = E_J(f)H_1(f, \theta) = \begin{cases} E_J(f)\frac{2}{\pi}\cos^2(\theta - \theta_0), & \text{if } |\theta - \theta_0| \leq \pi/2 \\ 0, & \text{elsewhere} \end{cases} \quad (2.18)$$

where  $H_1(f, \theta)$ , the spreading function, is a special case of Eq.(2.14) with S equal to 1, and  $\theta_0$  coincides with the downwind direction. By first substituting Eq.(2.18) into the transport equation, Eq.(2.15), and then intergrating the transport equation over the direction domain,  $0 < \theta \leq 2\pi$ , the direction-independent transport equation

is obtained as

$$\frac{dE_J(f)}{dt} = \frac{\partial E_J(f)}{\partial t} + \overline{C_{go}}(f) \frac{\partial E_J(f)}{\partial \ell} = G(f) \quad (2.19)$$

with the directional averaged group velocity  $\overline{C_{go}}(f)$  equal to

$$\overline{C_{go}}(f) = \frac{\int_{-\pi}^{\pi} C_{go}(f) E_J(f, \theta) d\theta}{E_J(f)} = \frac{8}{3\pi} \frac{g}{4\pi f} \quad (2.20)$$

and the directional integrated source function  $G(f)$  equal to

$$G(f) = \int_{-\pi}^{\pi} G(f, \theta) d\theta \quad (2.21)$$

Note that symbols  $\vec{s}$  and  $t$ , which stand for location and time, respectively, are not shown in Eqs.(2.19), (2.20), and (2.21), and in the following derivations for simplicity.

The source function  $G(f)$  is usually represented by three quantities, the energy input from the atmosphere,  $G_{in}(f)$ , the dissipation of energy,  $G_{dis}(f)$ , and the nonlinear energy transfer,  $G_{nl}(f)$ . That is,

$$G(f) = G_{in}(f) + G_{dis}(f) + G_{nl}(f) \quad (2.22)$$

Since the spectral shape is assumed to be consistent with the JONSWAP spectrum in the parametric model and is presumed in a state of equilibrium range, the dissipation  $G_{dis}(f)$  is in general dropped from Eq.(2.22). The rest two source terms  $G_{in}(f)$  and  $G_{nl}(f)$  are thought to be equally important for the growth and transfer of wave energy in the ocean. It was demonstrated by Resio and Vincent (1979) in numerical model studies that the duration required to achieve fetch-limited condition in the case dominated by atmospheric input is of the same order as the case dominated by the wave-wave interactions.

The growth rate  $G_{in}(f)$  is commonly approximated in terms of a linear function of one-dimensional frequency spectrum (Snyder and Cox, 1966). However, for convenience the quantity  $G_{in}(f)$  is often assumed to be proportional to  $E(f)$  in the

parametric model. For instance, the energy input source term utilized by Hasselmann et al.(1973) in their wave model is linearly proportional to one-dimensional frequency spectrum and has the following expression:

$$G_{in}(f) = 5s f \frac{U_{10}}{C} E_J(f) \quad (2.23)$$

where  $s \approx 0.0012$  is the ratio of air density to sea water density, and  $U_{10}$  is the wind speed at 10 m elevation above sea surface.

The general form of the nonlinear transfer source  $G_{nl}(f)$  for a single peaked spectrum is known to have a positive lobe appearing on the frontface of the spectrum, a negative second lobe appearing on the rearface of the spectrum closer to the spectral peak, and a positive third lobe appearing on the rearface of the spectrum away from the spectral peak (see Fig. 2.3). In wave hindcast, only the first two lobes are important since the energy transfer into the third lobe is at such frequencies that viscous and turbulent dissipations are assumed to keep the local energy components small.

The nonlinear transfer function deduced by Hasselmann et al.(1973) has the expression

$$G_{nl}(f) = D_1 \frac{g^2 \alpha^3}{f_m^4} \psi(f/f_m) \quad (2.24)$$

where  $D_1$  is a proportional constant whose magnitude is on the order of  $10^{-3}$ , and  $\psi(f/f_m)$  is a non-dimensional function depending on the spectral shape. By neglecting the energy transfer in the third lobe, where waves of high frequencies are more likely governed by the equilibrium  $f^{-5}$  law, Eq.(2.24) can be approximated by the expression

$$G_{nl}(f) = \begin{cases} 2.2\alpha^2 f_m E_J(f), & \text{if } f < f_m \\ -2.2\alpha^2 f_m E_J(f), & \text{if } f \geq f_m \end{cases} \quad (2.25)$$

With the source function given, the direction-independent transport equation, Eq.(2.19), can be then projected onto the JONSWAP parameter space to yield

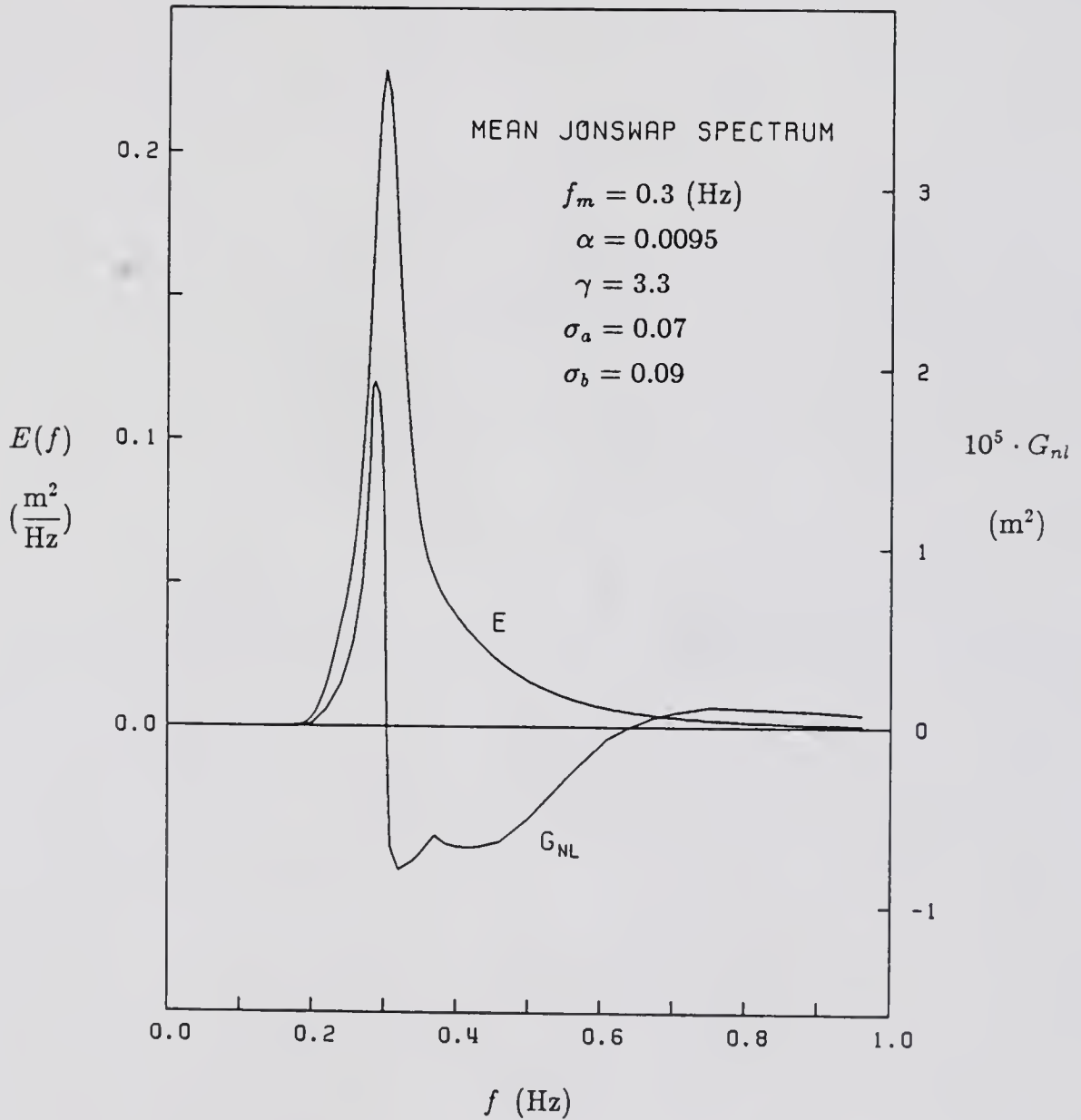


Figure 2.3: Nonlinear transfer of energy (Hasselmann et al., 1973).

(Hasselmann et al., 1973)

$$\frac{\partial b_i}{\partial t} + D_{ij} \frac{\partial b_i}{\partial \ell} = G_i, \quad i, j = 1, 2, 3, 4, 5 \quad (2.26)$$

where  $b_1 = f_m$ ,  $b_2 = \alpha$ ,  $b_3 = \gamma$ ,  $b_4 = \sigma_a$ , and  $b_5 = \sigma_b$ . The equations given in Eq.(2.26) are known as the ‘prognostic equations’ in the parametric model. The  $D_{ij}$  matrix is a generalized propagation velocity, and  $G_i$  are the generalized source functions. A list of the  $D_{ij}$  matrix and  $G_i$  functions so obtained, with  $G_{d_i s}(f)$  equal to zero, is given in Appendix A.

Thus, by solving Eqs.(2.26) simultaneously with given wind information, the five free JONSWAP parameters can be obtained and the resulting JONSWAP spectrum can be then expanded according to the  $H_1(f, \theta)$  spreading function to generate a directional distribution of wave energy densities.

The nature of the parametric approach is that only single-peaked spectra are allowed in the hindcast, and as a result temporal and spatial variations of swells can not be included in the model. To include the swell portion of the wave energy, it is necessary to incorporate a discrete spectral method to accommodate the transport of swells. Unlike the parametric method, which resorts to solving the free spectral parameters of a predesignated spectral function, the discrete spectral method tracks the spectral densities of both the preexisting and currently generated waves in the wave field of interest. Accordingly, the spectra so obtained could have arbitrary shapes including multiple peaks. The details of the discrete spectral method are given in the next section.

## 2.5 Deepwater Discrete Model

The development of deepwater discrete spectral models is again based on the wave energy transport equation given in Eq.(2.15). The method utilized in discrete spectral models generates directly the directional distributions of wave energy according to the local atmosphere energy input and then transfers them advectively in the horizontal domain according to the governing equation. Since the fundamental

structure of a discrete spectral model does not change from one model to another, the solution procedure used in a discrete spectral model will be described in this section through the presentation of the discrete model developed by Wave Information Study (WIS) group at the Waterways Experiment Station (WES), U.S. Army Corps of Engineers.

The WIS model was originally created to hindcast the deepwater waves in the Atlantic Ocean between 1956 and 1975. The documentation of the model can be found in the series of WIS reports of Vol. 8 (Jensen, 1983a) and 12 (Resio and Tracy, 1983). The version of the WIS model presented here is the one modified by the same WIS group in 1984 by studying the deepwater wave hindcast in the Pacific Ocean.

The WIS model solves Eq.(2.15) numerically based on the following discretized form:

$$E^{k+1}(f, \theta) = E^k(f, \theta) - C_{go}(f) \frac{\Delta E^k(f, \theta)}{\Delta \ell} \cdot \Delta t + G(f, \theta) \cdot \Delta t \quad (2.27)$$

where the superscript indicates the time level. The second term on the RHS is energy advection and the third term is the net energy source, and these two terms are uncoupled.

The advective transfer of wave energy is computed in the model using the method developed by Hasselmann et al.(1968). This method divides the entire direction domain,  $0 < \theta \leq 2\pi$ , uniformly into sixteen directional bands, each having an angular span of  $2\pi/16$  radian, and wave energy contained in each band is advected independently without coupling with others. To express the method in a numerical scheme, the advective energy  $E(f, \theta)_{ad}$  may be written explicitly as

$$E^{k+1}(f, \theta) = E^k(f, \theta) - C_{go}(f) \frac{\Delta E^k(f, \theta)}{\Delta \ell} \cdot \Delta t$$

The source term is further divided into three components:

$$G(f, \theta) \cdot \Delta t = [G_{in}^{k+1}(f, \theta) + G_{dis}^k(f, \theta) + G_{nl}^k(f, \theta)] \cdot \Delta t \quad (2.28)$$

where  $G_{in}$ ,  $G_{dis}$ , and  $G_{nl}$  represent atmospheric energy input, wave energy dissipation and nonlinear wave-wave interaction, respectively. The  $G_{in}$  term, which is computed at the current time level, is further split into two parts: (i)  $G_{in,1}(f, \theta)$ , the rate of growth of the prevailing waves and (ii)  $G_{in,2}(f, \theta)$ , the rate of generation of new wind waves in the downwind direction.

In WIS model, the two atmospheric input terms are formulated as follows:

$$G_{in,1}\Delta t = \begin{cases} 4.4 \Delta t f_m \frac{g^2 \alpha^3}{(2\pi)^4 f^5} \frac{8}{3\pi} \cos^4(\theta - \bar{\theta}), & \text{if } f \geq f_m \\ 0, & \text{elsewhere} \end{cases} \quad (2.29)$$

with the mean propagation direction,  $\bar{\theta}$ , defined as

$$\bar{\theta} = \tan^{-1} \left\{ \frac{\iint \sin \theta E(f, \theta) df d\theta}{\iint \cos \theta E(f, \theta) df d\theta} \right\} \quad (2.30)$$

where the scale parameters  $\alpha$  and  $f_m$  are to be determined later.

$$G_{in,2}\Delta t = \begin{cases} \frac{\alpha g^2}{(2\pi)^4 f_m^5} \exp[1 - (\frac{f_m}{f})^4] \frac{2}{\pi} \cos^2(\theta - \theta_w), & \text{if } f_s \geq 0.25 \text{ (Hz)}, f < f_m, \\ & f_m \geq 0.2 \text{ (Hz)} \\ \frac{\alpha g^2}{(2\pi)^4 f^5} \frac{2}{\pi} \cos^2(\theta - \theta_w), & \text{if } f_s \geq 0.25 \text{ (Hz)}, f \geq f_m, \\ & f_m \geq 0.2 \text{ (Hz)} \\ 0, & \text{elsewhere} \end{cases} \quad (2.31)$$

where  $\theta_w$  denotes downwind direction and  $f_s$  denotes a peak energy saturation frequency which is not necessarily equal to the peak spectral frequency and is defined as

$$E(f_s) = \max \{E(f) > E_s(f)\}$$

$E_s(f)$  is the one-dimensional saturation spectrum defined as

$$E_s(f) = \begin{cases} \frac{\alpha g^2}{(2\pi)^4 f^5}, & \text{if } f < f_0 = g/2\pi U_{10} \\ \frac{\alpha g^2}{(2\pi)^4 f^5} [1 - (f_0/f_m)^4] + E_{PM}(f)(f_0/f_m)^4, & \text{elsewhere} \end{cases} \quad (2.32)$$

where  $f_0$  is the wind-wave resonant frequency to which the corresponding wave phase speed is identical to the wind speed at 10 m elevation,  $U_{10}$ , and  $E_{PM}$  denotes the P-M spectrum.

There are two scale parameters  $\alpha$  and  $f_m$  to be determined first at time level  $k+1$ . The scale parameter  $f_m$  is obtained by solving the prognostic equations derived in the  $(\alpha, f_m)$  plane as described by Hasselmann et al.(1976) in their parametric model. By allowing variations of only two free parameters  $\alpha$  and  $f_m$  in the JONSWAP parametric space, the  $\alpha$ - and  $f_m$ - component prognostic equations can be derived as

$$\frac{\partial \alpha}{\partial t} + 0.47 \overline{C_{g0}}(f) \frac{\partial \alpha}{\partial \ell} + 0.2 \overline{C_{g0}}(f) \frac{\alpha}{f_m} \frac{\partial f_m}{\partial \ell} = 0.005 \left( \frac{f_m U_{10}}{g} \right)^{4/3} \alpha f_m - 5 \alpha^3 f_m \quad (2.33)$$

and

$$\frac{\partial f_m}{\partial t} + \overline{C_{g0}}(f) \frac{\partial f_m}{\partial \ell} - 0.07 \overline{C_{g0}}(f) \frac{f_m}{\alpha} \frac{\partial \alpha}{\partial \ell} = -0.54 \alpha^2 f_m^2 \quad (2.34)$$

If the changing wind speed can be expressed as a power law of time,

$$U_{10} = U_0 \left( \frac{g t}{U_0} \right)^q$$

with  $U_0$  a reference wind speed,  $f_m$  and  $\alpha$  can be solved from Eqs.(2.33) and (2.34)

as

$$\frac{f_m U_{10}}{g} = A \left( \frac{g t}{U_0} \right)^{(3/7)(q-1)} \quad (2.35)$$

and

$$\alpha = B \left( \frac{f_m U_{10}}{g} \right)^{2/3} \quad (2.36)$$

with constants A and B given by (Hasselmann et al., 1976)

$$A = 16.8 (1 + 1.51 q)^{3/7}, \quad B = 0.031 \left( \frac{1 + 1.33 q}{1 + 1.51 q} \right)^{1/2}$$

To obtain  $f_m$  at time level  $k+1$ , the value at  $t$  in Eq.(2.35) is replaced by  $t + \Delta t$ , which results in

$$\frac{U_{10}^{k+1} f_m^{k+1}}{g} = A \left( \frac{g t}{U_0} + \frac{g \Delta t}{U_0} \right)^{(3/7)(q-1)} \quad (2.37)$$

Eliminating  $g t/U_0$  from Eqs.(2.35) and (2.37) yields

$$\frac{U_{10}^{k+1}}{U_{10}^k} f_m^{k+1} = \left\{ (f_m^k)^{(7/3)(q-1)} + \frac{g \Delta t}{U_0} \left( \frac{U_{10}^k}{A g} \right)^{-(7/3)(q-1)} \right\}^{(3/7)(q-1)} \quad (2.38)$$

For constant wind speed within the duration  $\Delta t$ , the above equation reduces to

$$f_m^{k+1} = \left\{ (f_m^k)^{-7/3} + a_{nl} \left( \frac{U_{10}^k}{g} \right)^{4/3} \Delta t \right\}^{-3/7} \quad (2.39)$$

where  $a_{nl}$  is the nonlinear wave energy transport coefficient defined by Hasselmann et al.(1976) and suggested as equal to 0.00138. In WIS model, the  $f_m^{k+1}$  value is replaced by  $f_0$  if the spectral peak frequency is less than  $f_0$ . Also, instead of using Eq.(2.36) to compute  $\alpha$ , WIS model employs the following relationship suggested by Resio and Vincent (1977):

$$\alpha = 0.0489 \left( \frac{g^2 E_{total}}{U_*^4} \right)^{-0.2} \quad (2.40)$$

where  $U_*$  is the surface frictional velocity obtained by assuming logarithmic over water wind profile

$$\frac{U_z}{U_*} = \frac{1}{0.4} \ln \frac{z}{z_0} \quad (2.41)$$

where  $U_z$  is wind speed at a height  $z$  above the sea surface, and  $z_0$  is the equivalent roughness at water surface given by

$$z_0 = \frac{0.1525}{U_*} + 0.0144 \frac{U_*^2}{g} - 0.00371, \quad (\text{in cgs units}) \quad (2.42)$$

Although Eq.(2.36) is not used in the WIS model, it can be linked to an empirical relationship  $(g^2 E_{total}/U_{10}^4)(f_m U_{10}/g)^4/\alpha = \text{constant}$  suggested by Hasselmann et al.(1976) to yield a power law  $\alpha \sim (g^2 E_{total}/U_{10}^4)^{-0.2}$  which is similar to Eq.(2.40).

The transfer of wave energy due to a nonlinear wave-wave interaction source  $G_{nl}(f, \theta)$  is formulated based upon Kitaigorodskii spectrum (1962) and a spreading function with the central angle parallel to the mean wave direction  $\bar{\theta}$  (Resio, 1981).

$$G_{nl}\Delta t = \begin{cases} 0.0023 \Delta t \frac{g^2 \alpha^3}{f_m^4} \psi(f/f_m) \frac{8}{3\pi} \cos^4(\theta - \bar{\theta}), & \text{if } |\theta - \bar{\theta}| \leq \pi/2 \\ 0, & \text{elsewhere} \end{cases} \quad (2.43)$$

where

$$\psi(f/f_m) = \begin{cases} \exp[1 - (f_m/f)^4], & \text{if } f < f_m \\ -(f_m/f)^5, & \text{if } f \geq f_m \end{cases}$$

The dissipation includes two parts: the energy loss of wind waves and the energy loss of swell. The energy loss of wind waves is accounted for by restricting the growth to saturated spectral condition with  $f^{-5}$  law on the downslope side. The loss of wave energy in swell is adopted from Resio (1981), in terms of one-dimensional frequency spectrum

$$G_{dis}\Delta t = \begin{cases} -4 \Delta t \frac{E^2(f_{me})}{(2\pi)^8 g^4} f_{me}^{11} E(f), & \text{if } f_{me} < f < 0.7 f_m \\ 0, & \text{elsewhere} \end{cases} \quad (2.44)$$

where  $f_{me}$  indicates peak spectral frequency of swell.

## 2.6 Shallow Water Model

As deepwater waves propagate into area of shallow water, they will sense the bottom and wave energy will be redistributed and dissipated in the direction and frequency domains due to refraction, shoaling, bottom friction, percolation, etc. Among these shallow water effects, only refraction and shoaling can be handled fairly readily in many situations, others require further theoretical and experimental

studies. Shallow water waves can also grow if winds are present and large enough to add energy into waves as a result of air-sea interaction.

In shallow water the wave energy transport equation can be expressed as follows: (Chen and Wang, 1983)

$$\frac{\partial E(f, \theta)}{\partial t} + \frac{\partial E(f, \theta) C_g(f, \theta) \cos \theta}{\partial x} + \frac{\partial E(f, \theta) C_g(f, \theta) \sin \theta}{\partial y} = G(f, \theta) \quad (2.45)$$

where  $\theta$  is defined counterclockwise from the positive x axis. Here, unlike the deepwater case, both  $C_g$  and  $\theta$  are no longer independent at position (actually water depth). In order to track energy transport, changes in wave direction due to wave refraction must be considered simultaneously. This requires solving additional equation governing the change of wave number vector. According to the refraction law, the curl of wave number is identical to zero, or

$$\nabla \times \vec{k} = \frac{(\partial k \cos \theta)}{\partial y} - \frac{(\partial k \sin \theta)}{\partial x} = 0 \quad (2.46)$$

Therefore, if the source function  $G(f, \theta)$  is known in advance, the directional spectrum  $E(f, \theta)$  in shallow water can be obtained by solving both Eqs.(2.45) and (2.46). It should be noted that neither current nor tide is considered to influence the wave spectral transformation governed by Eqs.(2.45) and (2.46). Although it is possible to include the current and tide effects in solving the wave spectra in the shallow water (Chen and Wang, 1983), the influences of currents and tides to the wave spectral transformation in the shallow water will be exclusive in the present study for the following two reasons. First, the numerical model which includes the current and tide effects in estimating shallow water wave spectra is in general dealing with a large matrix of equations such that execution of the model is not efficient in the aspect of computational time. Second, the insufficient information about interactions among waves, currents, and tides, according to the present knowledge, may cause problem in defining the source terms associated with both current and tide influences.

The source function  $G(f, \theta)$  may still be represented by the summation of three contributions, namely, generation, dissipation, and nonlinear wave-wave interaction, although the formulas are expected to be different from the deepwater ones due to the influence of the bottom.

$$G(f, \theta) = G_{in}(f, \theta) + G_{dis}(f, \theta) + G_{nl}(f, \theta)$$

Explicit formulas for individual source terms are well documented in the past (Chen and Wang, 1983; Collins, 1972; Shemdin et al., 1978) and are briefly described in the remainings of this section.

The generation term is usually defined by a combined Phillips' and Miles' mechanism (Barnett, 1968; Chen and Wang, 1983), i.e.,

$$G_{in}(f, \theta) = a(f, \theta) + \beta E(f, \theta) \quad (2.47)$$

where  $a$  and  $\beta$  are linear and exponential growth coefficients, respectively. Contributions of the first term (Phillips' mechanism) is small but essential in their model to initiate wave growth. The coefficient  $\beta$  is proposed by Barnett (1968)

$$\beta = \begin{cases} 5 s f \left( \frac{U_{10}}{C} - 0.9 \right), & \text{if } \frac{U_{10}}{C} > 0.9 \\ 0, & \text{elsewhere} \end{cases} \quad (2.48)$$

Under this growth, wave energy is increasing faster in the high frequency components than the low frequency components. Therefore, saturation condition needs to be invoked to exclude the excessive energy by means of wave breaking. In shallow water region, the saturation condition has been suggested by Bouws et al.(1983) to be the product of the deepwater saturated spectrum, such as the one shown in Eq.(2.34), and an energy transfer function

$$\Phi(k, h) = \frac{k^3(f, \infty) C_g(f, \infty)}{k^3(f, h) C_g(f, h)} = \frac{1}{2n} \frac{k^2(f, \infty)}{k^2(f, h)} \quad (2.49)$$

The growth of a spectral component according to the combined Phillips' and Miles' mechanism can be studied for the hypothesized fetch-limited and duration-limited cases. For a steady state, one-dimensional, and frictionless situation, the

growth of a spectral frequency component in the downwind direction is governed by the following ordinary differential equation

$$C_g(f) \frac{d}{dx} E(f) = \alpha + \beta E(f)$$

By specifying  $E(f) = 0$  at  $x = 0$  as the boundary condition, the solution for spectral component  $E(f)$  is

$$E(f) = \frac{\alpha}{\beta} \left[ \exp\left(\frac{\beta x}{C_g}\right) - 1 \right]$$

For small fetch,  $E(f)$  approximates  $(\alpha/C_g)x$ , which corresponds to the Phillips' linear growth mechanism. For large fetch,  $E(f)$  approximates  $(\alpha/\beta) \exp(\beta x/C_g)$ , which corresponds to the Miles' exponential growth mechanism. In the real situation the exponential growth is limited to a saturation condition and an overshoot growth occurs between the exponential growth region and the saturation region. A typical growth curve for one spectral component in the fetch-limited case appears in Fig. 2.4(a).

For a duration-dependent, one-dimensional, and frictionless situation, the growth of a spectral component can be determined from the following ordinary differential equation

$$\frac{d}{dt} E(f) = \alpha + \beta E(f)$$

By specifying  $E(f) = 0$  at  $t = 0$  as the initial condition, the general solution for  $E(f)$  is

$$E(f) = \frac{\alpha}{\beta} \left[ \exp(\beta t) - 1 \right]$$

For small duration,  $E(f)$  approximates  $\alpha t$ , which corresponds to the Phillips' mechanism. For large duration,  $E(f)$  approximates  $(\alpha/\beta) \exp(\beta t)$ , which corresponds to the Miles' mechanism. In the real situation the exponential growth is again limited

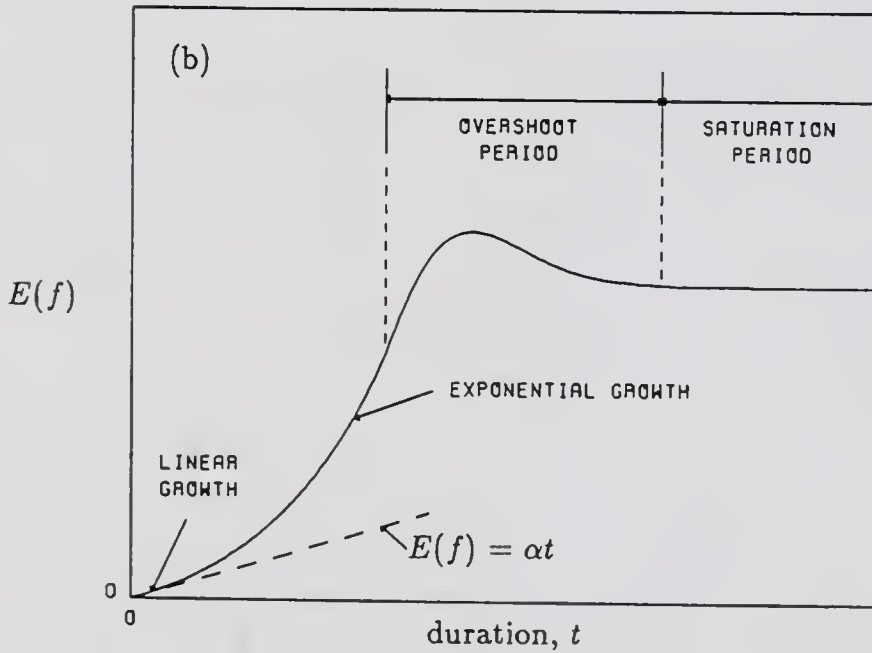
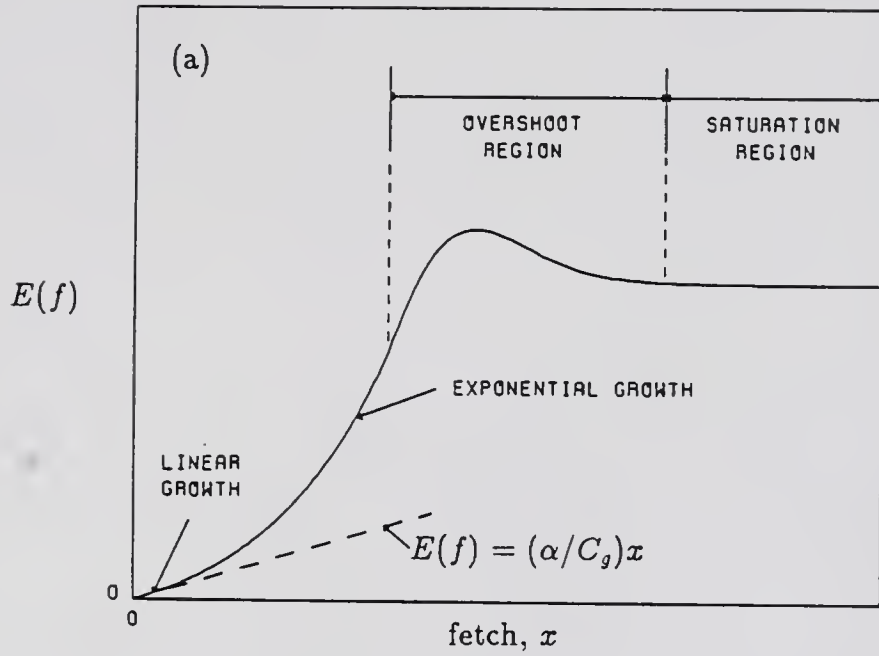


Figure 2.4: Schematic illustration of growth of a spectral component,  $E(f)$ , at (a) fetch-limited case and at (b) duration-limited case.

to a saturation condition and an overshoot growth occurs between the exponential growth and the saturation periods. A typical growth curve for one spectral component in the duration-limited case appears in Fig. 2.4(b).

The rate of dissipation in the shallow water,  $G_{dis}(f, \theta)$ , is in general thought to come from five sources: bottom friction, percolation, whitecaps, breaking in maintaining the equilibrium spectrum, and breaking due to the depth limitation.

The dissipation rate attributed to bottom friction can be determined by the work done by the bottom stress, i.e.,

$$G_{dis,b}(f, \theta) df d\theta = \overline{d\tau_b du_b(f, \theta)} / (\rho_w g)$$

where  $u_b$  is horizontal velocity component at sea bed,  $\tau_b$  is the bottom shear stress, and  $\rho_w$  is the water density. By expressing the bottom shear stress based on the empirical law

$$\tau_b = -\rho_w c_f u_b(f, \theta) |u_b(f, \theta)|$$

where  $c_f$  is bottom friction coefficient, and expressing  $du_b(f, \theta)$  in terms of  $d\eta(f, \theta)$  according to linear wave theory,

$$du_b(f, \theta) = \frac{g k}{\sigma \cosh kh} d\eta(f, \theta),$$

the rate  $G_{dis,b}(f, \theta)$  may be approximated by the equation (Collins, 1972)

$$G_{dis,b}(f, \theta) = -\frac{g k^2 c_f \langle u_b \rangle}{\sigma^2 \cosh^2 kh} E(f, \theta) \quad (2.50)$$

where  $\langle u_b \rangle$  denotes the root mean square value of horizontal wave orbital velocity component at bed and can be computed from the expression

$$\begin{aligned} \langle u_b \rangle^2 &= \overline{[u_b(\vec{s}, t)]^2} = \int_s \overline{[du_b(f, \theta)]^2} = \int_s \frac{g^2 k^2}{\sigma^2 \cosh^2 kh} \overline{[d\eta(f, \theta)]^2} \\ &= \int_0^\infty \int_{-\pi}^\pi \frac{g^2 k^2 E(f, \theta)}{\sigma^2 \cosh^2 kh} d\theta df \end{aligned} \quad (2.51)$$

The rate of dissipation of wave energy in the shallow water due to effect of a porous sandy bottom,  $G_{dis,p}(f, \theta)$ , can be estimated by the work done by the action of wave-induced dynamic pressure at the surface of the bed to cause the fluid motion in the porous sand layer.

$$G_{dis,p}(f, \theta) df d\theta = \overline{dp_b dw_b} / (\rho_w g) \quad (2.52)$$

where  $p_b$  and  $w_b$ , respectively, stand for the dynamic pressure and vertical water partial velocity at the surface of the bed. For porous sand layer of depth  $d$  this rate of dissipation derived by Shemdin et al.(1978) is

$$G_{dis,p}(f, \theta) = -k\sqrt{\lambda_1\lambda_2} \frac{\tanh(\sqrt{\lambda_1/\lambda_2} kd)}{\cosh^2 kh} E(f, \theta) \quad (2.53)$$

where  $\lambda_1$  and  $\lambda_2$  are the horizontal and vertical percolation coefficients, respectively, and they have the dimension of (length)/(time).

The dissipation of wave energy caused by damping due to kinematic viscosity,  $\nu_k$ , and turbulent eddy viscosity,  $\nu_t$ , according to a theoretical analysis made by Lamb (1932), can be shown as

$$G_{dis,v}(f, \theta) = -4(\nu_k + \nu_t)k^2 E(f, \theta) \quad (2.54)$$

The kinematic viscosity of sea water  $\nu_k$ , which is approximately equal to 0.018 cm<sup>2</sup>/sec at 32°F, is generally several orders of magnitude smaller than the turbulent eddy viscosity  $\nu_t$ . By neglecting the dissipation caused by the kinematic viscous effect in Eq.(2.54), and assuming the magnitude of turbulent viscosity induced in the water waves is linearly proportional to the product of wave phase speed and wave length, the resulting equation may be expressed in the form

$$G_{dis,v}(f, \theta) = -c_v f E(f, \theta) \quad (2.55)$$

where  $c_v$  is the constant of proportionality. This equation has been proposed by Hasselmann (1974) to limit the growth of wave energy on the rearface of the spec-

According to the JONSWAP study, the dissipation rate defined in Eq.(2.55) is generally found to be several orders of magnitude smaller than the generation rate. However, actual dissipation due to whitecaps may not be small as indicated by the JONSWAP study which utilized a hypothesized equilibrium spectral shape, i.e., JONSWAP spectrum, to define the energy generation term that has included the influence of dissipation due to whitecaps. Thus, without having a reasonable estimate of dissipation due to whitecaps, the limit of wave growth in the shallow water model is traditionally given by a saturation condition (Chen and Wang, 1983):

$$A(f) = B g^2 (2\pi f)^{-5} \Phi(k, h) \quad (2.56)$$

where  $B$  is a coefficient to be of the order of  $10^{-2}$ , and  $\Phi(k, h)$  is defined in Eq.(2.49).

The breaking of shallow water waves due to depth limitation occurs as a consequence of strong wave-bottom interaction in the nearshore region. It is this breaking mechanism that produces the turbulent flow and enhances the significant movement of bed materials responsible for either erosion or deposition of the bed. The estimation of energy dissipation for breaking due to depth limitation is important since it matters greatly the sediment transport in the coastal waters. However, an analytical estimation of the dissipation is not found and the determination of this value must rely on empirical formula. An empirical criterion, which estimates the total wave energy retained in waves after the waves break due to depth limitation, often used in the shallow water model is (Chen and Wang, 1983)

$$(E_{total,b})^{1/2} = \frac{0.2}{k_b} \tanh(k_b h) \quad (2.57)$$

where the subscript  $b$  indicates the breaking condition. The value  $k_b$  is usually taken as the wave number corresponding to modal period although it is in general not clear what value of  $k_b$  should be used in the equation.

## 2.7 Wave Data and Comparisons

In 1977, the Department of Coastal and Oceanographic Engineering at University of Florida (UF) initiated a shallow water wave data collection program around the State of Florida. By 1985, twelve wave stations have been established (See Fig. 2.5). In the offshore region, there are two NOAA maintained wave buoys with ID No. 41002 and 41006 as shown.

Of the twelve shallow water stations, data from Kings Bay, Marineland and Cape Caneveral are eventually being used here for comparison purposes. At Kings Bay, two PUV underwater packages as manufactured by Sea Data Inc. (Model 635-12) were deployed at 15 m and 18 m water depth. These packages are self-contained with the ability to measure two axes water particle velocities U and V, and the pressure information, P. Directional wave information is derived from the P-U-V data based on the method proposed by Longuet-Higgins et al.(1963). Detailed data handling and analysis procedures are given in the User's Guide by UF (1984). The gages at Marineland and Cape Caneveral are shore-connected underwater pressure transducers at 10 m and 8 m water depths respectively. Only wave height information can be retrieved from them.

The deepwater buoy stations are located at 29.3°N, 77.3°W (#41006) and at 32.3°N, 75.3°W (#41002). The water depths of these two stations are 970 m and 3200 m, respectively. These buoys also collect 5 m-level winds every hour, based on an 8.5 minute record.

One of the intentions of the field data measurement program is to provide wave climate information along the south eastern seaboard of the United States. To accomplish this goal, a numerical wave prediction model is required to fill in the data gaps and to extend data extrapolation.

The WIS model was first tested against the measured deepwater wave data at NOAA buoy #41006. A segment of the data covering the complete month of

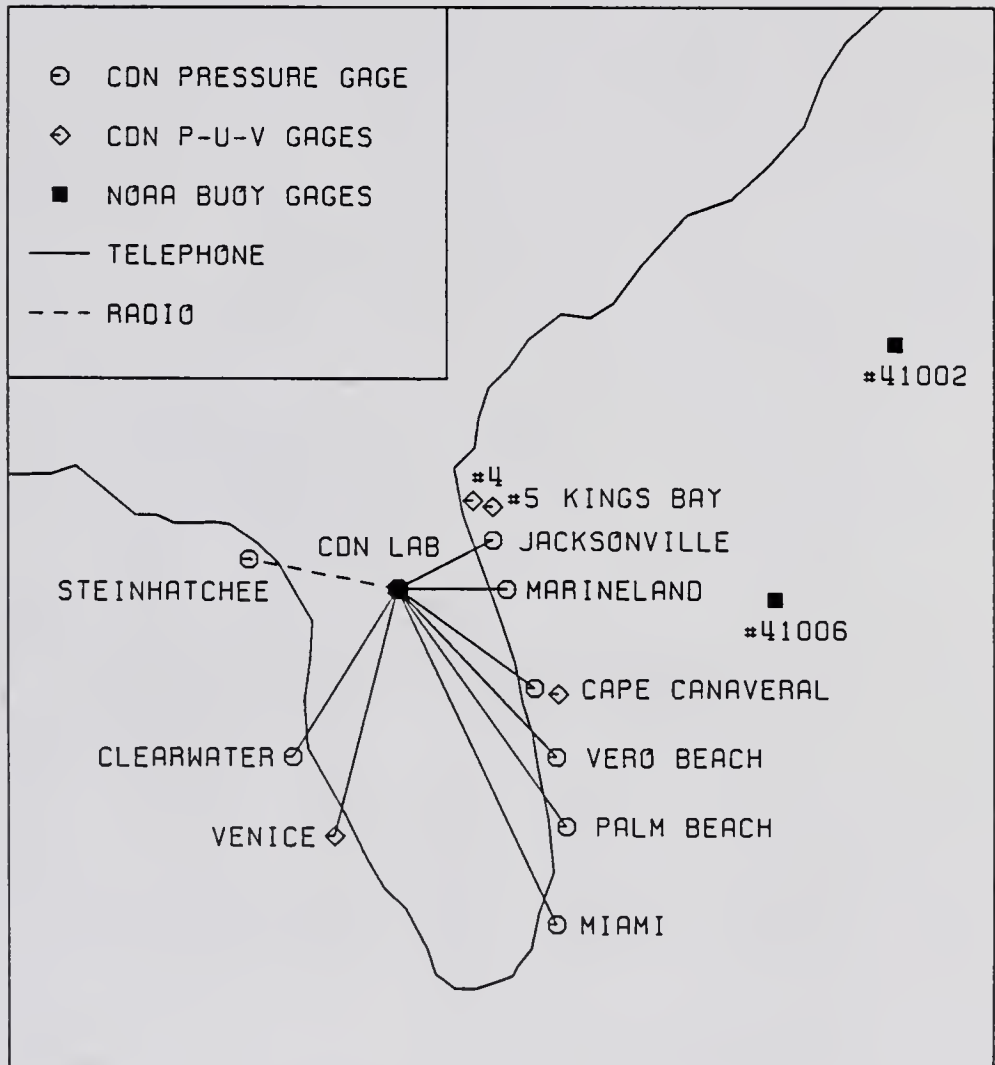


Figure 2.5: Wave gage stations.

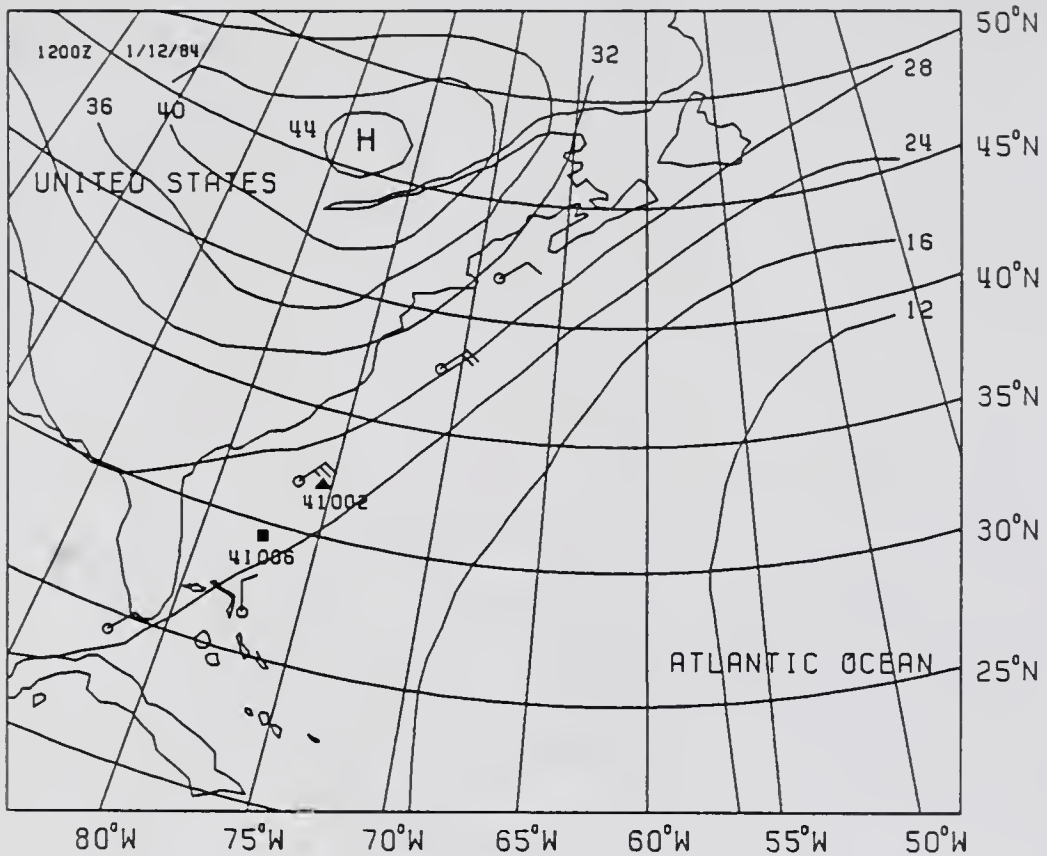


Figure 2.6: (a) Weather map showing northeast winds generated by a high pressure system (1/12/84).

January, 1984 was used for testing purposes for two reasons: (i) During this month, directional wave data at Kings Bay was available for the entire month and (ii) January is usually the month of high waves dominated by large scale high pressure systems. Figure 2.6(a) and 2.6(b) show two examples of typical large scale high pressure systems occurring in January. In these examples, the northeast winds developed from the high pressure systems will generate waves that propagate to the southeastern coast of the United States.

The grid system covers an orthogonal-spherical area with the east and the west boundaries coinciding with  $70.0^{\circ}\text{W}$  and  $82.5^{\circ}\text{W}$ , respectively, and with the north and south boundaries coinciding with  $42.5^{\circ}\text{N}$  and  $22.5^{\circ}\text{N}$ , respectively. The grids are all parallel to the longitudes and latitudes such that each grid is 2.5 degrees apart

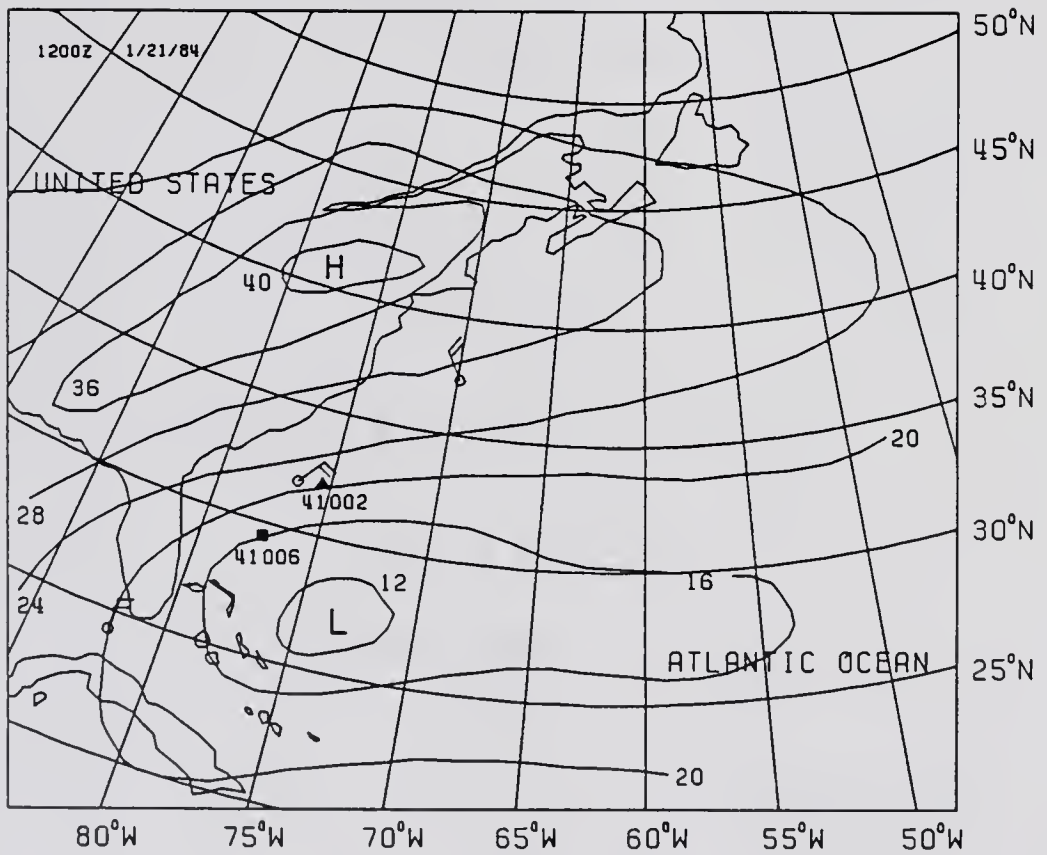


Figure 2.6: (b) Weather map showing northeast winds generated by a high pressure system (1/21/84).

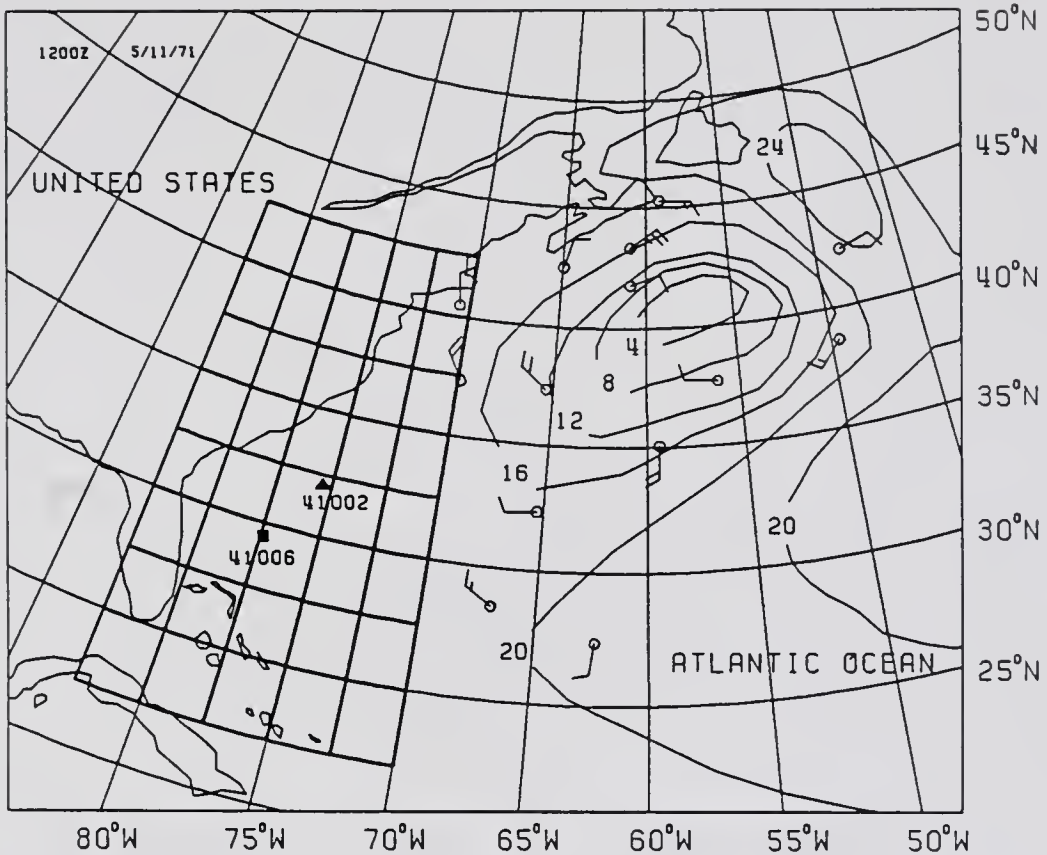


Figure 2.7: Deepwater grid coordinate system.

from the next and a total of  $6 \times 9$  grid points are found in the system (Fig. 2.7). The wind information served as the input for the model was obtained by analyzing surface pressures from daily weather maps. The theories of the geostrophic winds and planet boundary layers were used in the analysis (see Section 3.4 - wind model). The 10 m-level winds were generated at the grid system for forty days starting on December 21, 1983. The computed winds were then blended with the ones measured by the NOAA buoys.

The radiative boundary condition is utilized in the wave model. However, two modifications were made to the boundary condition. The first one was made to the boundary where the grid system is connected with land. It simply regulates

that no wave energy is transported to sea from land. The second one was made to the boundary where the grid system is connected with the sea. It regulates that the amount of wave energy advected from a grid point at the boundary to the grid points inside the boundary is the same as the wave energy transported from the area outside the boundary to the grid point at the boundary. Therefore, a quasi-stationary wave energy transport process is assumed at the seaboard grid boundaries.

The wave model was run at time increment equal to two hours for a total of forty-one days from December 21, 1983 to January 31, 1984. The first ten days were for initialization and the results were not used for comparison. Figure 2.8 shows the comparison of the time series of the wave energy spectral evolution process of the entire month. The correlations of the measured and computed modal period and significant wave height are shown in Fig. 2.9. The significant wave height, which is commonly denoted as  $H_{1/3}$  or  $H_s$ , is defined as the average height of the one-third highest waves. When the heights of individual waves in a deepwater wave record are ranked from the highest to lowest, the frequency of occurrence of waves above any given value is given to a close approximation by the cumulative form of the Rayleigh distribution. Therefore, the significant wave height can be determined approximately from the following equation:

$$H_s = 4.0 (E_{total})^{1/2}$$

The correlation coefficient,  $\delta$ , given in Fig. 2.9 is defined as follows:

$$\delta = \frac{\sum_{i=1}^N [(X_c)_i (X_m)_i - \overline{(X_c)_i} \overline{(X_m)_i}]}{\{[\sum_{i=1}^N [(X_c)_i - \overline{(X_c)_i}]^2 \sum_{i=1}^N [(X_m)_i - \overline{(X_m)_i}]^2]^{1/2}} \quad (2.58)$$

where  $X_c$  is a computed  $X$ ,  $X_m$  is a measured  $X$ ,  $N$  is the sample size, and the overhead bar indicates the operation of arithmetic mean.

The measured and hindcasted energy scale parameter,  $f_m^2 H_s / g$ , are plotted in Fig. 2.10 for waves with  $H_s \geq 3$  m,  $3 \text{ m} > H_s \geq 2$  m, and  $H_s < 2$  m.

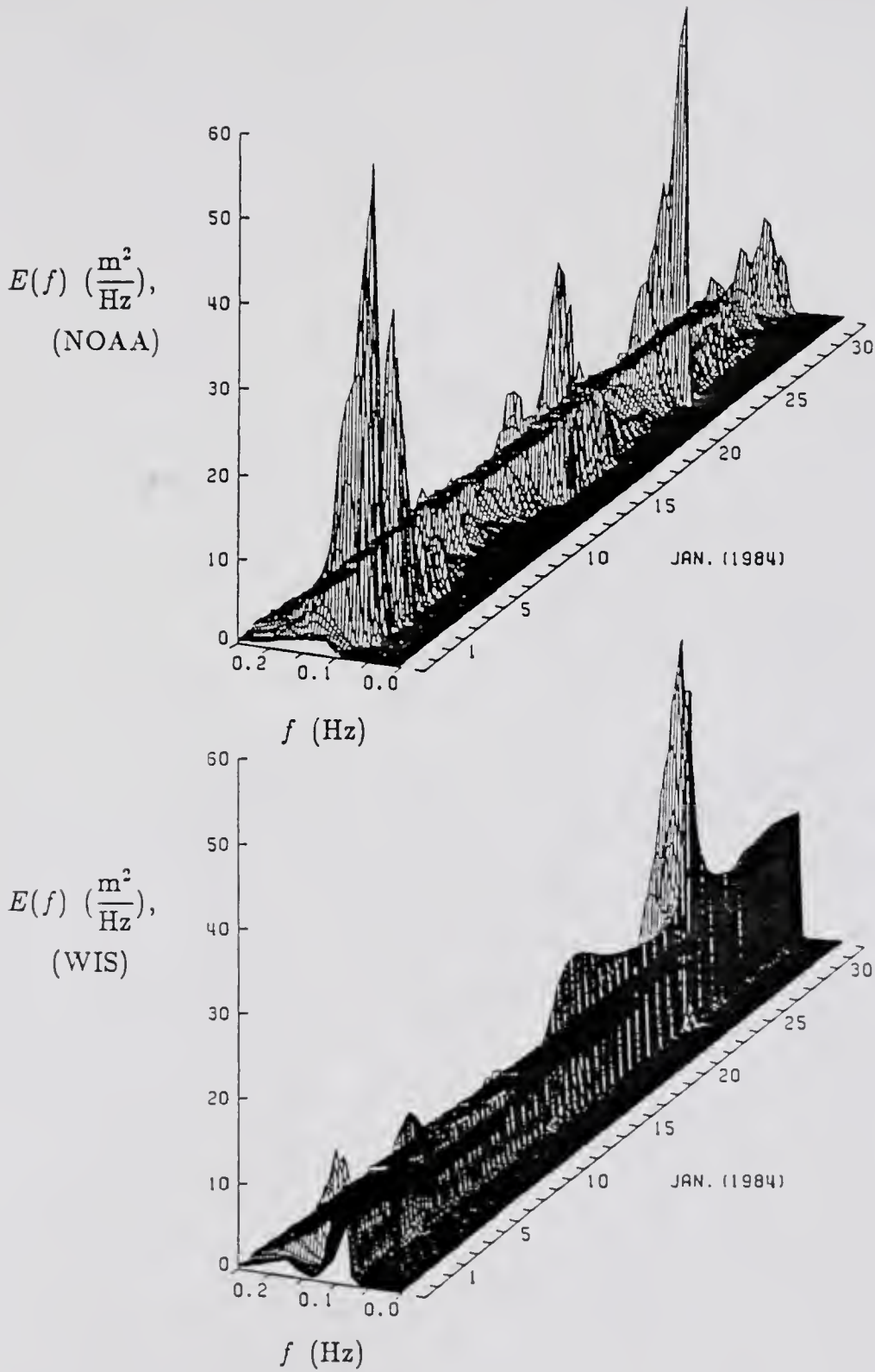


Figure 2.8: Comparison of NOAA and WIS wave spectra for January 1984 at the Buoy #41006 location.

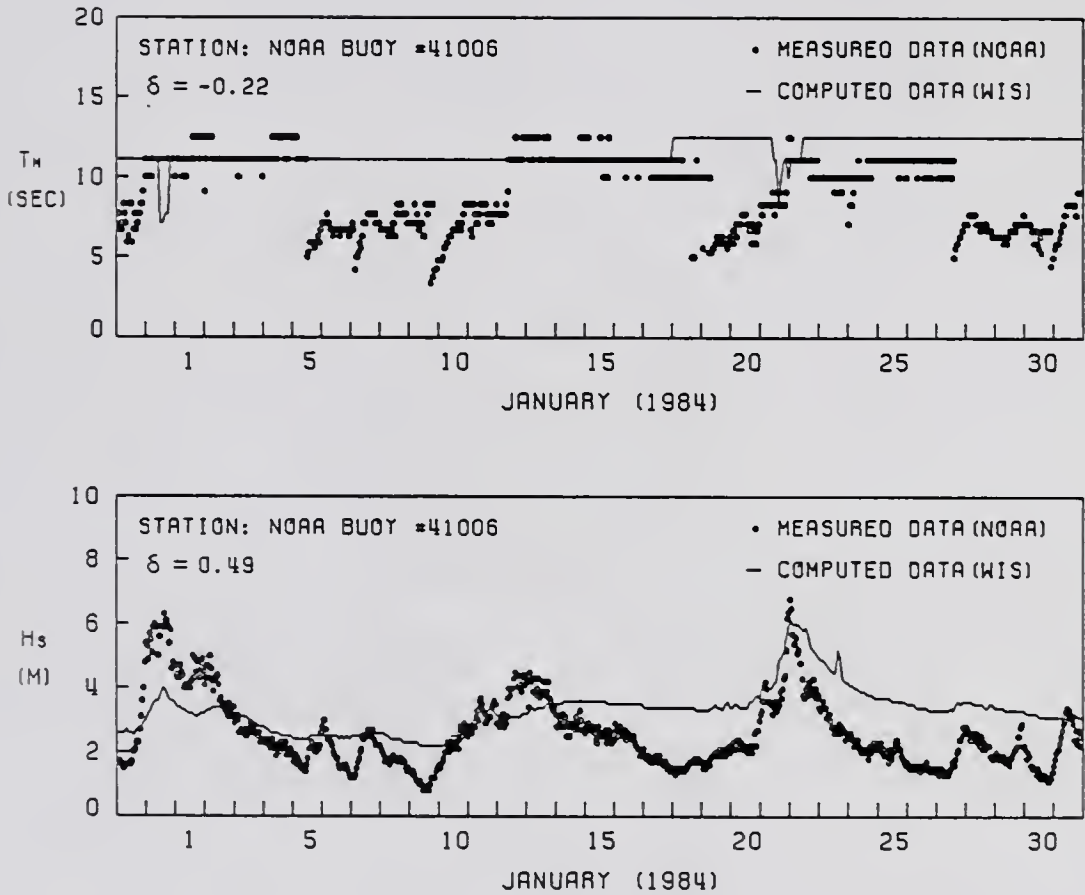


Figure 2.9: Comparisons of NOAA and WIS modal periods and significant wave heights at the Buoy #41006 location.

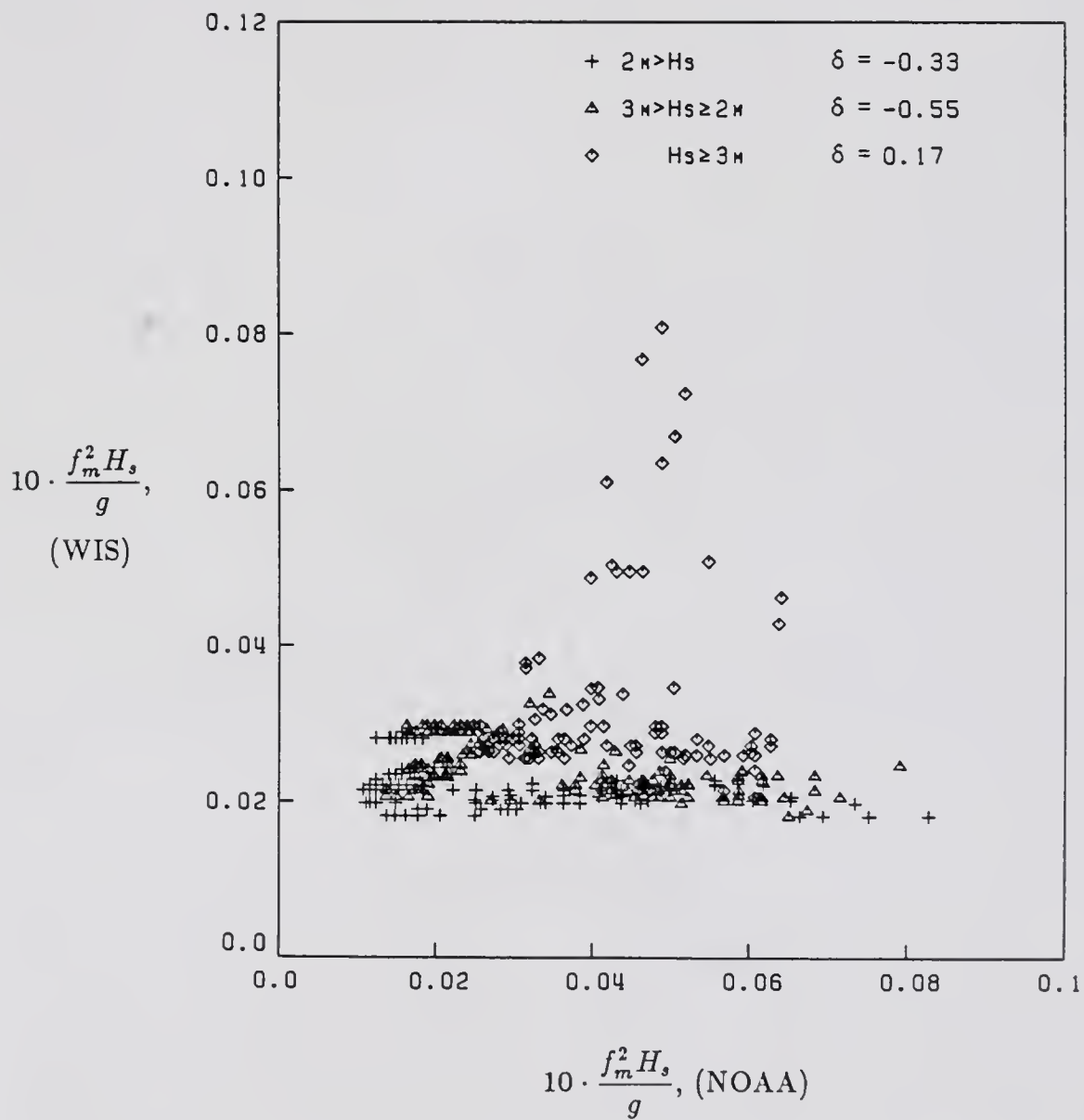


Figure 2.10: Comparison of NOAA and WIS wave energy scale parameters at the Buoy #41006 location.

Clearly, the model performs better for hindcasting wave height ( with a correlation of 0.5) than for wave frequency (with a negative correlation coefficient). The model performance also improves progressively for higher wave environment (Fig. 2.9) and this is particularly the case if the wind wave dominates. The model fares the worst on hindcasting the swell component. As can be seen in Fig. 2.8, both growth and decay of low frequency components hindcasted by the model are clearly inadequate.

## CHAPTER 3 A UNIFIED COASTAL WAVE PREDICTION MODEL

### 3.1 Introduction

It is shown in the last chapter that the parametric model and the discrete model are two alternative methods to hindcast waves in deep water. Growth rates of wave height predicted by the parametric model of Hasselmann et al.(1976) and the WIS model were consistent in the case which waves are growing either along a fetch or through time (Resio, 1981; Resio and Tracy, 1983). However, the comparison of the hindcast based upon either model to the measured wave heights from buoy in the open ocean often shows discernible deviations (Günther et al., 1979; Corson and Resio, 1981). The comparison of the modal periods computed from either model to the buoy data also shows certain degree of discrepancy (Günther et al., 1979). Thus, it seems necessary to modify the existing models in order to improve the accuracy of the hindcasted waves compared to the measured data.

A new unified wave model, named here as the Unified Coastal Wave Prediction (UCWP) model, was developed in the present study. The model is of discrete type and is comprised of deepwater and shallow water submodels. The deepwater submodel is a modified WIS model. The modifications are mainly in the source functions by incorporating some recent development in air-sea interaction. The model is calibrated by utilizing the field wind and wave data collected by NOAA buoys and it is suitable for hindcasting ocean waves generated by either high pressure or low pressure weather system. The shallow water submodel is based upon the numerical algorithm developed by Chen and Wang (1983) and it is suitable for hindcasting coastal water waves.

In the following sections of this chapter, both the UCWP deepwater and shallow water submodels will be introduced. The deepwater submodel is to be described in Section 3.2 and the shallow water submodel is in Section 3.3. A wind model which prepares the wind data for the generation of water surface waves in the UCWP model is described in Section 3.4.

### 3.2 UCWP Deepwater Submodel

The deepwater submodel is a spectral model of the discrete type. This model is more flexible in selecting source functions than a parametric model as it is not always an easy task to introduce new source functions in the JONSWAP parameter space.

The governing equations for the UCWP deepwater model are the same as the WIS model described earlier, i.e., Eqs.(2.27) and (2.28). The advection term in model is computed in the same manner as in the WIS model. The source terms including both generation and dissipation in the UCWP deepwater model are modified from WIS model.

#### 3.2.1 Generation terms

Recent studies made by Mitsuyasu and Honda (1982), and Mitsuyasu (1985) indicate that the mechanism corresponding to wave growth due to wind input shall be considered separately for the prevailing gravity waves and the locally generated wind waves. Therefore, the utilization of Eq.(2.23) alone to estimate wave growth does not seem to be a proper approach in the parametric model. On the other hand, the WIS model which utilizes two separate mechanisms expressed by Eqs.(2.29) and (2.31) to estimate, respectively, the growth of prevailing waves and new wind waves seems to be more consistent with the nature of wave growth.

In the WIS model, the wave generation comprises of three terms – growth of prevailing waves, generation of new wind waves and nonlinear transfer of energy among wave components. The growth terms are computed at time level  $k+1$  and the

transfer term is computed at time level  $k$ . The first and the last terms – Eqs.(2.29) and (2.43), respectively – are of a similar nature, responsible for the evolution of existing wave components. Their combined effect is shown in Fig. 3.1. Here, the nonlinear energy transfer is seen to be the dominant mechanism and has an abrupt cutoff at  $f = f_m$ . The growth of the down-slope face of the spectrum is shown to be a minor process. At peak spectral frequency,  $f = f_m$ , approximately 80 percent of the energy growth is being transferred to lower frequencies. By comparison with field data as discussed in the previous section, the predicted spectral shape is found to be too sharp peaked due to the abrupt cutoff and the low frequency components grow too fast because of the proposed nonlinear transfer process. A new growth term is proposed.

Since we have shown that the wave-wave interaction source term behaves like an apparent wind source term, it can be lumped into the wind source term for the growth of the prevailing waves. Based upon the common practice that this source term should be related to a stable spectral shape to maintain similarity, we confine our search to established spectral functions by testing them against field data collected during steady winds when the prevailing wave growth is the dominant mechanism. After various trails, a new source function is proposed here:

$$G_{in,1}(f, \theta) = \begin{cases} c_s \alpha^2 f E_{JM}(f) \frac{8}{3\pi} \cos^4(\theta - \bar{\theta}), & \text{if } |\theta - \bar{\theta}| \leq \frac{\pi}{2} \text{ and } |\theta_w - \bar{\theta}| \leq \frac{\pi}{2} \\ 0, & \text{elsewhere} \end{cases} \quad (3.1)$$

where  $c_s$  is a non-dimensional coefficient, regarded by some investigators to be a function of density ratio of air to water, and  $E_{JM}(f)$  is the one-dimensional modified JONSWAP spectrum proposed recently by Donelan et al.(1985):

$$E_{JM}(f) = \frac{\alpha g^2}{(2\pi)^4 f^4 f_m} \exp[-(f_m/f)^4] \gamma \exp[-\frac{1}{2}(\frac{f - f_m}{\sigma_{ab} f_m})^2] \quad (3.2)$$

with all its free parameters  $\alpha$ ,  $f_m$ ,  $\gamma$ , and  $\sigma_{ab}$  defined the same as in the JONSWAP

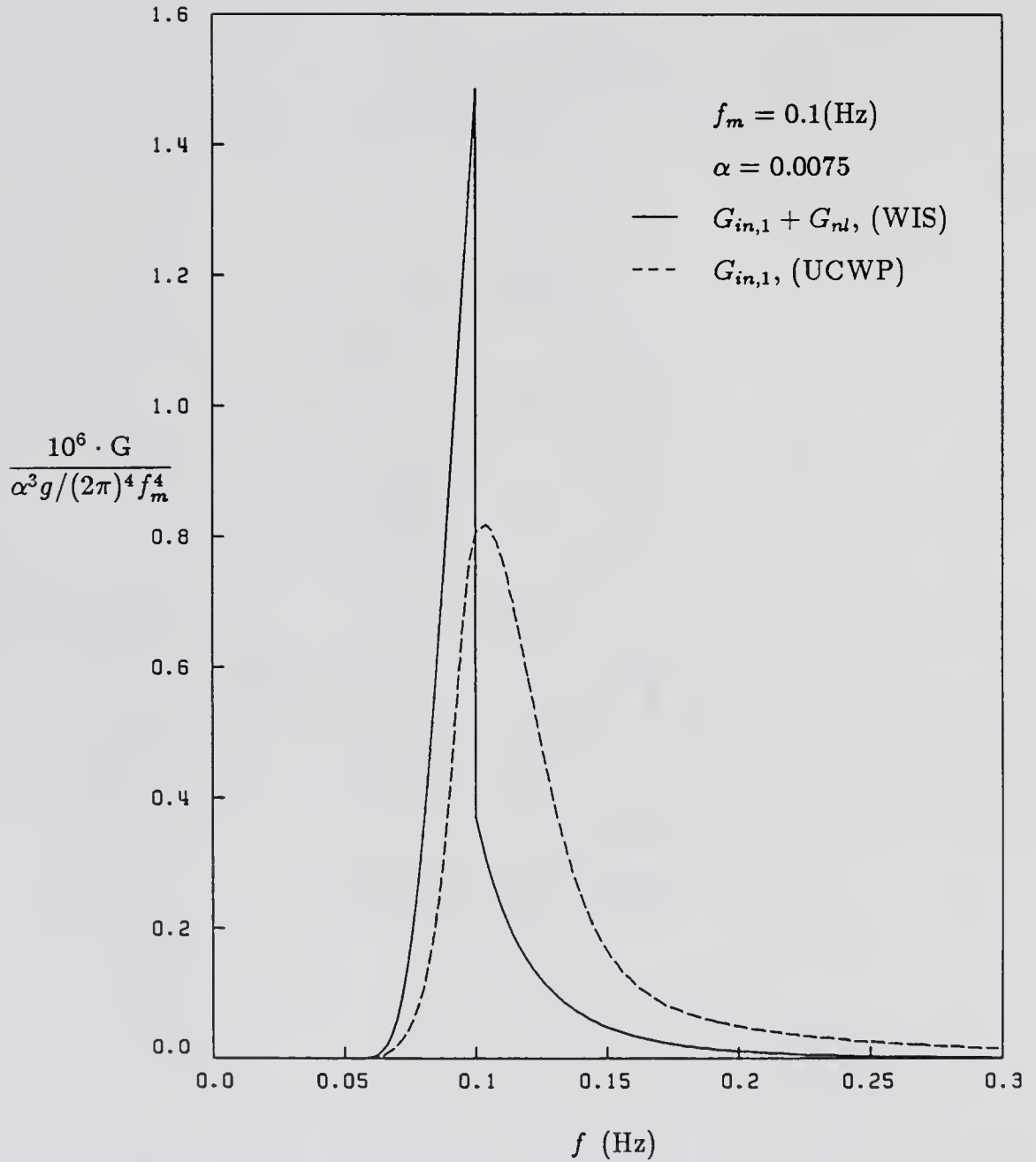


Figure 3.1: Combined sources of nonlinear term and generation term in WIS model.

spectrum. Substituting Eq.(3.2) into Eq.(3.1) and absorbing  $c_s$  into  $\alpha$ , we have

$$G_{in,1}(f, \theta) = \begin{cases} \frac{\alpha^3 g^2}{(2\pi)^4 f^3 f_m} \exp[-(f_m/f)^4] \gamma \exp[-\frac{1}{2}(\frac{f-f_m}{\sigma_{ab} f_m})^2] \frac{8}{3\pi} \cos^4(\theta - \bar{\theta}), & \text{if } |\theta - \bar{\theta}| \leq \frac{\pi}{2} \text{ and } |\theta_w - \bar{\theta}| \leq \frac{\pi}{2} \\ 0, & \text{elsewhere} \end{cases} \quad (3.3)$$

The peak frequency  $f_m$  is determined from the following equation:

$$f_m^{k+1} = \{(f_{ms}^k)^{-7/3} + a_{nl}(\frac{U_{10}^k \cos(\bar{\theta} - \theta_w)}{g})^{4/3} \Delta t\}^{-3/7} \quad (3.4)$$

which is similar to Eq.(2.39) with the exceptions that the wind component parallel to the mean wave propagation is used here instead of the absolute strength and that the spectral peak frequency  $f_m^k$  given in Eq.(2.39) is now replaced by a newly defined peak energy transfer frequency,  $f_{ms}$ . This peak energy transfer frequency is defined as

$$E(f_{ms}) = \max \{E(f) > E_c(f)\}$$

where  $E_c(f)$  is a threshold spectrum below which no energy transfer will occur from high frequency components to low frequency components. To use  $f_{ms}$  instead of  $f_m$  in Eq.(3.4) physically limits the energy transfer to those components exceeding the threshold condition.

At present, there is no established guideline to determine the threshold spectrum,  $E_c(f)$ . However, based upon physical reasonings, we observe here that  $E_c(f)$  should, at least, satisfy the following criteria: (i) The threshold spectrum should fall below the saturation (equalibrium) spectrum as energy transfer is expected to take place before the spectral energy reaches saturation. (ii) The threshold spectrum should be a monotonically increasing function with decreasing frequency and should approach equalibrium spectrum at low frequencies where energy transfers become more and more difficult.

To propose a suitable  $E_c(f)$ , two years measured data – 1984, 1985 – from NOAA buoys #41002 and #41006 were examined. Since we are dealing with the mechanism on the growth of prevailing waves, only those data corresponding to increasing in both wave energy and modal period were used. Figure 3.2 shows the plots of  $E(f_m)$  versus  $f_m$  from the data of buoys #41002 and #41006. If the mean values of the data points are connected, they form a skewed bell-shaped curve with a peak value,  $f_p$ , occurring at frequency between 0.09 and 0.11 Hz. This indicates that energy transfer experiences strong resistance when  $f_m$  becomes less than this peak value.

Based upon the above observations, we propose here the following functional form for  $E_c(f)$ :

$$E_c(f) = c_{ms} \frac{\alpha_p g^2}{(2\pi)^4 f^5} e^{-5/4} \exp\left[-\left(\frac{f}{f_p}\right)^2\right] \quad (3.5)$$

which is the P-M equilibrium spectrum modified by a multiplier. Here  $c_{ms}$  is an empirical scale factor which is chosen as equal to 0.183 by matching Eq.(3.5) with the data mean at designated  $f_p=0.1$  Hz. Both Eq.(3.5) and the original P-M equilibrium spectrum are shown in Fig. 3.2, with the data. As can be seen,  $E_c(f)$  has the basic characteristics as discussed with the most active energy transfer process taking place in the energy containing range.

It is noted here that plots of spectral peak energy versus spectral peak frequency in the wave growth cases in Fig. 3.2 show that the data are scattered in the equilibrium range indicated by the P-M spectrum. Although the data scattering could be exaggerated by the presence of swells, which generally appear as long waves, there is no indication that a simple curve, such as the P-M equilibrium spectrum, can represent the relationship. The data scattering suggests active nonlinear wave-wave interactions. That is, energy transfer from higher frequency components to lower frequency ones is a nonlinear process and it is dependent upon multi-variables including wind speed, wave phase speed, peak energy frequency, etc.

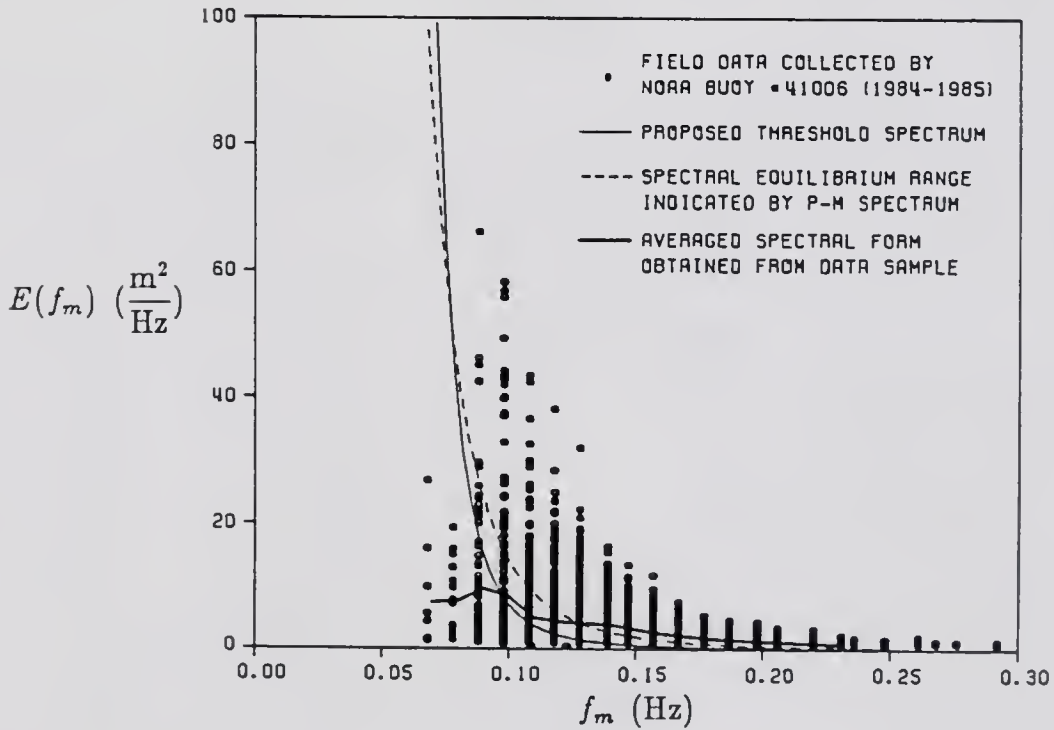
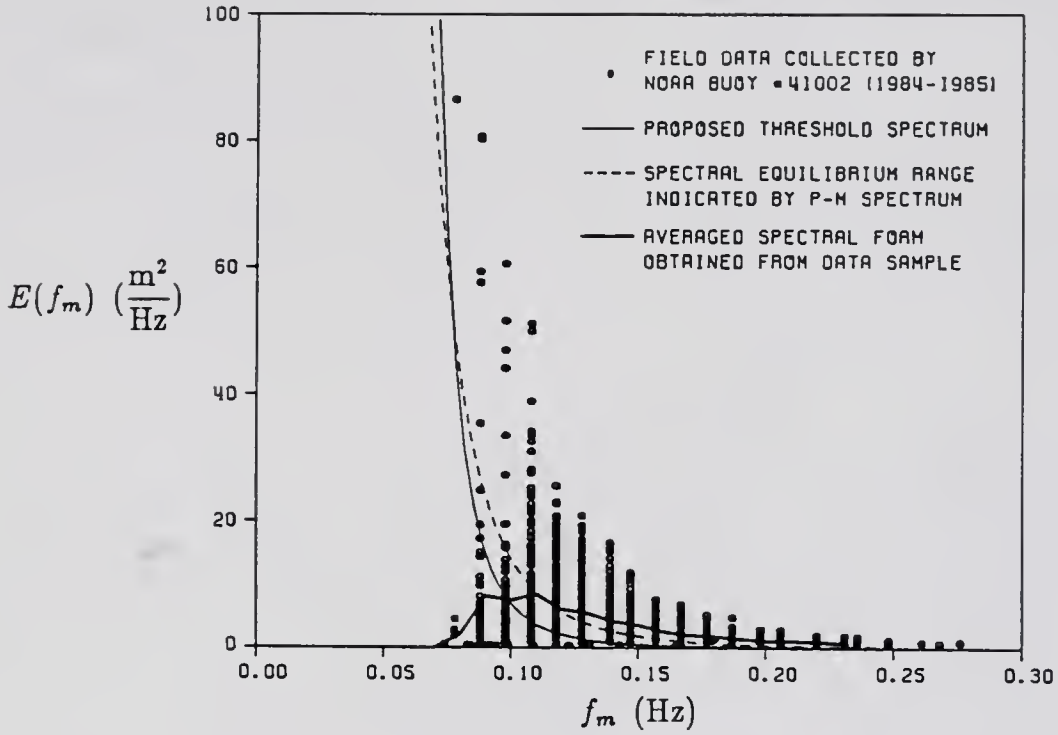


Figure 3.2: Plots of  $E(f_m)$  versus  $f_m$ .

The nonlinear transfer coefficient,  $a_{nl}$ , in Eq.(3.4) has been suggested by Hasselmann (1976) to assume a constant value of 0.00138 under the condition of steady wind within a duration  $\Delta t$ . However, the values of  $a_{nl}$  evaluated from the present NOAA buoy data appear to be varying instead of constant. Figure 3.3 shows  $a_{nl}$  values from buoys #41002 and #41006 plotted against the non-dimensional parameter  $f_0/(f_{ms}^2\Delta t)$ . It is clearly seen there exists a lower bound of the plotted data which are approximated by the dashlines in the figure. Above the dashlines, most data points are clustered in a narrow strip shown in the thickline box. Inside the box, the separation of data points into two large clusters is caused by the shortage in having the one-hour time interval,  $\Delta t$ , in computing  $a_{nl}$  in Fig. 3.3. Outside the box, the data shows considerable scatter, which is due to the contamination of swells moving into the region (data with dual spectral peaks). If a curve is fitted to the upper bound of the clustered data and using the condition that the value of  $a_{nl}$  approaches the Hasselmann's constant of 0.00138 when  $f_0/(f_{ms}^2\Delta t) \rightarrow 0$  (steady wind over long period), we arrive at

$$a_{nl} = 26[0.0195 + (\frac{f_0}{f_{ms}^2\Delta t})^{3/5}]^{5/2} \quad (3.6)$$

This is drawn in Fig. 3.3 as a solidline curve which approaches asymptotically to the dashline, the lower bound of the plotted data, as  $f_0/(f_{ms}^2\Delta t)$  approaches infinity. Equation (3.6) has been used in the new model as a unique parametric formula in accounting the migration rate of spectral peak in the frequency domain.

The same data set excluding those exhibit the swell property is then employed to determine the parametric formulas for the parameters  $\alpha$ ,  $\gamma$ ,  $\sigma_a$ , and  $\sigma_b$ . This is accomplished by minimizing the square errors over the ensemble of measured data,  $\Delta E(f)/\Delta t$ , and the computed ones from the proposed Eq.(3.3). The values of  $\alpha$  are plotted against  $f_{ms}/f_0$  in Fig. 3.4. The data are seen more scattering when  $f_{ms}/f_0$  is less than 0.5, which indicates that the generation of local wind waves becomes important in this situation to effect the nonlinear transfer process. Since

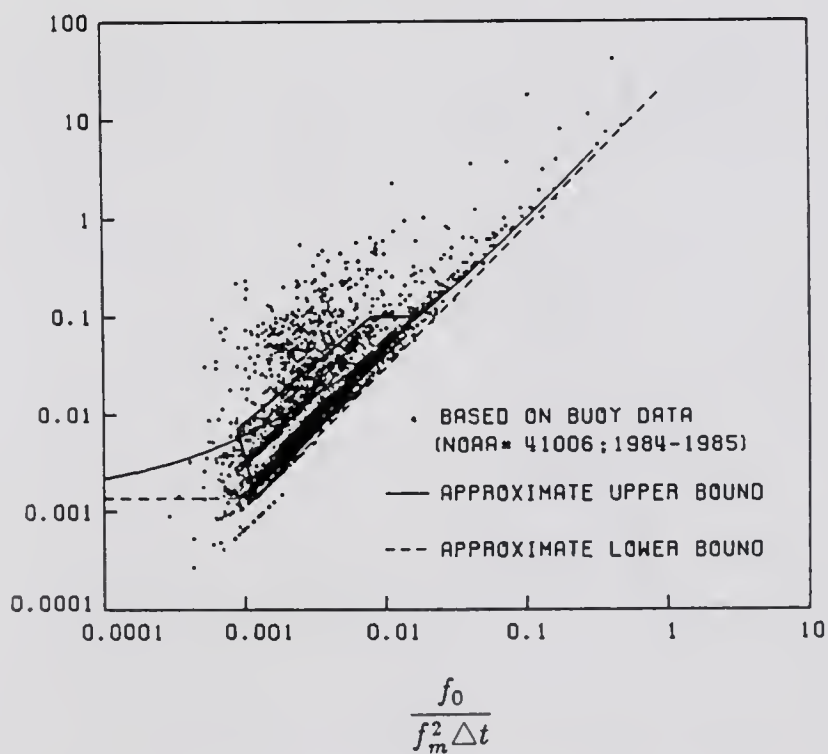
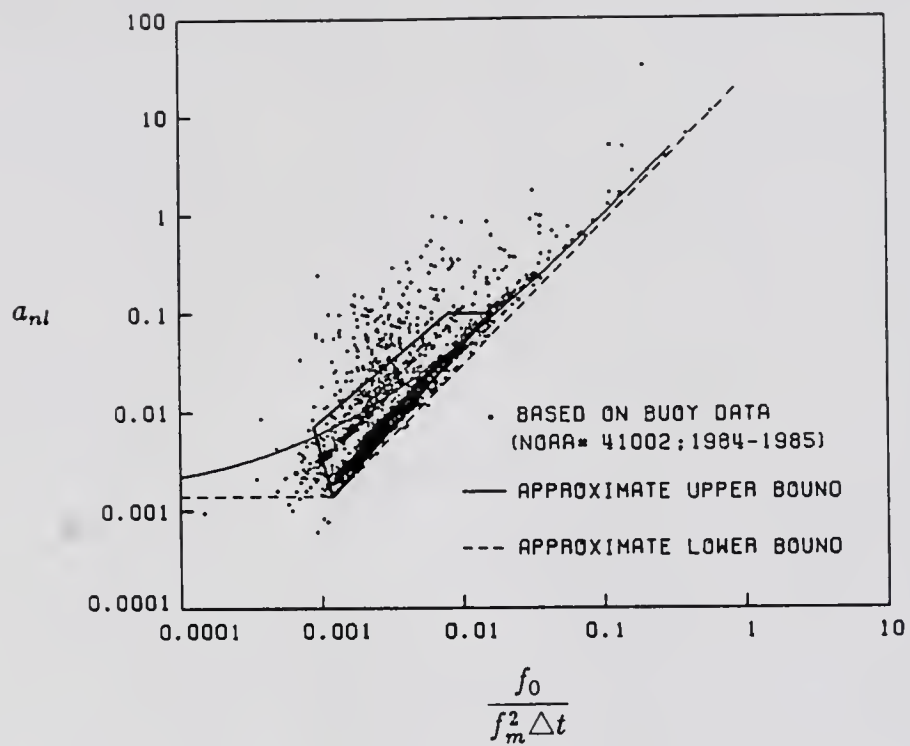


Figure 3.3: Plots of  $a_{nl}$  versus  $f_0/f_m^2 \Delta t$ .

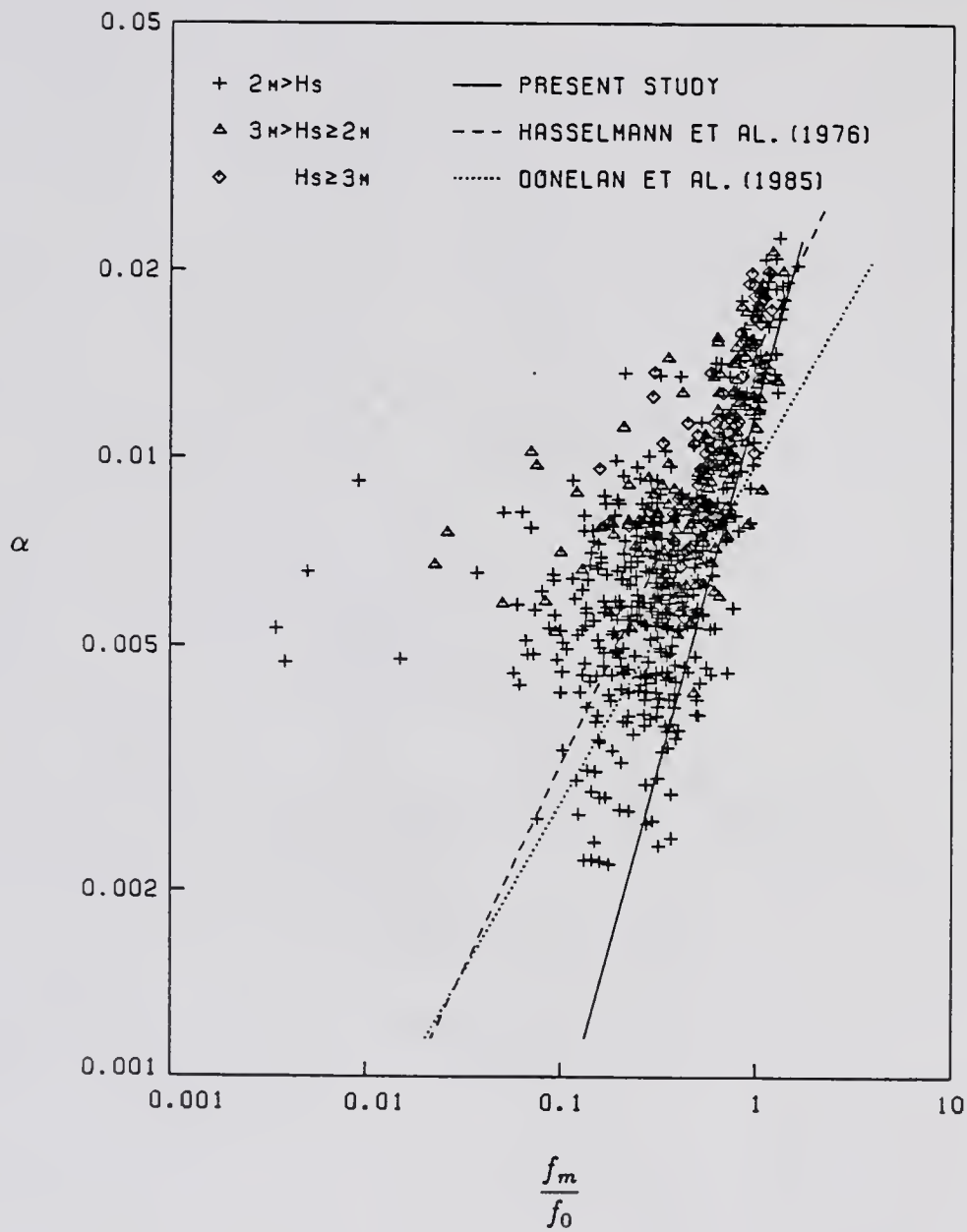


Figure 3.4: Plot of  $\alpha$  versus  $f_m/f_0$ .

the values of  $\Delta E(f)/\Delta t$  from the data are contaminated by the advected wave energy into the region, the best-fit curve of the lower bound values is believed to be more representative of the growth rate. This curve can be approximated by

$$\alpha = 0.0122 \left( \frac{f_{ms}}{f_0} \right)^{7/6} \quad (3.7)$$

or equivalently,

$$\alpha = 0.0122 \left( \frac{U_{10}}{C_{ms}} \right)^{7/6}$$

where  $C_{ms} = g/2\pi f_{ms}$  is the wave celerity at  $f_{ms}$ . The ratio  $f_{ms}/f_0$  is named the resonant parameter, which has been found important to estimate the nonlinear transfers of energy in previously developed models, for instance, it appeared in Eqs.(2.36) and (2.37), respectively, in the parametric and WIS models. Also shown in Fig. 3.4 are the empirical equations proposed for  $\alpha$  by Hasselmann et al. (1976) and Donelan et al.(1985). The equation proposed by Hasselmann et al. (1976) is obtained by defining a constant wind speed during  $\Delta t$  in Eq.(2.36), which is derived in the parametric model by allowing the variations of only  $\alpha$  and  $f_m$ .

$$\alpha = 0.0091 \left( \frac{f_{ms}}{f_0} \right)^{2/3}$$

The empirical equation for  $\alpha$  proposed by Donelan et al.(1983) is

$$\alpha = 0.006 \left( \frac{f_{ms}}{f_0} \right)^{0.55}$$

which is obtained based upon data collected in the Great Lakes. It should be noted here that when the above two equations were compared with Eq.(3.7) in Fig. 3.4 they were multiplied by a factor  $(4.4)^{1/3}$  which is the constant absorbed in  $\alpha$  in Eq.(3.7). Both empirical equations proposed by Hasselmann et al. (1976) and Donelan et al. (1985), as shown in Fig. 3.4, appeared to be less representative for the lower bound values. The equation proposed by Hasselmann et al. (1976) is more representative for the mean values. In the present study, Eq.(3.7) is adopted.

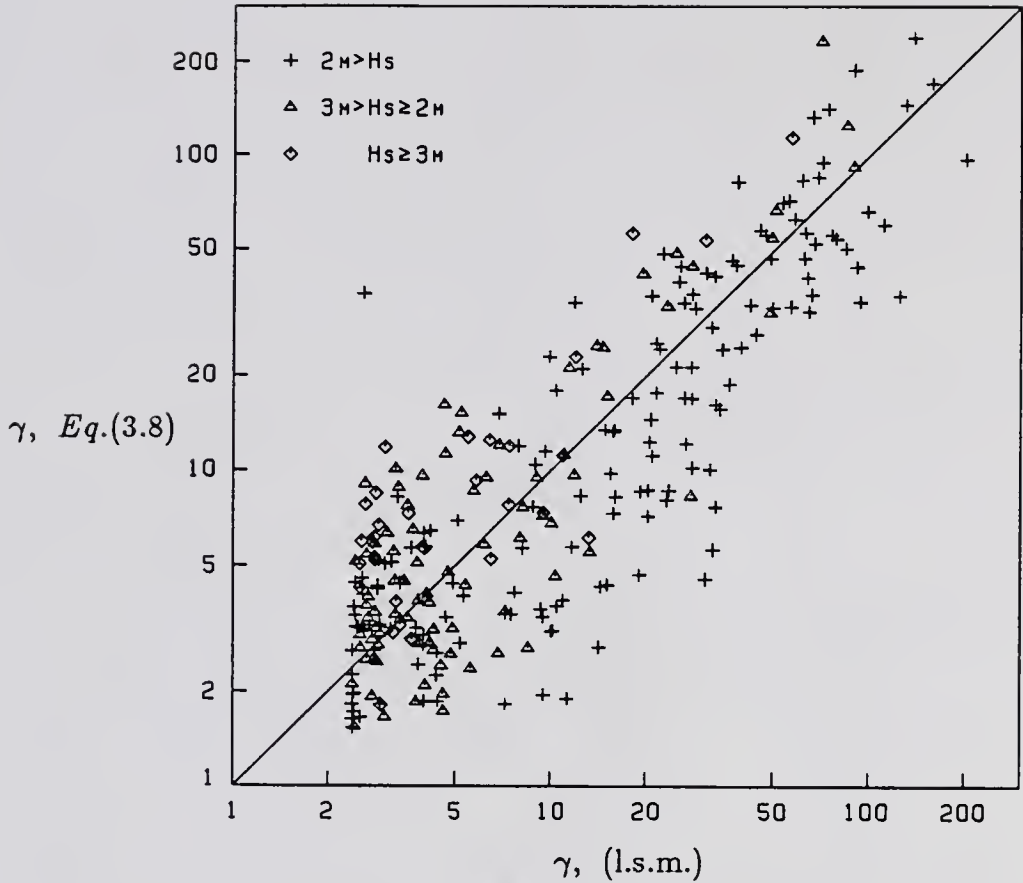


Figure 3.5: Plot of  $\gamma$  computed from Eq.(3.8) versus  $\gamma$  from the least square method.

The  $\gamma$  values solved from the least square method can be approximated by the following equation (see Fig. 3.5):

$$\gamma = \exp\left[2 \frac{f_{ms}}{f_0}\right] / 2.5 \left(\frac{f_{ms}}{f_0}\right)^3 \quad (3.8)$$

The above equation gives a minimum  $\gamma \approx 2.38$  when  $f_{ms}/f_0 = 1.5$ . Although  $\gamma$  is not bounded for small  $f_{ms}/f_0$ , the spectral peak value of  $G_{in,1}$ , which is proportional to  $\alpha^3 \gamma \sim \exp[2f_{ms}/f_0](f_{ms}/f_0)^{1/2}$ , is bounded for small  $f_{ms}/f_0$ .

Values  $\sigma_a$  and  $\sigma_b$  obtained from the field data are scattered (see Fig. 3.6). The arithmetic mean values of  $\sigma_a$  and  $\sigma_b$  are 0.12 and 0.08, respectively, and they are in the same order of magnitude as given by the JONSWAP spectrum. The values

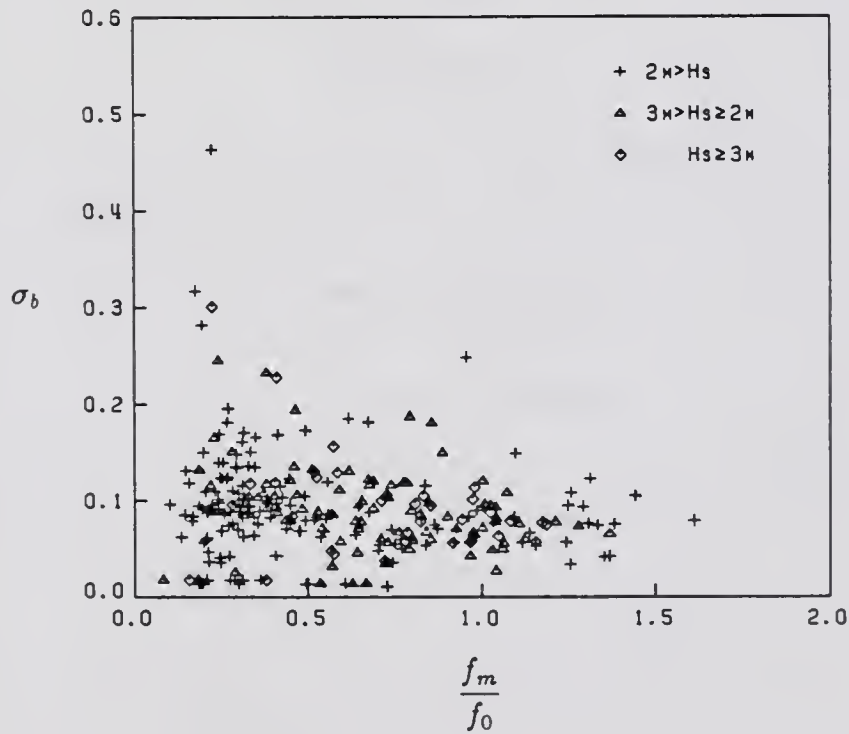
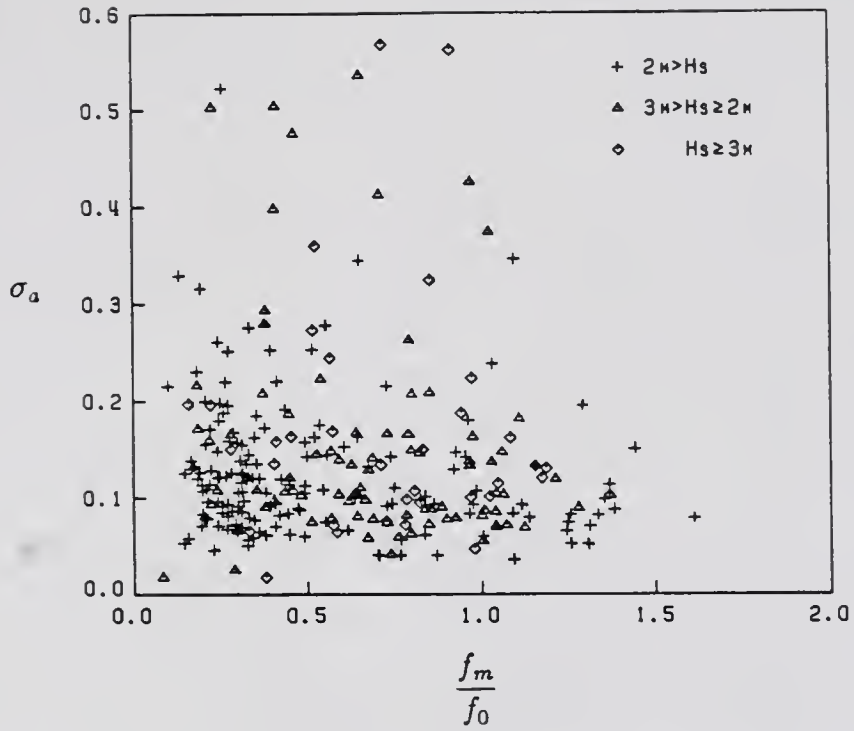


Figure 3.6: Plots of  $\sigma_{ab}$  versus  $f_m/f_0$ .

of  $\sigma_a$  and  $\sigma_b$  control the spectral width of the forward face and down-slope side of the spectrum, respectively. Since at any instant, the energy contained in the wave system, which is manifested by the magnitude and shape of the energy spectrum, is the cumulative difference between the gain and the loss. The measured  $\sigma_a$  and  $\sigma_b$  could also be viewed as parameters characterizing the net energy levels on each side of the spectrum. Since on the down-slope side (high frequency components), the loss of energy due to dissipation and transfer is expected to be very active during the growth period, the measured  $\sigma_b$  values evidently are too small to represent the gross gain. Based upon our estimate, a value of approximately four times as large should be used, i.e.,  $\sigma_b$  should be adjusted to 0.32. On the forward side, on the other hand, the loss due to dissipation is minimal. Therefore, the arithmetic mean value of measured  $\sigma_a$  should represent good estimate of energy gain due to energy transfer and no adjustment is made.

The source function  $G_{i,n,1}$  defined in Eq.(3.3) is also plotted in Fig. 3.1 for comparison. The energy growth on the down-slope face of the spectrum is seen to be much stronger than that in the WIS model, and the unnatural abrupt cutoff is smoothed out.

In the calibrations of parameters  $\alpha$  and  $\gamma$ , the past practice is to assume wind direction has to be parallel to the mean wave direction. However, in the real situation, winds and waves may have different directions, and the wind-wave resonance can be greatly reduced when the wind direction deviates significantly from the wave propagation direction. Therefore, this difference between the wind and wave directions needs to be properly incorporated into the resonance condition. This is accomplished in the model by redefining  $f_0 = g/2\pi U_{10} \cos(\bar{\theta} - \theta_w)$  in Eqs.(3.7) and (3.8), which are used to estimate  $\alpha$  and  $\gamma$ , respectively.

The rate of growth of newly generated waves in WIS model is treated in such a way that the total energy growth during time step  $\Delta t$  is independent of the length

of  $\Delta t$ . This requires either the wind to be sufficiently strong or the duration to be sufficiently long, so that in every time step the growth of local waves reaches its upper limit. The WIS model was found to have a tendency of overpredicting wave growth under mild wind condition (see Fig. 2.8) and this source term might be partially responsible.

We observe here that the growth of local waves due to winds at the current time step can take place in one of the following three forms:

- a. If the shift in wind direction from the previous time step is sufficiently large, say over a certain threshold value,  $\theta_c$ , new fresh waves will be generated in the direction of new wind.
- b. If the shift in wind direction from the previous time step is small and the wind direction is different from the prevailing wave direction, wind waves generated from the previous time step will continue to grow in the direction of the wind.
- c. If the shift in wind direction from the previous time step is small and the wind direction is the same as the prevailing wave direction, this source term will vanish and growth will be limited to prevailing waves only.

Accordingly, the source terms for the generation of new wind waves,  $G_{in,2}$ , are proposed as follows:

Case a.  $\Delta\theta_w > \theta_c$  In this case, it is generally recognized that two wave generation mechanisms are at work, the Phillips' (1957) resonance mechanism and the Miles' (1957, 1959a,b, 1962) instability mechanism. It is also recognized that for practical application, the resonance mechanism which is only important at the very initial stage can be neglected. Therefore, it is common to assume that the instability mechanism dominates, or  $G_{in,2} \propto E(f, \theta)$ . We further observe that the growth at a location will eventually reach duration limited condition, the following functional form should be satisfied:

$$G_{in,2}(f, \theta) = b[E_{\infty}(f, \theta) - E(f, \theta)] \quad (3.9)$$

where  $b$  is a growth coefficient and  $E_\infty$  is the duration unlimited spectrum, and is, in general, fetch dependent. For the present model of deepwater application  $b$  is chosen as equal to  $0.1sf(U_{10}/C)^4$  with  $s$  the density ratio of air to water and  $C$  the wave celerity at frequency  $f$ , and  $E_\infty$  is the P-M spectrum with the scale parameter,  $\alpha_p$ , equal to 0.015, i.e.,

$$G_{in,2}(f, \theta) = \begin{cases} 0.1sf\left(\frac{U_{10}}{C}\right)^4 [E_\infty(f) \frac{2}{\pi} \cos^2(\theta - \theta_w) - E(f, \theta)], & \text{if } |\theta - \theta_w| \leq \pi/2 \\ 0, & \text{elsewhere} \end{cases} \quad (3.10)$$

The above equation is applied in the present model to initiate wave generation at high frequency ( $f_0 \geq 0.2$  Hz) and whenever the shift in wind direction exceeds  $\theta_c$ . At present, there is no known criterion on selecting  $\theta_c$ . For convenience, we have chosen

$$\theta_c = \left(\frac{\pi}{18} \text{ rad/hr}\right) \cdot \Delta t \quad (3.11)$$

Case b.  $\Delta\theta_w < \theta_c$  In this case, the growth mechanism should be similar to that of the prevailing wave components as discussed earlier with the exception that now the growth should be centered around the wind direction,  $\theta_w$ , instead of the prevailing wind direction,  $\bar{\theta}$ . Thus, the source function is assumed to have similar form as Eq.(3.3) with  $\bar{\theta}$  being substituted by  $\theta_w$ , i.e.,

$$G_{in,2}(f, \theta) = \begin{cases} \frac{\alpha_o^3 g^2}{(2\pi)^4 f^3 f_{mo}} \exp\left[-\left(\frac{f_{mo}}{f}\right)^4\right] \frac{8}{3\pi} \cos^4(\theta - \theta_w), & \text{if } |\theta - \theta_w| \leq \pi/2 \\ 0, & \text{elsewhere} \end{cases} \quad (3.12)$$

The spectral peak frequency  $f_{mo}$  and scale parameter  $\alpha$  are determined by the same equations used in the prevailing wave case, i.e., Eqs.(3.4) and (3.7), or

$$f_{mo}^{k+1} = \{(f_{mo}^k)^{-7/3} + a_{nd} \left(\frac{U_{10}^k \cos(\bar{\theta} - \theta_w)}{g}\right)^{4/3} \Delta t\}^{-3/7} \quad (3.13)$$

and

$$\alpha_o = 0.0122 \left(\frac{f_{mo}}{f_0}\right)^{7/6} \quad (3.14)$$

with  $f_0 = g/2\pi U_{10} \cos(\Delta\theta_w)$  being defined in Eq.(3.14) to account for the influence of  $\Delta\theta_w$  to the resonance condition.

Case c.  $\theta_w = \bar{\theta}$  In this case, the wind direction is the same as the prevailing wave direction, we have  $G_{in,2}(f, \theta) = 0$ .

Particular interest should be noted to the source function given in Eq.(3.10). If this is the only source term for spectral evolution at the duration-limited case, the transport equation can be solved analytically to yield the spectrum

$$E(f, \theta) = E_\infty(f) \left\{ 1 - \exp\left[-0.1 sf \left(\frac{U_{10}}{C}\right)^4 t\right] \right\} \frac{2}{\pi} \cos^2(\theta - \theta_w) \quad (3.15)$$

which vanishes at  $t = 0$ , and is equal to  $E_\infty(f) (2/\pi) \cos^2(\theta - \theta_w)$  at  $t = \infty$ . A simulation of the growth of wave spectrum based on Eq.(3.15) under 30-knot winds is shown in Fig. 3.7. The result is compared to Barnett's (1968) model, also shown in Fig. 3.7, and the comparison shows a good agreement between the two simulations although the spectra predicted based on Eq.(3.15) have wider and flatter shape than these predicted from Barnett's model.

If  $E_\infty(f)$  is eliminated from Eq.(3.10) by using Eq.(3.15), the source function  $G_{in,2}(f, \theta)$  can be rewritten as

$$G_{in,2}(f, \theta) = 0.1 sf E_{in,2}(f, \theta) \frac{\exp[-0.1 sf (U_{10}/C)^4 t]}{1 - \exp[-0.1 sf (U_{10}/C)^4 t]} \left(\frac{U_{10}}{C}\right)^4 \quad (3.16)$$

This equation indicates that the growth rate is equal to the product of a spectrum and a forcing function which is dependent on wind strength, wave frequency, and time. The relation described in Eq.(3.16) is different from Barnett's formula described in Eq.(2.48) which states that the growth rate is equal to the product of a spectrum and a forcing function which is dependent only on wind strength and wave frequency. Since growth rate proposed by Barnett (1968) can not predict a steady state spectrum and it has an artificial cutoff of energy growth as the ratio  $U_{10}/C$  is less than 0.9, it is more appropriate to use Eq.(3.10) rather than Barnett's formula in predicting the local generation of wind waves.

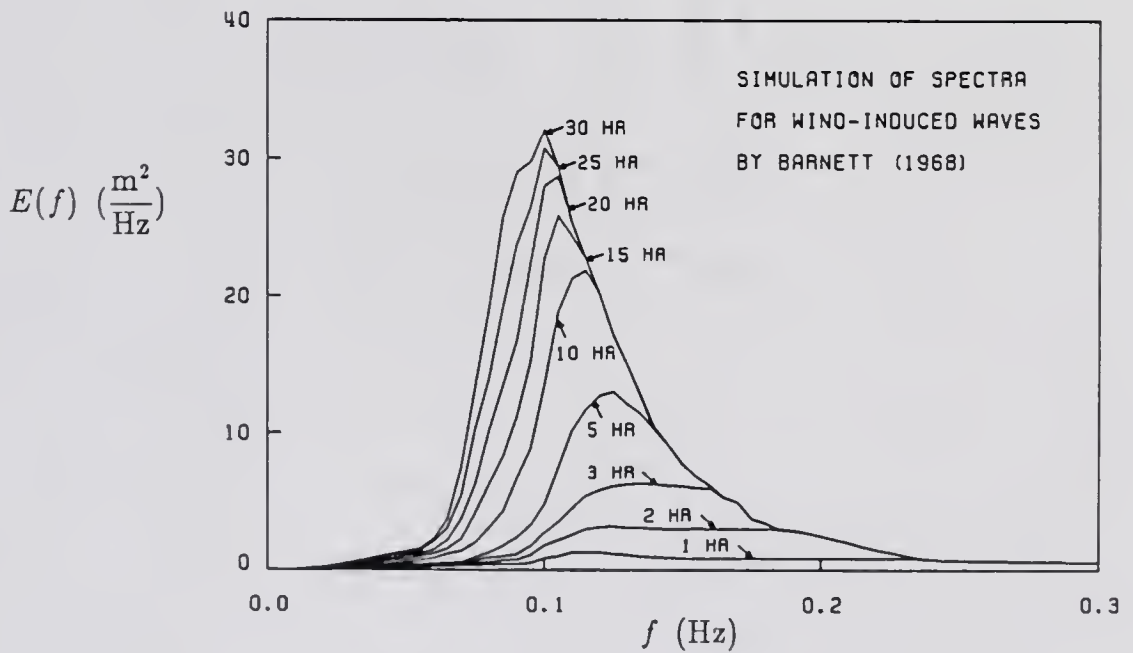
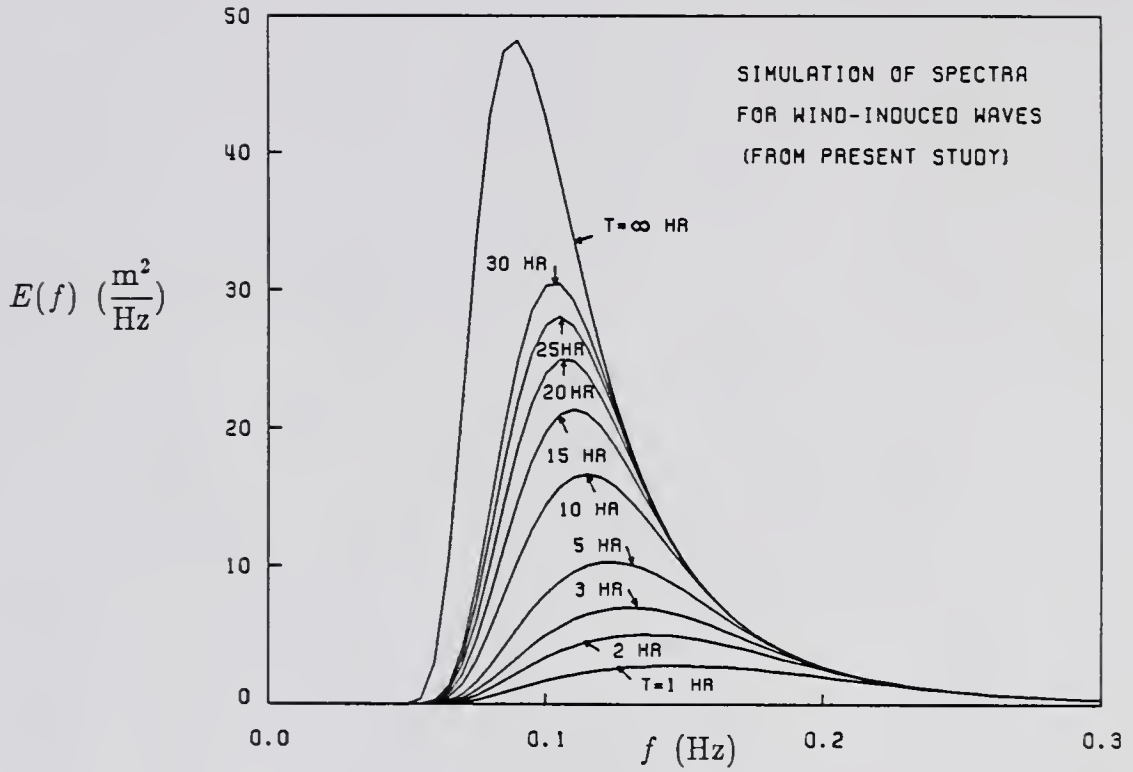


Figure 3.7: Simulations of spectral growth at duration-limited case;  $U_{10} = 30$  knots.

### 3.2.2 Dissipation Terms

The dissipation of wave energy caused by turbulence has been studied by a number of investigators. In deep water, the functional form suggested by Hasselmann (1974) is represented by

$$G_{dis}(f, \theta) = -c_v f E(f, \theta) \quad (3.17)$$

where  $c_v$  is an dissipation coefficient and its value is usually obtained by utilizing field wave data obtained during successively decreasing winds with steady direction. The value selected in the present model is  $s/6$ . Substituting this value into the above equation and integrating at the duration-limited case, we obtain

$$E_{dis}^{k+1}(f, \theta) = E_{dis}^k(f, \theta) e^{-sf\Delta t/6} \quad (3.18)$$

Figure 3.8 offers a comparison of wave decays between computed values and field data. Owing to this calibration practice, the above dissipation function is found to be more suitable for large weather systems such as related to high pressure cells, in which the wind direction is relatively stable.

For low pressure systems, such as hurricane winds, the wind direction could be completely opposite on the forward and the trailing phases of the eye while the wind strengths are usually on the same order of magnitude. With such a weather system the process of wave energy dissipation is much more vigorous as wind in the trailing phase often blows against the prevailing waves and, thus, promotes wave breakings. For low pressure systems, the dissipation function may be determined based on that proposed by Lamb (1932):

$$G_{dis}(f, \theta) = -c_v f E(f, \theta) - \frac{|\bar{d}\bar{p}|}{\rho_w C |\bar{d}\eta|} E(f, \theta) \quad (3.19)$$

where  $\bar{p}$  is the normal pressure disturbance and  $\eta$  is the water surface fluctuation. By assuming  $\bar{d}\bar{p}$  is of the same order of magnitude as the downwind flux of the horizontal momentum of the wind,  $d(\rho_a U_{10}^2)$  (Phillips, 1967; Longuet-Higgins, Cartwright, and

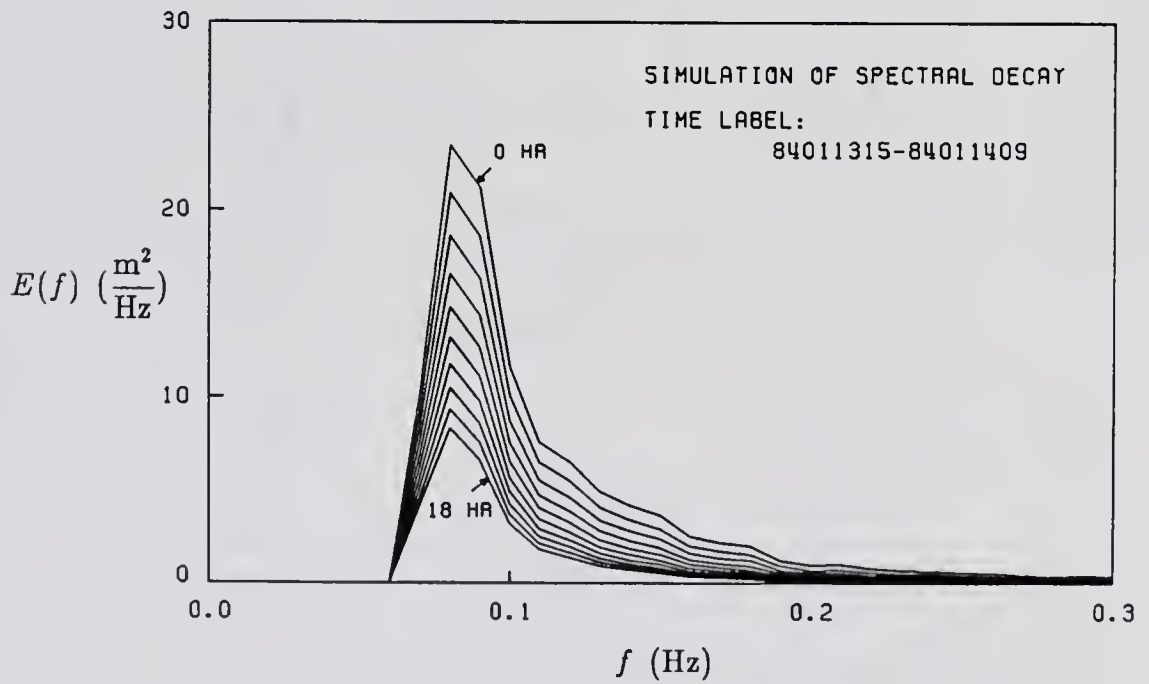
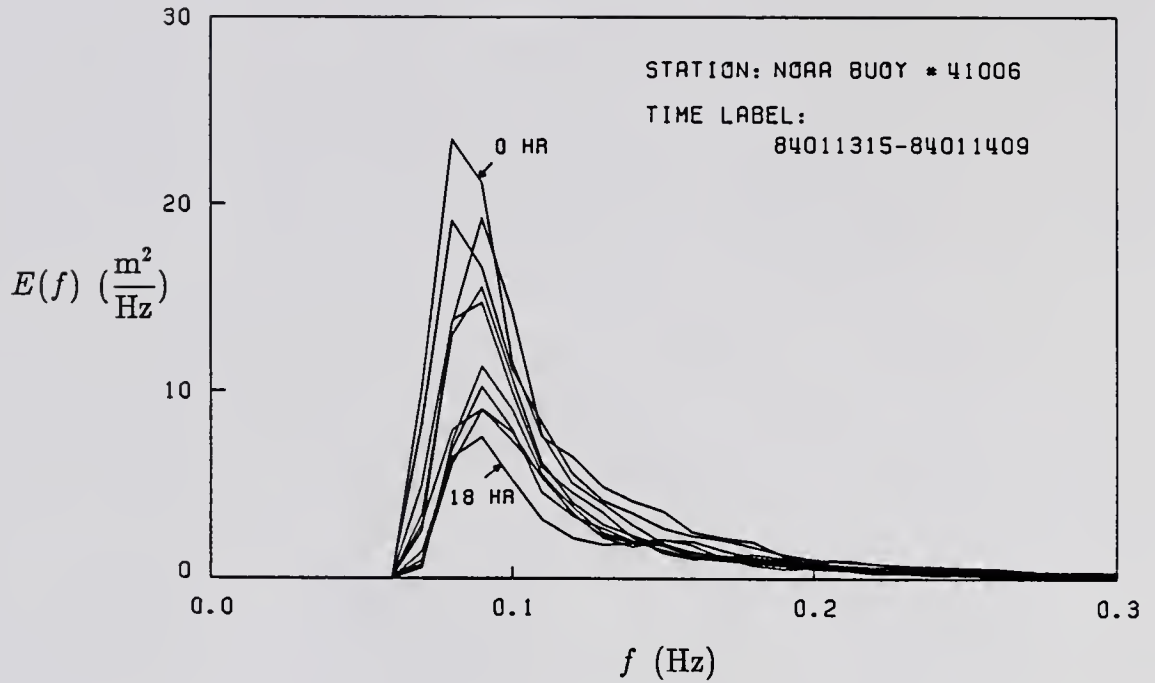


Figure 3.8: Comparison of spectral decays between measured and computed values.

Smith, 1963), Eq.(3.19) can be approximated by the following expression:

$$G_{dis}(f, \theta) = -c_v f E(f, \theta) - 0.02 \frac{sU_{10}^2}{C H_s} E(f, \theta) \quad (3.20)$$

which is a modification of that in high pressure systems by adding an additional term  $-0.02[sU_{10}^2/CH_s]E(f, \theta)$ . If this is the only source term in the transport equation, the wave energy evolution at the duration-limited condition can be found as

$$E_{dis}^{k+1}(f, \theta) = E_{dis}^k(f, \theta) e^{-sf\Delta t/6 - \lambda\Delta t} \quad (3.21)$$

where  $\lambda = 0.02sU_{10}^2/CH_s$ . The characteristics of  $e^{-\lambda\Delta t}$  are such that it varies from 0 to 1 depending upon the maturity of the sea and that smaller waves dissipate more energy against wind than that of larger waves.

### 3.3 UCWP Shallow Water Submodel

The shallow water submodel is based upon the numerical algorithm developed by Chen and Wang (1983) which is a nonstationary spectral transformation model of discrete type. The governing equations utilized in the model are given in Eqs.(2.45) and (2.46). In the present application, a number of source terms are modified.

#### 3.3.1 Wave Energy Growth in Shallow Water

In Chen and Wang's (1983) model, the generation term is again defined by Eq.(2.47). In order to be consistent with the deepwater model, we propose to use the same functional form here for local wave generations as for deepwater case:

$$G_{in} = \begin{cases} 0.1 sf \left(\frac{U_{10}}{C}\right)^4 [E_s(f) \frac{2}{\pi} \cos^2(\theta - \theta_w) - E(f, \theta)], & \text{if } |\theta - \theta_w| \leq \pi/2 \\ 0, & \text{elsewhere} \end{cases} \quad (3.22)$$

where  $E_s(f)$  is the duration unlimited shallow water spectrum. The spectral evolution based upon Equation (3.22) at a duration-limited case can be expressed as

$$E^{k+1}(f, \theta) = E_{in,2}^k(f, \theta) \exp[-0.1 sf \left(\frac{U_{10}}{C}\right)^4 \Delta t] + E_s(f) \{1 - \exp[-0.1 sf \left(\frac{U_{10}}{C}\right)^4 \Delta t]\} \frac{2}{\pi} \cos^2(\theta - \theta_w) \quad (3.23)$$

This equation is actually used in the UCWP shallow water model, and it is used to compute the wave components for  $U_{10}/C > 0.9$  such that it will not contaminate swells.

Currently, our knowledge on  $E_s(f)$  is limited. In the present model we adopted the TMA spectral form proposed by Bouws et al.(1983):

$$E_s(f) = \frac{\alpha g^2}{(2\pi)^4 f^5} \exp\left[-\frac{5}{4}\left(\frac{f_m}{f}\right)^4\right] \gamma \exp\left[-\frac{1}{2}\left(\frac{f - f_m}{\sigma_{ab} f_m}\right)^2\right] \Phi(k, h) \quad (3.24)$$

where  $\Phi(k, h)$  is a transfer function defined earlier in Eq.(2.49):

$$\Phi(k, h) = \frac{k^3(f, \infty) C_g(f, \infty)}{k^3(f, h) C_g(f, h)}$$

The spectral parameter  $\alpha$  is estimated in the model by the following formula:

$$\alpha = 0.0156 \left(\frac{U_{10}^2 k_m}{g}\right)^{0.49} \quad (3.25)$$

where  $k_m$  is the corresponding wave number at peak spectral frequency,  $f_m$ , which in turn is related to the resonant frequency as  $f_m = 0.88 f_0$ . Equation (3.25) describes a best-fit curve of the upper bound values of  $\alpha$  computed, based on field data, by Vincent (1984). The spectral parameters  $\gamma$ , and  $\sigma_{ab}$  are also adopted from Vincent (1984):

$$\gamma = 2.47 \left(\frac{U_{10}^2 k_m}{g}\right)^{0.39}, \quad (3.26)$$

$$\sigma_{ab} = \begin{cases} 0.07 & \text{if } f < f_m, \\ 0.09 & \text{if } f \geq f_m. \end{cases} \quad (3.27)$$

However, since a significant amount of wave energy is continuously being dissipated in the low frequency range under the influence of shallow water, the energy densities in this range may not be sufficiently large to maintain the spectral peak near the resonant frequency. Vincent (1984) suggested that the peak spectral frequency should have a lower bound

$$f_m \geq \frac{A}{2\pi} \left(\frac{g}{h}\right)^{1/2} \quad (3.28)$$

where  $A$  lies between 0.8 and 1.0.

### 3.3.2 Wave Energy Dissipation in Shallow Water

The dissipation of wave energy in the shallow water may be attributed to the following effects: (i) flow turbulence, (ii) bottom friction, (iii) bottom percolation, (iv) breaking due to depth limitation and (v) breaking due to energy saturation of spectral components.

The dissipation mechanism due to flow turbulence is essentially the same as in deep water, or Eqs.(3.17) and (3.18) still apply. The bottom friction effect is estimated from Eqs.(2.50) and (2.51). The dissipation of wave energy due to percolation of porous sand bottom is estimated from Eq.(2.53). However, this quantity is found to be very small and can be neglected. The water depth limited condition is given by Eq.(2.57).

The limiting of spectral growth due to energy saturation is based on Eq.(2.56),  
or

$$A(f) = B g^2 (2\pi f)^{-5} \Phi(k, h)$$

where  $B$  is chosen equal to 0.073 in this study.

### 3.4 Wind Model

Wind is an important factor for generating water surface waves. The wind information required as input to a wave model is the time series of the overwater wind vector fields. The wind information can be obtained either from the field measurement or from a wind model. Since measurement of the winds over an entire water surface region is almost impossible, numerical generation of the wind field is generally the only means to prepare the wind information as input to a wave model.

The numerical model utilized to generate the wind information here follows the method described by Clarke and Hess (1974). It generates wind field based upon the input of sea surface pressure distribution. The procedures are summarized as follows:

(i) The geostrophic gradient winds are produced directly from the pressure gradient information by the following equation (Byers, 1974)

$$uf + \frac{u^2}{r} = -\frac{1}{\rho_a} \frac{\partial p}{\partial n} \quad (3.29)$$

where  $u=|\vec{u}|$  is the magnitude of wind speed,  $r$  and  $n$  are, respectively, the radius of curvature and the directional normal of the isobars,  $\rho_a$  is air density,  $f=2\Omega \sin \phi$  is the local component of the planetary vorticity normal to the earth's surface, or the Coriolis parameter with  $\Omega$  the angular velocity of earth rotation and  $\phi$  the latitude, and  $p$  is the atmospheric pressure. If the geostrophic gradient wind is to be solved in the Cartesian coordinates,  $(x, y)$ ,  $\partial p/\partial n$  can be obtained from the expression

$$\frac{\partial p}{\partial n} = [(\frac{\partial p}{\partial x})^2 + (\frac{\partial p}{\partial y})^2]^{1/2}$$

and the radius of curvature,  $r$ , is obtained from

$$r = 1/(\frac{\partial \varphi}{\partial \ell}), \quad \text{with} \quad \frac{\partial \varphi}{\partial \ell} = \frac{\partial \varphi}{\partial x} \frac{\partial x}{\partial \ell} + \frac{\partial \varphi}{\partial y} \frac{\partial y}{\partial \ell} = \frac{\partial \varphi}{\partial x} \cos \theta_g + \frac{\partial \varphi}{\partial y} \sin \theta_g$$

where  $\ell$  is the distance along the path where air flows, and  $\theta_g$  is the downwind direction tangent to the isobar. It should be noted that in the Northern Hemisphere a positive  $r$  indicates the cyclones and a negative  $r$  indicates the anticyclones. The geostrophic gradient winds solved from Eq.(3.29) are then used to compute the winds at a reference level above the sea surface.

(ii) The surface winds are then obtained by the corrections of frictional effects. The wind speed,  $U_z$ , and wind direction,  $\theta_w$ , are adjusted according to the following equations:

$$\frac{U_z}{U_*} = \frac{1}{0.4} \ln \frac{z}{z_0} \quad (3.30)$$

and

$$\theta_w - \theta_g = \sin^{-1}(B_0/\frac{0.4 u}{U_*}) \quad (3.31)$$

where the frictional velocity,  $U_*$ , and the frictional height,  $z_0$ , are computed by (Clarke and Hess, 1974)

$$\left(\frac{0.4 u}{U_*}\right)^2 = (B_0)^2 + \left[\ln\left(\frac{U_*}{f z_0}\right) - A_0\right]^2 \quad (3.32)$$

and Eq.(2.42), or

$$z_0 = \frac{0.1525}{U_*} + 0.0144 \frac{U_*^2}{g} - 0.00371, \quad (\text{in cgs units})$$

where  $A_0$  and  $B_0$  are non-dimensional parameters, depending on horizontal temperature gradient and vertical heat flux in the surface boundary layer. At adiabatic condition  $A_0$  and  $B_0$  are constants and equal to 0.8 and 3.5, respectively. More information about the values  $A_0$  and  $B_0$  in the nonadiabatic condition can be found in Resio et al.(1982), and Large and Pond (1982).

## CHAPTER 4 MODEL PERFORMANCE

### 4.1 Introduction

The new UCWP model is to be tested here for hypothetical and real cases. The hypothetical cases consider the wave generation at either fetch limitation or duration limitation under stationary wind fields. Only the deepwater submodel is tested for the hypothetical cases. The real cases consider the hindcastings of deepwater waves in the Northwest Atlantic Ocean and shallow water waves along the East Florida Coast. Both the deepwater and shallow water submodels are tested in the real cases.

In Section 4.2 the UCWP deepwater submodel was tested against those of the WIS model, the SMB model, and Hasselmann's (1976) parametric model. Such tests were made for either fetch-limited or duration-limited condition at selected constant wind speeds. In Section 4.3 the UCWP model was tested against the measured data from NOAA buoy deployed in the Northwest Atlantic Ocean and from CDN gages installed along the East Florida Coast. In Section 4.4 the relationship between wind and wave for a fully aroused sea is studied. In Section 4.5 the relative importance of each factor affecting deep and shallow water spectral transformations is analyzed. Finally, in Section 4.6 various values of bottom friction coefficient were tested in the UCWP shallow water model to examine their effect on the wave transformation process.

## 4.2 Model Performance in Hypothetical Cases

In this section, the UCWP model is compared with three standard wave hind-casting models, the WIS model, the SMB model, and the Hasselmann's (1976) parametric model, for fetch-limited and duration-limited deepwater wave generations. The deepwater WIS model and Hasselmann's parametric model have been reviewed in Chapter 2. The SMB model is known as a semiempirical method for deepwater wave prediction; it was first developed by Sverdrup and Munk at 1947 and then revised by Bretschneider at 1952 and 1958 with additional empirical data. The wave properties used for comparisons are the significant wave height and modal period.

The UCWP deepwater submodel was tested first in fetch-limited cases with constant wind speeds equal to 20, 30, 40, and 50 knots, respectively. The results of significant wave height  $H_s$ , and modal period  $T_m$  are plotted against fetch at 20, 50, 100, 150, 200, 250, 300, 350, 400, 450, 500, and 550 kilometers in Fig. 4.1.

According to the SMB model the significant wave height,  $H_s$ , and modal period,  $T_m$  along a fetch  $F$  are estimated from the following formulas, respectively:

$$\frac{g H_s}{U_a^2} = 0.283 \tanh\left[0.0125\left(\frac{g F}{U_a^2}\right)^{3/7}\right] \quad (4.1)$$

$$\frac{g T_m}{U_{10}} = 7.54 \tanh\left[0.077\left(\frac{g F}{U_{10}^2}\right)^{1/4}\right] \quad (4.2)$$

where  $U_a$ , the adjusted wind speed, is defined as a power function of  $U_{10}$  (Shore Protection Manual, 1984):

$$U_a = 0.71 U_{10}^{5/4} \quad (\text{in meter-second units}) \quad (4.3)$$

According to Hasselmann's parametric model the significant waves and modal periods, along a fetch  $F$ , are estimated from the following equations:

$$\frac{g H_s}{U_a^2} = 0.0016 \left(\frac{g F}{U_a^2}\right)^{1/2} \quad (4.4)$$

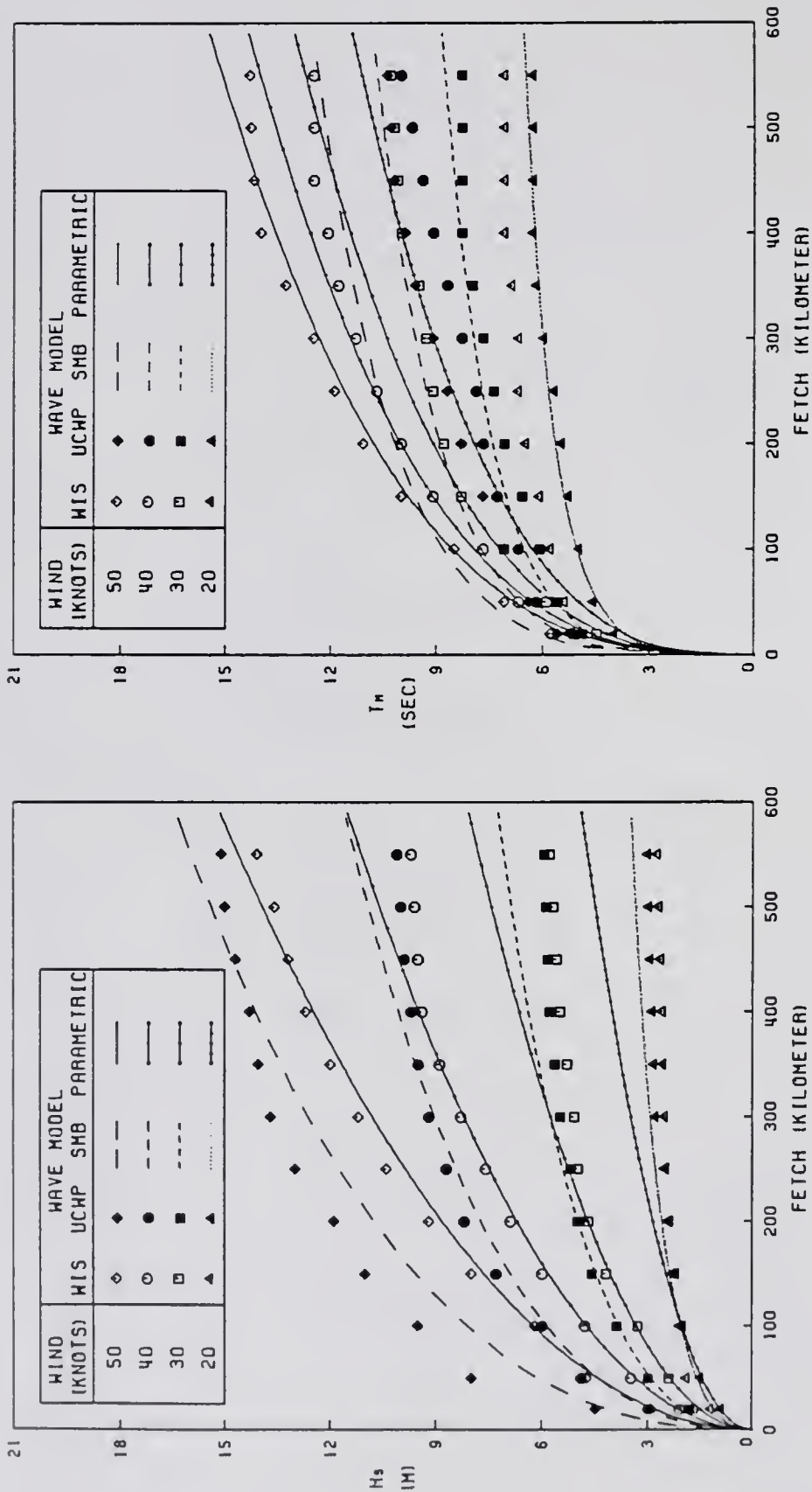


Figure 4.1: Comparison of Deepwater hindcast models in fetch-limited cases.

$$\frac{g T_m}{U_{10}} = 0.286 \left( \frac{g F}{U_{10}^2} \right)^{1/3} \quad (4.5)$$

In the classical SMB and parametric models, the adjusted wind speed  $U_a$  is equal to the wind speed  $U_{10}$ . However, it is found later that a correction to  $U_a$  is necessary since both the classical SMB model and the Hasselmann's model tend to underestimate the wave heights. The utilization of  $U_a$  according to Eq.(4.3) in the both models is suggested by the Corps of Engineers, U.S. Army, and  $U_a$  obtained from the equation will be greater than  $U_{10}$  if  $U_{10}$  is greater than 4 meters per second. Therefore, by using the adjusted wind speed  $U_a$  as defined in Eq.(4.3), the SMB and parametric models will predict higher wave heights than the classical ones if  $U_{10}$  is greater than 4 meters per second.

The significant wave heights and modal periods obtained from the WIS model, the SMB model, and Hasselmann's parametric model are compared to the UCWP model in Figure 4.1. At low and moderate wind speeds (20, 30 and 40 knots) and large fetch (greater than 400 km), the significant wave heights obtained from the UCWP model are quite consistent with these obtained from the WIS model. At high wind speeds (40 and 50 knots) and small fetch (less than 400 km), the significant wave heights obtained from the UCWP model are the highest among the four models, while the significant heights obtained from the WIS model and the parametric model agree with each others. As fetch increases, the significant wave heights obtained from the UCWP model, WIS model, and SMB model tend to reach to a height limit due to energy saturation. The parametric model, however, is not bounded.

The modal periods obtained from the UCWP model are consistent with those obtained from the SMB model at low and moderate wind speeds (20 and 30 knots). At high wind speeds (40 and 50 knots), the modal periods obtained from the UCWP model are much smaller than the other three models. For high wind speeds (40 and 50 knots) and small fetch (less than 400 km), the modal periods computed

from the WIS model and the parametric model agree with each other. At large fetch, the modal periods obtained from the UCWP model, the WIS model, and the SMB model again tend to reach an upper limit due to saturated conditions. The parametric model does not have an upper bound on modal period.

The UCWP deepwater submodel was compared next in the duration-limited cases with the WIS model, the SMB model, and Hasselmann's model at the constant wind speed of 20, 30, 40, and 50 knots, respectively. The comparisons are shown in Figure 4.2.

The significant wave height and modal period, respectively, for a duration  $t$  are estimated in the SMB model from the following formulas:

$$\frac{g H_s}{U_a^2} = 0.283 \tanh\left[0.00087\left(\frac{g t}{U_a}\right)^{5/8}\right] \quad (4.6)$$

$$\frac{g T_m}{U_{10}} = 7.54 \tanh\left[0.016\left(\frac{g t}{U_{10}}\right)^{3/8}\right] \quad (4.7)$$

where the adjusted wind speed,  $U_a$ , is defined in Eq.(4.3).

The significant waves and modal periods for a duration  $t$ , are estimated in the Hasselmann's parametric model from the following equations:

$$\frac{g H_s}{U_a^2} = 0.000082 \left(\frac{g t}{U_a}\right)^{5/7} \quad (4.8)$$

$$\frac{g T_m}{U_{10}} = 0.06 \left(\frac{g t}{U_{10}}\right)^{3/7} \quad (4.9)$$

It is seen in Figure 4.2 that at short duration (less than 20 hrs) consistent significant wave heights are found between the UCWP and SMB models, and between the WIS and Hasselmann's models. At high wind speeds (40 and 50 knots) and short duration (less than 20 hrs), the significant wave heights obtained from the UCWP and SMB models are found to be much greater than the WIS and parametric models. As a matter of fact, the significant wave heights obtained from the UCWP model are the highest among the four models at short duration. At long duration (greater than 20 hrs), both the SMB and parametric models predict much

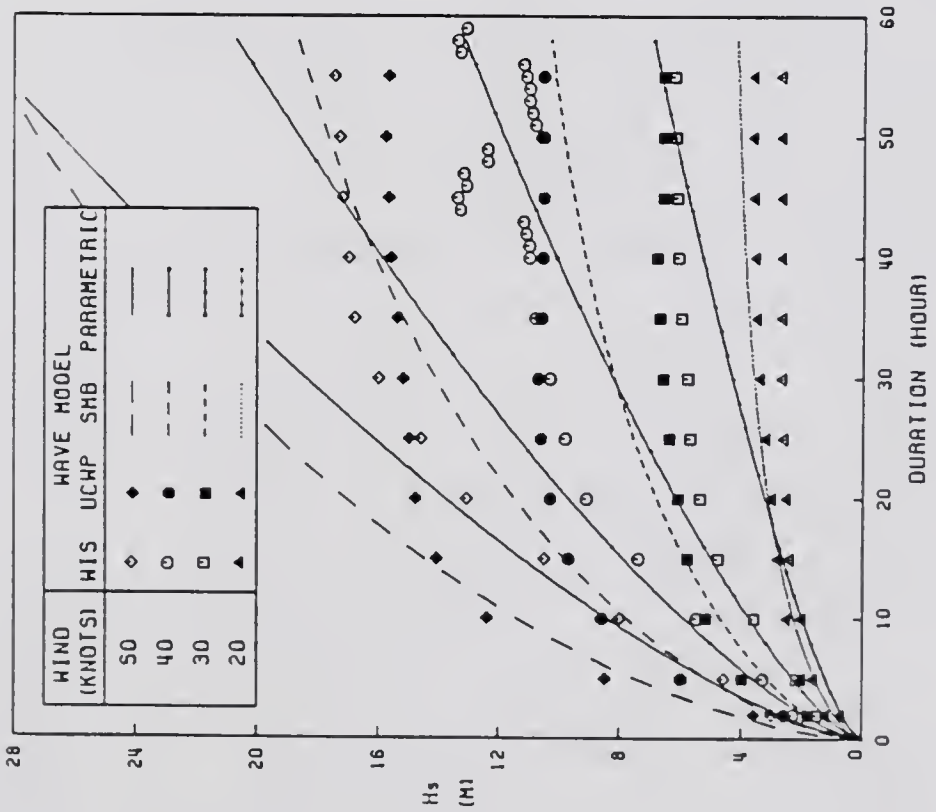
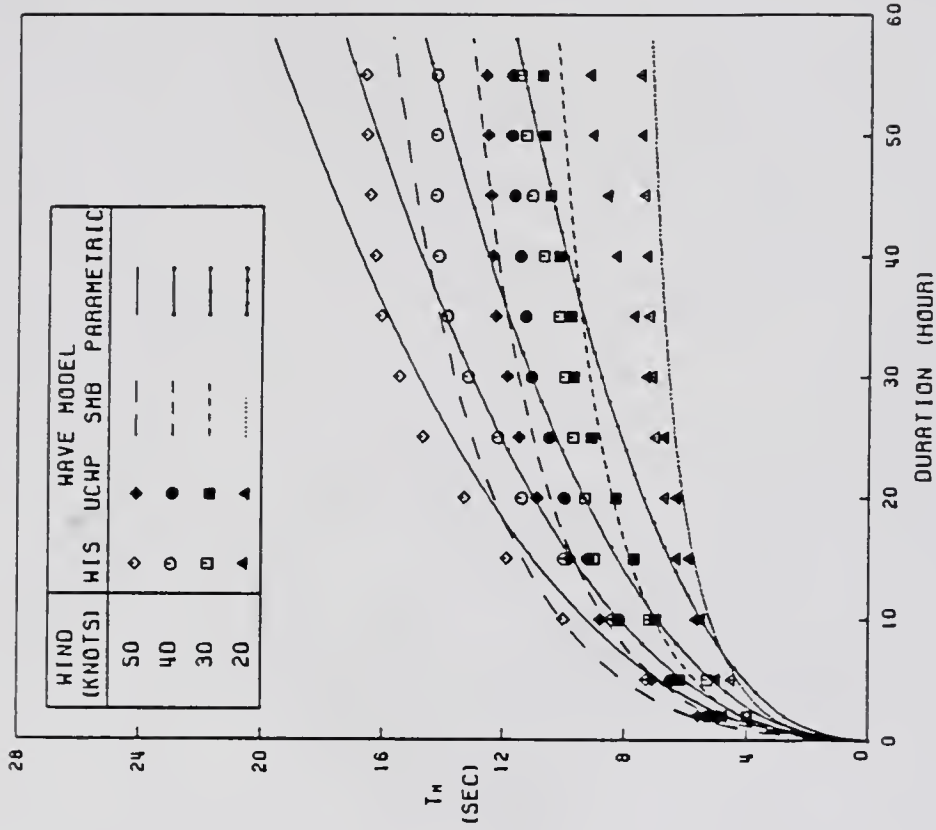


Figure 4.2: Comparison of Deepwater hindcast models in duration-limited cases.

higher waves than the UCWP and WIS models. At long duration, wave heights generated from the UCWP and SMB models have upper limits. The significant heights generated from the UCWP model show 'overshoot' patterns in Fig. 4.2. In other words, waves become over saturated before settle to a stable saturation condition. The largest 'overshoot' 0.2 m associated at 30 knots winds; it is still very small (only 3 %) compared with a 6.6 m height at saturation. The 'overshoot' of wave height is overall small but it is essential to gain enough energy for establishing the saturation condition in the UCWP model. The 'overshoot' does not occur in the WIS model nor in the SMB and parametric models. None of the four models shows overshoot behavior in the fetch-limited cases.

The significant wave heights predicted from the WIS model at 40 knots wind show a peculiar periodic, irregular damping pattern when duration becomes longer than 40 hrs. This damped wave height which is unlikely to occur in the real situation ranges from 10.6 m to 13.4 m and repeats its pattern every 12 hrs. It appears that it is caused by an improper choice of saturation spectrum  $E_s(f)$ , or Eq.(2.32), which function is to limit the growth of waves in the WIS model.

The modal periods obtained from the four models do not differ appreciably to each others for small duration (less than 10 hrs). For moderate duration (between 10 hrs and 40 hrs), the modal periods obtained from the WIS model agree with the SMB model at low wind speed (20 and 30 knots) but become closer to that predicted by the parametric model at high wind speed (40 and 50 knots). For long duration (greater than 40 hrs), consistent modal periods are found between the WIS and SMB models. At long duration, the modal periods obtained from the parametric model are the largest among the four models. At long duration and high winds (40 and 50 knots), the modal periods obtained from the UCWP model are found to be much less than the other three models.

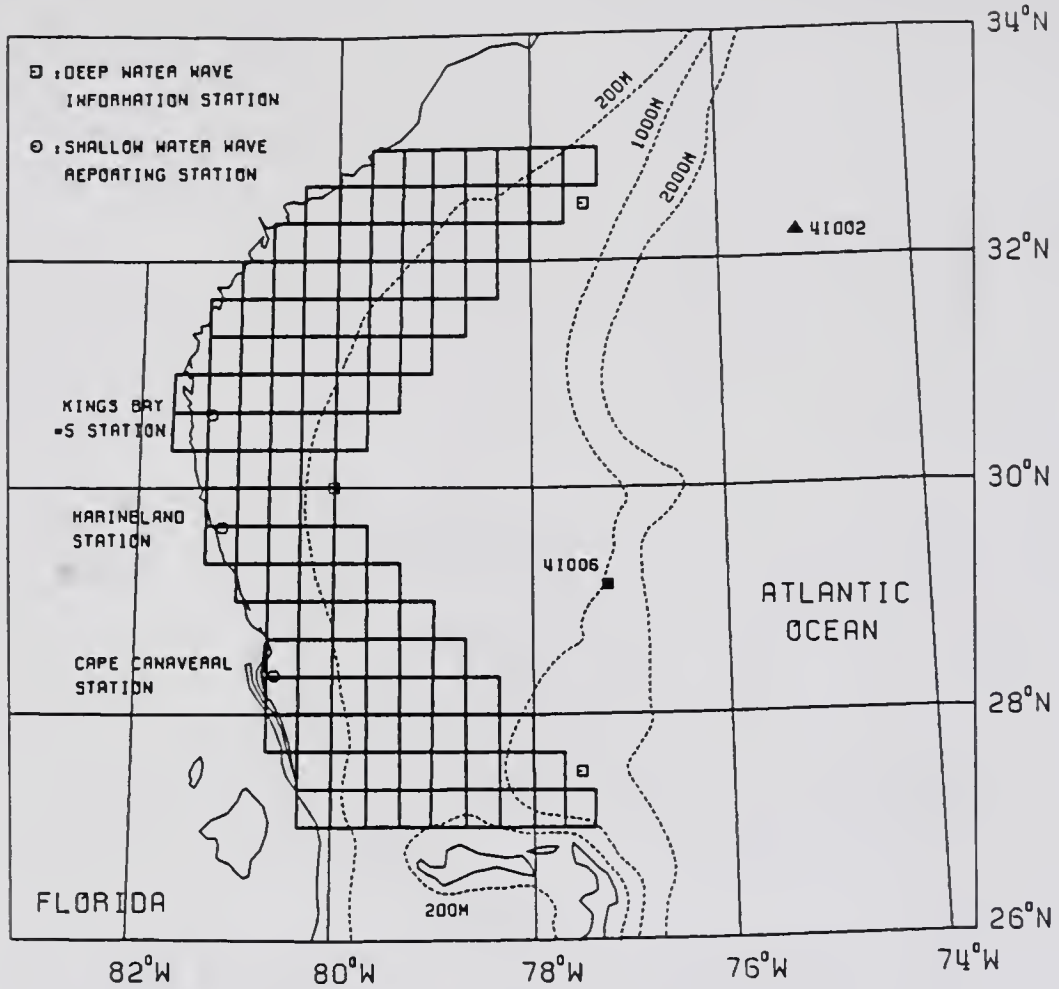


Figure 4.3: Shallow water grid system.

#### 4.3 Model Performance in Real Cases

The UCWP model was first tested against the bench mark case of the period December 21, 1983, to January, 1984 to offer comparisons with the WIS model and field data. For the deepwater model, the test conditions including grid size, time step, etc., are identical to that described in the WIS model testing as shown in Section 2.7. For the shallow water model the grid system is given in Fig. 4.3. The grid system covers an area 300 kilometers long – from mid Georgia to the northern edge of Bahama Islands, and about 100 kilometers wide – from shoreline to approximately 600 m contour line offshore.

The wind information was generated by the wind model with daily synoptic

surface pressure as input. Since the surface chart is given daily at 7:00 a.m., E.S.T. only, linear extrapolations are used for winds at other times. The computed wind directions and speeds for January 1984 at grid point 30.0°N and 77.5°W are shown in Fig. 4.4 together with the measured winds from NOAA buoy #41006, located at 29.3°N and 77.3°W. The correlation,  $\delta$ , given in Fig. 4.4 has been defined in Eq.(2.58). The root mean square difference in wind direction,  $\theta_{RMSE}$ , given in Fig. 4.4 is defined as follows:

$$\theta_{RMSE} = \left\{ \sum_{i=1}^N [(\theta_{w,c})_i - (\theta_{w,m})_i]^2 \right\}^{1/2} / N \quad (4.10)$$

where  $\theta_{w,c}$  is the computed wind direction,  $\theta_{w,m}$  is the measured wind direction,  $N$  is the sample size, and the overhead bar indicates the operation of arithmetic mean.

The wind strength exhibits a periodical behavior with a periodicity of roughly equal to 7 days. The wind direction associated with high winds are found to be more stable and to have better agreement with the predicted values. The small winds are less stable, thus, less predictable.

The measured wind speeds are seen in Fig. 4.4 to be slightly scattered around the computed ones within  $\pm 10$  knots. This is because the measured winds are reported in an every hour schedule while the computed winds are from the wind model at an every 24 hrs interval. The fluctuations of either magnitude or direction of hourly recorded winds, as seen in Fig. 4.4, may be caused by abrupt changes of temperature between the air and sea water, and between the stratified air layers above the sea surface. For simplicity the temperature effect is not include in the wind model which assumes a neutral condition.

The wind information used as input to the wave model are the computed winds adjusted by the measured values at the buoy. That is, the wind speed at any grid point is the computed value multiplied by a factor which is the ratio of measured and computed ones. However, this factor is limited in the range between 0.5 and 1.5 to limit the influence of abnormal data values.

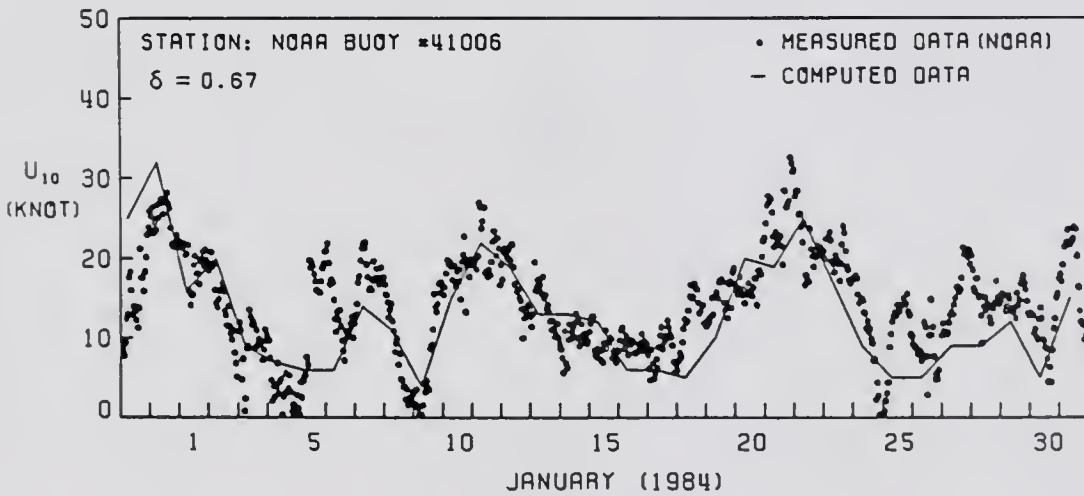
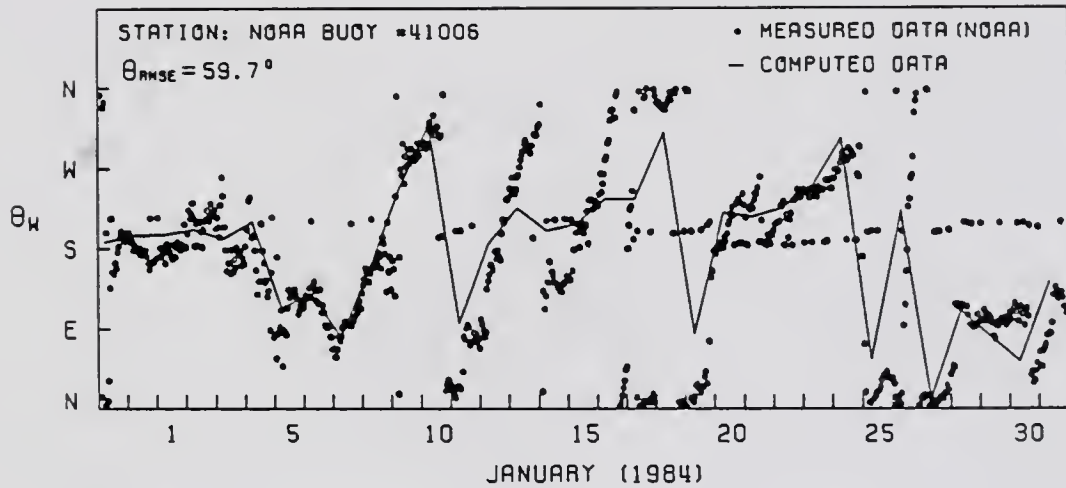


Figure 4.4: Comparison of hindcasted and measured winds at the Buoy #41006 location.

Figure 4.5 shows the comparison of the time series of the wave energy spectral evolution process of the entire month. Figure 4.6 shows the comparisons between the measured and computed modal periods and significant wave heights at the buoy location. Figure 4.7 shows the comparison between the measured and computed energy scale parameters at the buoy location. The model performs well for this data set. The good agreement, however, should be viewed as partially artificial as the model was calibrated on this data set. The model outputs in the ensuing cases are data independent.

In the shallow water model, only one empirical value, the bottom friction coefficient, needs to be defined as input. Shemdin et al.(1978) suggested values ranging from 0.006 to 0.05 along the east Florida coast. A medium value 0.02 was chosen for the model. Directional wave spectra from deepwater model are used as input boundary conditions. The wind field is spatially linearly extrapolated from the adjusted output from the wind model as discussed earlier. All the input conditions are upgraded at 2 hrs interval but the time step in the shallow water model is chosen as 24 minutes to insure numerical stability. The dissipation of wave energy due to percolation is not considered in the shallow water model since it was found to be a minor effect to the wave transformation process in the water region near the East Florida Coast (Shemdin et al., 1978).

For the case of January, 1984, the hindcast results from the shallow water model are compared with the directional wave information collected at the offshore Kings Bay Station (St.#5 in Fig. 2.4). Figure 4.8 shows the comparison of the time series of the one-dimensional spectra. By comparing Fig. 4.8 with Fig. 4.5, the measured deepwater and shallow water wave spectra, we noticed the significant reduction in wave energy and the reduction is particularly severe in low frequency components. This point will be further discussed later. The time series of the marginal directional spectra, which are obtained by integrating the two-dimensional spectra over the

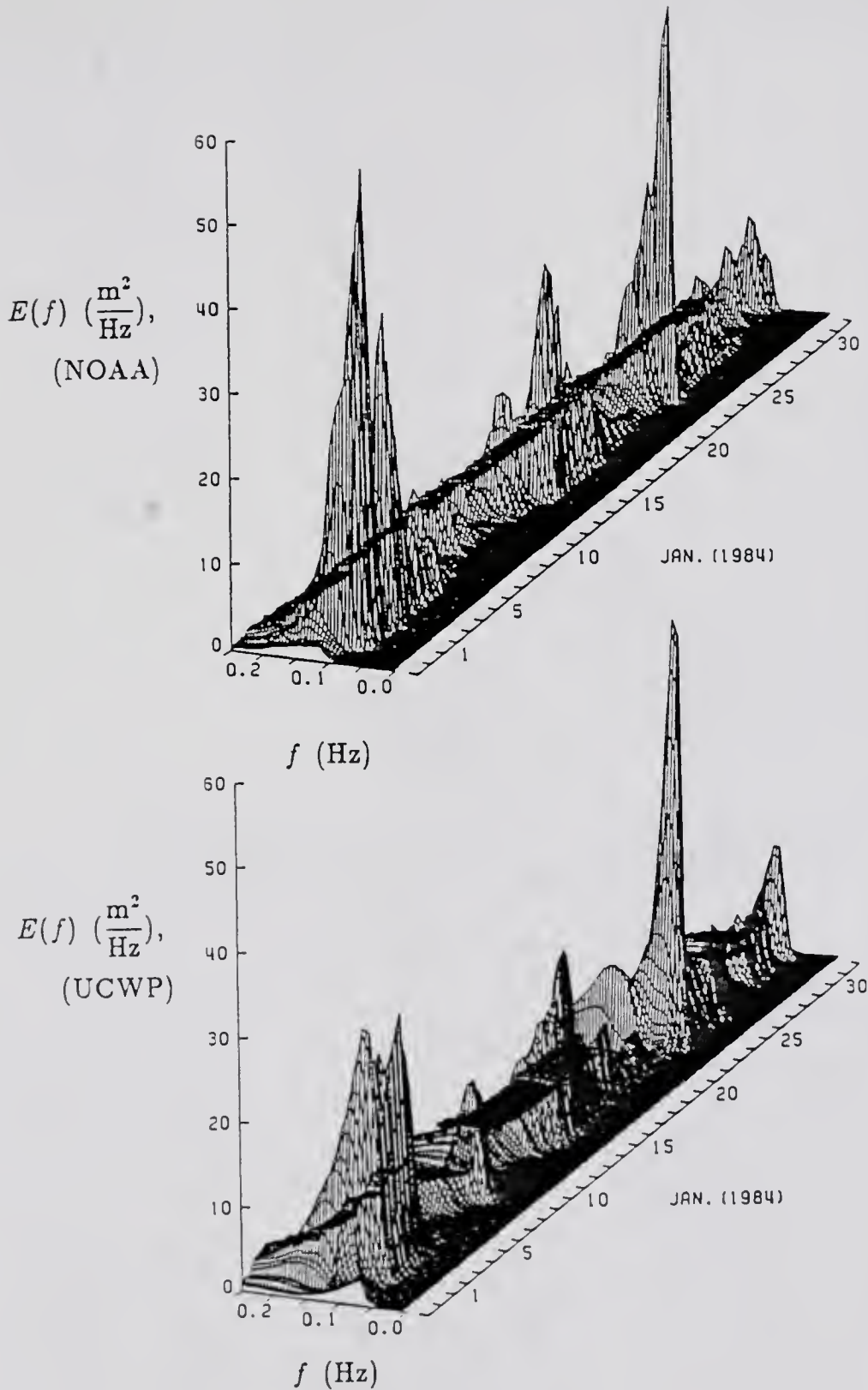


Figure 4.5: Comparison of NOAA and UCWP wave spectra for January 1984 at the Buoy #41006 location.

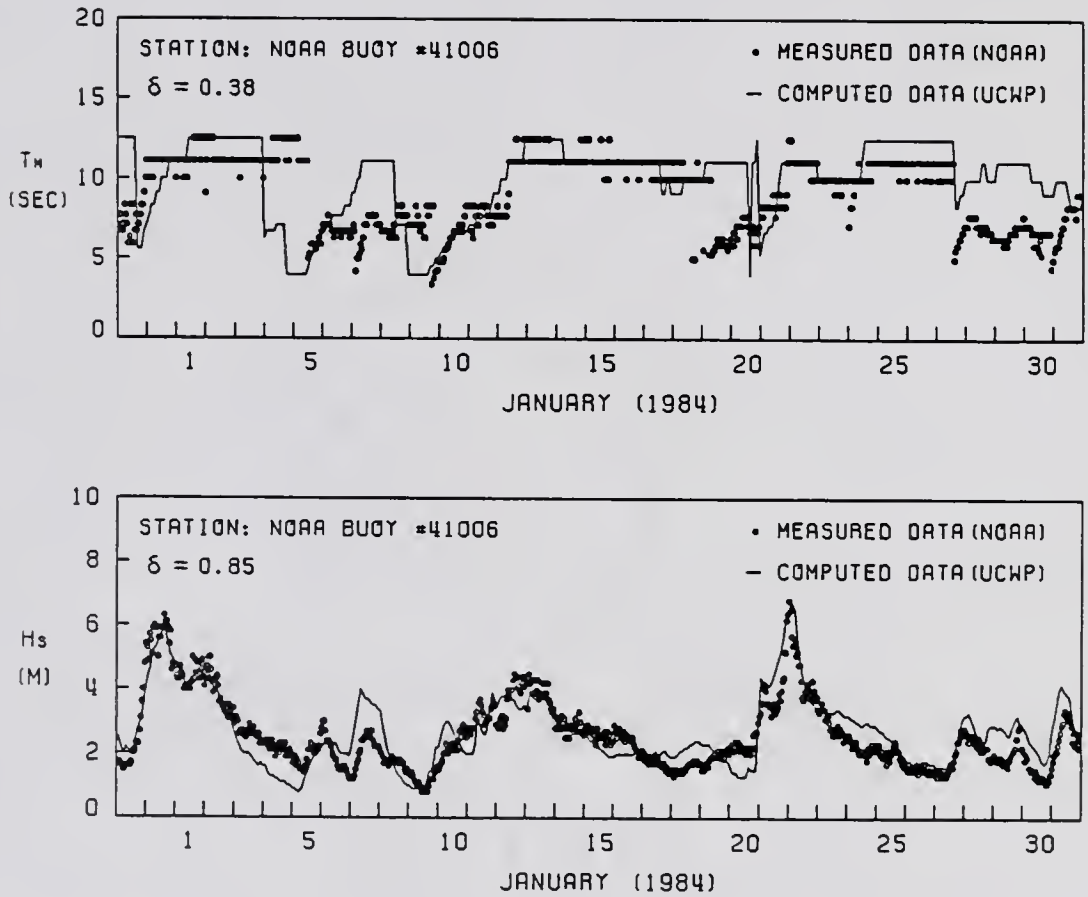


Figure 4.6: Comparisons of NOAA and UCWP modal periods and significant wave heights at the Buoy #41006 location.

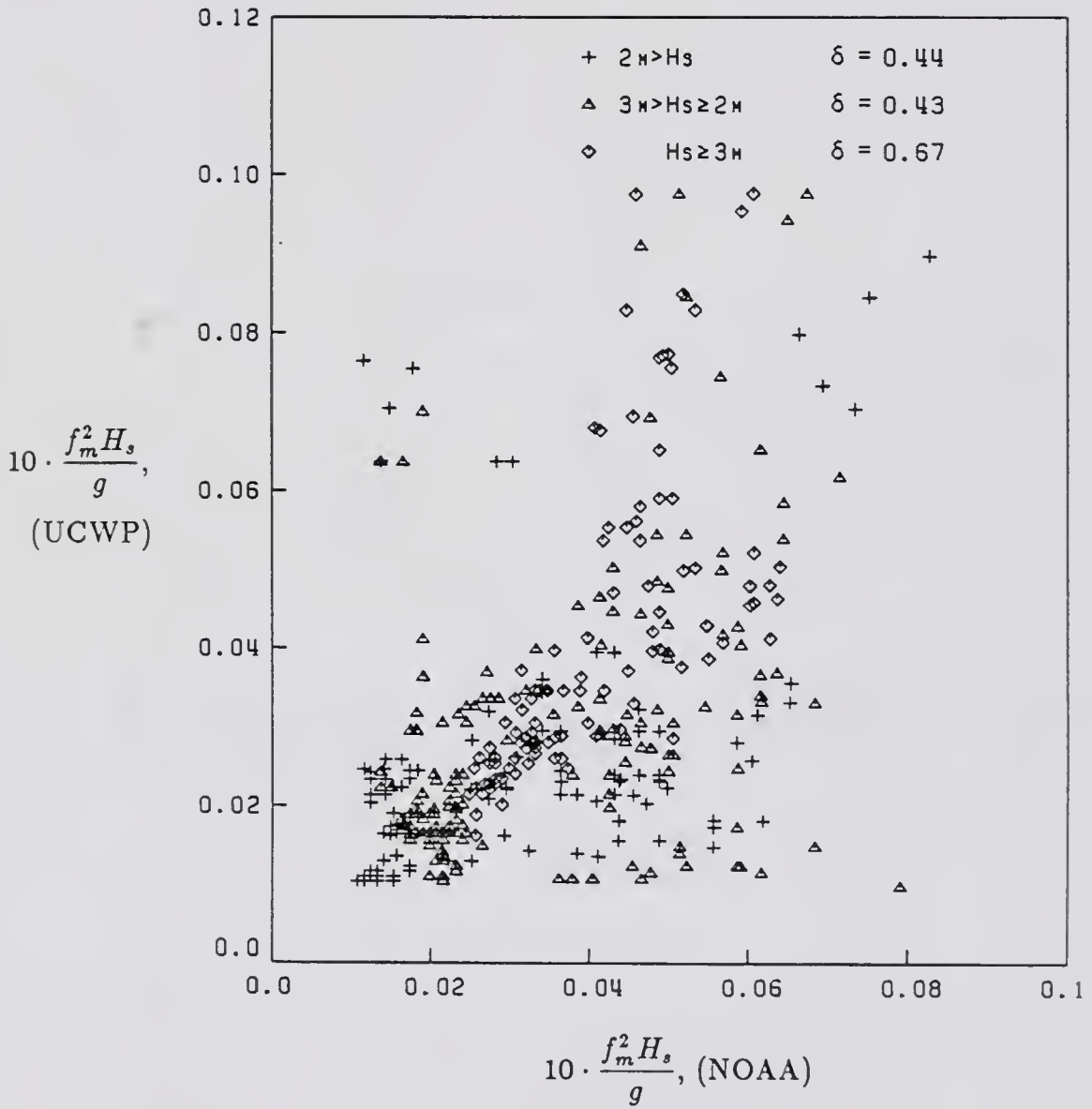


Figure 4.7: Comparison of NOAA and UCWP energy scale parameters at the Buoy #41006 location.

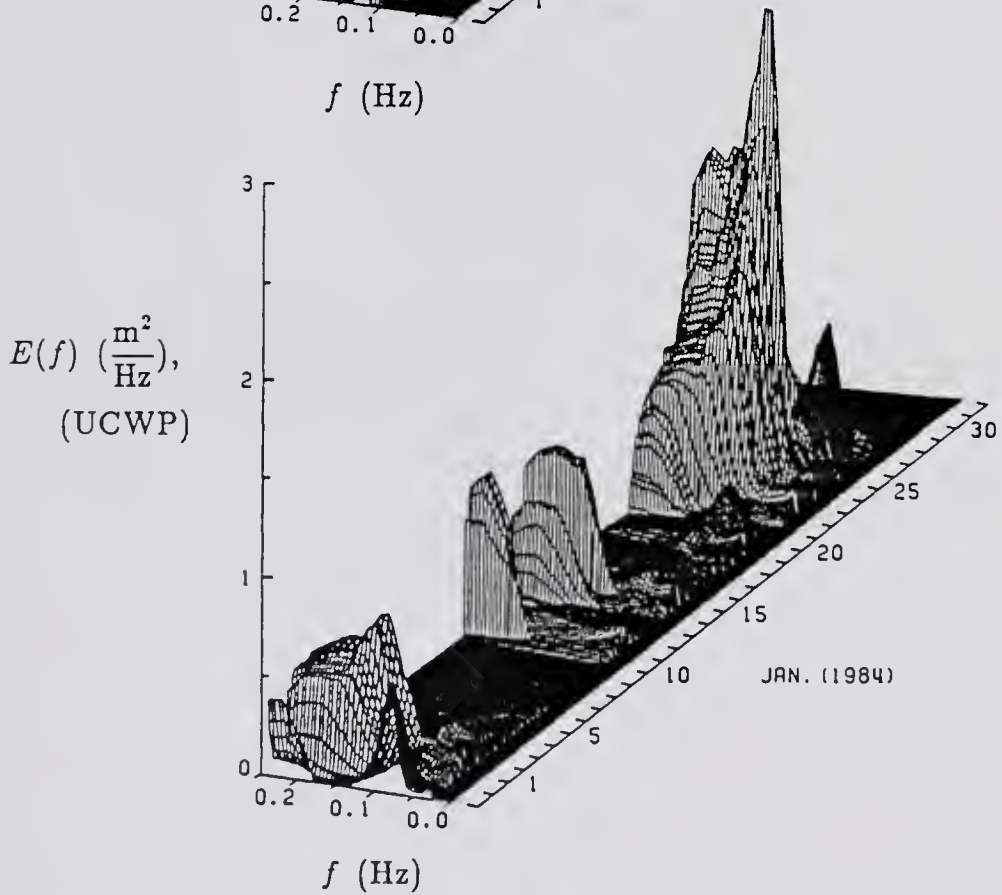
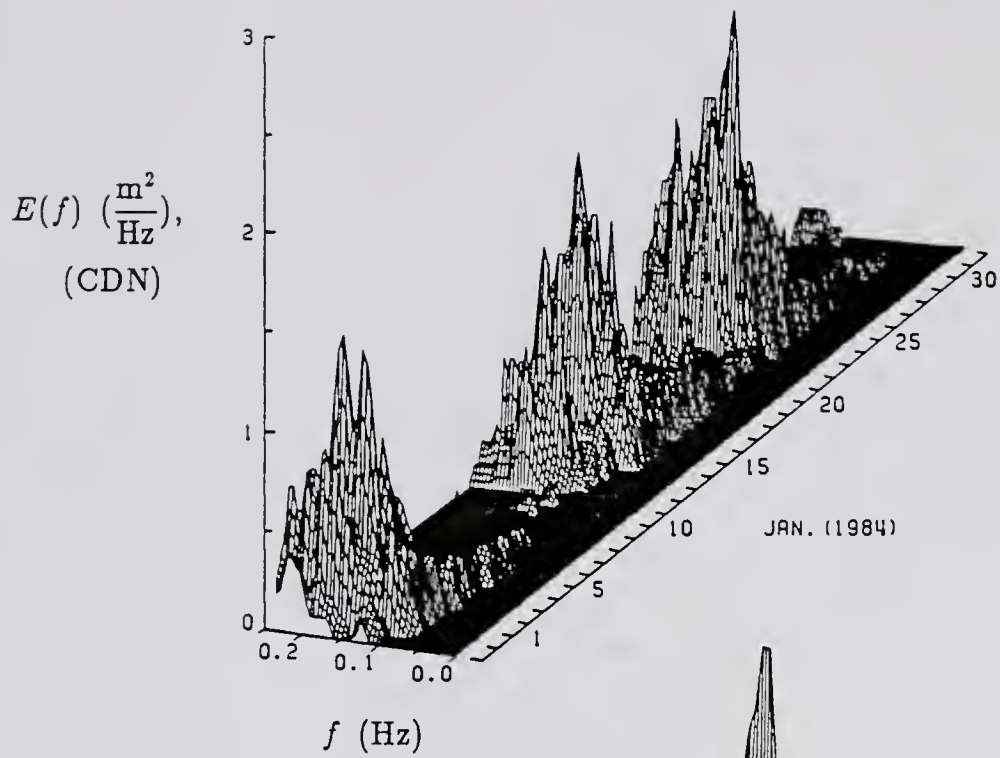


Figure 4.8: Comparison of CDN and UCWP wave spectra for January 1984 at the Kings Bay gage location.

frequency domain, are shown and compared in Fig. 4.9. Finally, the measured and computed mean wave directions, modal periods, and significant wave heights are summarized in Fig. 4.10.

In the case illustrated above, the winds were predominantly induced by high pressure systems which are large scale and relatively stationary. In the following case, wave hindcasting was performed in September and October, 1984 to assess the model performance for low pressure system and other coastal locations.

In September and October, 1984, three hurricanes occurred in the Mid Atlantic Ocean (see Fig. 4.11). The three hurricanes are Hurricane Diana, Isidore, and Josephine. The cyclones found during these hurricanes are good examples of low pressure system found in September and October; they are small scale and relatively nonstationary. Synoptic charts showing low pressure systems of Hurricane Diana, Isidore, and Josephine are given in Figs. 4.12(a), 4.12(b), and 4.12(c), respectively. All three cyclones generate strong northeast winds and, hence, large waves heading to the southeastern coast of the United States.

Hurricane Diana came near the Florida east coast in the morning of September 8, 1984. After looped off the northeast Florida coast for almost 36 hours, it moved north toward the coast of North Carolina. The highest wave recorded at the Marineland CDN station during the visit of Hurricane Diana reached 3 m in terms of the significant wave height. Hurricane Isidore came ashore near Miami Beach, Florida, during the morning of September 27, 1984. It then moved northward across central Florida and returned to the Atlantic Ocean near the border between Florida and Georgia. The highest wave caused by the Hurricane winds was recorded at the CDN wave gauge station at Cape Canaveral and reached 3.2 m in terms of the significant waves. Hurricane Josephine was developed in the Mid Atlantic Ocean on October 10, 1984. The path of the hurricane is nearly parallel to the east coast of North America. The closest distance between the hurricane's

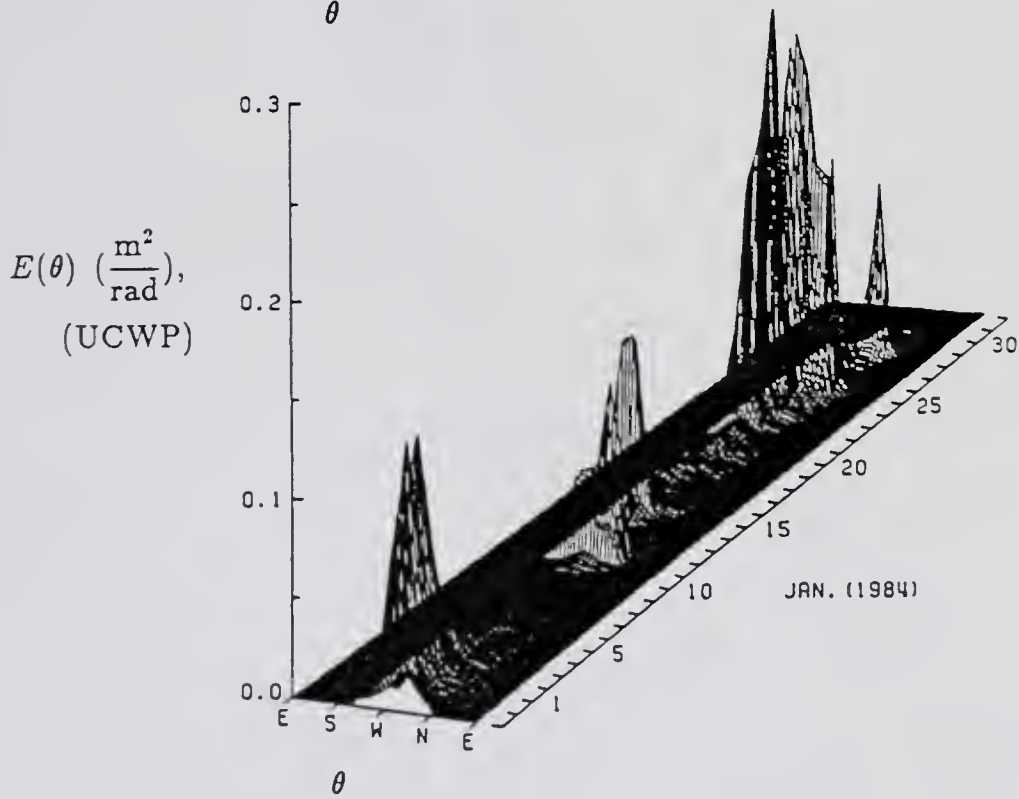
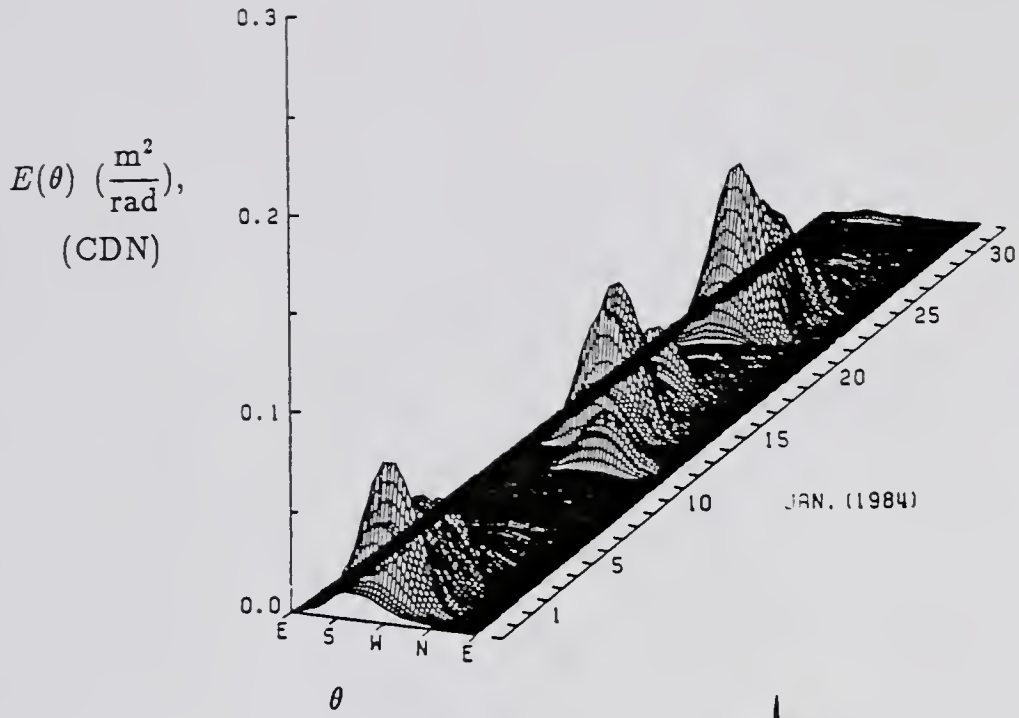


Figure 4.9: Comparison of CDN and UCWP marginal directional spectra at the Kings Bay gage location.

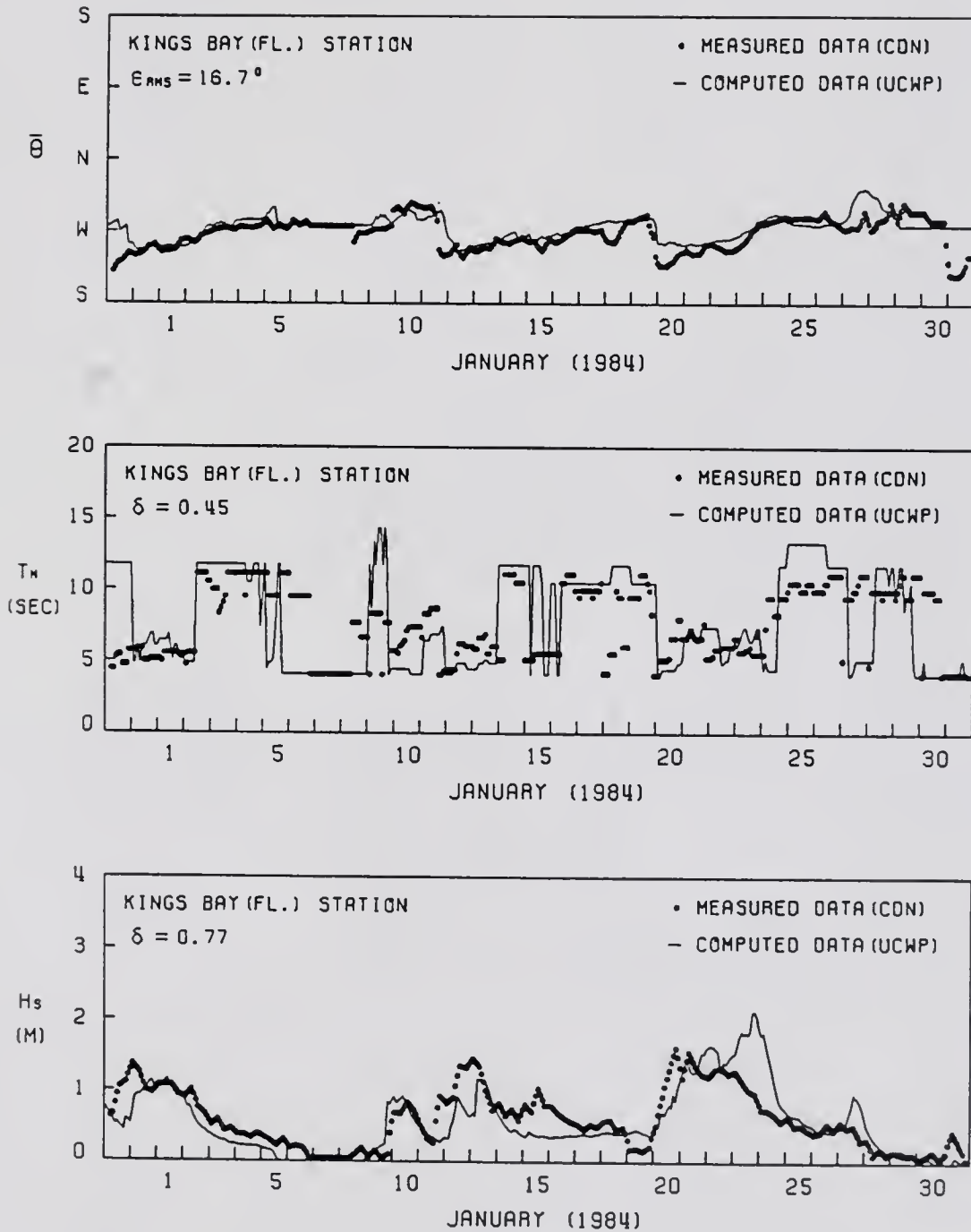


Figure 4.10: Comparisons of CDN and UCWP average wave direction, modal periods and significant wave heights at the Kings Bay station.

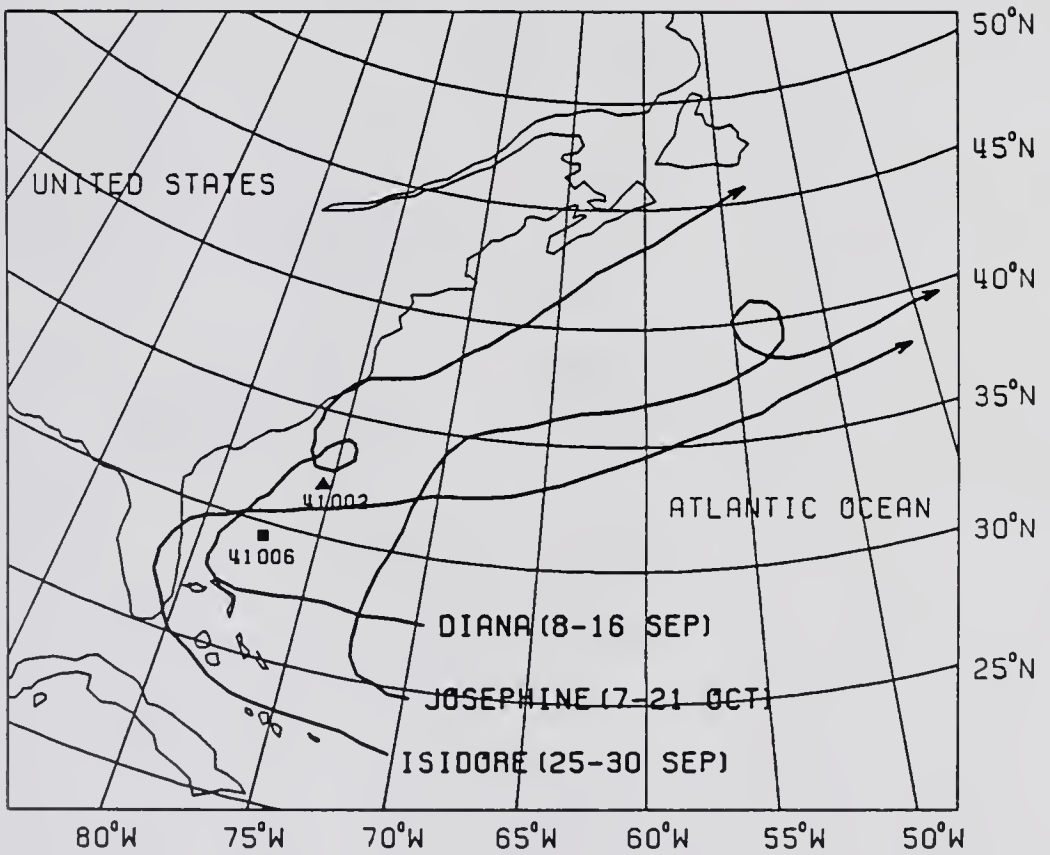


Figure 4.11: Tracks of Hurricanes Diana, Isidore, and Josephine (1984).

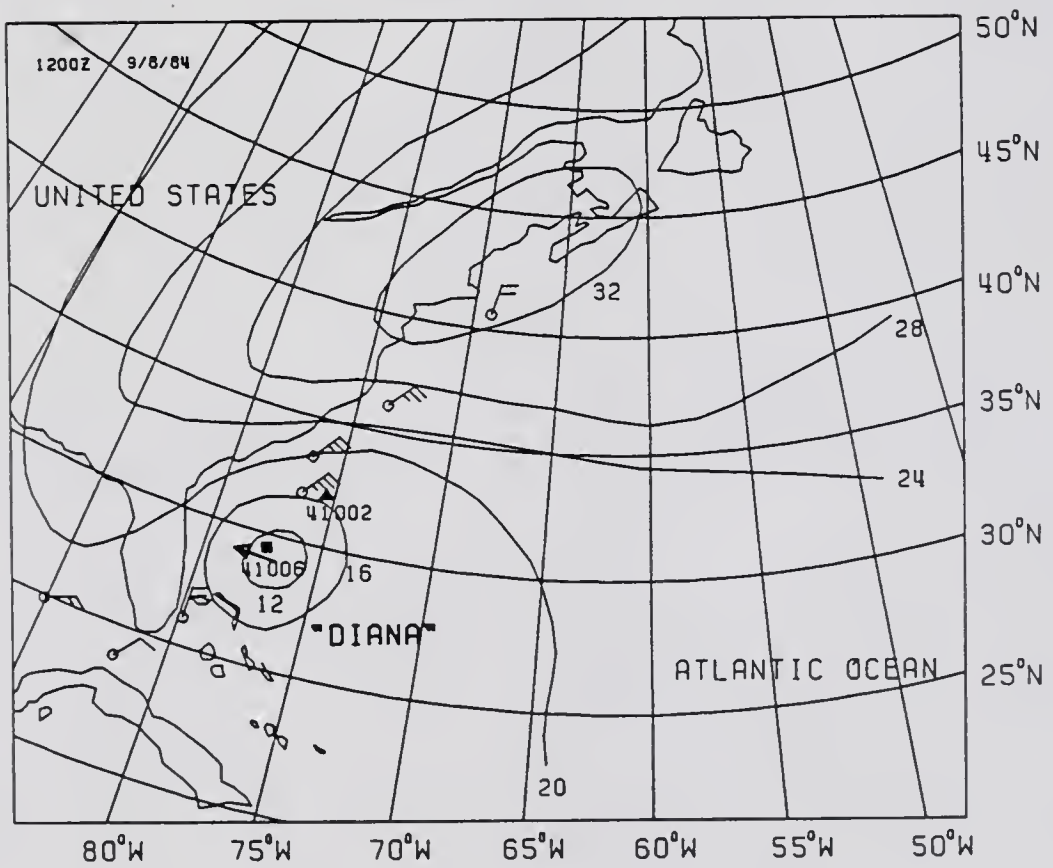


Figure 4.12: (a) Weather map showing northeast winds generated by the Hurricane Diana (9/8/84).

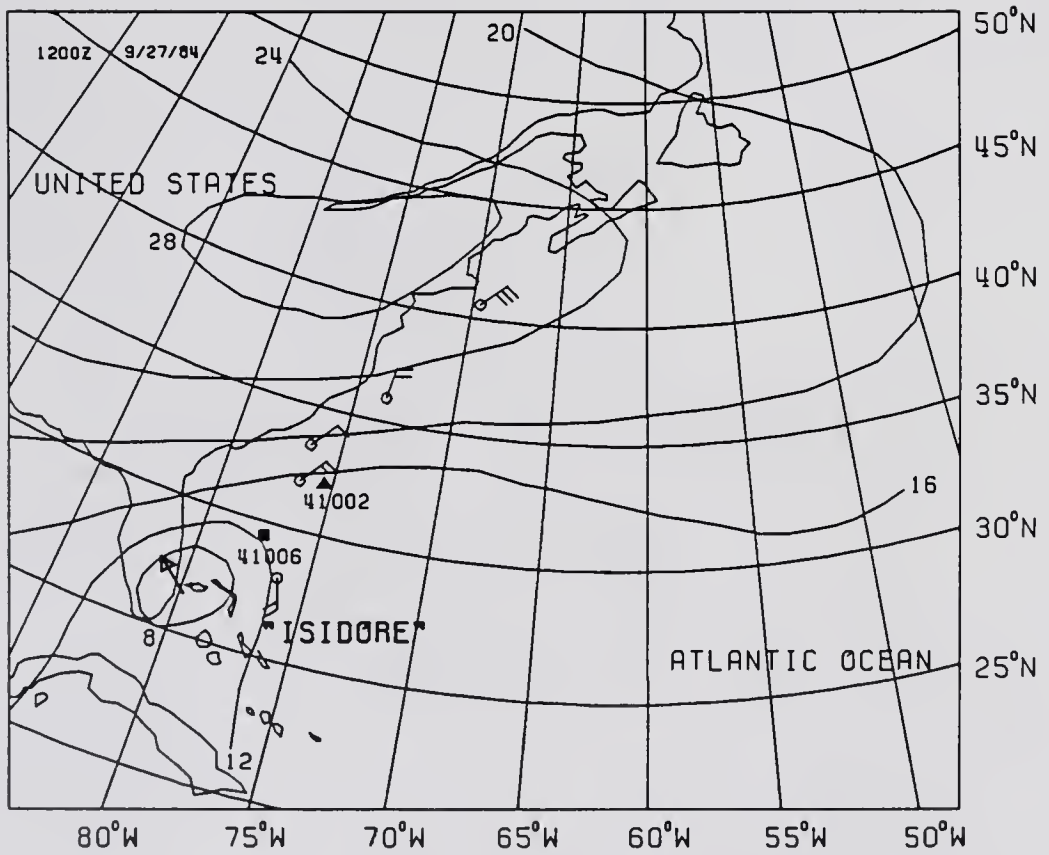


Figure 4.12: (b) Weather map showing northeast winds generated by the Hurricane Isidore (9/27/84).

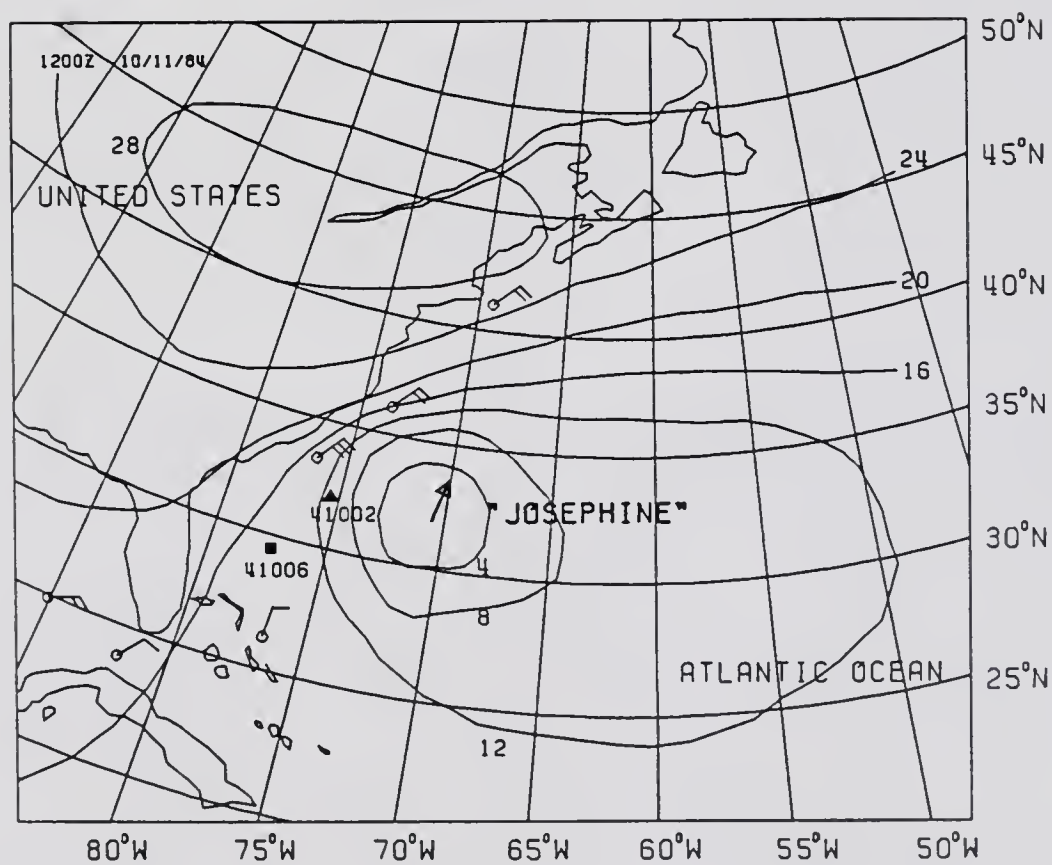


Figure 4.12: (c) Weather map showing northeast winds generated by the Hurricane Josephine (10/11/84).

center and the east coast of Florida is about 800 kilometers. The hurricane never threatened Florida coast. However, due to its track, strong northeasters were experienced along the coast of Florida and large waves were observed. The significant wave height recorded 2.2 m at the Marineland CDN station.

Two large scale high pressure weather systems were also developed over the Northwest Atlantic Ocean in September and October 1984. The first one was originally formed in the central area of North America and later moved eastward into the Atlantic Ocean on the 22nd of September. It stayed over the water regions near the coast of North Carolina for about three days while generating persistent strong winds blowing to the waters surrounding the southern coast of North America. During the presence of the anticyclones the highest significant wave height was recorded at the Kings Bay Station at 2.5 meters. The second large scale high pressure system appeared over the coastal waters near the coast of North Carolina on the 25th of October. It lingered there for about two days before moving northward. During the anticyclone period the significant wave height reached 2.1 m at the Marineland CDN station.

The comparisons of hindcasted values and measured data are given in a series of graphics. Figure 4.13 shows the comparisons between modal periods and significant wave heights at the deepwater buoy location. Figures 4.14(a), 4.14(b), and 4.14(c) shows the comparisons between average wave directions, modal periods, and significant wave heights at the shallow water stations of Kings Bay, Marineland and Cape Canaveral, respectively. A summary of comparisons of the computed and measured unidirectional frequency spectra at the buoy #41006 location, for all January, September and October 1984 data is given in Appendix C.

Table 4.1 summarizes the correlations between the computed and measured values for significant wave height and modal period at the buoy #41006 location. From the table it is evident that higher correlations are achieved for both wave height

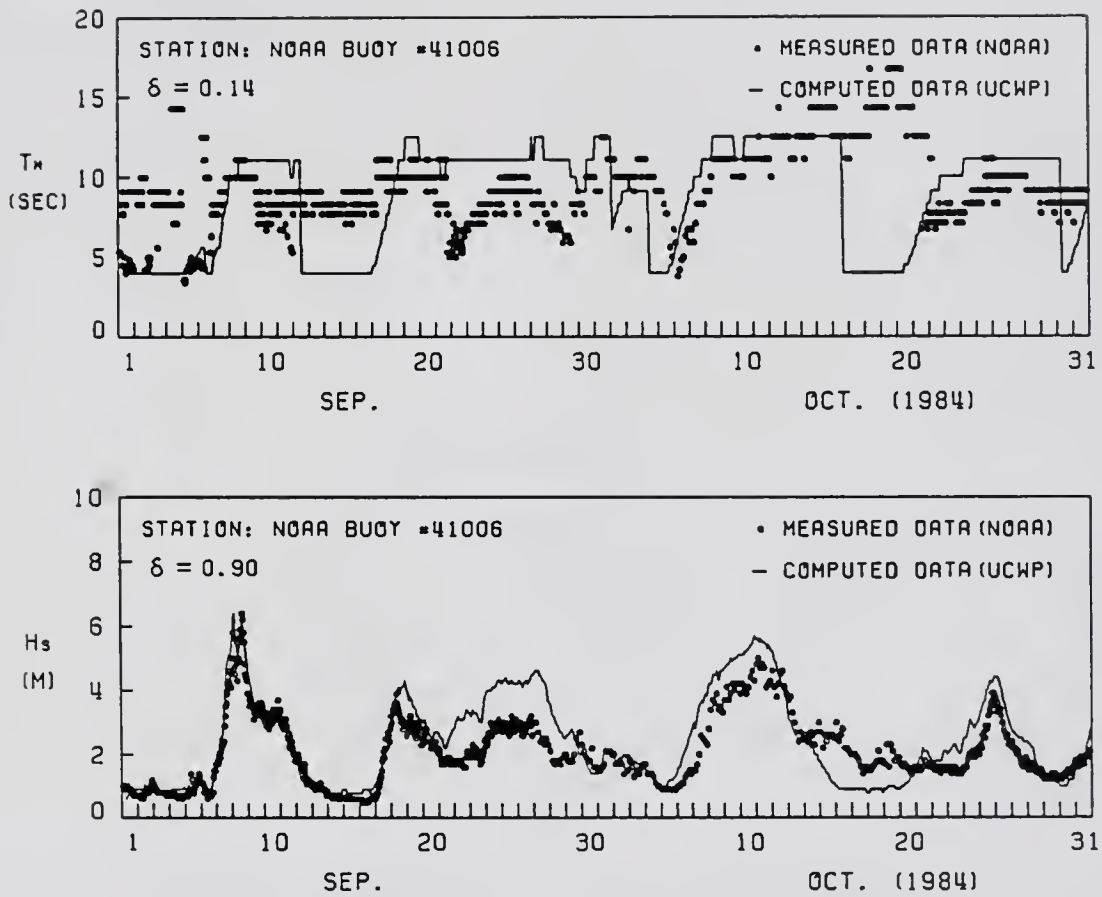


Figure 4.13: Comparisons of NOAA and UCWP modal periods and significant wave heights at the Buoy #41006 location.

Table 4.1: Summary of Correlations between computed and measured values of  $H_s$  and  $T_m$  at the buoy #41006 location.

station	month	WIS model			
NOAA buoy #41006	Jan.(84)	$\delta_{H_s,c H_s,m}$		$\delta_{T_m,c T_m,m}$	
		0.49	0.49*	-0.22	-0.21*
	Sep.- Oct.(84)	0.88	0.90*	0.30	0.50*
station	month	UCWP model			
NOAA buoy #41006	Jan.(84)	$\delta_{H_s,c H_s,m}$		$\delta_{T_m,c T_m,m}$	
		0.85	0.86*	0.38	0.53*
	Sep.- Oct.(84)	0.90	0.92*	0.14	0.51*

\*swell data ( $H_{s,c} < 2m, T_{m,m} > 8sec$ ) are excluded in correlation calculations

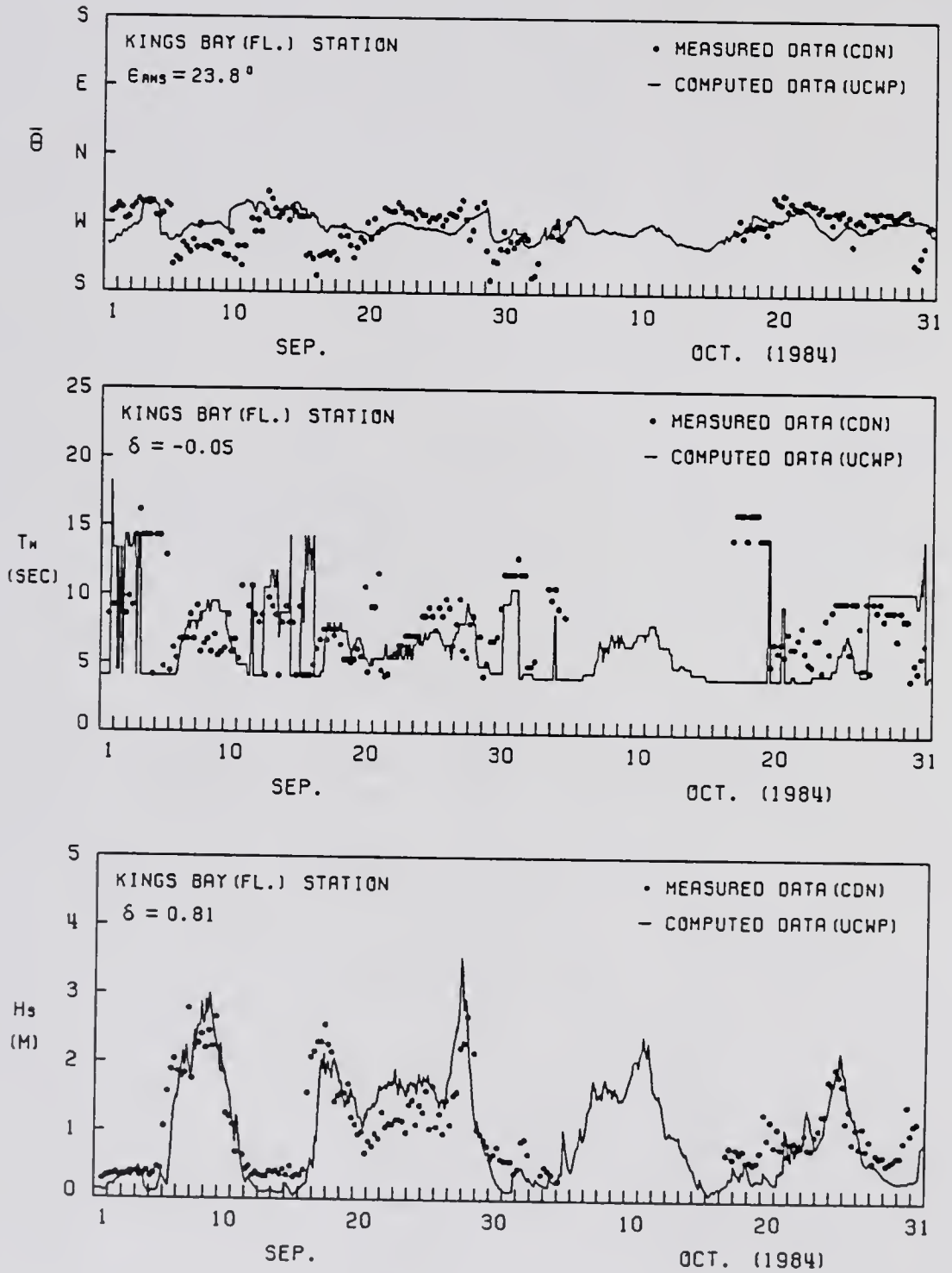


Figure 4.14: (a) Comparisons of CDN and UCWP average wave direction, modal periods and significant wave heights at the Kings Bay gage location.

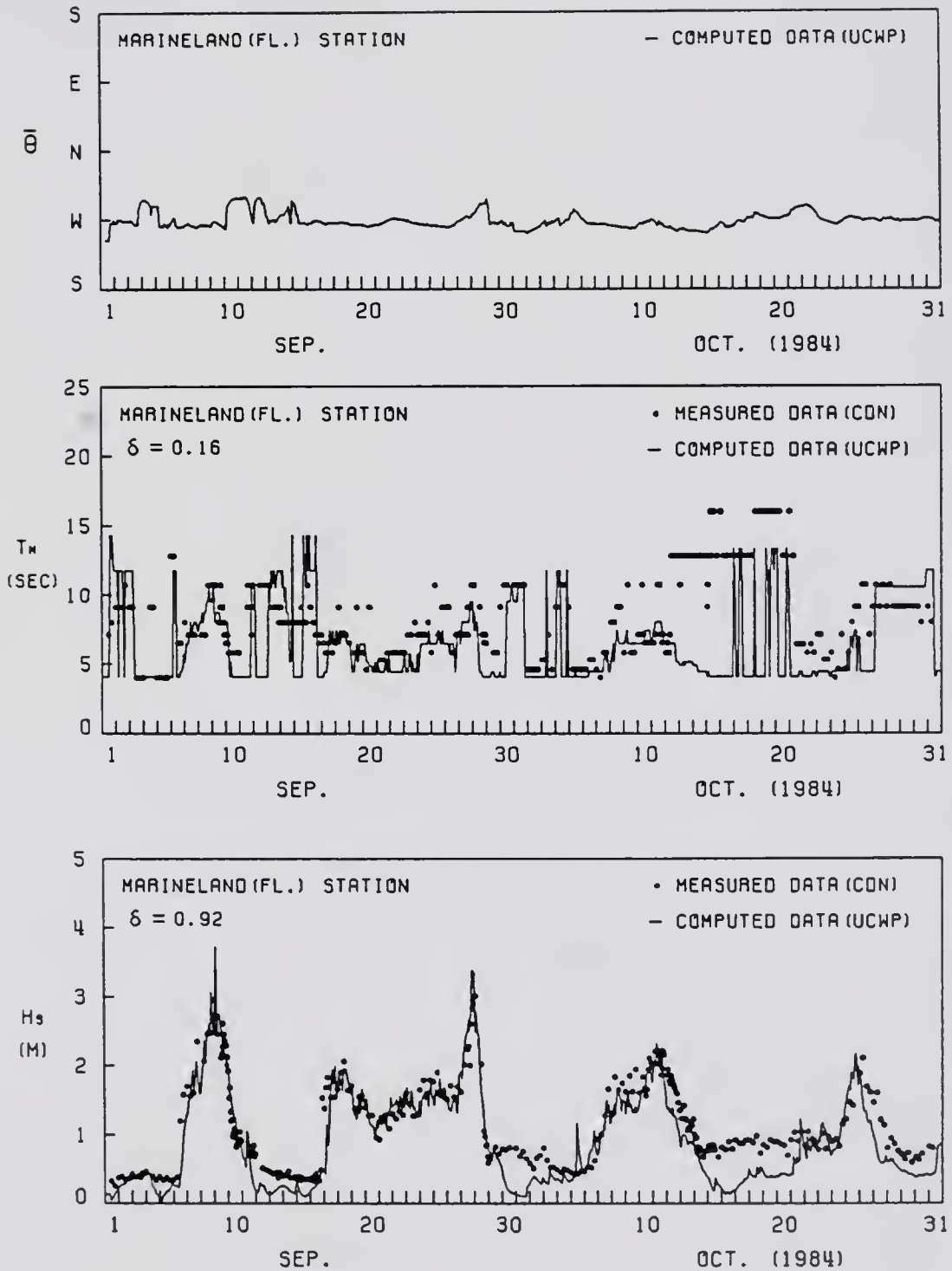


Figure 4.14: (b) Comparisons of CDN and UCWP average wave direction, modal periods and significant wave heights at the Marineland gage location.

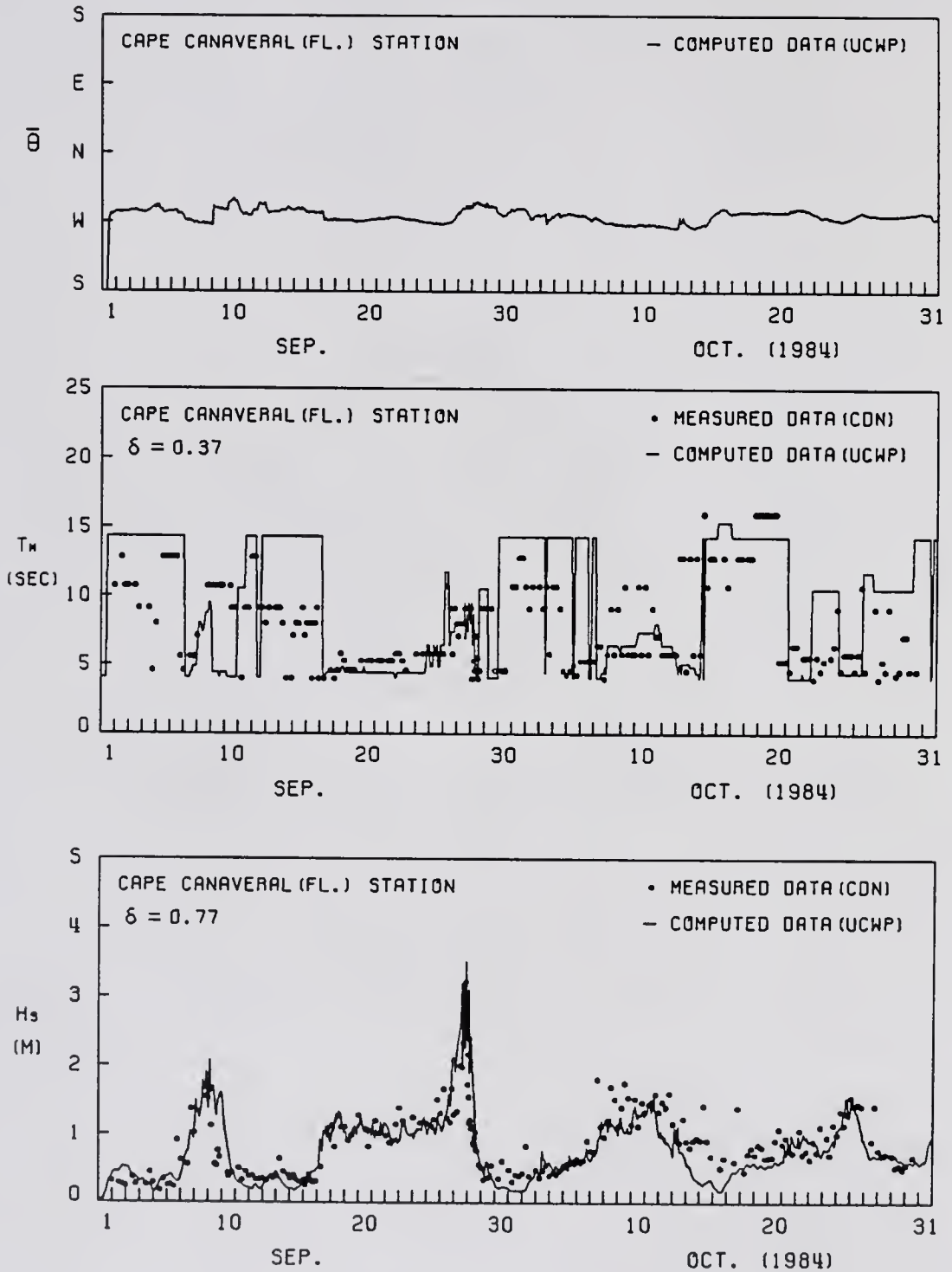


Figure 4.14: (c) Comparisons of CDN and UCWP average wave direction, modal periods and significant wave heights at the Cape Canaveral Station.

Table 4.2: Summary of Correlations between computed and measured values of  $H_s$  and  $T_m$  at three shallow water stations.

station	month	UCWP model			
		$\delta_{H_{s,c} H_{s,m}}$		$\delta_{T_{m,c} T_{m,m}}$	
Kings Bay	Jan.(84)	0.77	0.77*	0.45	0.34*
	Sep.	0.81	0.79*	-0.05	0.13*
Marineland	-	0.92	0.93*	0.16	0.57*
Cape Canaveral	Oct.(84)	0.77	0.80*	0.37	0.22*

\*swell data ( $H_{s,c} < 1m, T_{m,m} > 10sec$ ) are excluded in correlation calculations

and wave period when swell data are excluded. The comparisons of correlations also show that the UCWP deepwater submodel yields higher and more consistent correlations than the WIS deepwater model. Table 4.2 shows the correlations between the computed and measured significant wave heights, as well as modal periods, at the shallow water stations of Kings Bay, Marineland and Cape Canaveral. The correlations between the computed and measured significant wave heights do not change appreciably whether or not swell data are included in the computation of correlations. However, the correlations of the computed and measured modal periods improved significantly if swell data are excluded in the correlation calculations.

In summary, the model performed well in wave height and direction hindcastings especially for severe weather cases. Under no wind or weak wind condition, the model tended to underestimate the waves. The overall performance on modal period hindcasting was, at best, fair. The computed modal periods are consistent with the measured ones for large waves but fare poorly for small waves. Also, for mixed swell and sea conditions, modal period,  $T_m$ , appears to be a poor indicator of wave property.

#### 4.4 Wind-Wave Relationship in a Fully Developed Sea

In Section 4.2 the significant wave heights and modal periods computed from the UCWP model are shown to converge to their respective saturation limits at

different wind speeds in both fetch and duration dependent cases. Based upon these wave data, Fig. 4.15 shows on log-log scale the plots of the significant wave height versus wind speed, and the modal period versus wind speed for different fetchs and durations. It is seen in the plot of  $H_s$  versus  $U_{10}$  both fetch-limited and duration-limited curves tend to approach to a single limit for large fetch and long duration, which indicates a fully developed condition for wind generated waves. For duration dependent case, it is interesting to observe here that wave height and wave period approach to their respective upper limits at approximately the same rate. If the fetch is unlimited, the wave can be considered virtually saturated (both height and length reached limit) when duration exceeds 60 hours. For fetch dependent case, on the other hand, wave height reaches its upper limit before the wave period, that is, as the fetch increases beyond 600 km, wave height virtually reaches its limit and becomes more difficult to grow while wave period can still increase easily to some extent until it reaches the upper limit.

In fetch dependent case, an empirical equation for  $H_s$ , similar to that of SMB formula is proposed here:

$$\frac{gH_s}{U_{10}^2} = c_1 \left[ \frac{gF_s}{U_{10}^2} \cdot R_1 \cdot \tanh\left(c_2 \frac{F}{F_s}\right) \right]^{c_3} \quad (4.11)$$

where  $c_1$ ,  $c_2$ ,  $c_3$  are constants,  $F_s$  is the fetch corresponding to maximum overshoot (see Fig. 2.4), and  $R_1$  is a overshoot enhancement factor. The overshoot enhancement parameter  $\gamma_1$  and the width parameter  $\sigma_1$  are functions of  $U_{10}$ . The above equation has similar functional form as the parametric model when  $F/F_s$  is small, i.e.,

$$\frac{gH_s}{U_{10}^2} = \chi_1 \left( \frac{gF}{U_{10}^2} \right)^{c_3}, \quad \text{for } F \ll F_s$$

where  $\chi_1$  is a proportional constant. For large  $F/F_s$ ,  $R_1$  approaches to unity and Eq.(4.11) can be expressed as

$$\frac{gH_s}{U_{10}^2} = c_1 \left( \frac{gF_s}{U_{10}^2} \right)^{c_3}, \quad \text{for } F \gg F_s \quad (4.12)$$

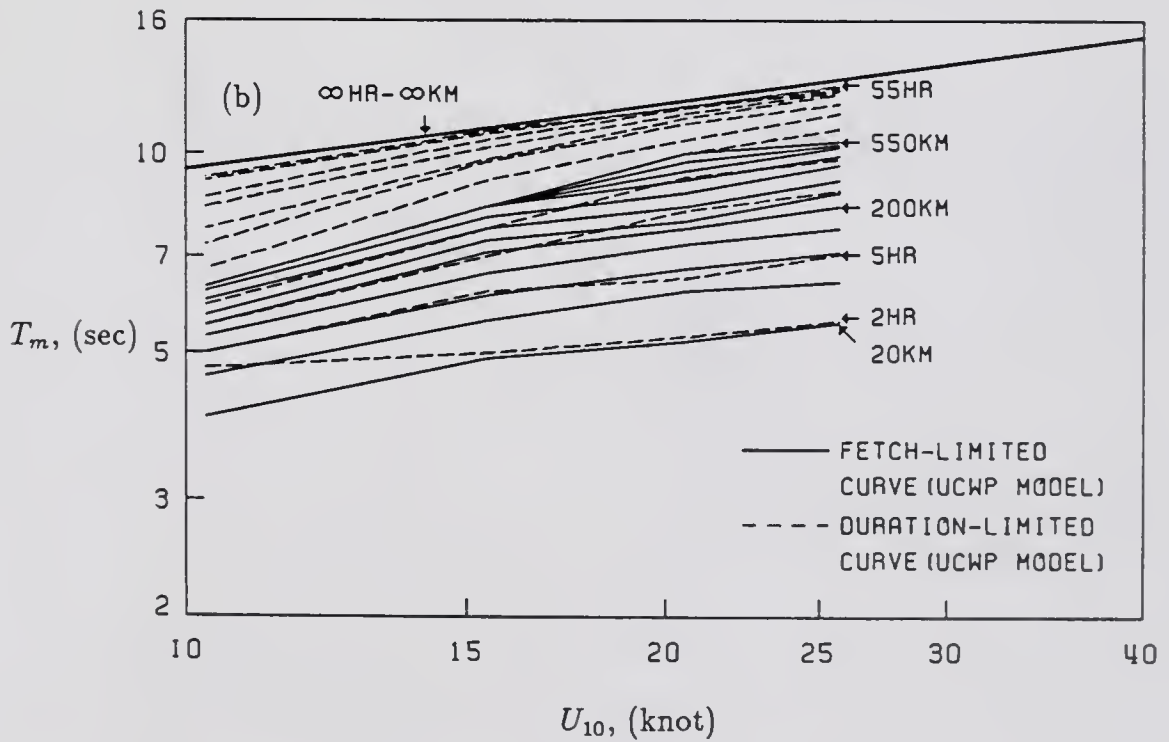
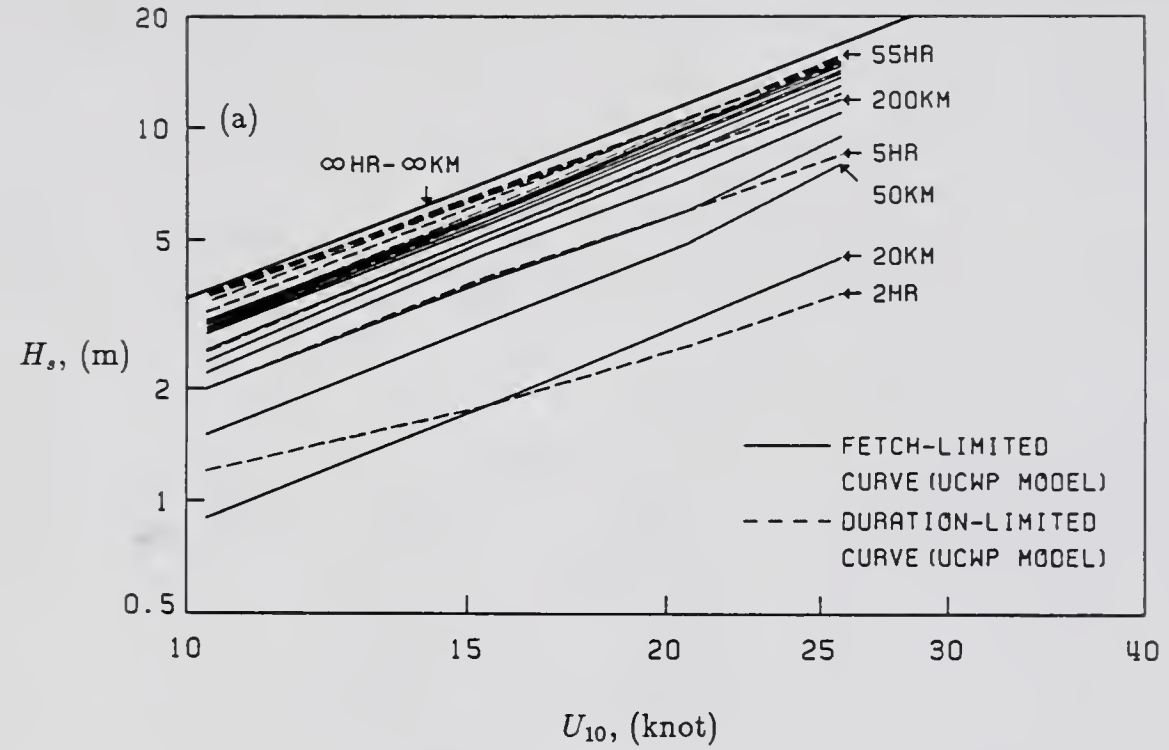


Figure 4.15: Plots of (a)  $H_s$  versus  $U_{10}$ , and (b)  $T_m$  versus  $U_{10}$  at various fetch and duration.

Thus,  $F_s$  can be treated as the practical upper limit of the fetch influence.

In duration dependent case, an empirical equation for  $H_s$  may be expressed as

$$\frac{gH_s}{U_{10}^2} = c_4 \left[ \frac{gt_s}{U_{10}} \cdot R_2 \cdot \tanh\left(c_5 \frac{t}{t_s}\right) \right]^{c_6} \quad (4.13)$$

where  $c_4$ ,  $c_5$ ,  $c_6$  are constants,  $t_s$  is the duration required for maximum overshoot, and  $R_2$  is again a overshoot enhancement factor. Similarly, when  $t \ll t_s$ , Eq.(4.13) can be approximated by the expression:

$$\frac{gH_s}{U_{10}^2} = \chi_2 \left( \frac{gt}{U_{10}^2} \right)^{c_6}, \quad \text{for } t \ll t_s,$$

where  $\chi_2$  is a proportional constant, and when  $t \gg t_s$ , Eq.(4.11) can be expressed as

$$\frac{gH_s}{U_{10}^2} = c_4 \left( \frac{gt_s}{U_{10}^2} \right)^{c_6}, \quad \text{for } t \gg t_s, \quad (4.14)$$

At the fully developed condition, for fetch and duration unlimited case Eq.(4.12) shall be identical to Eq.(4.14), or

$$\frac{gH_{s,\infty}}{U_{10}^2} = c_7 (U_{10})^{c_8} \quad (4.15)$$

where  $H_{s,\infty}$  indicates the significant height at the fully developed sea. If this fully developed condition is approximated by a upper bound of  $H_s - U_{10}$  curves, drawn as a solid line in Fig. 4.15, we find  $c_7 \approx 0.738 \text{ (m/sec)}^{1/3}$  and  $c_8 \approx -1/3$ , or  $H_{s,\infty} \sim U_{10}^{5/3}$ .

In fetch dependent case, an empirical equation for  $T_m$  is proposed here as

$$\frac{gT_m}{U_{10}} = d_1 \left[ \frac{gF_s}{U_{10}^2} \cdot \tanh\left(d_2 \frac{F}{F_s}\right) \right]^{d_3} \quad (4.16)$$

where  $d_1$ ,  $d_2$ , and  $d_3$  are constants. For large  $F/F_s$ , Eq.(4.16) approaches to

$$\frac{gT_m}{U_{10}} = d_1 \left( \frac{gF_s}{U_{10}^2} \right)^{d_3}, \quad \text{for } F \gg F_s, \quad (4.17)$$

In duration dependent case,  $T_m$  is proposed here as

$$\frac{gT_m}{U_{10}} = d_4 \left[ \frac{gt_s}{U_{10}} \cdot \tanh\left(d_5 \frac{t}{t_s}\right) \right]^{d_6} \quad (4.18)$$

where  $d_4$ ,  $d_5$  and  $d_6$  are constants. For large  $t/t_s$ , Eq.(4.18) approaches to

$$\frac{gT_m}{U_{10}} = d_4 \left( \frac{gt_s}{U_{10}^2} \right)^{d_6}, \quad \text{for } t \gg t_s, \quad (4.19)$$

Thus, based on either Eq.(4.17) or (4.19), the upper limit of  $T_m$  corresponding to  $U_{10}$  can be approximated by the following expression:

$$\frac{gT_{m,\infty}}{U_{10}} = d_7 (U_{10})^{d_8} \quad (4.20)$$

where  $T_{m,\infty}$  indicates the modal period at the fully developed sea. If this fully developed condition is approximated by a upper bound of  $T_m - U_{10}$  curves, drawn as a solid line in Fig. 4.15, we find  $d_7 \approx 43.0 \text{ (m/sec)}^{2/3}$  and  $d_8 \approx -2/3$ , or  $T_{m,\infty} \sim U_{10}^{1/3}$ .

In order to examine the relationship between the resonant parameter,  $2\pi U_{10}/gT_m$  ( $= f_m/f_0$ ), and the energy scale parameter,  $H_s/gT_m^2$  ( $= f_m^2 H_s/g$ ), when the wind generated waves develop into a saturation condition, their computed values based on the UCWP model are plotted against each other in Fig. 4.16. It can be seen that the fetch limited case and the duration limited case behave in a similar manner and both approach to the same limiting curve. The long-dash lines shown in Fig. 4.16 indicate the fully developed condition solved from Eqs.(4.12) and (4.17) by eliminating the common term  $gF_s/U_{10}^2$ , or from Eqs.(4.14) and (4.19) by eliminating the common term  $gt_s/U_{10}$ :

$$\frac{2\pi U_{10}}{gT_m} = 26.95 \left( \frac{H_s}{gT_m^2} \right)^{2/3} \quad (4.21)$$

Also shown in Fig. 4.16 is the saturation condition, drawn in short-dash lines, obtained from the classical SMB method which utilizes  $U_a = U_{10}$  in Eqs.(4.1) and (4.6):

$$\frac{2\pi U_{10}}{gT_m} = 11.81 \left( \frac{H_s}{gT_m^2} \right)^{1/2} \quad (4.22)$$

It is seen that the UCWP model yields greater energy scale parameter than the SMB model when the resonant parameter is small (approximately less than unity), and it yields less energy scale parameter than the SMB model when the resonant parameter is large (approximately greater than unity).

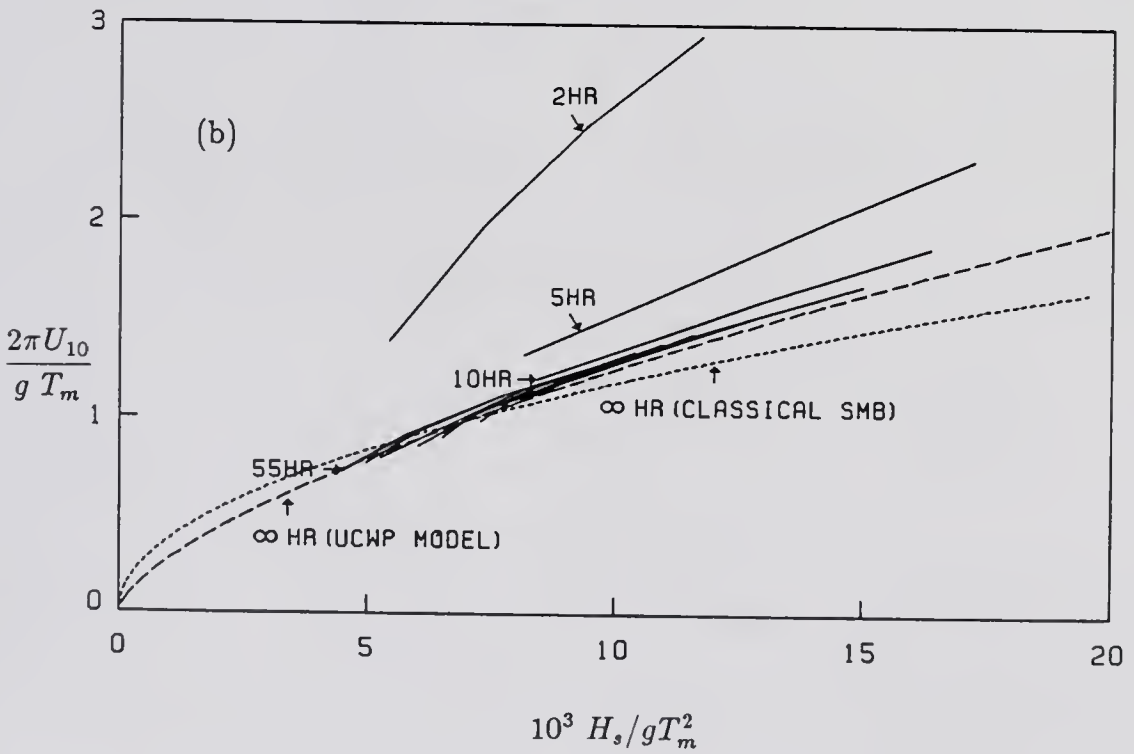
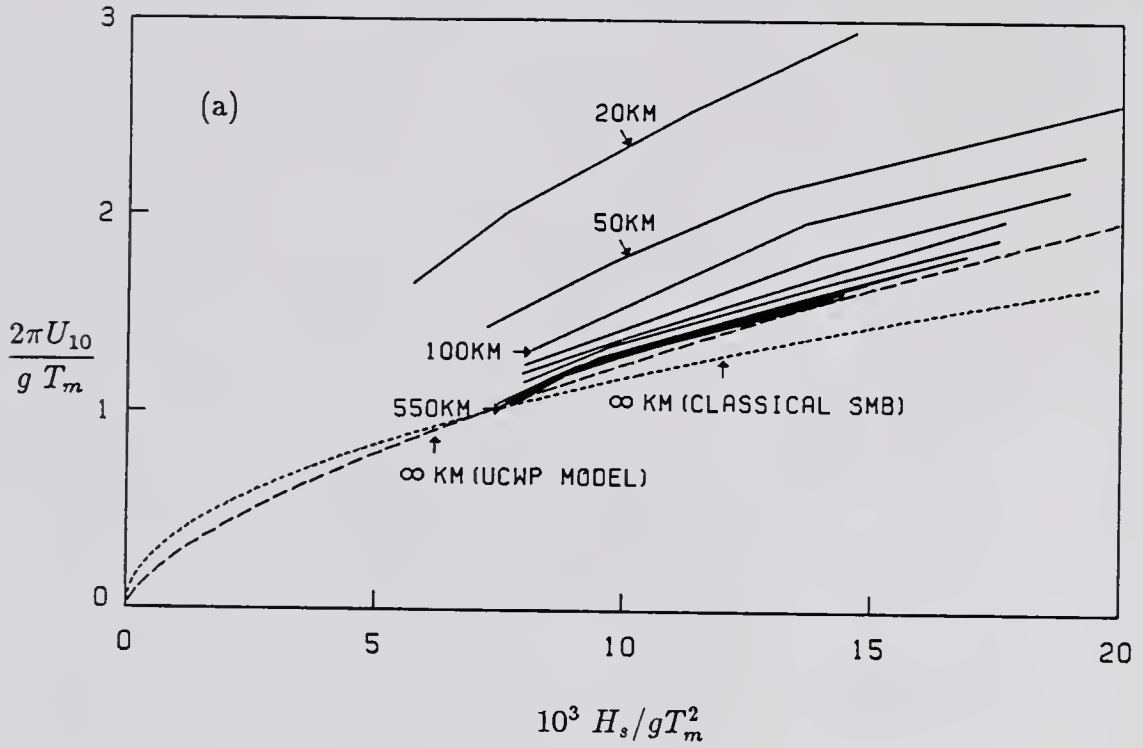


Figure 4.16: Plots of  $2\pi U_{10}/g T_m$  versus  $10^3 H_s/g T_m^2$  in (a) fetch-limited case and in (b) duration-limited case.

The resonant parameters and the energy scale parameters based on measured buoy data are then used to show the contour lines of  $H_s$  in Fig. 4.17. Also shown are the saturation lines given by the UCWP model and the SMB model. These limits are good indicators of the maximal wave height under optimum wind conditions. It is seen that the UCWP model shows better agreement with the measured data than the classical SMB method for high wave condition. For instance, the long-dash line which represents the saturation relation obtained from the UCWP model passes through the centers of the maximum contour of 7-meter for the 1984 data and the one of 8-meter for the 1985 data whereas the short-dash line which represents the classical SMB model crosses the maximum contour only for the 1984 data.

Waves above the saturation condition in Fig. 4.17 are in the growing stage and they are influenced by the limited fetch and duration. Waves below the long-dash line are in the decaying stage when experiencing the dissipation under the relatively low winds.

#### 4.5 Comparison of Various Wave Energy Flux Elements

For wave generation in the deep water, the turbulent dissipation has been mentioned to be a dominant factor in the UCWP model. Its contribution to the total energy flux is to be compared with the advection and wind input terms in this section. The comparisons are shown for three cases; the first two consider the growing and decaying stages, and the last one, the small wind and wave condition. The first case, Case 1, is during a growing period under increasing wind condition at 1:00 a.m. September 8, 1984, when the winds increasing from 26 knots to 31 knots. A net gain of wave energy is observed in the case. The second case, Case 2, is a decaying case at 5:00 a.m. September 8, 1984, while onshore winds decreased from 30 knots to 28 knots in two hours. A net loss of energy is noticed in the case. The last case, Case 3, shown in Fig. 4.20 is a local wind wave growth case at 23:00 p.m. October 13, 1984, when winds remain a constant speed at 12 knots for the last twelve hours.

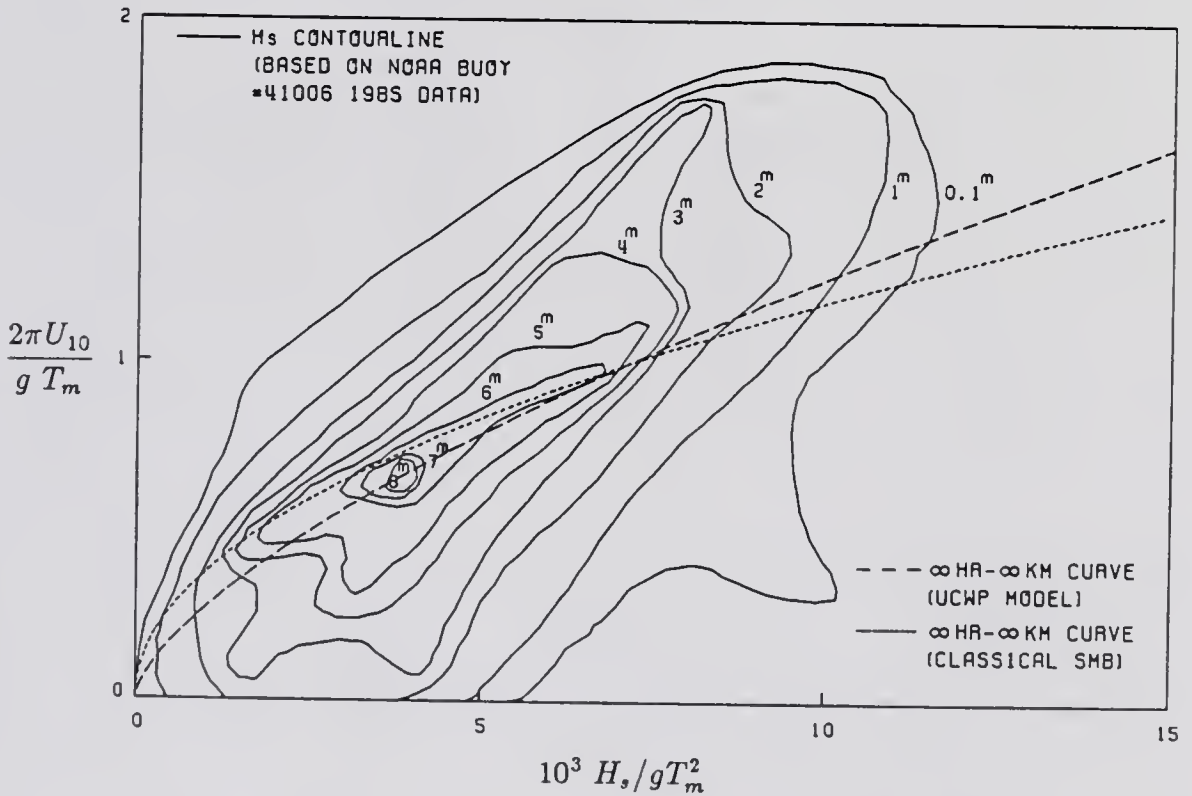
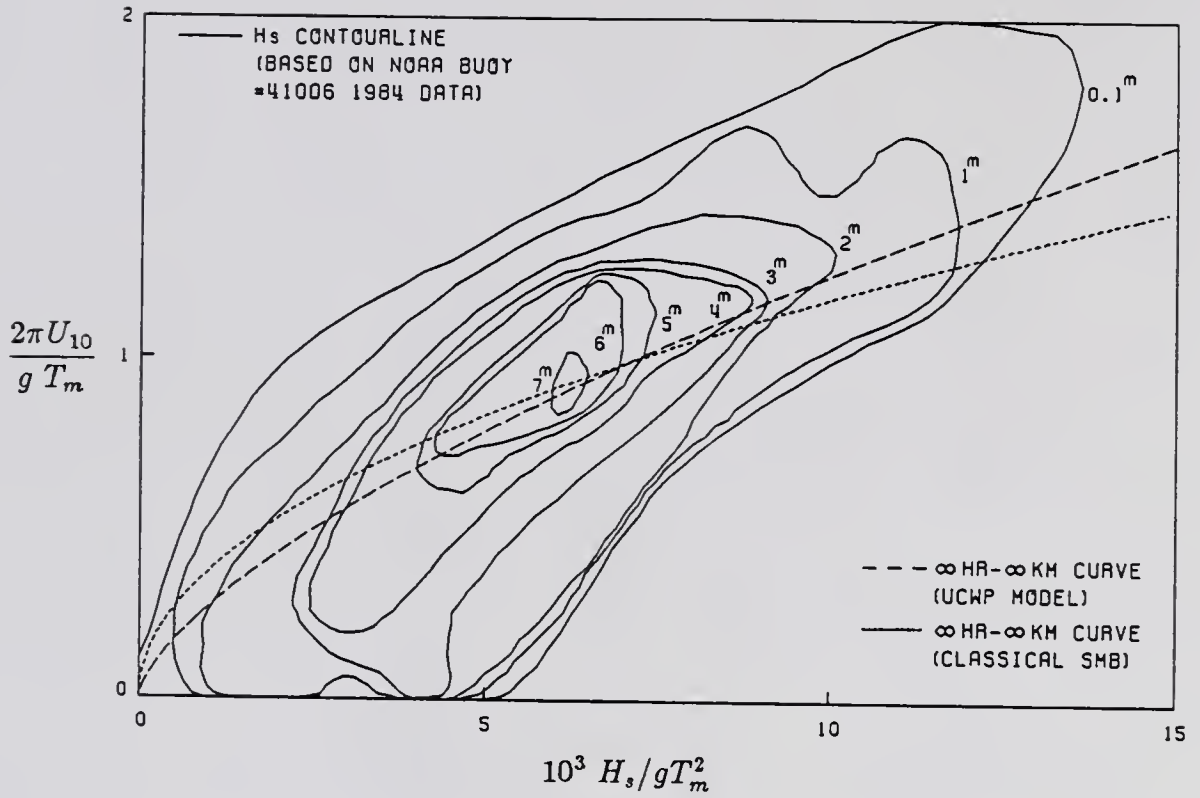


Figure 4.17: Plots of  $2\pi U_{10}/gT_m$  versus  $10^3 H_s/gT_m^2$  based on the NOAA buoy #41006 1984-1985 data.

Table 4.3: Summary of energy flux budget at the buoy #41006 location.

mechanism	$10^5 \Delta E / \Delta t$ ( $\text{m}^2/\text{sec}$ )		
	Case 1	Case 2	Case 3
advection	-2.93	-4.80	-0.09
$G_{in,1}$ wind input term	13.97	3.01	0.64
$G_{in,2}$ wind input term	0.63	0.64	0.08
turbulent viscous loss	-3.91	-5.15	-0.65
net (temporal change)	7.76	-6.30	-0.02

Table 4.3 shows the energy flux budget for the three cases at the buoy #41006 location. In all three cases, the turbulent dissipation is important. The local wind input term,  $G_{in,2}$  is overall relatively small in all three cases. In Case 3, where waves are nearly in stationary condition under constant wind speed, temporal change is found to be very small when the  $G_{in,1}$  term is approximately balanced by the turbulent dissipation term. Plots of rate of change of individual deepwater effect sources over the frequencies for all three cases are given in Appendix D.

It is found here that the bottom effects in shallow water are quite pronounced for the Florida Coast. Three cases showing the contributions of various elements to the energy flux at a shallow water location are presented here. In each case the rates of change of spectrum due to the temporal variation, the advection, which includes shoaling and refraction effects, the atmospheric input, the turbulent dissipation, and the bottom frictional loss, are evaluated from the shallow water UCWP model. Thus, the relative importance of individual spectral components can be noticed directly from these cases.

The first case, Case 4, is during a growing period under increasing wind condition at 5:00 a.m. September 8, 1984, when the onshore winds increasing from 27 knots to 30 knots in two hours. A net gain of wave energy is observed. The second case, Case 5, is a decaying case at 1:00 a.m. September 10, 1984, while onshore winds decreased from 34 knots to 29 knots in two hours. A net loss of energy is

Table 4.4: Summary of energy flux budget at the Marineland station.

mechanism	$10^5 \Delta E / \Delta t$ ( $\text{m}^2/\text{sec}$ )		
	Case 4	Case 5	Case 6
advection, shoaling, and refraction	1.79	1.75	1.68
atmospheric input	13.72	3.13	3.72
turbulent viscous loss	-0.77	-0.68	-0.45
bottom frictional loss	-9.15	-11.07	-4.41
net (temporal change)	5.59	-6.87	0.54

noticed in the case. The third case, Case 6, occurred at 3:00 a.m. September 10, 1984, when onshore winds were dropping from 29 knots to 26 knots in two hours. In this last case, a net loss of energy is seen at low frequencies and a net gain of energy is found at the high frequency range, which is due to the entering of high frequency waves from the neighbored area. Table 4.4 shows the energy flux budget for the three cases at the Marineland station. In the all three cases, the bottom friction and advection effects dominate the other processes. More than 65 percent of the wind input is being dissipated by bottom friction. Temporal changes, often neglected in shallow water wave transformation computations, are found to be also significant. The dissipation of wave energy due to turbulent viscosity is seen to be less important in these cases. The plots of rate of change of individual shallow water effect sources over the frequencies for the above three cases are also given in Appendix D.

#### 4.6 Influence of $c_f$ in Shallow Water Wave Transformation Process

An important factor that influences the shallow water wave transformation is the bottom friction. To estimate it according to Eq.(2.50) in a wave model, bottom friction coefficient  $c_f$  needs to be first determined. The magnitude of  $c_f$  has been suggested to range from 0.005 to 0.05 at various locations along the Florida coast. Five values of the friction coefficient,  $c_f = 0.0, 0.005, 0.01, 0.02, \text{ and } 0.04$ , are selected

here to test their influences on the bottom frictional loss. Figure 4.18 shows the comparisons of wave heights and modal periods hindcasted in September 1984 with respect to the five  $c_f$  values. Both the time series of the hindcasted wave height and modal periods plotted in Fig. 4.18 were smoothed by three points running average over a six-hour interval to provide better visual comparison. As expected, waves hindcasted from the UCWP model based on  $c_f=0.0$  have the largest heights and modal periods than the other four  $c_f$  values. That is, when the dissipation mechanism due to bottom friction is absent in the model, long waves can survive and result more wave energy in the low frequency region. On the other hands, waves hindcasted based on  $c_f = 0.04$ , which is the largest among the five tested values, are seen to generate the least heights and modal periods compared with the ones based on the other four  $c_f$  values. This is because tremendous energy has been dissipated in the low frequency regions due to the utilization of strong bottom friction in the model. The wave heights and modal periods computed from the model based on the  $c_f$  equal to 0.005, 0.01, and 0.02, respectively, are seen to be monotonically decreasing between the ones with  $c_f=0.0$  (null bottom friction condition) and the ones with  $c_f=0.04$  (strong bottom friction condition). By using different  $c_f$  values in the UCWP model, the wave heights are seen to change significantly for large wave condition but insignificantly for small wave condition. However, the modal periods may change dramatically for small but long waves since the bottom frictional dissipation is more active in low frequency components than in high frequency components. The change of modal period for high waves according to various  $c_f$  values is relatively small but detectable.

Also included in Fig. 4.18 are the measured wave heights and modal periods which allow a statistical analysis between the computed and measured data. The statistic parameters chosen here for the analysis are the correlation coefficient and a root-mean-square error normalized by the root-mean-square value of measured

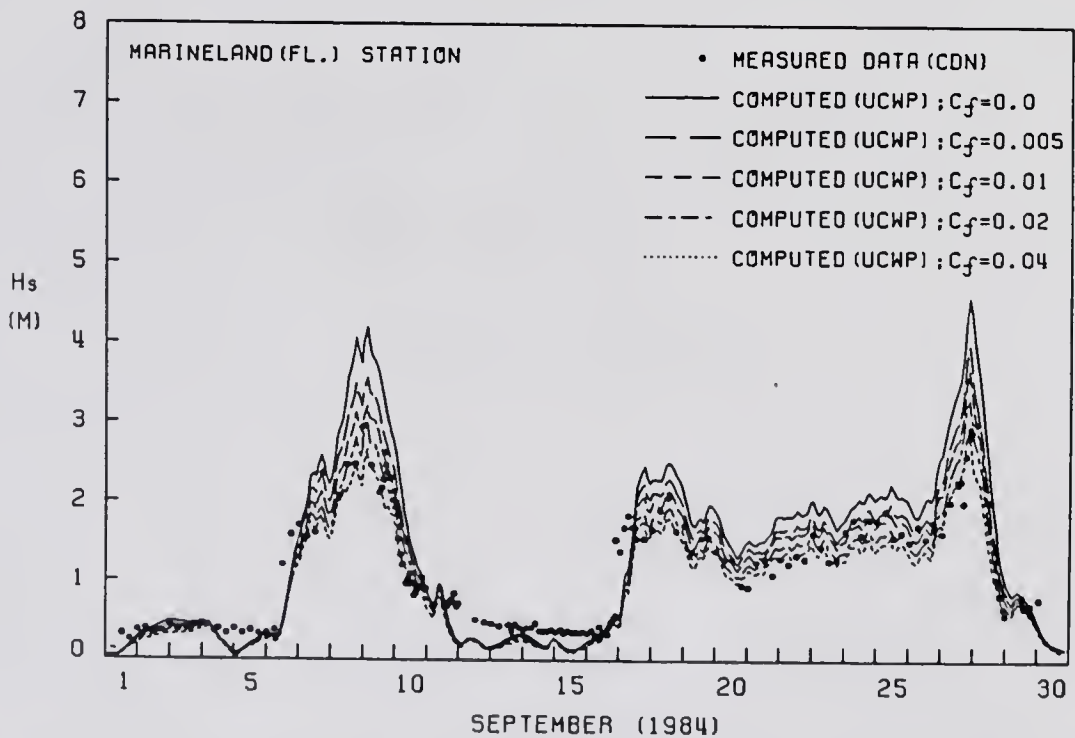
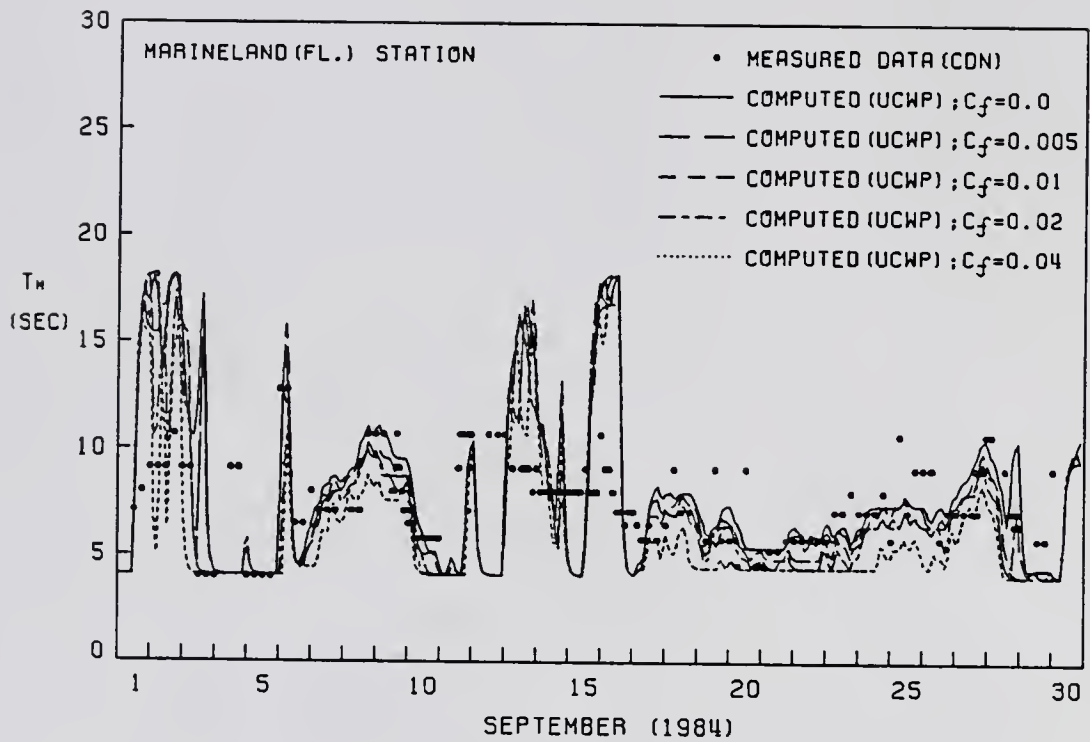


Figure 4.18: Comparisons of wave heights and modal periods computed in September 1984 for  $c_f=0.0, 0.005, 0.01, 0.02, \text{ and } 0.04$ .

Table 4.5: Comparison of  $\delta_{H_e, c H_e, m}$ ,  $\delta_{T_m, c T_m, m}$ ,  $\epsilon_{H_e, c H_e, m}$ , and  $\epsilon_{T_m, c T_m, m}$  for  $c_f=0.0, 0.005, 0.01, 0.02,$  and  $0.04$ .

$c_f$	$\delta_{H_e, c H_e, m}^*$	$\delta_{T_m, c T_m, m}^*$	$\epsilon_{H_e, c H_e, m}^*$	$\epsilon_{T_m, c T_m, m}^*$
0.0	0.93	0.30	0.43	0.52
0.005	0.94	0.32	0.30	0.51
0.01	0.94	0.31	0.25	0.51
0.02	0.95	0.38	0.23	0.37
0.04	0.92	0.30	0.26	0.51

\*Computations are based on the Sep. 1984 data at Marineland Station

data. The latter can be expressed as:

$$\epsilon_{X_c X_m} = \sqrt{\frac{\sum_{i=1}^N [(X_c)_i - (X_m)_i]^2}{\sum_{i=1}^N (X_m)_i^2}} \quad (4.23)$$

where  $X_c$  is a computed  $X$ ,  $X_m$  is a measured  $X$ , and  $N$  is the sample size. The higher correlation and the lower normalized root-mean-square error indicate better agreement between the computed and measured data. Table 4.5 shows the comparison of these statistical parameters between computed and measured wave heights and modal period for  $c_f=0.0, 0.005, 0.01, 0.02,$  and  $0.04$ . It is noticed the correlations between the computed and measured wave heights based upon the five different  $c_f$  values are all high and they do not differ significantly from one to the others although the one based on  $c_f=0.02$  gives the highest correlation. The correlations between the computed and measured modal periods are found between 0.3 and 0.38 based on the five  $c_f$  values. The one based on  $c_f=0.02$  again gives the highest correlation. The comparison of normalized root-mean-square error for different  $c_f$  values shows that errors calculated from wave height and modal period, respectively, based on  $c_f=0.02$  are smaller than the others. Therefore, the utilization of  $c_f=0.02$  in computing bottom friction is good for the wave hindcast along the Florida coast.

Figure 4.19 (a), (b), (c), (d), and (e), respectively, give examples of how the bottom frictional dissipation contributes to the total energy flux for  $c_f=0.0,$

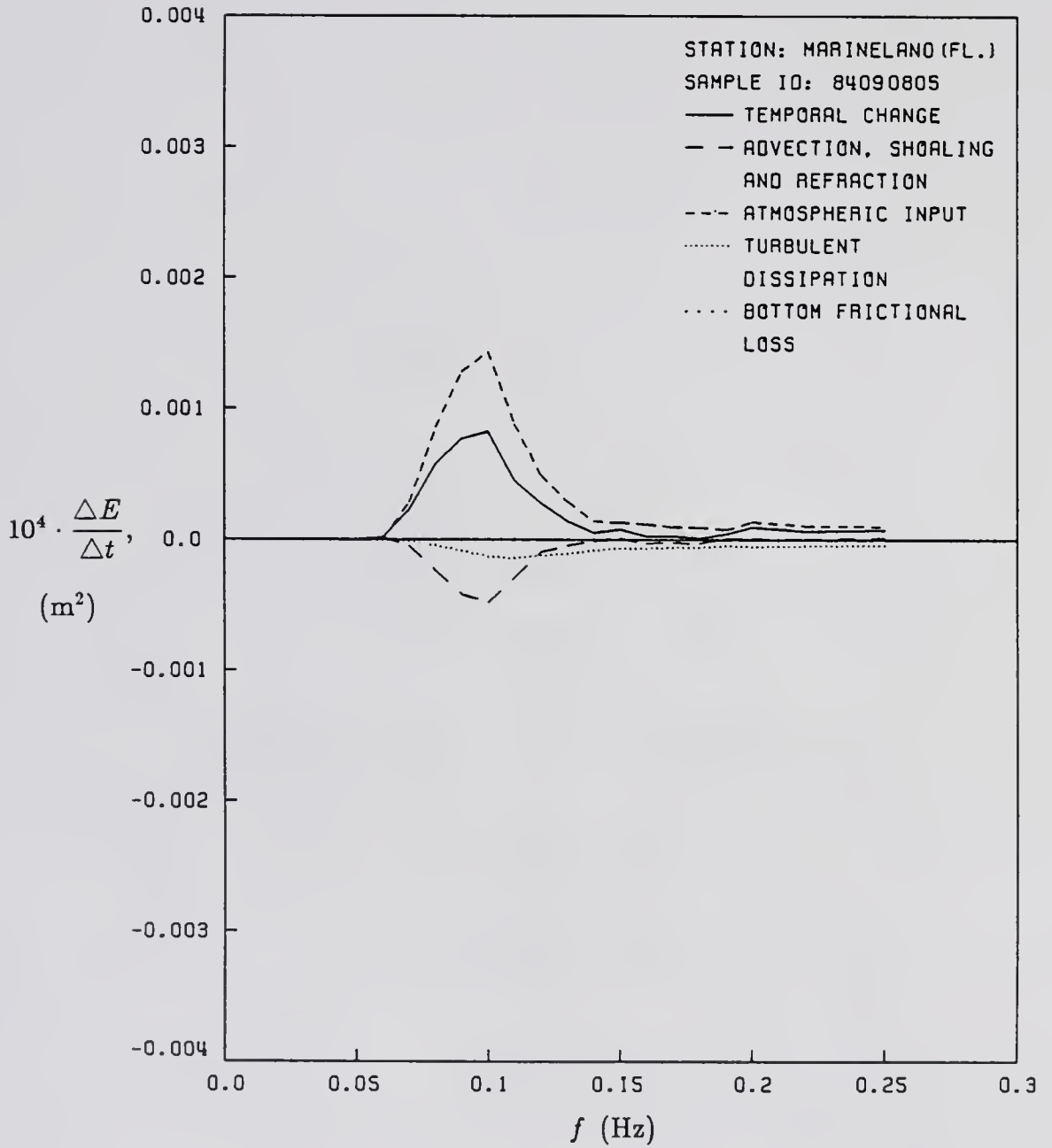


Figure 4.19: (a) Plot of individual shallow water effect sources for  $c_f=0.0$

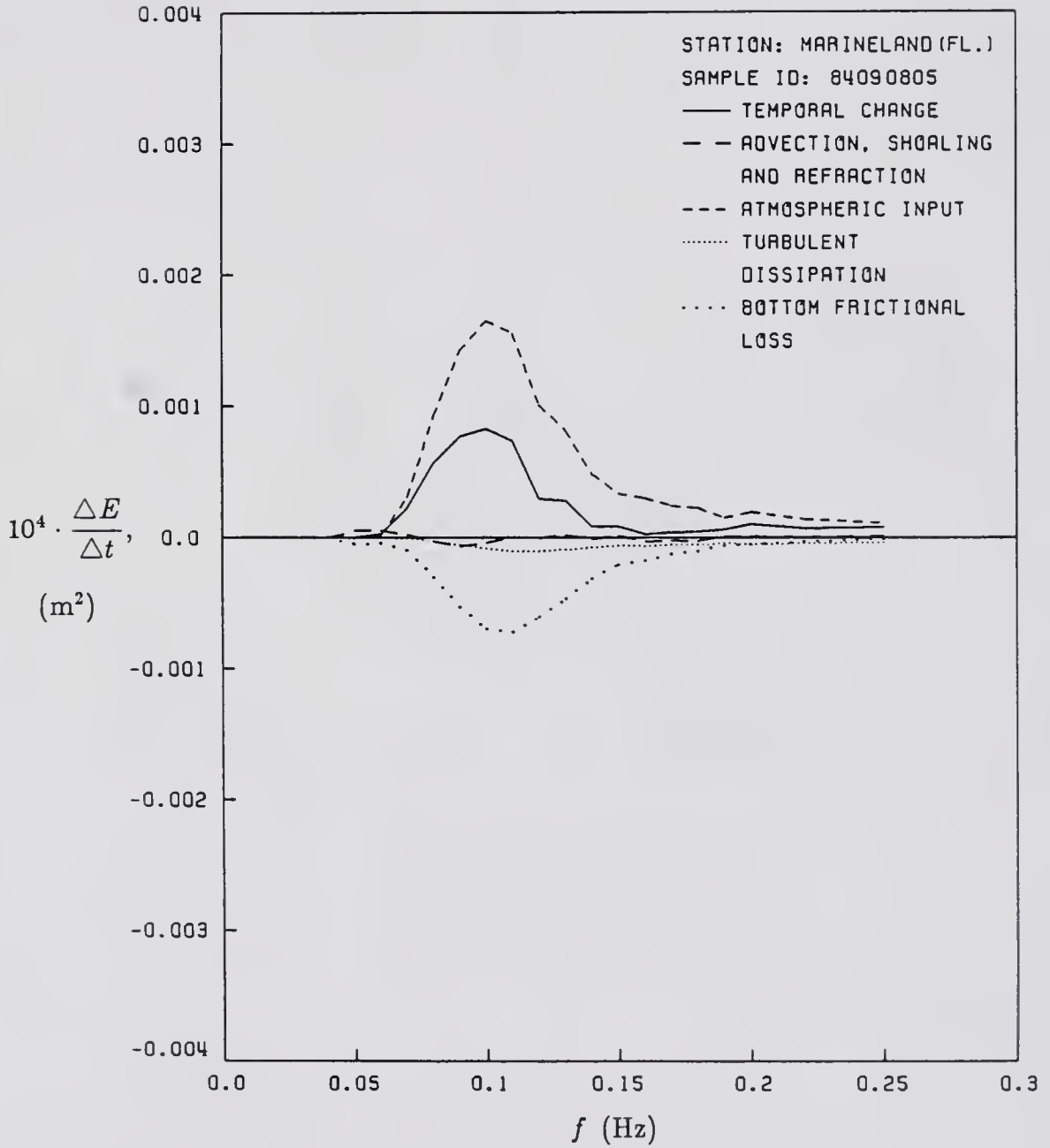


Figure 4.19: (b) Plot of individual shallow water effect sources for  $c_f=0.005$

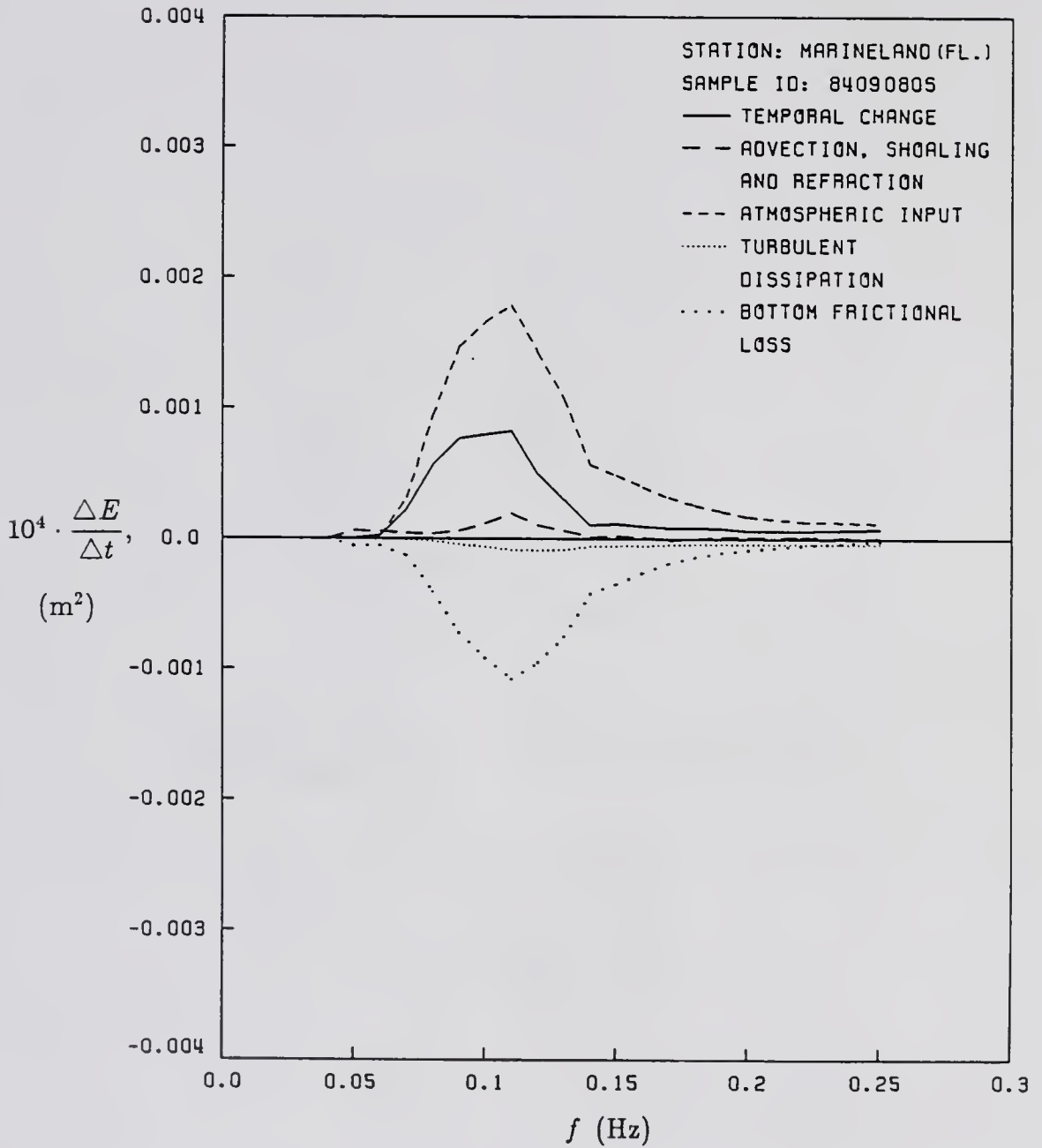


Figure 4.19: (c) Plot of individual shallow water effect sources for  $c_f=0.01$

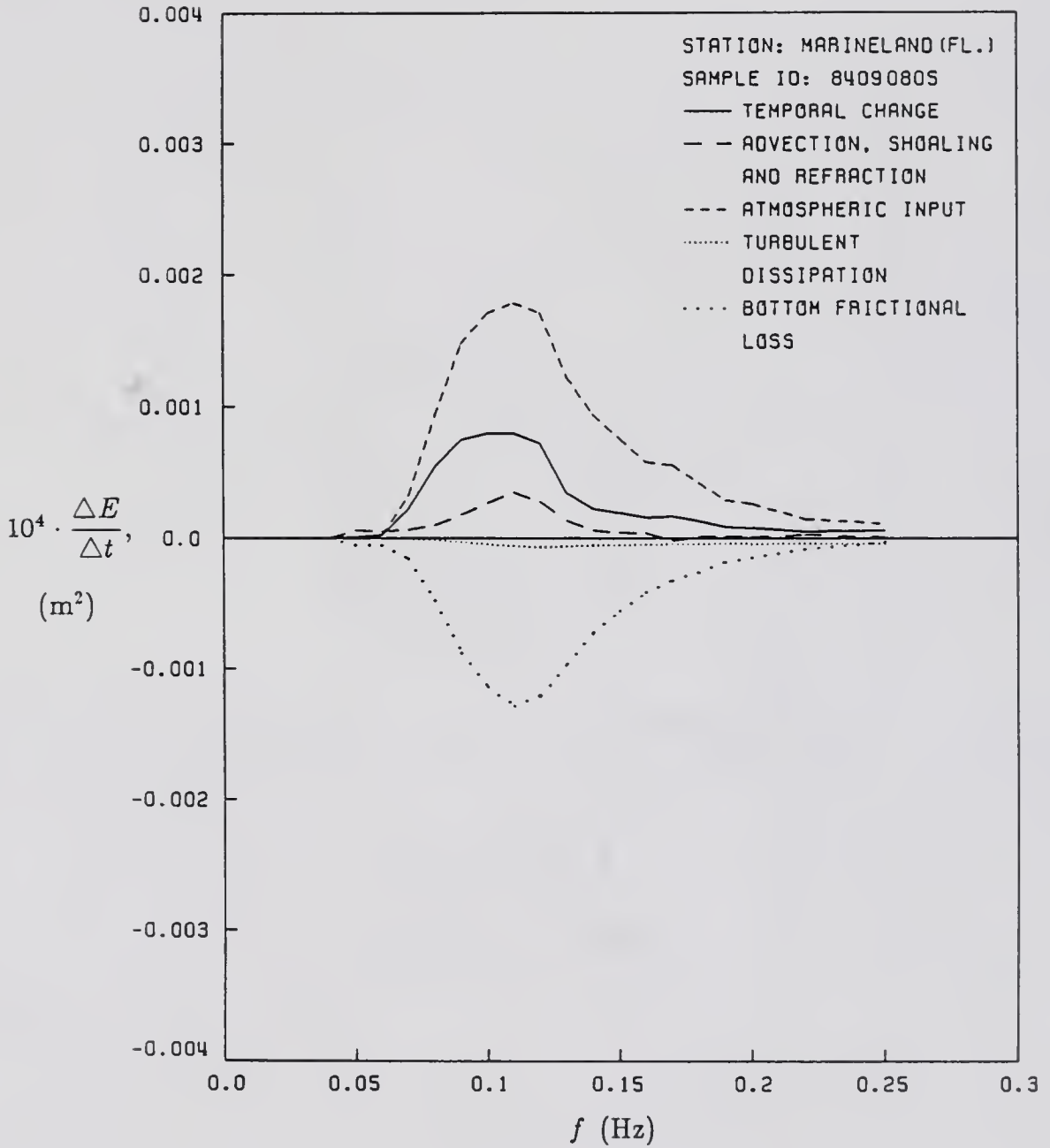


Figure 4.19: (d) Plot of individual shallow water effect sources for  $c_f=0.02$

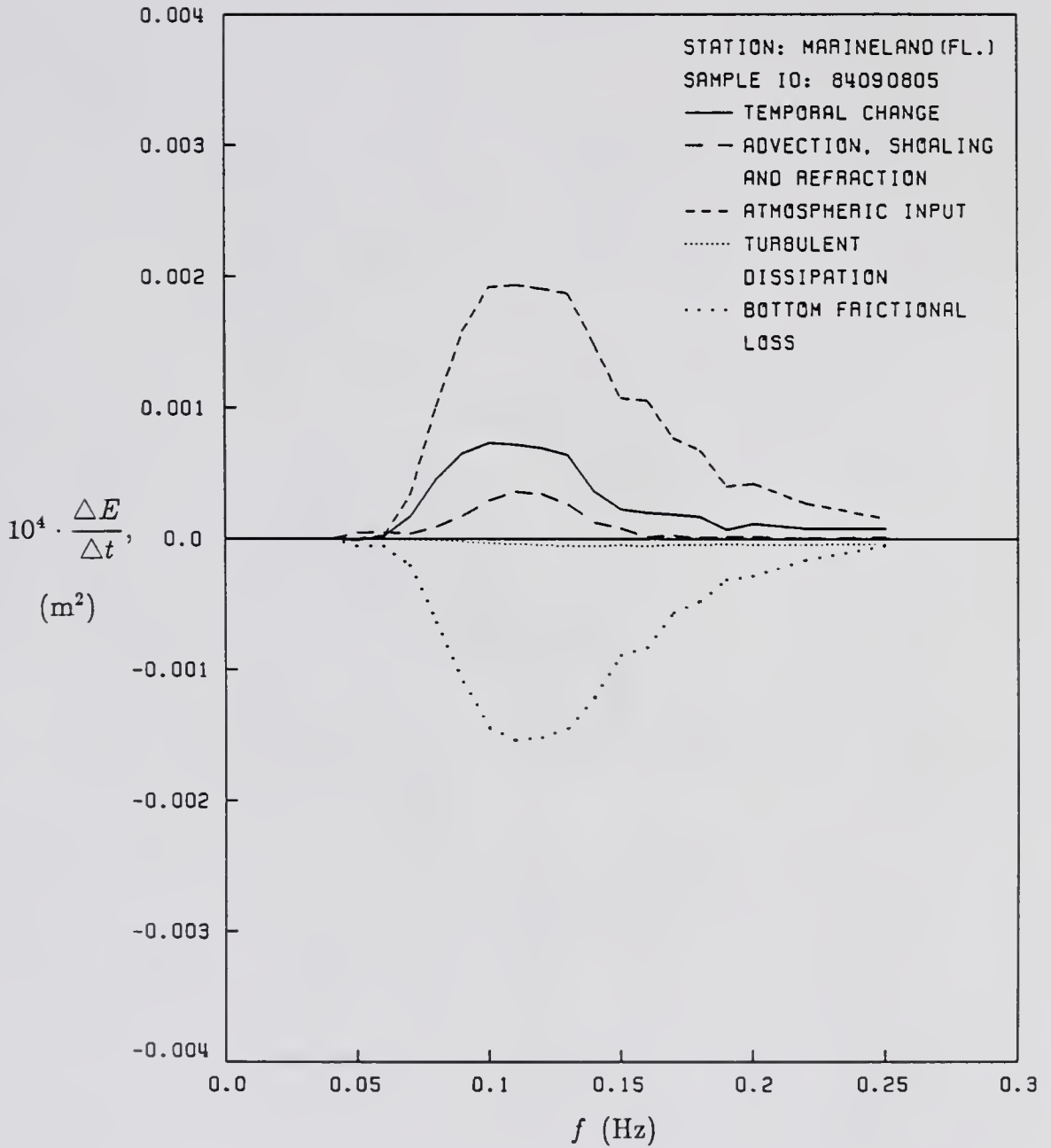


Figure 4.19: (e) Plot of individual shallow water effect sources for  $c_f=0.04$

Table 4.6: Summary of energy flux budget for cases with  $c_f=0.0, 0.005, 0.01, 0.02,$  and  $0.04,$  respectively.

mechanism	$10^5 \Delta E / \Delta t \text{ (m}^2/\text{sec)}$				
	$c_f = 0$	$c_f = 0.005$	$c_f = 0.01$	$c_f = 0.02$	$c_f = 0.04$
advection, shoaling, and refraction	-1.59	0.00	0.89	1.79	2.02
atmospheric input	6.86	10.27	11.77	13.72	17.63
turbulent viscous loss	-1.25	-1.06	-0.90	-0.77	-0.70
bottom frictional loss	0.00	-4.66	-6.77	-9.15	-13.13
net (temporal change)	4.02	4.55	4.99	5.59	5.82

0.005, 0.01, 0.02, and 0.04 at 5:00 a.m. September 8, 1984. The bottom frictional dissipation increases from zero at no bottom friction situation in Fig. 4.19(a) to the greater frictional loss cases in Figs. 4.19(b), (c), (d), and (e). Table 4.6 shows the summary of energy flux budget for the five cases indicated in Fig. 4.19. In stronger bottom friction case which corresponds to higher  $c_f$  value, more energy flux components associated with wind input are seen to shift to the high frequency region. This is because in the stronger friction case more energies are dissipated in the low frequency region than in the high frequency region.

## CHAPTER 5 CONCLUSIONS

### 5.1 Summary

This study examines wave models in hindcasting waves in an area of the Atlantic Ocean covering the southeastern coast of the United States. For wave models, the input required is the wind information over the sea surface. The numerical methods employed in wave models are based upon the energy balance equation which states that the total difference of wave energy is equal to the summation of the energy fluxes due to wave growth, dissipation, and wave-wave interaction. Wave models in general consist of a deepwater model and a shallow water model. The shallow water model includes the influences from the shallow water effects, such as refraction, shoaling, percolation, bottom friction, etc., which are excluded in the deepwater model.

In deep water, the growth of waves, as a result of atmospheric input, is a highly nonlinear process. The growth rate associated with this mechanism is usually estimated in deepwater model from two contributions: (i) the growth of prevailing waves, which is taken to be proportional to the third power of an energy scale parameter,  $\alpha$ , and (ii) the growth of local wind waves, which is taken to be linearly proportional to  $\alpha$ . The dissipation of waves is mainly from wave breakings which generates turbulence induced in wave motion. This dissipation mechanism is generally considered in the model by maintaining an  $f^{-5}$  law on the down-slope face of spectrum. The advection is often transacted in the model by using a free propagation algorithm. Thus, wave energies between directional and frequency bands are not coupled.

In shallow water, the refraction, shoaling, percolation, and bottom friction become important in the wave energy transport process. Wave paths are no longer independent on water depth. Wave rays are traditionally determined in the shallow wave model from the equation of nondivergence of wave number vectors in the horizontal plane. Shoaling and refraction are taken into account in the model by redistributing wave energies among the neighbouring wave rays according to the wave balance equation. There is no coupling of wave energies among individual frequency bands. The percolation and bottom friction effects are considered as sink terms in the model. The spectral growth rate due to wind input in the model commonly follows a combined Phillips' and Miles' growth mechanism, which says that the growth rate is a linear function of wave spectrum.

Two previously developed deepwater wave hindcasting models, the discrete model by Wave Information Study (WIS) group (Resio and Tracy, 1983) and the parametric model by Hasselmann et al.(1973), are reviewed. It is demonstrated in the present study that in fetch-limited cases the two models generally consistent in predicting wave heights and modal periods for small fetch (less than 400 km), and the parametric model predicts much higher wave heights and modal periods than the WIS model for large feth (greater than 400 km). In duration-limited cases the two models are consistent in predicting the significant wave heights only when the duration is less than 20 hours. The parametric model predicts again much higher wave heights and modal periods than the WIS model.

The new deepwater model developed here is of discrete type and is based on WIS model with modified growth and dissipation terms. The wave growth rate due to atmospheric input is again estimated in the model for the growths of prevailing waves and local wind waves. The growth rate of prevailing waves are based upon the modified JONSWAP spectrum defined by Donelan et al.(1985) and it is proportional to  $\alpha^3$  which reflects the nonlinear nature in accounting for the wave-wave interaction.

The growth of local wind waves is, however, taken to be one of the three cases: (a) if the shift of wind direction from the previous time step is quite large, new fresh wind waves will be generated, (b) if the shift of wind direction from the previous time step is small but not null, wind waves generated from the previous time step will continue to grow in the direction of the wind, and (c) if the shift of wind direction is small from the previous time step and the wind direction is the same as the prevailing wave direction, this source term will vanish. In the first case the generation of new waves is based on the spectral form of P-M spectrum and is proportional to  $\alpha$  which, therefore, reflects a linear growth process. In the second case the growth of wind waves is treated as a minor nonlinear process which is proportional to  $\alpha^3$ . In the last case the growth of wind waves follows the same mechanism as the growth of prevailing waves. The turbulent dissipation is estimated in the model according to the algorithm proposed by Hasselmann (1974). The dissipation rate is expressed as the product of the spectrum, a wave frequency, and a proportional constant. The proportional constant is calibrated by means of field ocean wave spectral data.

The test of the new deepwater model is performed in both hypothetical and real cases. In the hypothetical cases, the new model is tested against the WIS model, the SMB model and the parametric model. In fetch-limited cases the significant wave heights obtained from the model agree well with those obtained from the WIS model at small winds (20 and 30 knots), and they agree well with those obtained from the SMB model at moderate wind speeds (40 knots); they are higher than those obtained from the other three models at high wind speeds (50 knots) when fetch is less than 400 km. The modal periods obtained from the new model are consistent with those obtained from the SMB model at low wind speeds (20 and 30 knots). At higher wind speed, the modal periods obtained from the new model are much higher than the other three models.

In the hypothetical duration-limited cases the significant wave heights obtained from the new model agree well to those obtained from the SMB model when duration is less than 20 hrs. For duration greater than 20 hrs, the significant heights computed from the new model are not much different from those computed from the WIS model except at 40 knots winds where wave heights obtained from the WIS model has a non-realistic damping pattern. The wave heights obtained from the new model are much smaller than those obtained from the SMB and parametric models for duration greater than 20 hrs. The model periods computed from the new model are not much different from those computed from the SMB model at small and moderate wind speeds (20, 30, and 40 knots); they are, however, much smaller than those obtained from the parametric model when duration is greater than 20 hrs.

In the real cases, the new deepwater model is compared with measured waves. The wave heights computed from the model are highly correlated to those measured by NOAA maintained buoys. The modal periods computed from the model are not well correlated to the measured ones. However, the computed modal periods are found to be more in accord with the measured data for large waves. Swells not be properly traced in the model.

The shallow water model developed in this study follows Chen and Wang's (1983) model with modified generation term. The refraction and shoaling are evaluated with the advection term in the energy balance equation. Percolation and bottom friction are included in the model by using the formulas derived by Shemdin et al.(1978) and Collins (1972), respectively. The turbulent dissipation is estimated in the model the same as in the deepwater model. The spectral growth rate due to wind input is estimated by using the same functional form for local wave generations in the deepwater case; it depends not only on the strength of the current wind strength but also on the current wave condition.

## 5.2 Conclusions

A coupled discrete spectral model, named here as the Unified Coastal Wave Prediction (UCWP) model, has been developed using surface pressure information as input to predict wind waves in both deep and shallow water regions. The model has been applied to hindcasting wind waves along the east coast of Florida and it performed well for both low- and high-pressure weather systems. The significant wave heights and directions of wave propagation are highly correlated to the measured data. The results of modal period prediction are good only for high wind waves but poor for low wave conditions.

The fundamental processes employed in the UCWP model are similar to those used by other widely-accepted discrete and parametric models. New source and sink terms are proposed on the basis of field evidence.

Several conclusions relating to this research are summarized in the following paragraphs.

(1) Plots of spectral peak energy versus spectral peak frequency in the wave growth cases show that the data are very scattered in the equilibrium range indicated by the P-M spectrum. Although the data scattering could be exaggerated by the presence of swell, which generally appears as long waves, there is no indication that a simple curve, such as the P-M equilibrium spectrum, can represent the relationship. The scattering of the data suggests active nonlinear wave-wave interactions. That is, energy transfer from higher frequency components to lower frequency components is a nonlinear process which is dependent upon multi-variables including wind speed, wave phase speed, peak energy frequency, etc. The nonlinear energy transfer can be even stronger as indicated by the plots of nonlinear transfer coefficient  $a_{nl}$  versus  $f_0/f_m^2 \Delta t$  which show that  $a_{nl}$  is more likely a function of  $f_0/f_m^2 \Delta t$  than a constant value suggested by Hasselmann (1976) and used in the WIS deepwater model.

(2) In the growth of prevailing wave components, energy transfers due to atmospheric input and wave-wave interactions are both highly nonlinear and of similar nature. Thus, they can be treated as one growth term. It also implies that the energy transfer process is mainly governed by the components receiving the energy irrespective of energy source forms. The scale parameter,  $\alpha$ , which controls the nonlinear growth rate is approximated by a power function of  $f_{ms}/f_0$ . A power of 7/6 is selected based on data, instead of the value of 2/3 as suggested by Hasselmann et al.(1976). This results in a much stronger growth under severe weather.

(3) The 'overshoot' phenomenon, which indicates waves with slightly higher height than the saturation height occur before reaching a fully-developed condition, is observed in the test of the UCWP deepwater model in the duration-limited case. The phenomenon is in general quite weak as revealed by the data but essential in building enough energy to reach the later saturation condition. It is not found in fetch-limited case, and it is neither observed in the WIS model nor in the SMB and parametric models.

(4) Based upon wave data obtained from the UCWP deepwater model, both significant wave height and modal period can be approximated by power functions of wind speed at infinite fetch and duration. The significant height is found to be proportional to wind speed with the power equal to 5/3 and the modal period is found to be proportional to wind speed with the power equal to 1/3. These two empirical equations were then combined to yield a fully-developed condition and compared with the field wave data. The comparison shows that the combined empirical relation agrees well to these measured data at high wave condition. The fully-developed condition given by the classical SMB model is also plotted against the same field data set. It is shown that the fully-developed relation between wind and wave obtained from the classical SMB model is less consistent with the measured data than the one obtained from the UCWP deepwater model.

(5) Dissipation of wave energy due to turbulence included in the UCWP model follows Hasselmann's formula which is proportional to the product of a wave spectrum and wave frequency. Its contribution to the total energy flux is found to be important compared with the advection and wind input terms in the deepwater spectral transformation process. However, it is generally of a small order of magnitude compared with the advection, shoaling, refraction, and bottom friction terms in the shallow water spectral transformation process.

(6) In shallow water, bottom friction always plays an important role. It consumes much of the wind energy input for the cases tested along the Florida coast. Long swell components are severely curtailed when propagating from deep to shallow water. The waves in shallow water could be highly nonstationary and this is particularly the case under high winds. Hence, the validity of ray method which can only be applied to stationary cases is doubtful for high wind waves.

(7) Test of response of the UCWP shallow water model to different values of bottom friction coefficient,  $c_f$ , shows some interesting results. By using different  $c_f$  values in the UCWP model, the wave heights can change significantly for large wave condition but insignificantly for small wave condition. The modal periods may change dramatically for small but long waves since the bottom frictional dissipation is more active in low frequency components than in high frequency components. The change of modal period for high wave condition according to various  $c_f$  values is in general small. The statistical analysis between the computed and measured wave heights based upon different  $c_f$  values shows that correlation coefficients are overall high and they do not differ significantly from one to the others although the one based on  $c_f=0.02$  gives the highest value. The correlations between the computed and measured modal periods are found between 0.3 and 0.38 for all the test cases; the one based on  $c_f=0.02$  again gives the highest value. The comparison of normalized root-mean-square error for different  $c_f$  values shows that errors calculated from

wave height and modal period, respectively, based upon  $c_f=0.02$  are smaller than the others. Therefore,  $c_f=0.02$  is chosen in the UCWP shallow water model for wave hindcast along the Florida coast.

### 5.3 Future Studies

Further studies related to this work are suggested as follows:

(1) Experiments producing deepwater waves in the ideal wind condition need to be conducted in a large scale physical model in order to establish a dependable data base for the use in calibration of numerical wave models.

(2) Wave-current interaction effect, which is definitely important in the presence of strong current in the wave field, should be included in the wave model.

(3) Performance of a deepwater wave model in the entire ocean basin is required so as to include the complete swell system and, therefore, to increase the ability in predicting the peak energy frequency as well as the significant wave height.

APPENDIX A  
SUMMARY OF PARAMETERIZED PROGNOSTIC EQUATIONS

A.1 Prognostic Equations

$$\frac{\partial b_i}{\partial t} + D_{ij} \frac{\partial b_i}{\partial \ell} = G_i, \quad i, j = 1, 2, 3, 4, 5 \quad (\text{A.1})$$

where  $b_1 = f_m$ ,  $b_2 = \alpha$ ,  $b_3 = \gamma$ ,  $b_4 = \sigma_a$ ,  $b_5 = \sigma_b$ ,  $\ell$  represents the horizontal axis along which waves propagate,  $D_{ij}$  denotes the matrix of generalized propagation velocity, and  $G_i$  denotes the vector of projected source function.

A.2 Elements of  $D_{ij}$  and  $G_i$

$$\begin{aligned} D_{11} &= v(1 + 5K), & D_{12} &= -v \frac{f_m}{\alpha} K, & D_{13} &= -v \frac{f_m}{\gamma} K, \\ D_{21} &= v \frac{\alpha}{f_m} (0.263 + 3.61K), & D_{22} &= v(0.605 - 0.722K), & D_{23} &= -v \frac{\alpha}{\gamma} 0.722K, \\ D_{31} &= -v \frac{\gamma}{f_m} (0.263 - 21.4K), & D_{32} &= v \frac{\gamma}{\alpha} (0.4 - 4.28K), & D_{33} &= v(1 - 4.278K), \\ \\ D_{41} &= -\frac{v}{f_m} \{5K(\sigma_a - 1) + \sigma_a + \frac{\sigma_a}{\ln \gamma} [8.2436\sigma_a + 0.1705 - K(164.87\sigma_a + 13.877)]\}, \\ D_{42} &= \frac{v}{\alpha} \{K(\sigma_a - 1) + \frac{\sigma_a}{\ln \gamma} [-K(2.7755 + 32.974\sigma_a) + 1.6487\sigma_a + 0.25644]\}, \\ D_{43} &= \frac{v}{\gamma} \{K(\sigma_a - 1) + \frac{\sigma_a}{\ln \gamma} [\sigma_a - K(32.974\sigma_a + 2.7755)]\}, \\ D_{51} &= -\frac{v}{f_m} \{5K(\sigma_b + 1) + \sigma_b - \frac{\sigma_b}{\ln \gamma} [8.2436\sigma_b - 0.1705 - K(164.87\sigma_b - 13.877)]\}, \\ D_{52} &= \frac{v}{\alpha} \{K(\sigma_b + 1) - \frac{\sigma_b}{\ln \gamma} [K(2.7755 - 32.974\sigma_b) + 1.6487\sigma_b - 0.25644]\}, \\ D_{53} &= \frac{v}{\gamma} \{K(\sigma_b + 1) - \frac{\sigma_b}{\ln \gamma} [\sigma_b - K(32.974\sigma_b - 2.7755)]\} \end{aligned} \quad (\text{A.2})$$

where  $v = g/4\pi f_m$ ,  $K = \sigma^2/(20\sigma^2 + \ln \gamma)$ , and  $\sigma = (\sigma_a + \sigma_b)/2$ .

$$G_1 = \begin{cases} -0.586 \alpha^2 f_m^2 \frac{\gamma - 1}{2.3}, & \text{if } \xi > 0.13, \\ 0, & \text{otherwise,} \end{cases} \quad (\text{A.3})$$

$$G_2 = (0.005022 \xi^{4/3} - 5 \alpha^2) \alpha f_m, \quad (\text{A.4})$$

$$G_3 = 16(\gamma_o - \gamma) \alpha^2 f_m, \quad (\text{A.5})$$

$$G_4 = [25.5(0.07\chi - \sigma_a) - 0.5(\sigma_b - 0.09\chi)] \alpha^2 f_m, \quad (\text{A.6})$$

$$G_5 = [25.5(0.09\chi - \sigma_b) - 0.5(\sigma_a - 0.07\chi)] \alpha^2 f_m, \quad (\text{A.7})$$

where

$$\xi = \frac{f_m U_{10}}{g}, \quad \chi = \left( \frac{4}{\gamma + 0.7} \right)^2 \quad (\text{A.8})$$

and

$$\gamma_o = \begin{cases} 3.3, & \text{if } \xi \geq 0.13, \\ 1 + 2.3 \frac{\xi - 0.13}{0.03}, & \text{if } 0.16 > \xi > 0.13, \\ 1, & \text{if } 0.13 \geq \xi \end{cases} \quad (\text{A.9})$$

APPENDIX B  
PROCEDURE IN SOLVING PARAMETERIZED  $G_{in,1}(f)$

$$G_{in,1}(f_n) = \frac{\alpha^3 g^2}{(2\pi)^4 f_n^3 f_m} \gamma^\beta \exp[-(\frac{f_m}{f_n})^4] \quad (B.1)$$

where

$$\beta = \exp[-\frac{1}{2}(\frac{f_n - f_m}{\sigma_{ab} f_m})^2],$$

$$\sigma_{ab} = \begin{cases} \sigma_a, & \text{for } f_n < f_m, \\ \sigma_b, & \text{for } f_n \geq f_m, \end{cases} \quad n = 1, 2, \dots, n_m, \dots, N$$

$n_m$  = index of frequency at maximum  $E(f_n)$ ,

$f_m$  = frequency at maximum  $E(f_n)$ ,

$N$  = total number of frequency bands

The parameters are determined by minimizing the root-mean-square error

$$\epsilon_{rms} = \sqrt{\frac{\sum_{n=1}^N [G_{in,1}(f_n) - G(f_n)]^2}{\sum_{n=1}^N G(f_n)}} \quad (B.2)$$

where

$$G(f_n) = \Delta E(f_n) / \Delta t$$

is obtained based on measured wave spectra. Taking the derivatives of  $\epsilon_{rms}$  with respect to  $\alpha$ ,  $\gamma$ ,  $\sigma_a$ ,  $\sigma_b$  and equating them to zero, four equations can be obtained and expressed as follows:

$$\alpha^3 \sum_{n=1}^N \frac{g^2 \gamma^{2\beta}}{(2\pi)^4 f_n^6 f_m} \exp[-2(\frac{f_m}{f_n})^4] = \sum_{n=1}^N E(f_n) \frac{\gamma^\beta}{f_n^3} \exp[-(\frac{f_m}{f_n})^4] \quad (B.3)$$

$$\alpha^3 \sum_{n=1}^N \frac{g^2 \beta \gamma^{2\beta-1}}{(2\pi)^4 f_n^6 f_m} \exp[-2(\frac{f_m}{f_n})^4] = \sum_{n=1}^N E(f_n) \frac{\beta \gamma^{\beta-1}}{f_n^3} \exp[-(\frac{f_m}{f_n})^4] \quad (\text{B.4})$$

$$\begin{aligned} \alpha^3 \sum_{n=1}^{n_m} \frac{g^2 \beta_a \gamma^{2\beta_a}}{(2\pi)^4 f_n^6 f_m} (f_n - f_m)^2 \exp[-2(\frac{f_m}{f_n})^4] \\ = \sum_{n=1}^{n_m} E(f_n) \frac{\beta_a \gamma^{\beta_a}}{f_n^3} (f_n - f_m)^2 \exp[-(\frac{f_m}{f_n})^4] \end{aligned} \quad (\text{B.5})$$

$$\begin{aligned} \alpha^3 \sum_{n=n_m}^N \frac{g^2 \beta_b \gamma^{2\beta_b}}{(2\pi)^4 f_n^6 f_m} (f_n - f_m)^2 \exp[-2(\frac{f_m}{f_n})^4] \\ = \sum_{n=n_m}^N E(f_n) \frac{\beta_b \gamma^{\beta_b}}{f_n^3} (f_n - f_m)^2 \exp[-(\frac{f_m}{f_n})^4] \end{aligned} \quad (\text{B.6})$$

where  $\beta_a$  and  $\beta_b$  are corresponding to  $\sigma_a$  and  $\sigma_b$ , respectively.

In order to solve these non-linear equations, a numerical iteration procedure is utilized. The spectral peak is previously known and provided by the actual spectrum. Thus,

$$\gamma = \frac{(2\pi)^4 f_m^4}{\alpha^3 g^2} e^1 E(f_m) \quad (\text{B.7})$$

To start the numerical iteration, initial conditions are assigned, by experience, as

$$\alpha = 0.01, \quad 0.01 \leq \sigma_a \leq 4, \quad 0.01 \leq \sigma_b \leq 4 \quad (\text{B.8})$$

The initial value  $\gamma$  is evaluated by Eq.(B.7). Then,  $\sigma_a$  and  $\sigma_b$  are calculated from Eqs.(B.5) and (B.6), respectively, utilizing the Bisection method. The Bisection method is a procedure which is used to approximate a root of the function  $F(x)$  in a known interval. Suppose that  $F(x)$  has a unique root between  $x_1$  and  $x_2$ , there must exist the relationship  $F(x_1)F(x_2) < 0$ . Let  $x_o = (x_1+x_2)/2$ ; if  $F(x_1)F(x_o) < 0$ , there must be a root between  $x_1$  and  $x_o$ . Otherwise, if  $F(x_1)F(x_o) > 0$ , there must be a root between  $x_2$  and  $x_o$ . Thus, one may reiterate the procedure until the resulting root converges in a satisfactorily small interval.

By using  $\sigma_a$  and  $\sigma_b$  solved from the Bisection method, two solutions of  $\alpha$  can be obtained from Eqs.(B.3) and (B.4), respectively. Taking the average of the two

values of  $\alpha$  and replacing this average value into Eq.(B.7), one may evaluate a new  $\gamma$ . Therefore, one may reiterate the entire procedure until an acceptable closure error is obtained.

APPENDIX C  
SUMMARY OF COMPUTED AND MEASURED NON-DIRECTIONAL  
FREQUENCY SPECTRA AT THE BUOY #41006 LOCATION

C.1 Introduction

The wave spectra that summarized here include the one-dimensional frequency spectra computed by the UCWP deepwater sub-model and these measured from the field at the NOAA buoy #41006 location in January, September, and October 1984. Both the computed and measured spectra are presented by graphs. They are managed in a single figure if occur at the same time. The eight-digit number shown in each figure indicates the time when spectra occurred, and corresponds to the year, month, day, and hour, each represented by two digits, respectively. The further informations shown in each figure are the significant wave heights and modal periods corresponding to the computed and measured spectra, respectively.

C.2 Summary of Figures

The one-dimensional frequency spectra, which are computed and measured during the period of January, September, and October 1984, are summarized in the following pages.

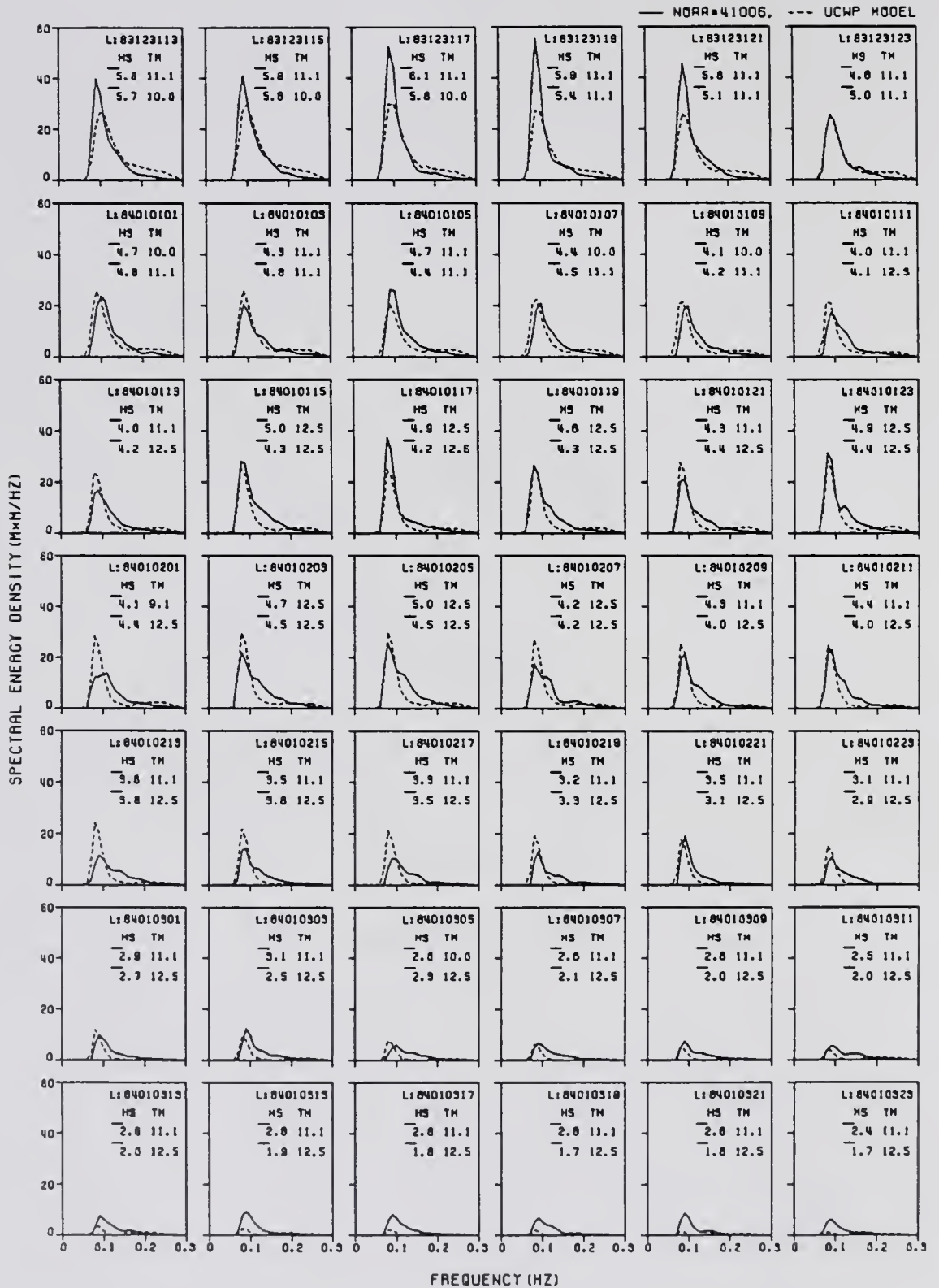


Figure C.1: Summary of computed and measured frequency spectra.

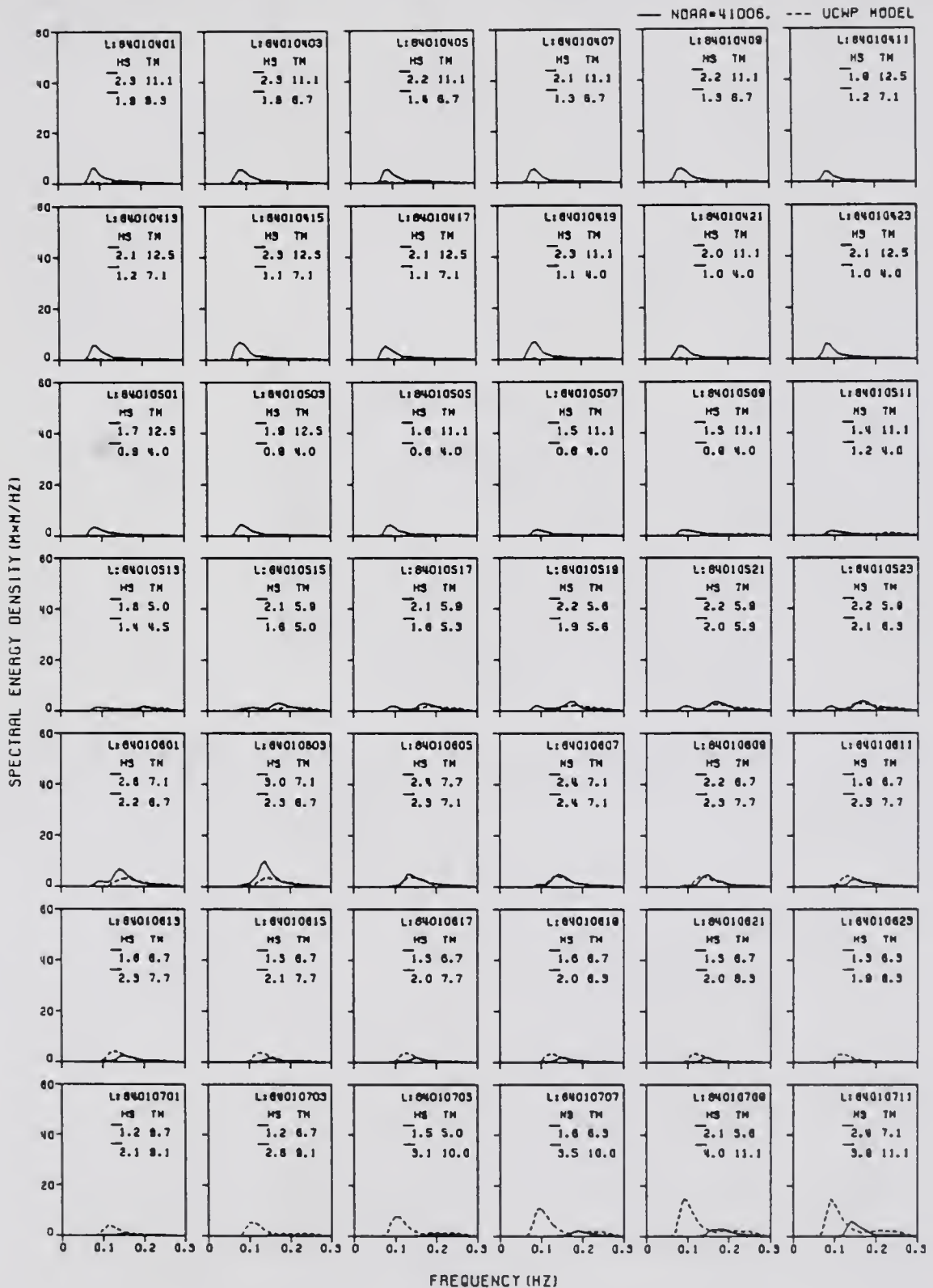


Figure C.1: Summary of computed and measured frequency spectra(continue).

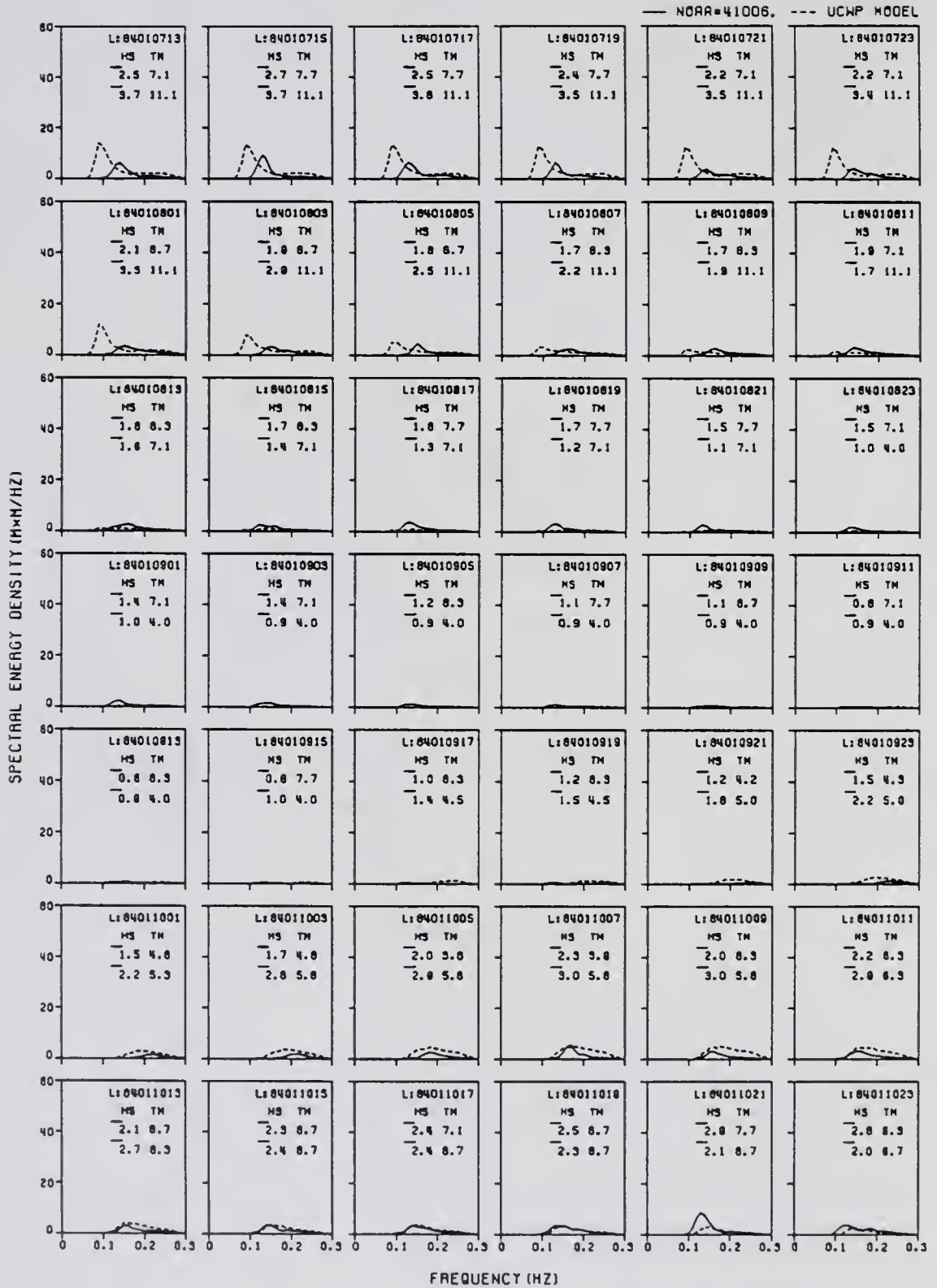


Figure C.1: Summary of computed and measured frequency spectra(continue).

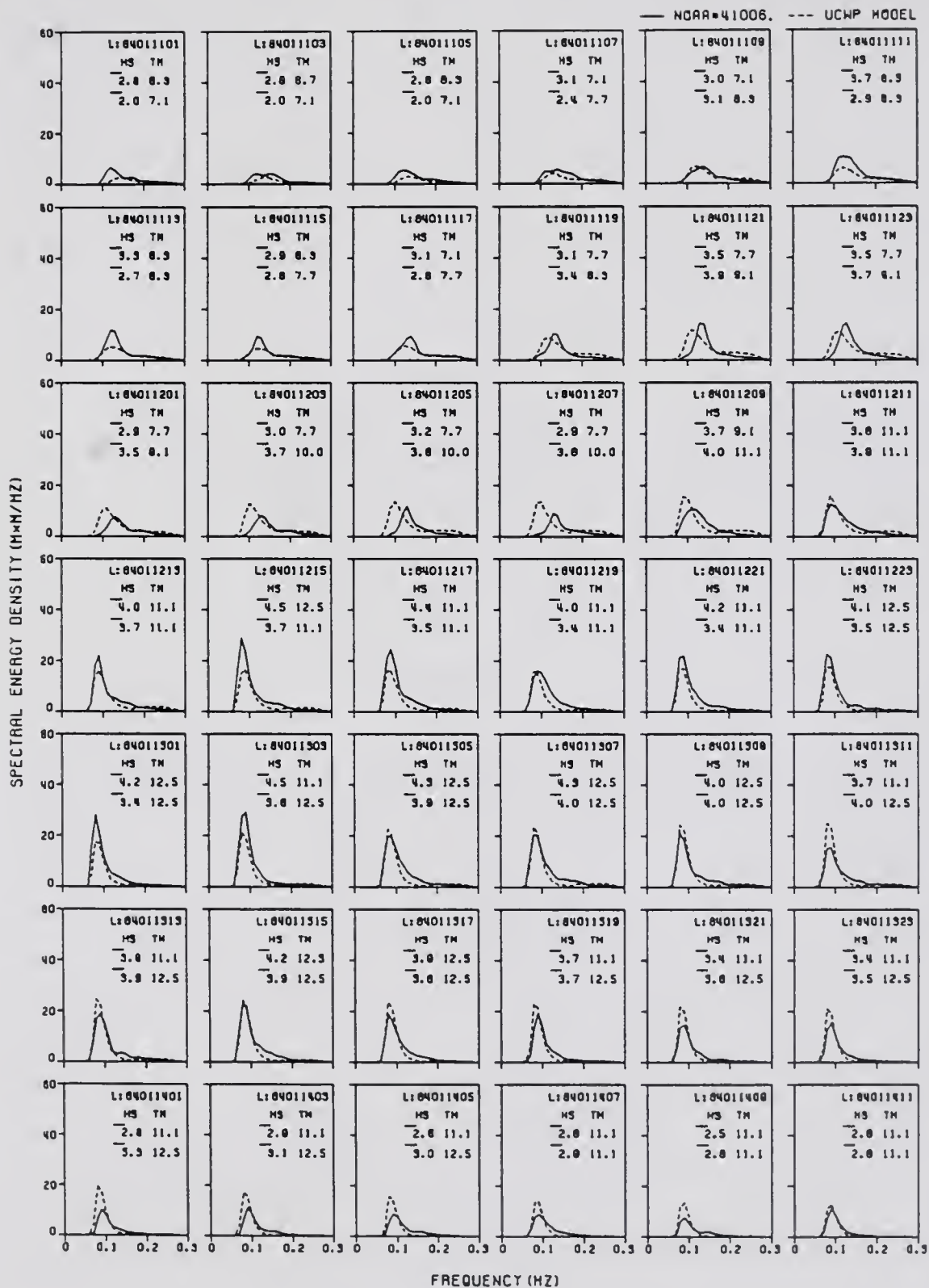


Figure C.1: Summary of computed and measured frequency spectra(continue).

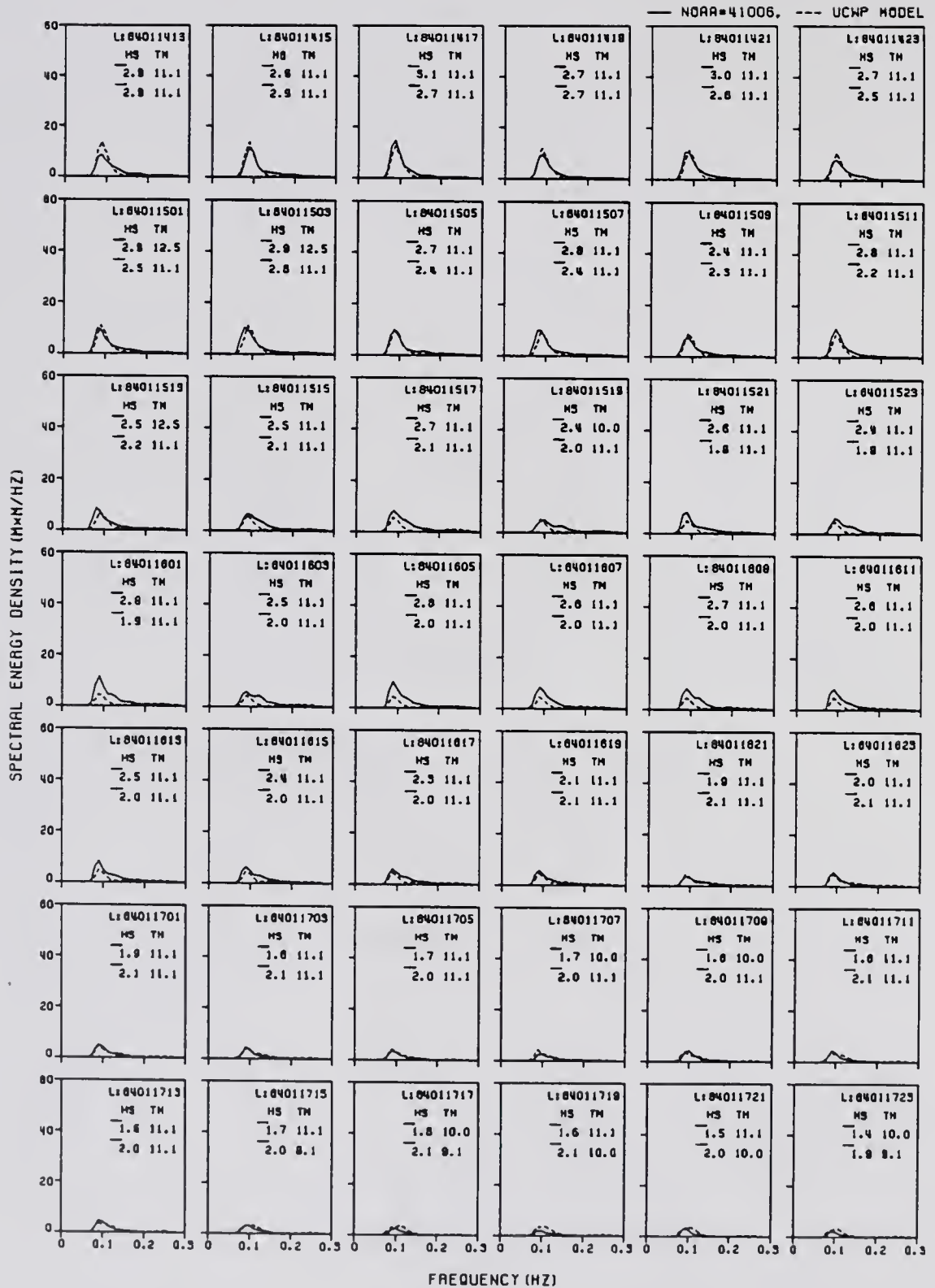


Figure C.1: Summary of computed and measured frequency spectra(continue).

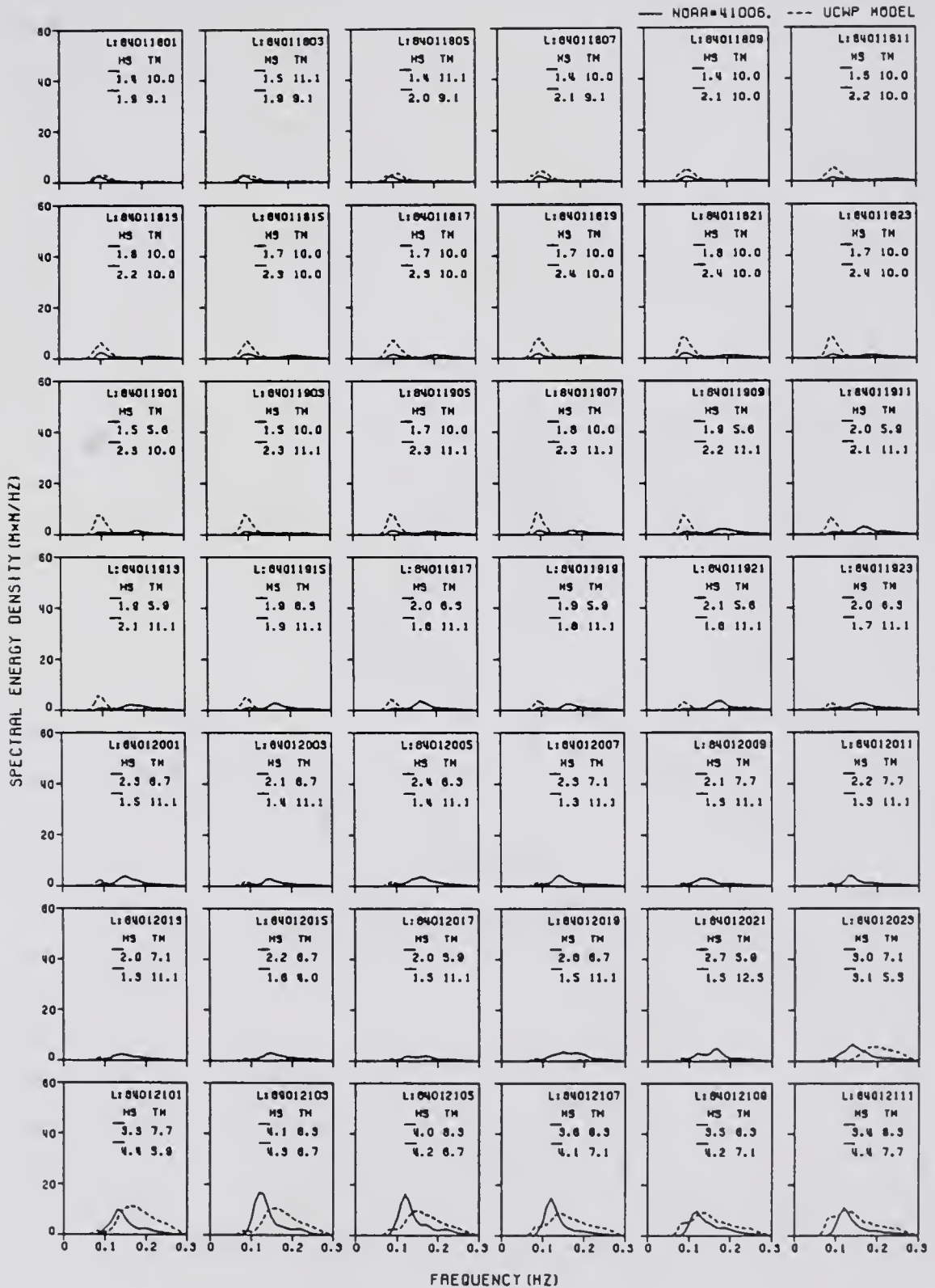


Figure C.1: Summary of computed and measured frequency spectra(continue).

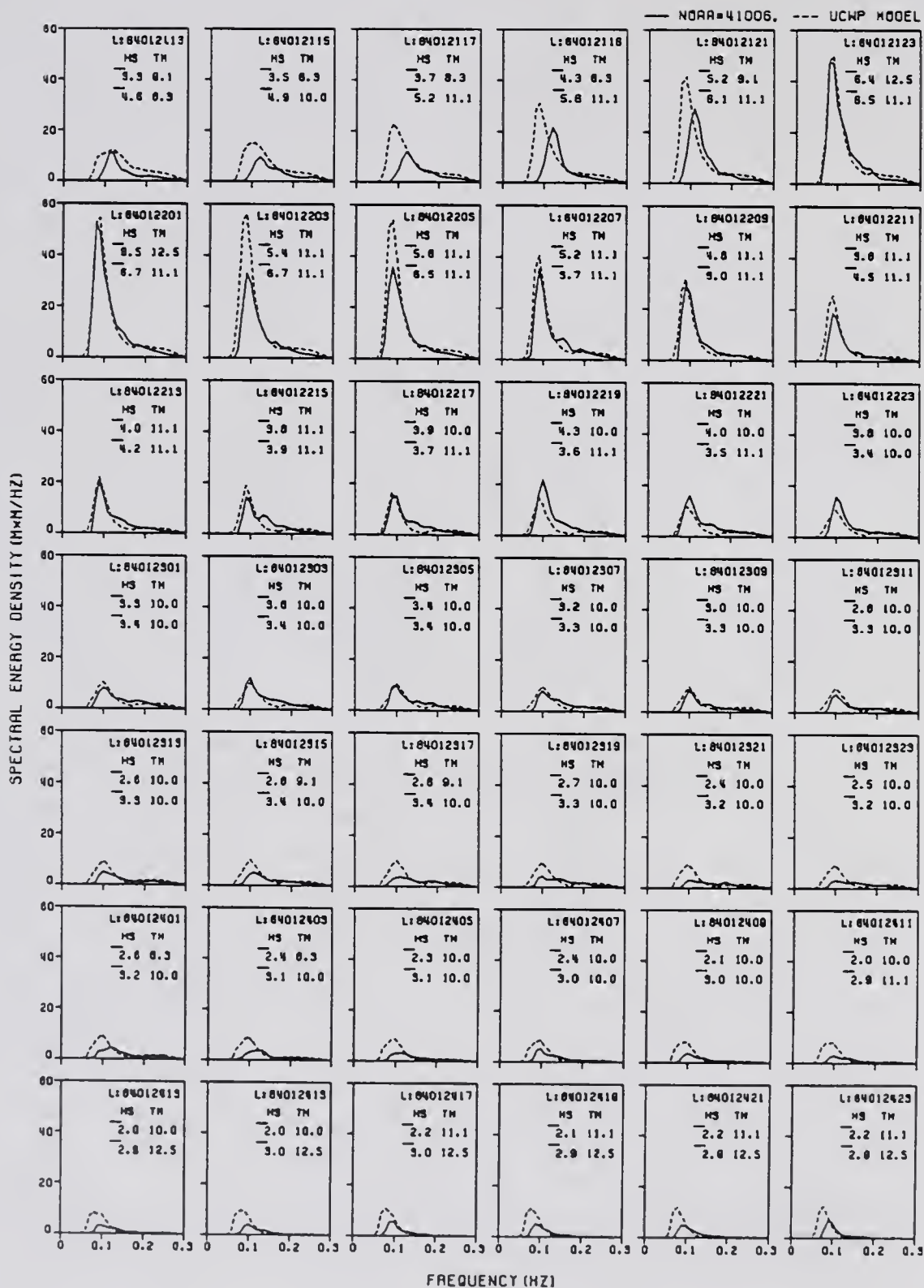


Figure C.1: Summary of computed and measured frequency spectra(continue).

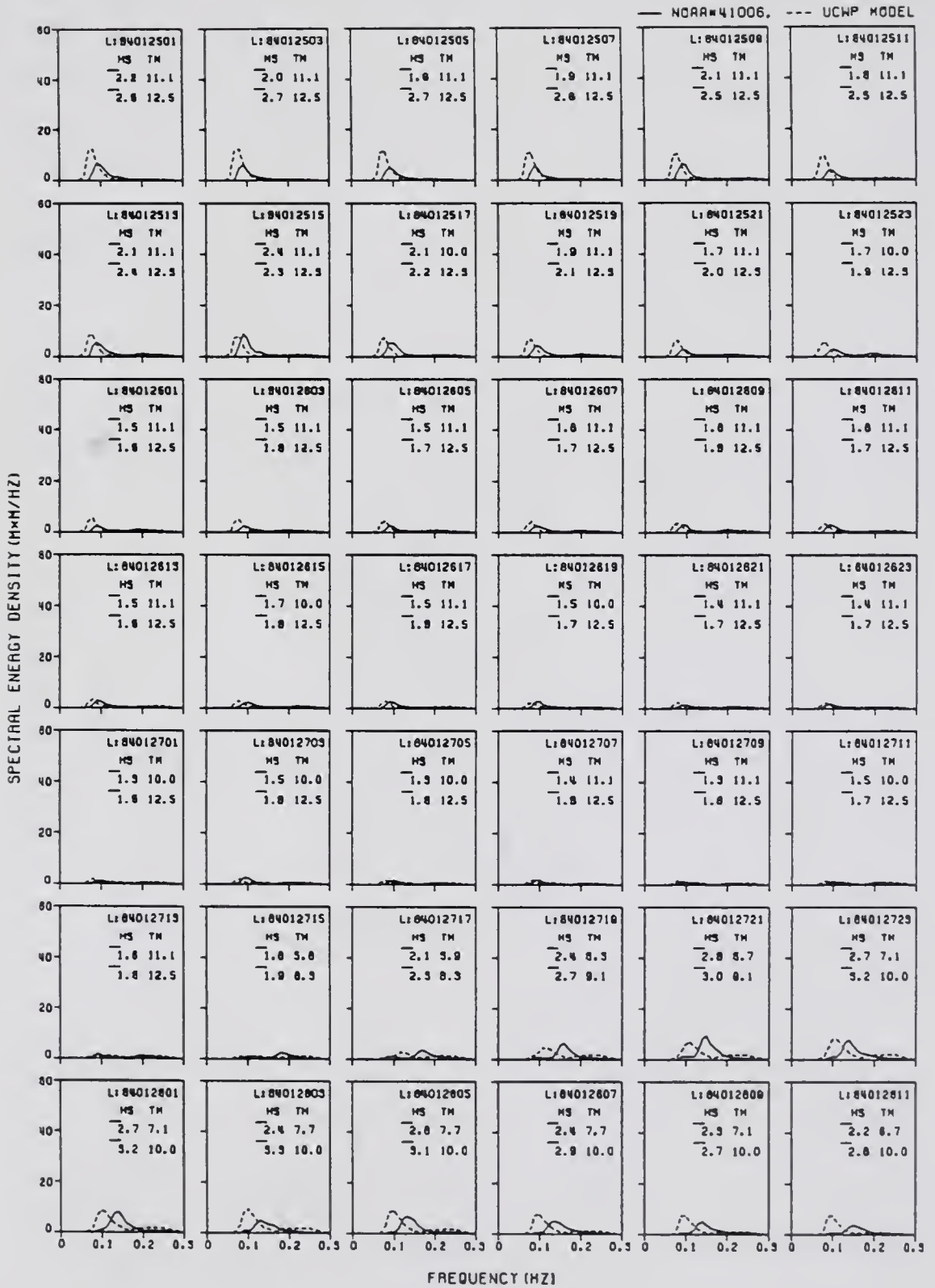


Figure C.1: Summary of computed and measured frequency spectra(continue).

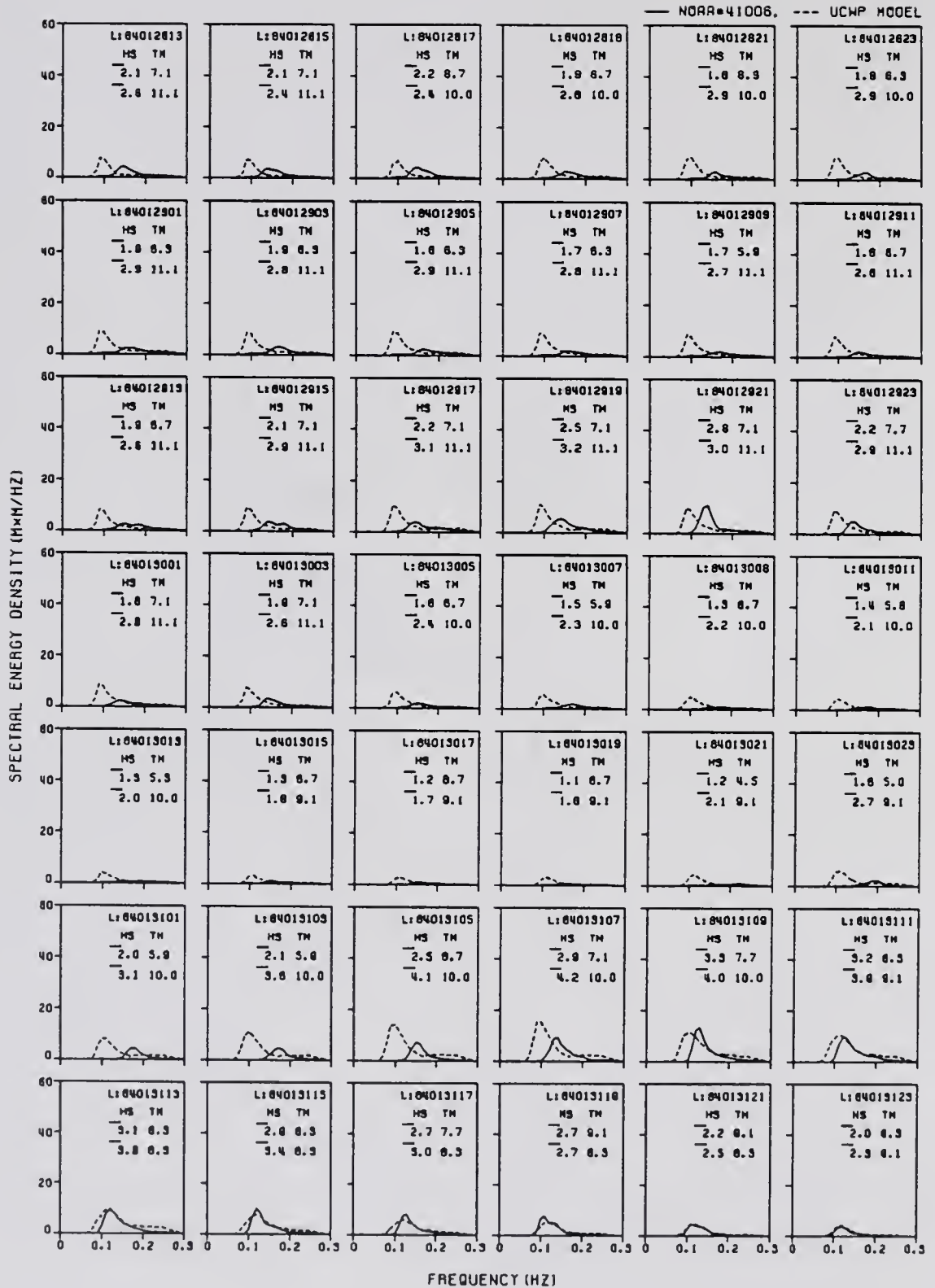


Figure C.1: Summary of computed and measured frequency spectra(continue).

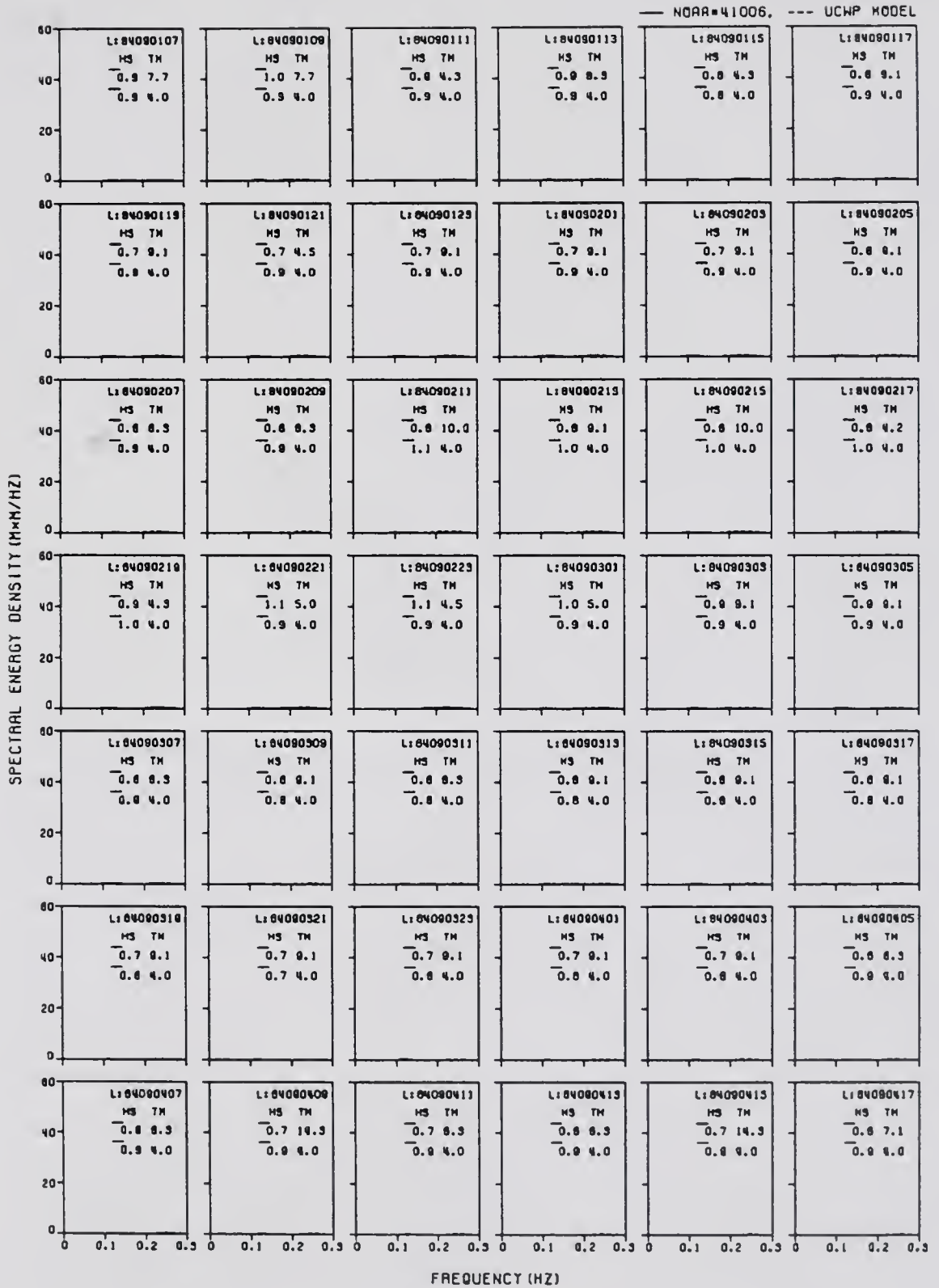


Figure C.1: Summary of computed and measured frequency spectra(continue).

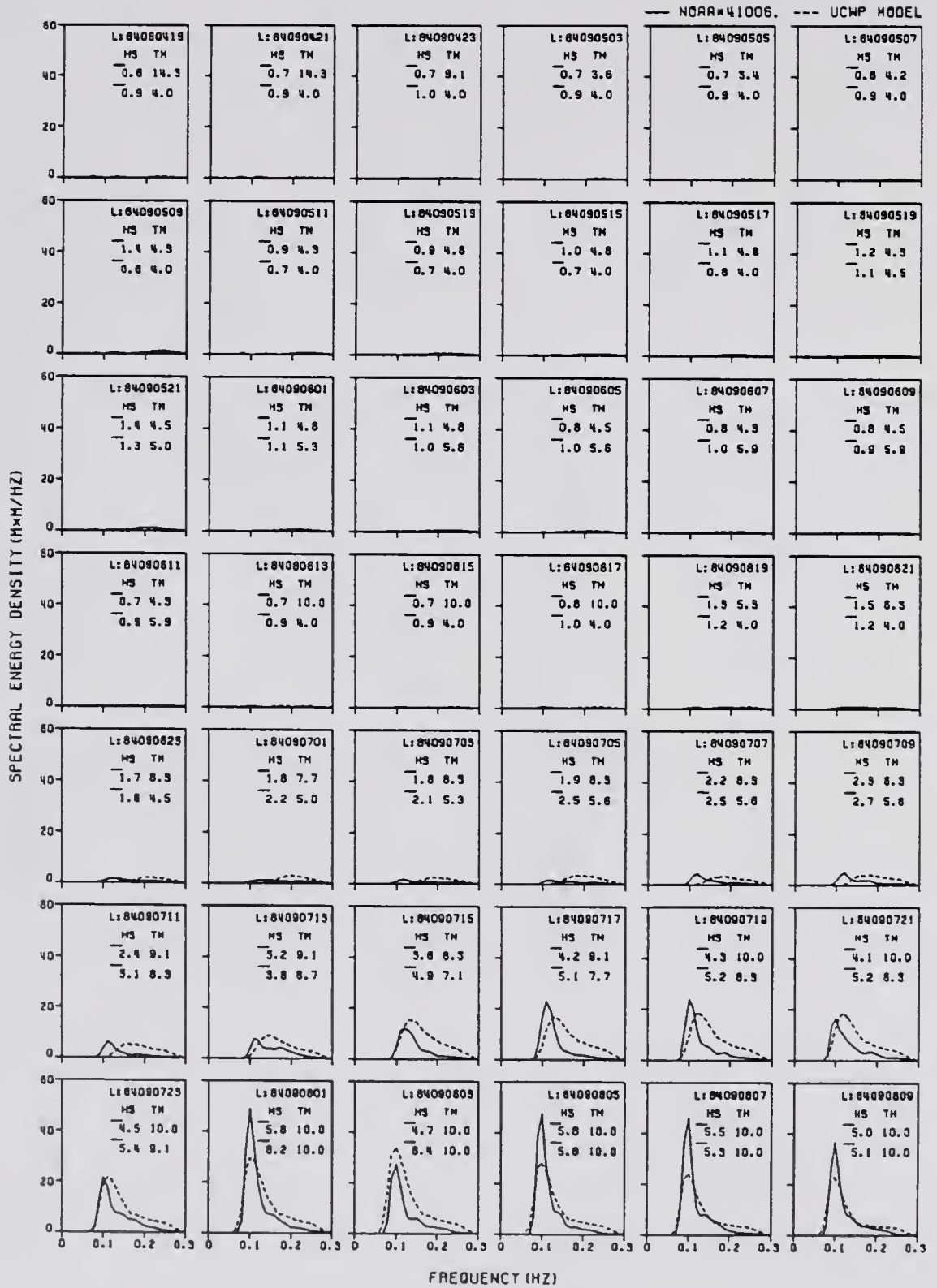


Figure C.1: Summary of computed and measured frequency spectra(continue).

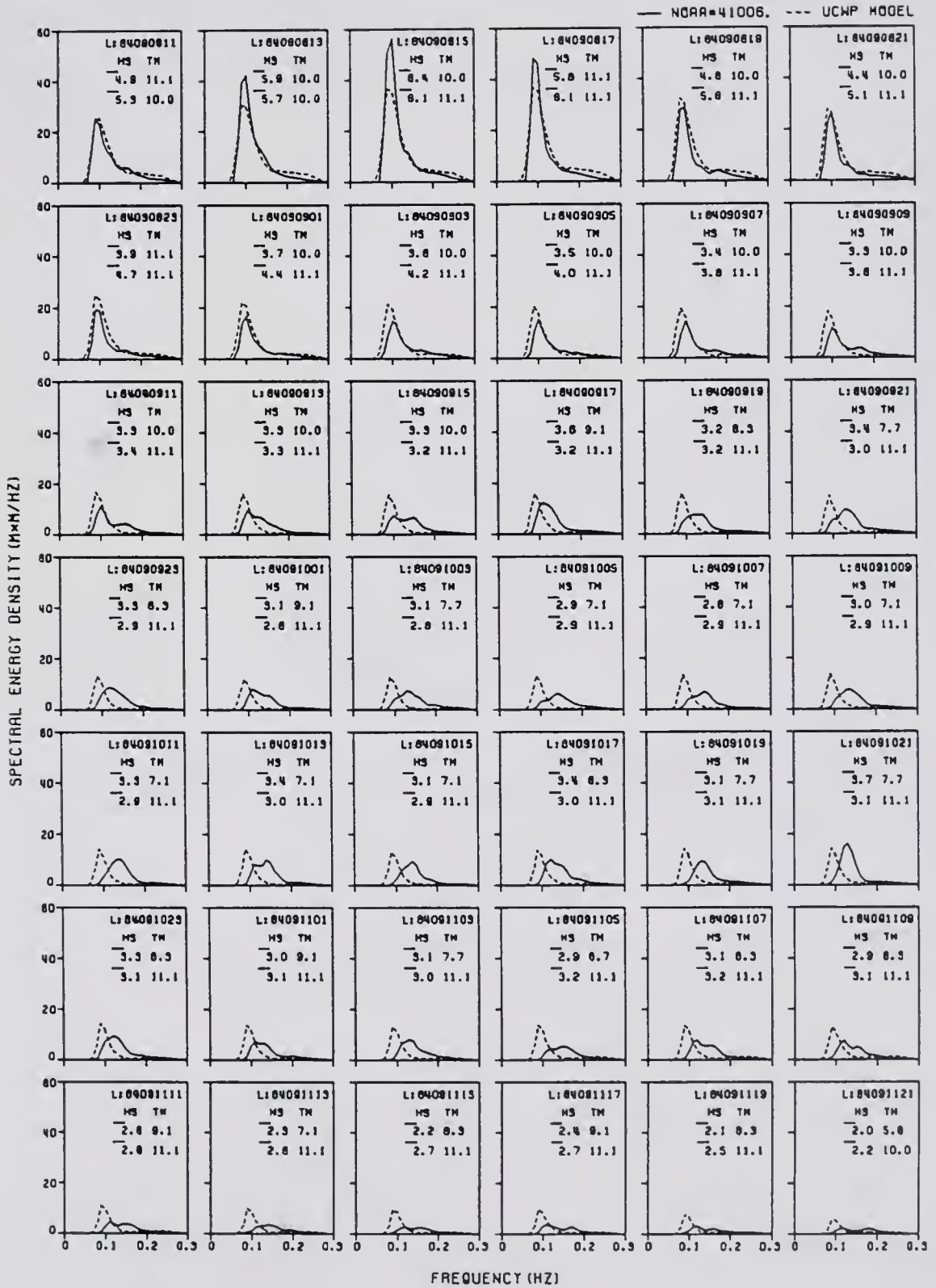


Figure C.1: Summary of computed and measured frequency spectra(continue).

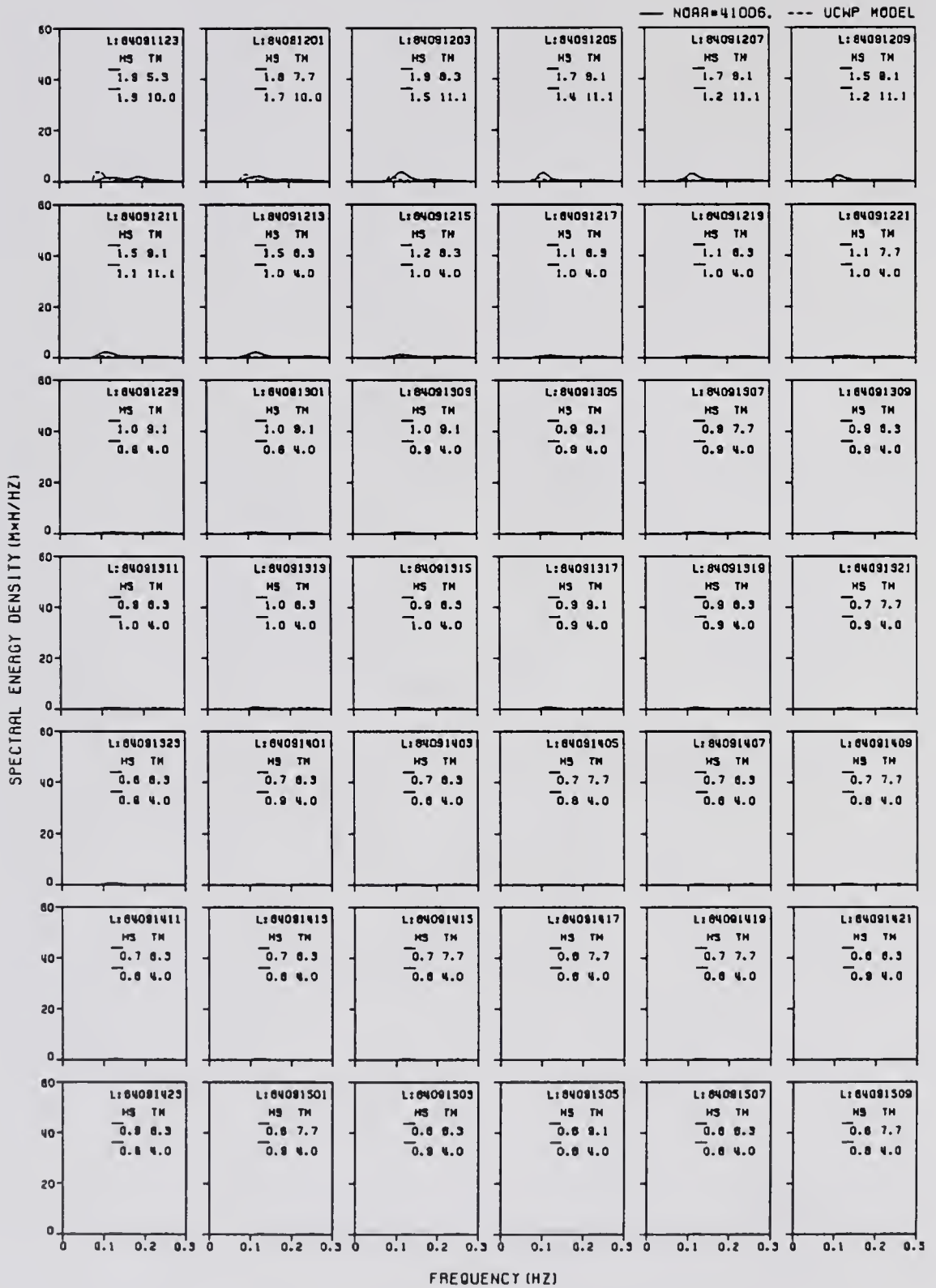


Figure C.1: Summary of computed and measured frequency spectra(continue).

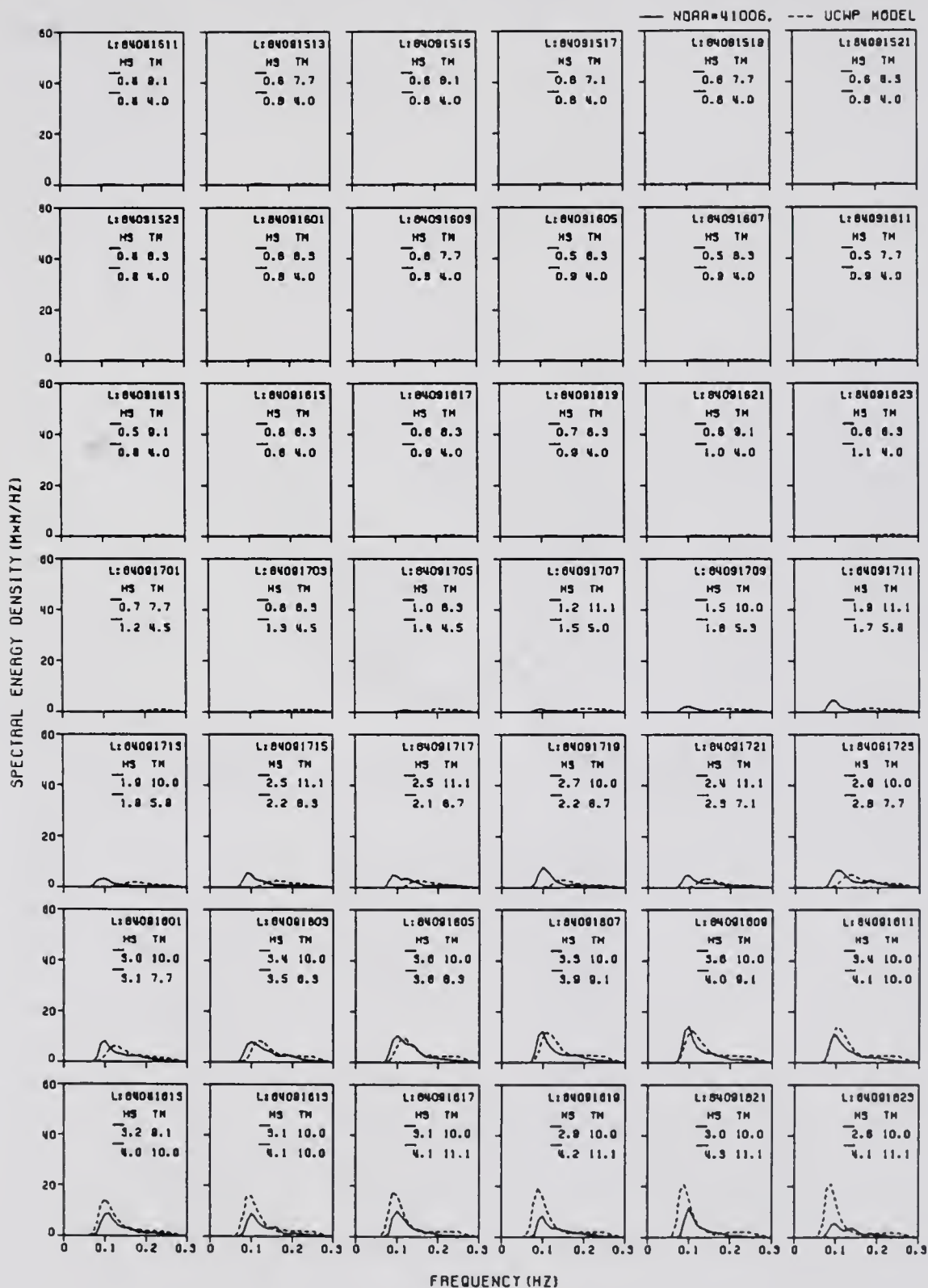


Figure C.1: Summary of computed and measured frequency spectra(continue).

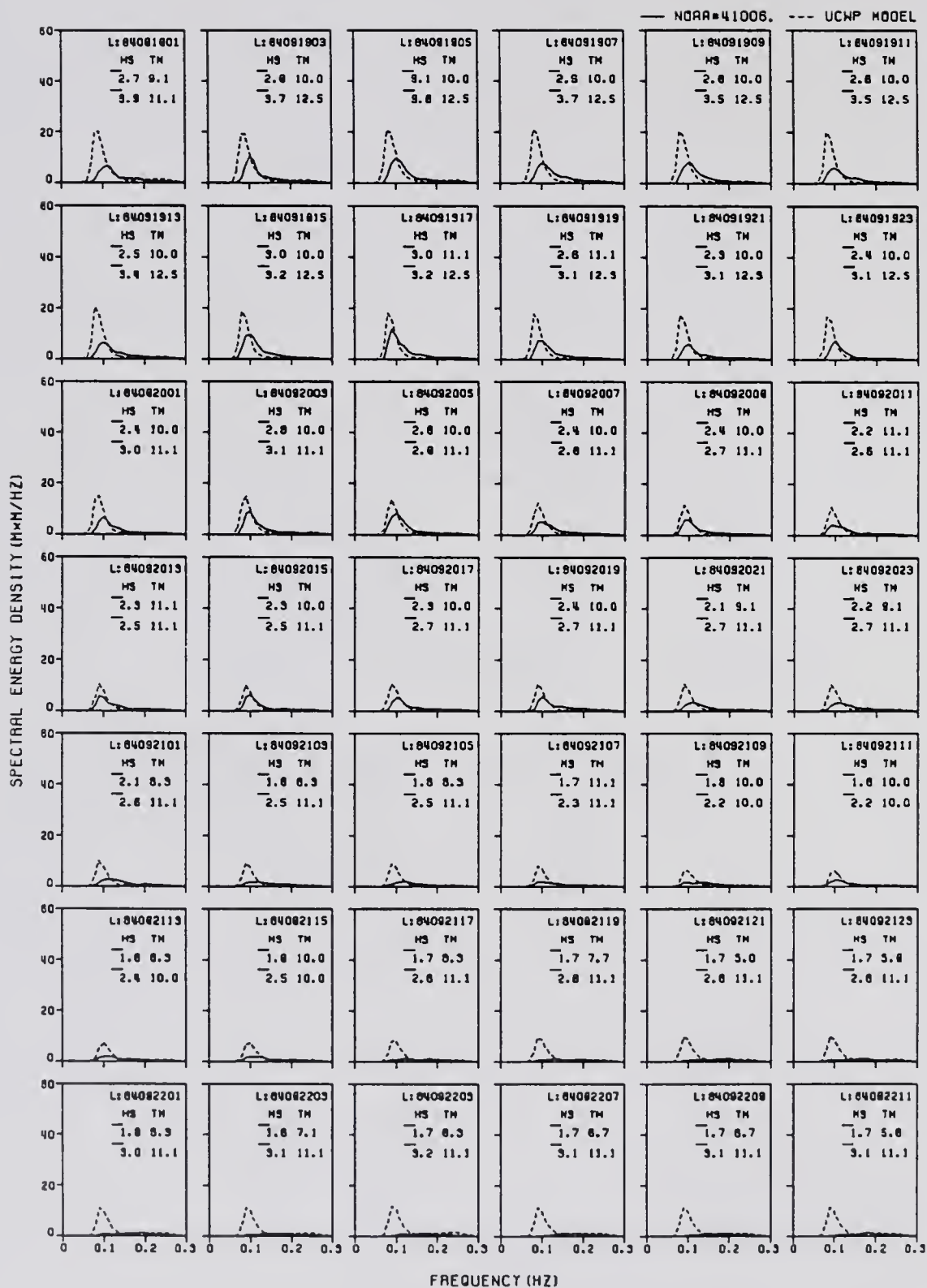


Figure C.1: Summary of computed and measured frequency spectra(continue).

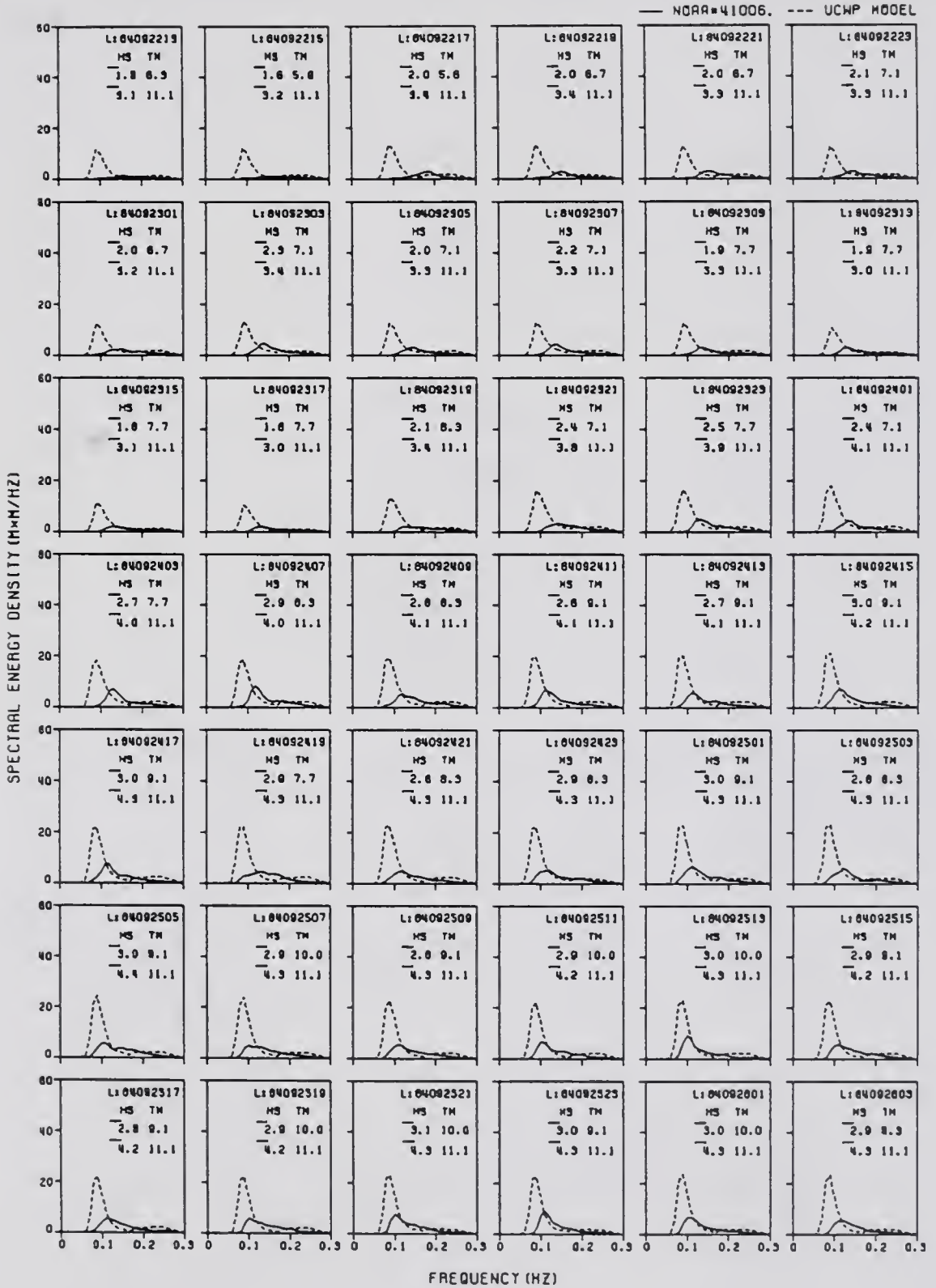


Figure C.1: Summary of computed and measured frequency spectra(continue).

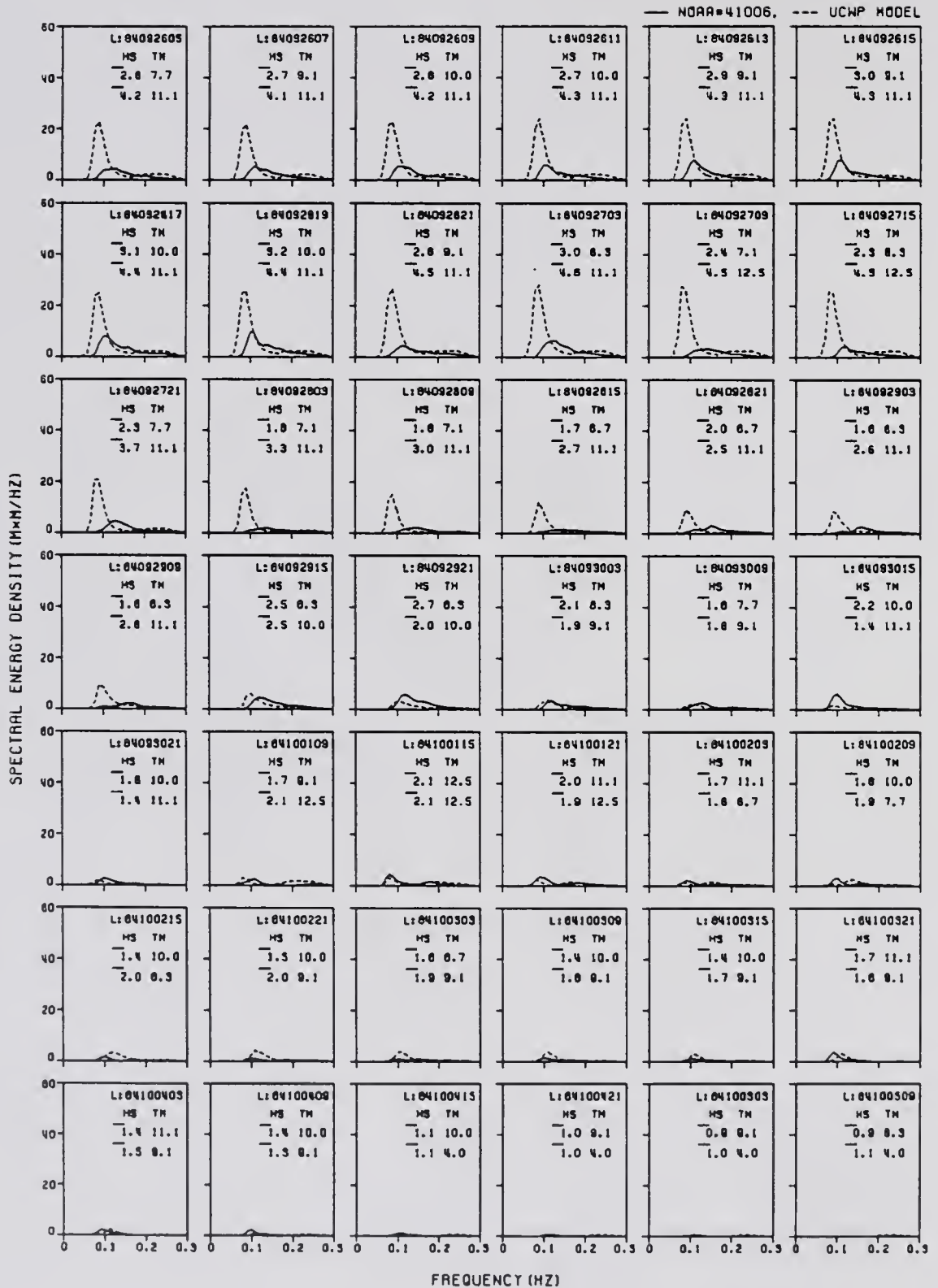


Figure C.1: Summary of computed and measured frequency spectra(continue).

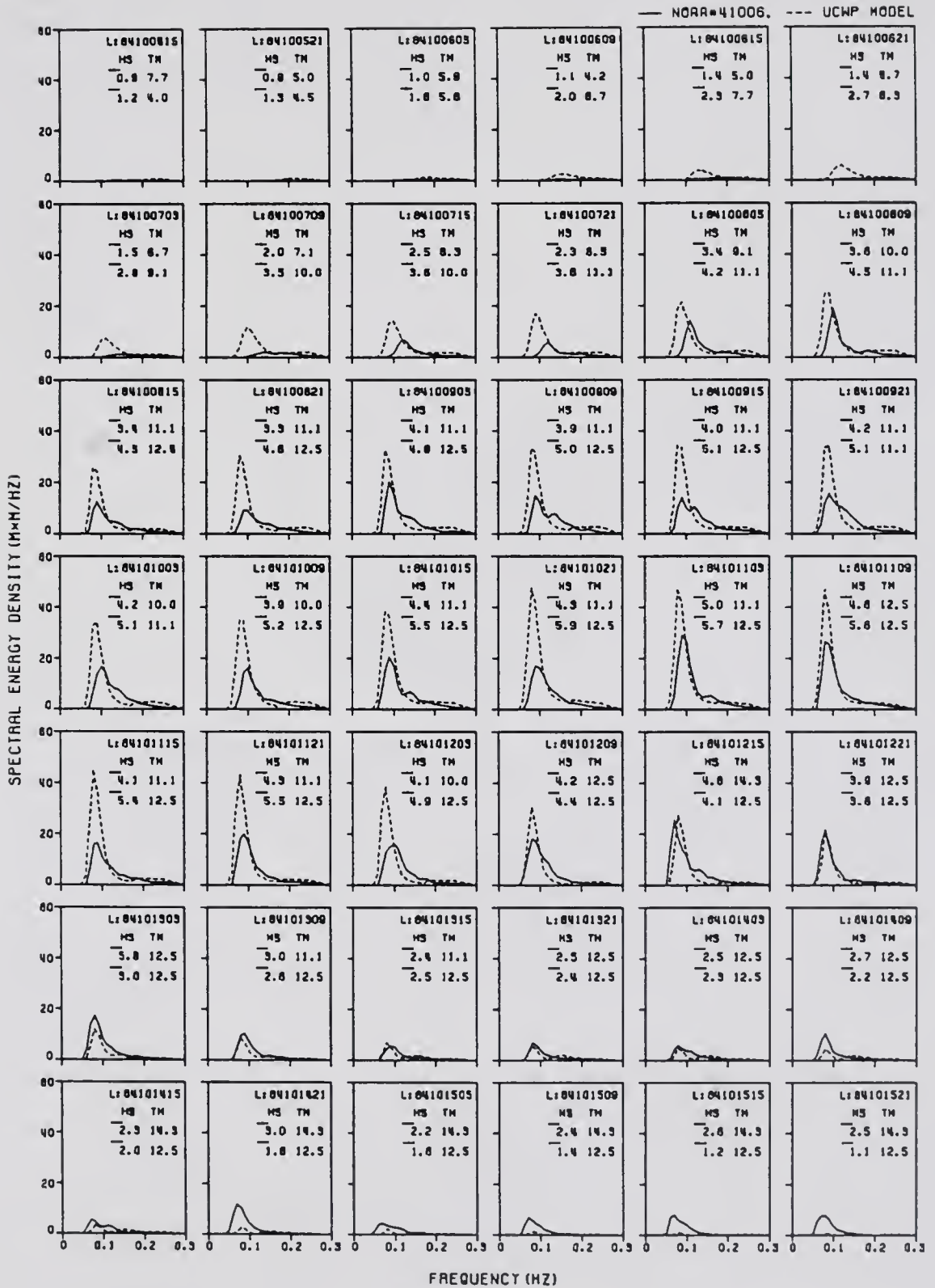


Figure C.1: Summary of computed and measured frequency spectra(continue).

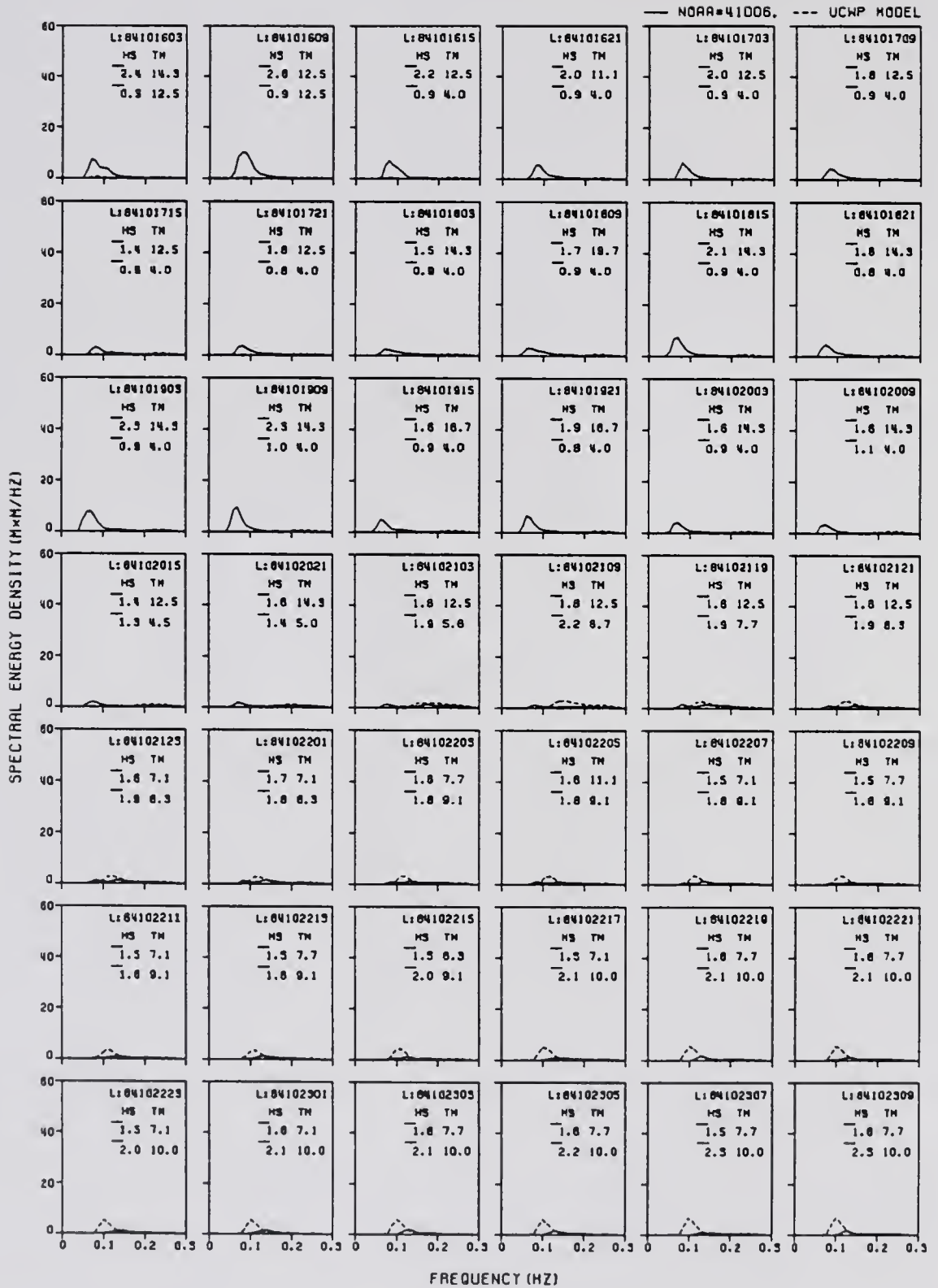


Figure C.1: Summary of computed and measured frequency spectra(continue).

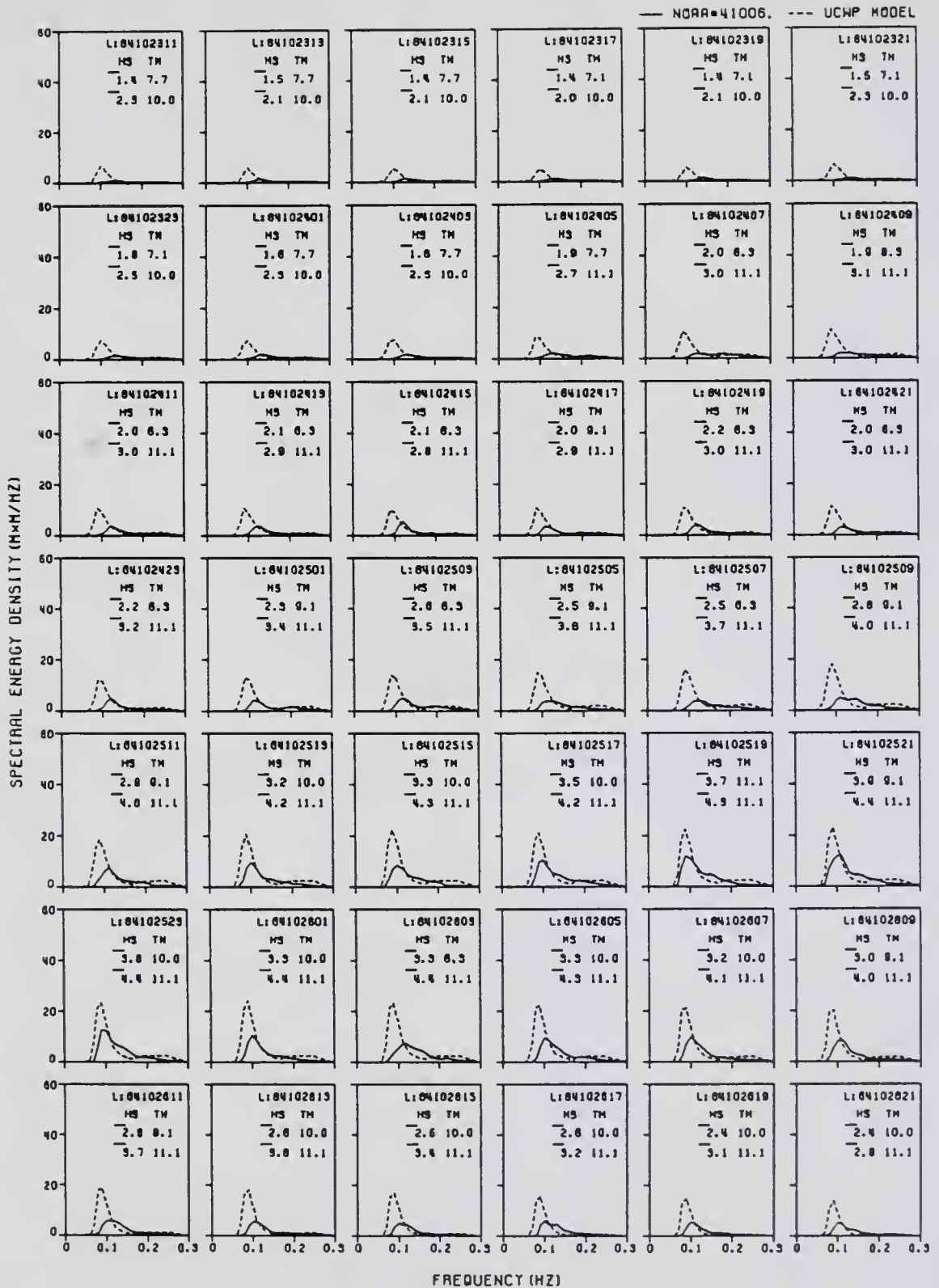


Figure C.1: Summary of computed and measured frequency spectra(continue).

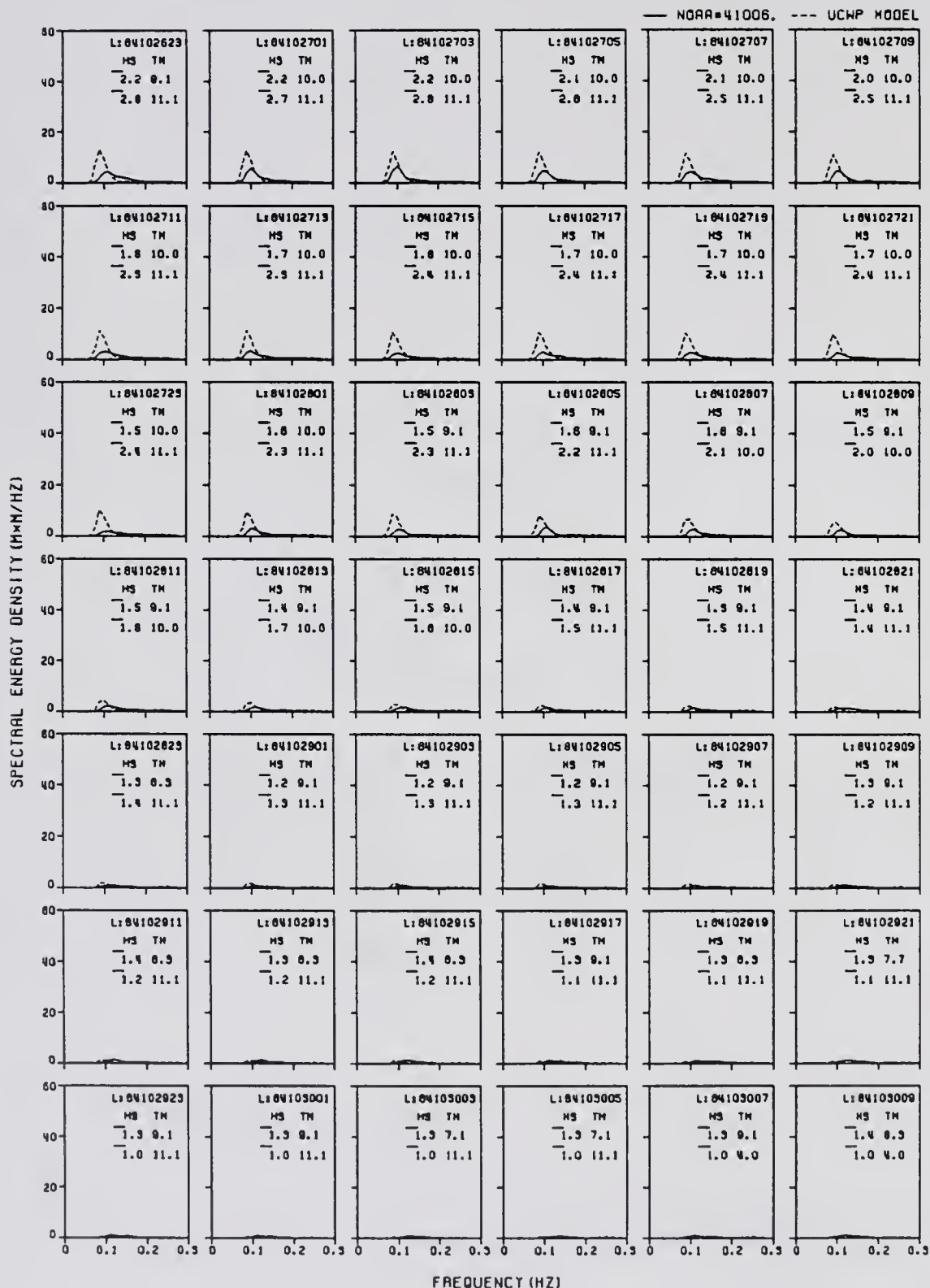


Figure C.1: Summary of computed and measured frequency spectra(continue).

## APPENDIX D PLOTS OF WAVE ENERGY FLUX ELEMENTS

### D.1 Summary of Figures

The rates of change of individual energy sources on the frequency domain are shown in the following figures for the six cases, Case 1 to Case 6, studied in Section 4.5. They are plotted here based on the result of numerical hindcasts from the UCWP model. Case 1 to Case 3 are in the deep water at the buoy #41006 location. Case 4 to Case 6 are in the shallow water at the CDN Marineland station. Case 1 occurred during a growing period under increasing wind condition at 1:00 a.m. Sep. 8, 1984, when winds were increasing from 26 knots to 31 knots. Case 2 is a decaying case at 5:00 a.m. Sep. 8, 1984, while onshore winds decreased from 30 knots to 28 knots in two hours. Case 3 is a local wind wave growth case at 23:00 p.m. Oct. 13, 1984, when winds remained a constant speed at 12 knots for the last twelve hours. Case 4 occurred during a growing period under increasing winds at 5:00 a.m. Sep. 8, 1984, when the onshore winds increasing from 27 knots to 30 knots in two hours. Case 5 is a decaying case at 1:00 a.m. Sep. 10, 1984, while onshore winds decreased from 34 knots to 29 knots in two hours. Case 6 occurred at 3:00 a.m. Sep. 10, 1984, when onshore winds kept dropping from 29 knots to 26 knots in two hours.

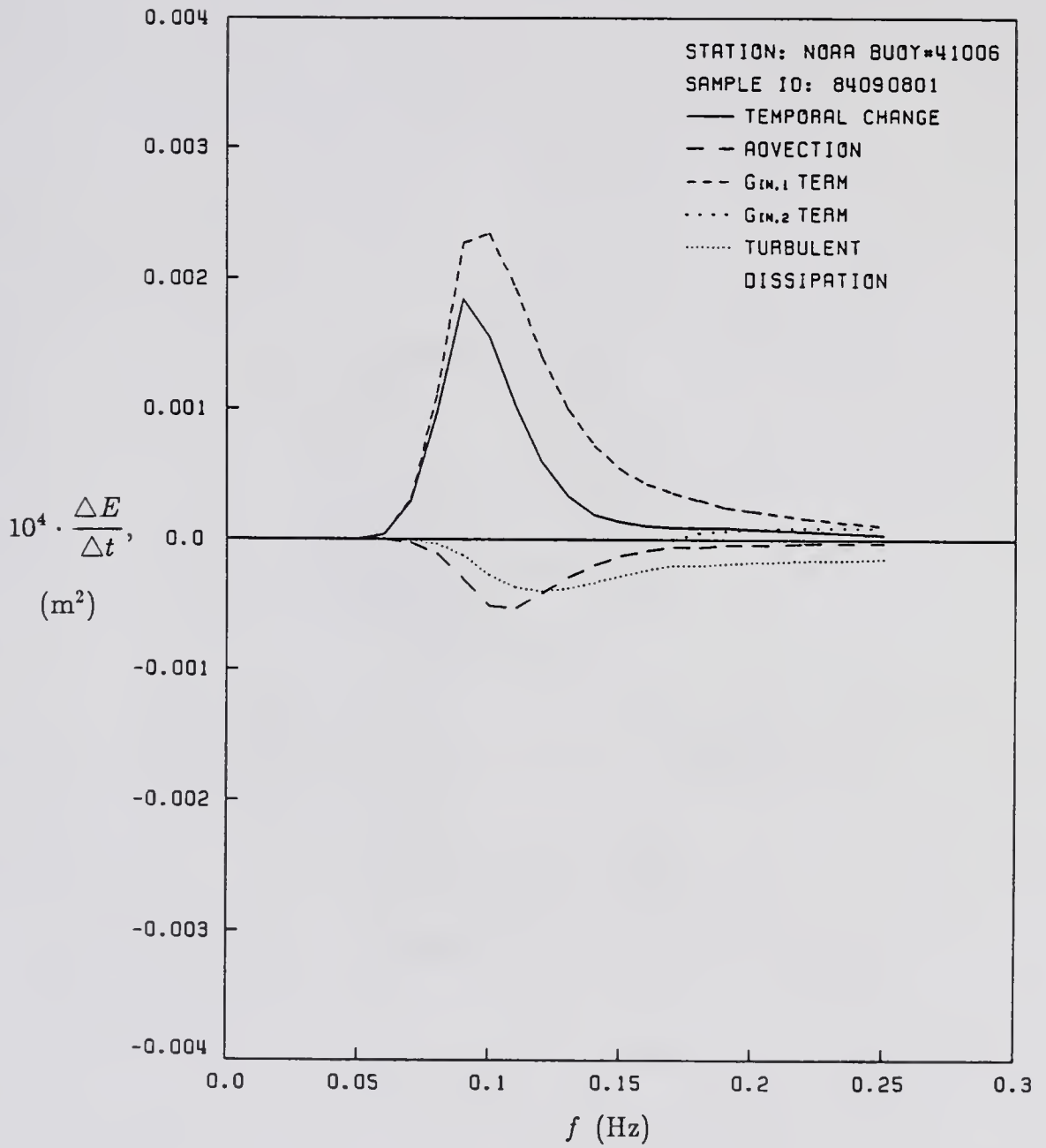


Figure D.1: Plot of deepwater energy fluxes in growing period; Case 1.

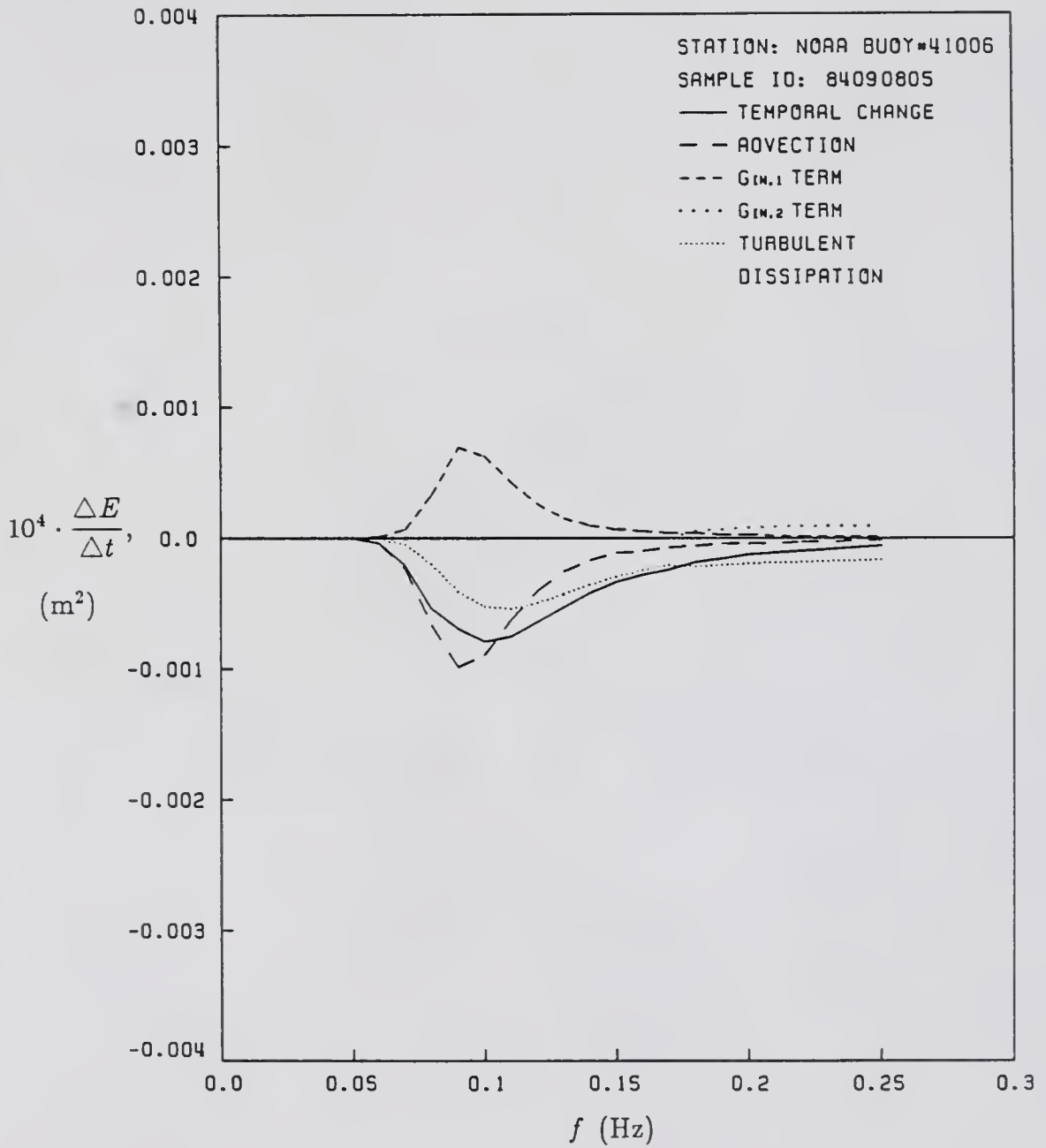


Figure D.2: Plot of deepwater energy fluxes in decaying period; Case 2.

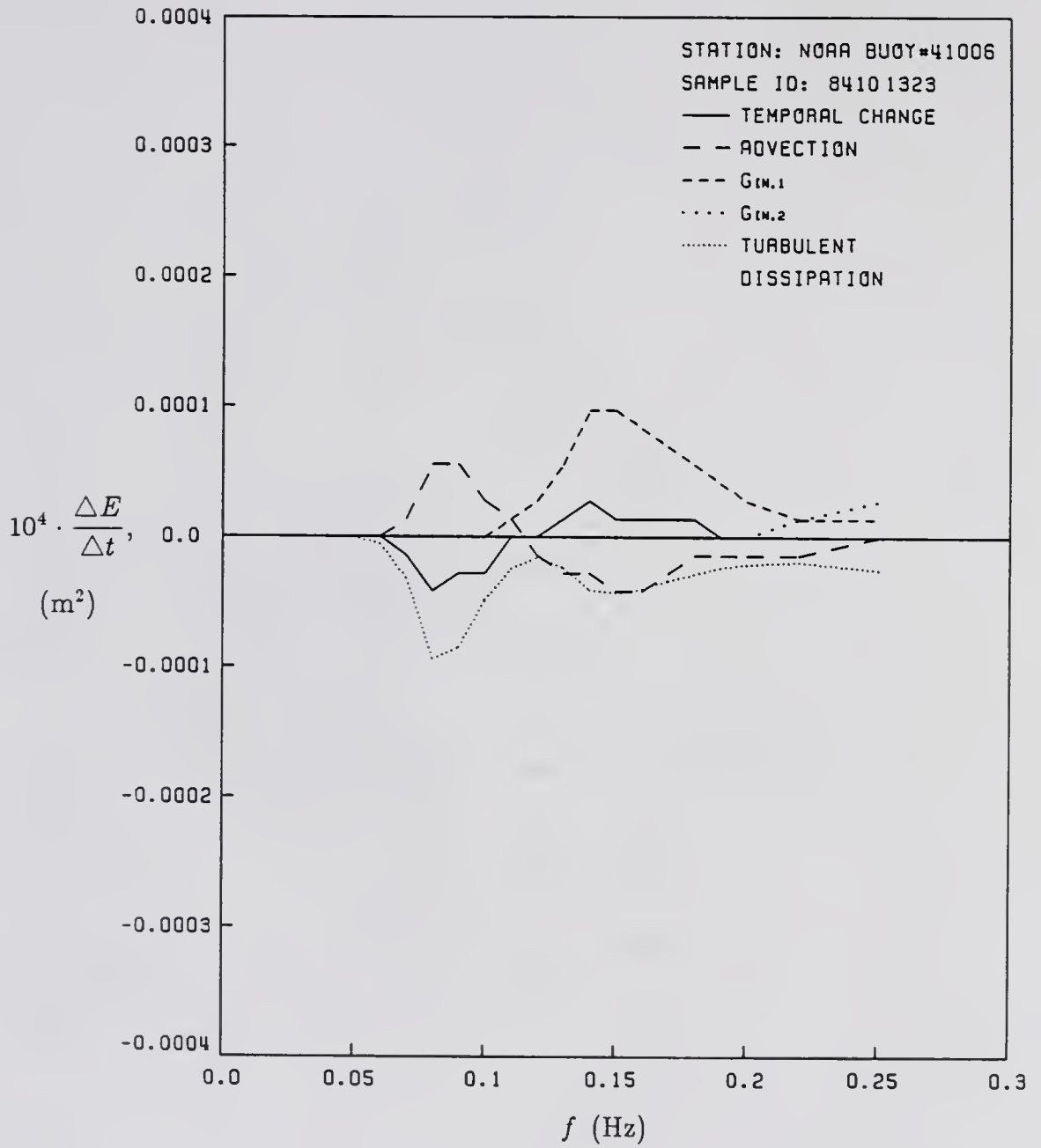


Figure D.3: Plot of deepwater energy fluxes during small winds; Case 3.

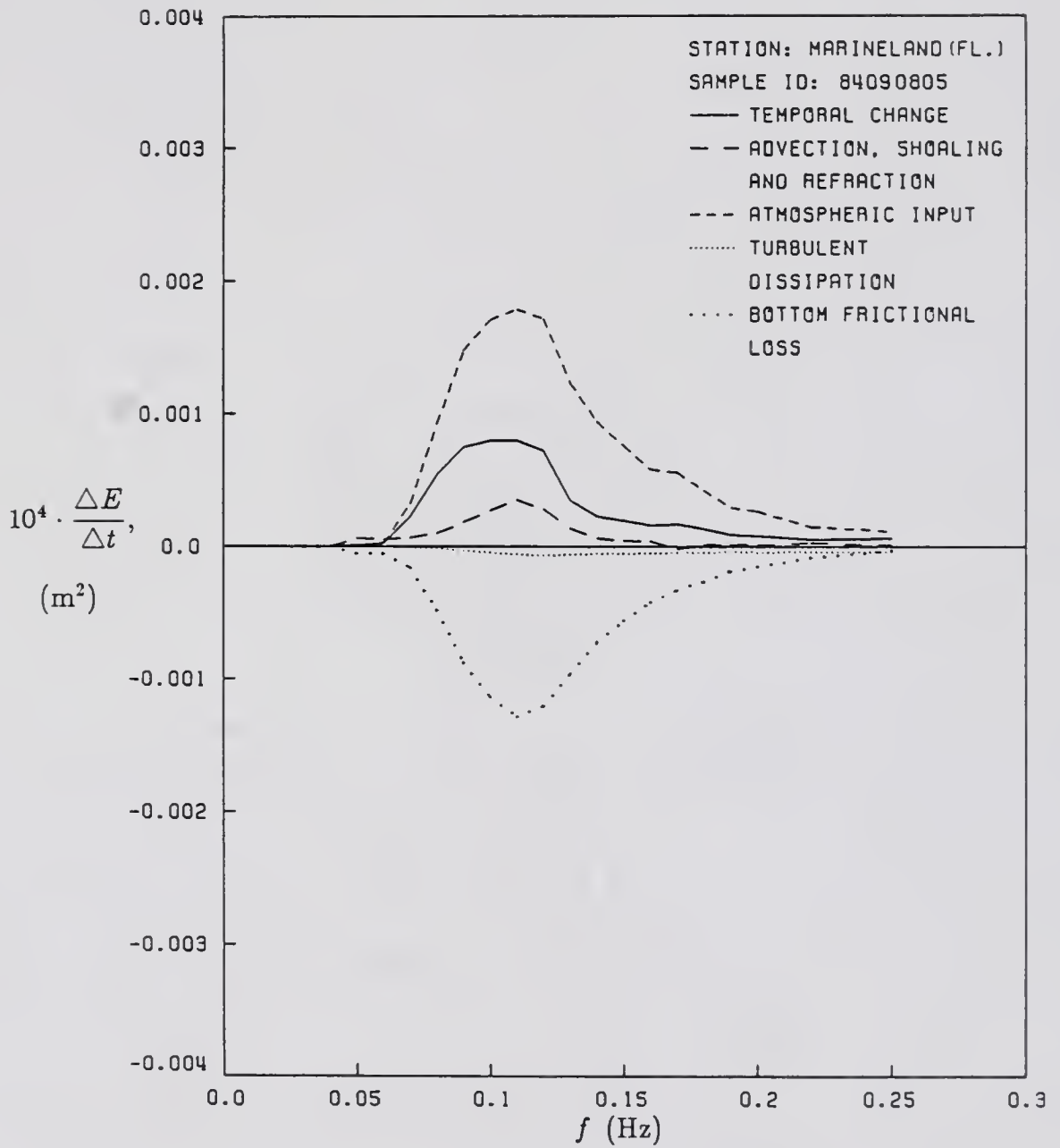


Figure D.4: Plot of individual shallow water effect sources during growing period; Case 4.

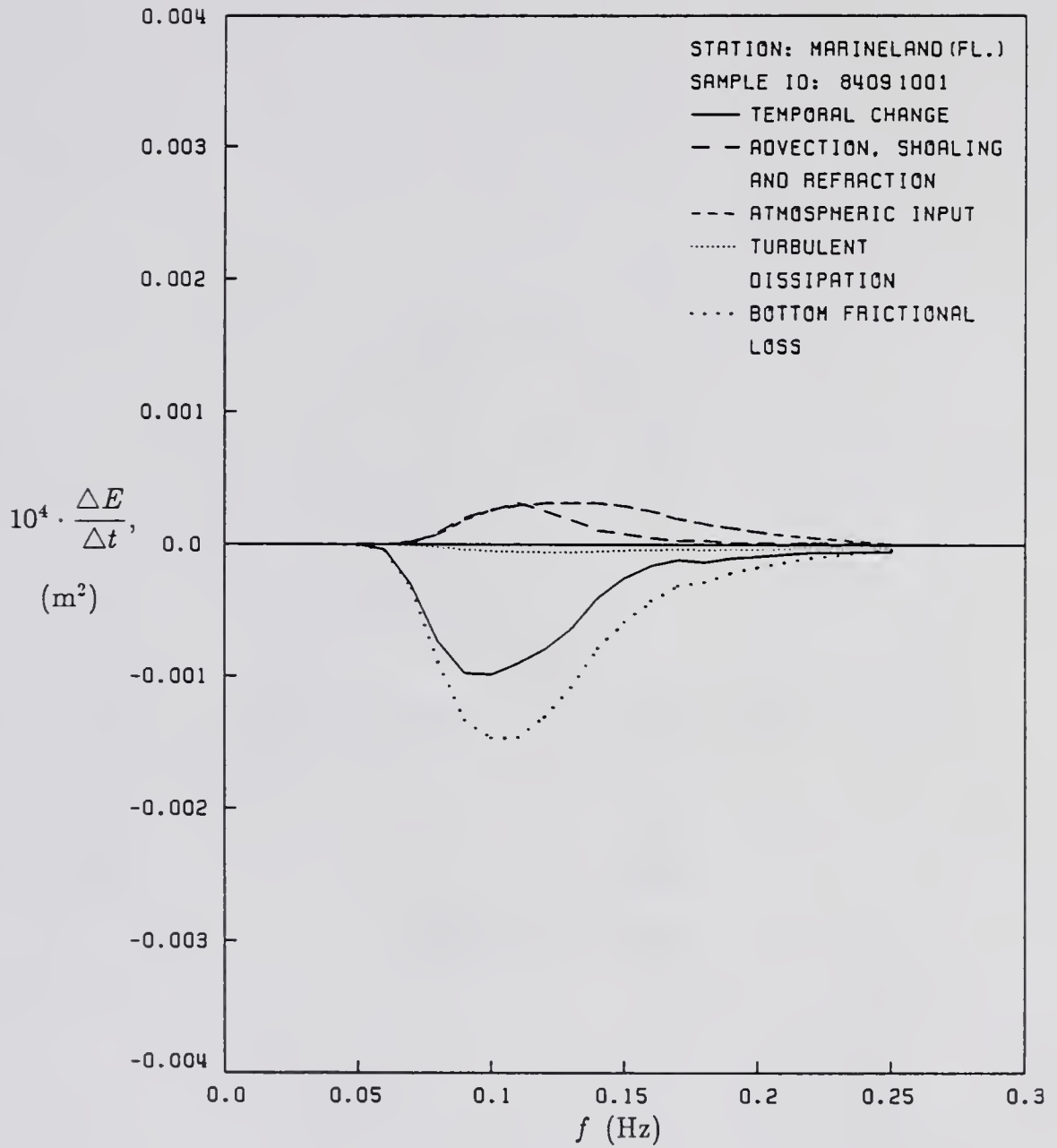


Figure D.5: Plot of individual shallow water effect sources during decaying period; Case 5.

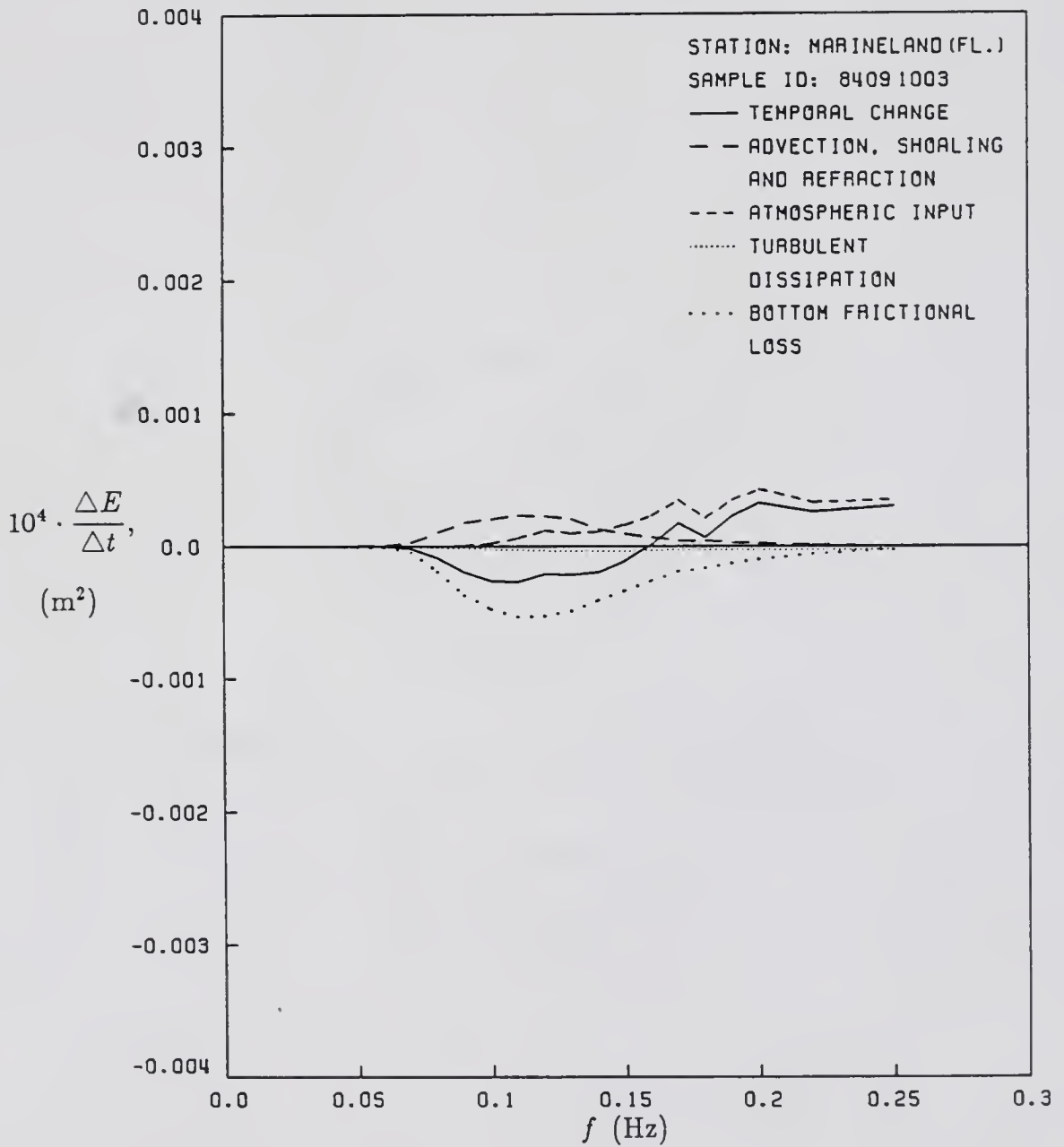


Figure D.6: Plot of individual shallow water effect sources during decaying period; Case 6.

## BIBLIOGRAPHY

- Barnett, T. P., 1968. "On the Generation, Dissipation, and Prediction of Ocean Wind Waves," *J. Geophys. Res.*, 73, 513-530.
- Battjes, J. A., T. J. Zitman, and L. H. Holthuijsen, 1987. "A Reanalysis of the Spectra Observed in JONSWAP," *J. Phys. Oceanogr.*, 17, 1288-1295.
- Bouws, E., H. Günther, W. Rosenthal, and C. L. Vincent, 1983. "A Similarity Based Spectral Form for Finite Depth Water: Wave Growth Relationships for the Entire Depth TMA Spectral Form," International Association for Hydraulic Research, Conference, Moscow.
- Byers, H. R., 1974. "General Meteorology," McGraw-Hill Book Company, New York and London.
- Cartwright, D. E., 1963. "The Use of Directional Spectra in Studying Output of a Wave Recorder on a Moving Ship," *Ocean Wave Spectra, Proc. of a Conf.*, Prentice-Hall, Inc., Englewood Cliffs, N. J., 203-218.
- Chen, Y., and H. Wang, 1983. "Numerical Model for Nonstationary Shallow Water Wave Spectral Transformations," *J. Geophys. Res.*, 88, 9851-9863.
- Clark, R. H., and G. D. Hess, 1974. "Geostrophic Departure and the Functions A and B of Rossby - Number Similarity Theory," *Boundary Meteorology* 7, Reidel Publ. Co., Dordrecht-Holland, 267-287.
- Collins, J. I., 1972. "Prediction of Shallow Water Spectra," *J. Geophys. Res.*, 77(15), 2693-2707.
- Corson, W. D., and D. T. Resio, 1981. "Comparisons of Hindcast and Measured Deepwater, Significant Wave Heights," WIS Report 3, U. S. Army Engineer Waterways Experiment Station, Hydraulics Laboratory, Vicksburg, Mississippi.
- Donelan, M. A., J. Hamilton, and W. H. Hui, 1985. "Directional Spectra of Wind-generated Waves," *Phil. Trans. Res. Soc., London*, A 315, 509-562.
- Günther, H., W. Rosenthal, T. J. Weare, B. A. Worthington, K. Hasselmann, and J. A. Ewing, 1979. "A Hybrid Parametrical Wave Prediction Model," *J. Geophys. Res.*, 84, 5727-5738.
- Hasselmann, K., 1974. "On the Spectral Dissipation of Ocean Waves due to Whitecapping," *Boundary-layer Meteo.*, 6, 107-127.

- Hasselmann, K., T. P. Barnett, E. Bouws, H. Carlson, D. E. Cartwright, K. Enke, J. A. Wieng, H. Gienapp, D. E. Hasselmann, P. Krusemann, A. Meerburg, P. Müller, D. J. Olbers, K. Richter, W. Sell, and H. Walden, 1973. "Measurements of Wind-Wave Growth and Swell Decay during the Joint North Sea Wave Project (JONSWAP)," *Deutsch. Hydrogr. X.*, suppl. A., 8(12).
- Hasselmann, K., D. B. Ross, P. Müller, and W. Sell, 1976. "A Parametrical Wave Prediction Model," *J. Phys. Oceanogr.*, 6, 201-228.
- Hasselmann, K., T. D. Taylor, and T. Y. Wu, 1968. "Basic Developments in Fluid Dynamics," Volume 2, edited by M. Holt, Academic Press, New York and London.
- Ippen, A. T., 1966. "Estuary and Coastline Hydrodynamics," McGraw-Hill Book Co., New York.
- Jensen, R. E., 1983a. "Methodology for the Calculation of a Shallow Water Wave Climate," Wave Information Study (WIS) Report 8, U. S. Army Engineer Waterways Experiment Station, Hydraulics Laboratory, Vicksburg, Mississippi.
- Jensen, R. E., 1983b. "Atlantic Coast Hindcast, Shallow-Water, Significant Wave Information," Wave Information Study (WIS) Report 9, U. S. Army Engineer Waterways Experiment Station, Hydraulics Laboratory, Vicksburg, Mississippi.
- Kitaigorodskii, S. A., 1962. "Application of the Theory of Similarity to the Analysis of Wind-generated Wave Motion as a Stochastic Process," *Bull. Acad. Sci. USSR Ser. Geophys.*, No. 1, Vol. 1, 105-117.
- Lamb, H., 1932. "Hydrodynamics," Cambridge University Press, Dover Publications, New York.
- Large W. G., and S. Pond, 1982. "Sensible and Latent Heat Flux Measurements over the Ocean," *J. Phys. Oceanogr.*, 12, 464-472.
- Longuet-Higgins, M. S., D. E. Cartwright, and N. D. Smith, 1963. "Observations of the Directional Spectrum of Sea Waves Using the Motions of a Floating Buoy," *Ocean Wave Spectra, Proc. of a Conf.*, 111-132.
- Miles, J. W., 1957. "On the Generation of Surface Waves by Shear Flows," *J. Fluid Mech.*, 3, 185-204.
- Miles, J. W., 1959a. "On the Generation of Surface Waves by Shear Flows, II," *J. Fluid Mech.*, 6, 568-582.
- Miles, J. W., 1959b. "On the Generation of Surface Waves by Shear Flows, III," *J. Fluid Mech.*, 6, 583-598.
- Miles, J. W., 1962. "On the Generation of Surface Waves by Shear Flows, IV," *J. Fluid Mech.*, 13, 433-448.

- Mitsuyasu, H., 1985. "A Note on the Momentum Transfer From Wind to Waves," *J. Geophys. Res.*, 90, 3343-3345.
- Mitsuyasu, H., and T. Honda, 1982. "Wind-induced Growth of Water Waves," *J. Fluid Mech.*, 123, 425-442.
- Phillips O. M., 1957. "On the Generation of Waves by Turbulent Wind," *J. Fluid Mech.*, 2, 417-445.
- Pierson, W. J., and L. Moskowitz, 1964. "A Proposed Spectral Form for Fully Developed Wind Seas Based on the Similarity Theory of S. A. Kitaigorodskii," *J. Geophys. Res.*, 69, 5181-5190.
- Pierson, W. J., L. J. Tick, and L. Baer, 1966. "Computer Based Procedures for Preparing Global Wave Forecasts and Wind Field Analyses Capable of Using Wave Data Obtained by a Spacecraft," Sixth Naval Hydrodynamics Symposium, Office of Naval Research, Washington, D. C., 499-532.
- Resio, D. T., 1981. "The Estimation of Wind-Wave Generation in a Discrete Spectral Model," *J. Phys. Oceanogr.*, 11, 510-525.
- Resio, D. T., and B. A. Tracy, 1983. "A Numerical Model for Wind-Wave Prediction in Deepwater," Wave Information Study (WIS) Report 12, U. S. Army Engineer Waterways Experiment Station, Hydraulics Laboratory, Vicksburg, Mississippi.
- Resio, D. T., and C. L. Vincent, 1977. "A Numerical Hindcast Model for Wave Spectra on Water Bodies with Irregular Shoreline Geometry; Report 1: Test of Nondimensional Growth Rates," Misc. Paper H-77-9, U. S. Army Engineer Waterways Experiment Station, Hydraulics Laboratory, Vicksburg, Mississippi.
- Resio, D. T., and C. L. Vincent, 1978. "A Numerical Hindcast Model for Wave Spectra on Water Bodies with Irregular Shoreline Geometry; Report 2: Model Verification with Observed Wave Data," Misc. Paper H-77-9, U. S. Army Engineer Waterways Experiment Station, Hydraulics Laboratory, Vicksburg, Mississippi.
- Resio, D. T., and C. L. Vincent, 1979. "A Comparison of Various Numerical Wave Prediction Techniques," Presented at Offshore Technology Conf., Houston, Mar. Tech. Soc. and Amer. Soc. Civ. Eng., Pap. 3642, 2471-2478.
- Resio, D. T., C. L. Vincent, and W. D. Corson, 1982. "Objective Specification of Atlantic Ocean Windfields from Historical Data," Wave Information Study (WIS) Report 4, U. S. Army Engineer Waterways Experiment Station, Hydraulics Laboratory, Vicksburg, Mississippi.
- Sand, S. E., 1979. "Three-dimensional Deterministic Structure of Ocean Waves," *Inst. Hydrodyn. and Hydr. Engrg. Tech. Univ. Denmark*, Series paper 24, xi-177.

- Shemdin, O., K. Hasselmann, S. V. Hsiao, and K. Herterich, 1978. "Nonlinear and Linear Bottom Interaction Effects in Shallow Water," *Turbulent Fluxes through the Sea Surface, Wave Dynamics, and Prediction*, edited by A. Favre and K. Hasselmann, Plenum Press, New York, 347-372.
- Snyder, R. L., and C. S. Cox, 1966. "A Field Study of the Wind Generation of Ocean Waves," *J. Marine Res.*, 24(2), 141-178.
- Thomson, W. T., 1972. "Theory of Vibration with Applications," Prentice-Hall, Inc., Englewood Cliffs, New Jersey, 333-364.
- U. S. Army Coastal Engineering Research Center, 1984. "Shore Protection Manual," Vol. 1, U. S. Army Corps of Engineers, Fort Belvoir, Virginia.
- User Guide, 1984. "Data Processing Software Package," Version 1.1, Coastal and Oceanogr. Engr., Univ. of Florida, Gainesville, Florida.
- Vincent, C. L., 1984. "Shallow Water Waves: A Spectral Approach," 19th Coastal Eng. Conf., Houston, Texas, 370-382.
- Weare, T. J., and B. Worthington, 1978. "A Numerical Model Hindcast of Severe Wave Conditions for the North Sea," *Turbulent Fluxes through the Sea Surface, Wave Dynamics, and Prediction*, edited by A. Favre and K. Hasselmann, Plenum Press, New York, 617-628.

## BIOGRAPHICAL SKETCH

Li-Hwa Lin was born on January 16, 1956, in Taiwan. He received his Bachelor of Science degree in hydraulic engineering from the National Cheng-Kung University, Taiwan, in 1978. He then worked as a surveying officer in the military for two years. Upon completion of his military service, he was married to Miss Li-Chu Lee in July 1983, and in the same year came to the United States and enrolled in the Oregon State University as a graduate student. In 1983, he graduated with a master's degree in ocean engineering. In January, 1984, he entered the graduate school at the University of Florida in the Department of Civil Engineering. He has worked as a research assistant while earning the Doctor of Philosophy degree.

I certify that I have read this study and that in my opinion it conforms to acceptable standards of scholarly presentation and is fully adequate, in scope and quality, as a dissertation for the degree of Doctor of Philosophy.



---

Bent A. Christensen, Chairman  
Professor of Civil Engineering

I certify that I have read this study and that in my opinion it conforms to acceptable standards of scholarly presentation and is fully adequate, in scope and quality, as a dissertation for the degree of Doctor of Philosophy.



---

Hsiang Wang, Cochairman  
Professor of Coastal and Oceanographic  
Engineering

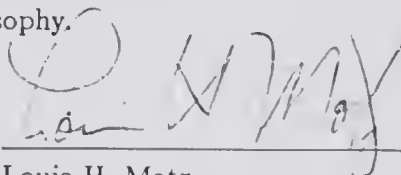
I certify that I have read this study and that in my opinion it conforms to acceptable standards of scholarly presentation and is fully adequate, in scope and quality, as a dissertation for the degree of Doctor of Philosophy.



---

Ashish J. Mehta  
Professor of Coastal and Oceanographic  
Engineering

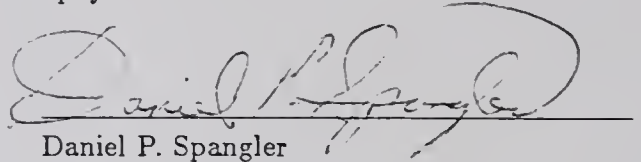
I certify that I have read this study and that in my opinion it conforms to acceptable standards of scholarly presentation and is fully adequate, in scope and quality, as a dissertation for the degree of Doctor of Philosophy.



---

Louis H. Motz  
Associate Professor of Civil Engineering

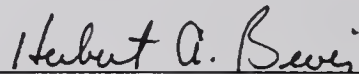
I certify that I have read this study and that in my opinion it conforms to acceptable standards of scholarly presentation and is fully adequate, in scope and quality, as a dissertation for the degree of Doctor of Philosophy.

A handwritten signature in cursive script, reading "Daniel P. Spangler", written over a horizontal line.

Daniel P. Spangler  
Associate Professor of Geology

This dissertation was submitted to the Graduate Faculty of the College of Engineering and to the Graduate School and was accepted as partial fulfillment of the requirements for the degree of Doctor of Philosophy.

April, 1988

A handwritten signature in cursive script, reading "Herbert A. Bewis", written over a horizontal line.

Dean, College of Engineering

---

Dean, Graduate School